UNIVERSITY OF CALIFORNIA
SANTA CRUZ

A GEOPHYSICAL STUDY OF ACTIVE VOLCANIC REGIONS AND SUBDUCTION ZONES

A dissertation submitted in partial satisfaction
of the requirements for the degree of

DOCTOR OF PHILOSOPHY

in

EARTH SCIENCES

by

Ricardo Garza-Giron

September 2021

The Dissertation of Ricardo Garza-Giron is approved:

_____
Professor Emily E. Brodsky, Chair

_____
Professor Slawek Tulaczyk

_____
Professor Thorne Lay

_____
Professor Susan Y. Schwartz

_____
Peter Biehl
Vice Provost and Dean of Graduate Studies

Table of Contents

List of Figures

List of Tables

Abstract

A GEOPHYSICAL STUDY OF ACTIVE VOLCANIC REGIONS AND SUBDUCTION ZONES

Ricardo Garza-Giron

The solid Earth is a dynamic system and as such is constantly changing. Some of these changes involve the large energetic release of volcanic eruptions, megathrust earthquakes or the moving of large ice sheets at the poles towards the oceans. Each of these phenomena have either a direct or an indirect impact for human populations and understanding them might be the only solution to be more resilient to their effects. Particularly, I am interested in understanding how volcanoes work and the effect that they might have in the places that surround them. Are volcanic regions intrinsically different from other places on Earth? Do they produce more earthquakes or less? What exactly happens inside, and nearby, of a volcano between and during major explosive eruptions? And do they influence the thermal structure of the surrounding crust? My doctoral dissertation has focused on addressing these types of questions by utilizing geophysical methods that include modern techniques applied to old data and the application of classic methods to modern data.

Chapter 1 explores the hypothesis that volcanic regions might be seismically different from non-volcanic regions by studying aftershock productivity, the ability for any given earthquake in a region to trigger another

earthquake, in Japan. Focusing our study area on Japan provides a great advantage for studying the statistical relationship of earthquakes and volcanoes, since the country has more than 120 active volcanoes and it is densely instrumented with seismometers. Our study showed that, in general, earthquakes in volcanic regions have the same chance of triggering another earthquake than earthquakes in non-volcanic regions, suggesting that aftershock productivity is not controlled by heat-flux in the crust but rather by other mechanisms such as the thickness of brittle crust.

Chapter 2 addresses the question of what happens inside a volcano while it is undergoing a prolonged explosive eruption sequence. The case study is Okmok Volcano in the Aleutian Islands in Alaska. In 2008 Okmok broke its historical pattern of effusive activity during the last 100 years by undergoing a Volcanic Explosivity Index (VEI) 4 hydromagmatic eruption. Co-eruptive seismicity is difficult to measure but essential to interpreting an eruption. It is potentially the highest resolution technique to chronicle the failure of the volcanic edifice and the evolution of volcanic vents. Standard earthquake detection methods often fail during this time as the eruption itself produces seismic waves that obscure the earthquake signals. We address this problem by applying template matching combined with machine-learning and fingerprint-based techniques (EQTransformer and FAST) to expand the existing seismic catalog of the Alaska Volcano Observatory (AVO) by finding seismic signals during the continuous eruptive sequence. We find that: (1) the most significant

co-eruptive seismic sequences occurred nearly half-way through the eruption and included a burst of long-period (LP) earthquakes directly under the eruptive vent followed by ash-rich plumes. Subsequent LP episodes occurred in bursts that migrated and were again followed by plumes. The LP earthquake rate and the plume rates anti-correlate. (2) A distinct population of volcano-tectonic (VT) earthquakes maintain a steady rate over a large region on the southern side of the caldera. These co-eruptive VTs have a larger b-value than before or after the eruption, which agrees with an open (extraction)/close(injection) system. (3) The cessation of the eruption is marked by a sudden burst of LP earthquakes which is accompanied and followed by a steady stream of small VT earthquakes that occur south (and therefore distinct) from the previous concentration of seismicity at the active vents. (4) The opening sequence extends to ~15 km depth and is marked by a migration, within minutes of the onset of the eruption, towards the previously identified center of deformation, which is located under the center of the caldera and is distinct from the eruptive vent. (5) The center of the caldera lacks any type of seismicity throughout the eruption. These previously inaccessible observations demonstrate that the co-eruptive LP and VTs show distinct behavior, likely signifying distinct controlling processes. LPs are strongly localized in space and time and directly precede, but are not concurrent with, mass ejection in contrast with the steady, widely distributed VTs. This distinction is consistent with LPs being the signature of an eruptive process that occurs when the pressurization state is high, i.e., volcanic system

partially closed, whereas VTs are a secondary effect that does not track the deflation of the magma reservoir and occur at a low stress-state, as indicated by the b-value, during the eruption which may be indicative of an at least partly open volcanic system.

Chapter 3 focuses on studying the effects of active volcanism on the thermal structure of a polar region, where such effects can have implications for how fast ice-sheets and glaciers flow into the Southern Oceans. In this study, we used the data of an airborne transient electromagnetic survey conducted in the McMurdo Sound, Antarctica, to investigate spatial variations of geothermal heat-flux (GHF) on a regional scale. We successfully increased the number of geothermal heat-flux constraints in the region by a factor of 5 and our results show that GHF variations are weakly controlled by the tectonic structure in the region but strongly controlled by the active volcanic province. We found that the only area clearly exhibiting high GHF (>100 mW/m^2) is Ross Island, which hosts one of the most active mafic volcanoes in the world, Mount Erebus. The GHF measurements from the western portion of the Terror Rift, the coastal ranges of the McMurdo Dry Valleys, show the lowest GHF values (e.g., 60-70 mW/m^2), but they also reveal local variations within the study area possibly related to cooling magma bodies from >~5Ma, while the rift-shoulder uplift to the west is typified by somewhat higher values (80-90 mW/m^2). The regional compilation of GHF constraints combined with our new data further reinforces the conjecture that areas of high GHF in Antarctica will generally be associated with Cenozoic

volcanic and magmatic activity while tectonic history has comparatively smaller impact on GHF distribution. These lessons from this best studied part of Antarctica may aid further improvements of a continent-wide GHF dataset which in turn can help improve future ice-sheet models and the projections of Antarctica's contribution to near-future global sea level rise.

Finally, chapter 4 discusses the occurrence of large, repeated earthquakes along the southeastern Mexican subduction zone and the relationship of the microseismic foreshocks and slow slip phenomena during the nucleation process of one of these earthquakes. After a complex sequence of tectonic events that started with the large M_w8.2 intraplate Tehuantepec earthquake, in February 2018, a M_w7.2 earthquake ruptured under Pinotepa Nacional, Oaxaca (hereby referred to as the Pinotepa earthquake). As it will be shown, this earthquake was preceded by an increase in Coulomb Failure Stress change as well as an increase in the interface coupling influenced by the growth of a slow-slip event (SSE) caused by the large Tehuantepec earthquake. At the same time, a cascade of microseismicity showed an increasing rate in the hypocentral region, leading up to the rupture of the Pinotepa earthquake. These observations suggest that the nucleation process of the Pinotepa earthquake was driven by a long-range change in the stress regime due to the SSE that was developing downdip but could not penetrate the hypocentral region. Furthermore, the rupture area of the M_w7.2 Pinotepa earthquake superimposes the area covered by the aftershocks of the M_s7.1 1968 earthquake. Multiple teleseismic records

available for both earthquakes provide an unprecedented dataset and the possibility to test the hypothesis that they ruptured the same distinct asperity along the megathrust boundary. The comparison of these records reveals that both earthquakes produced nearly identical seismic waveforms, indicating that, indeed, they ruptured the same frictional patch, and it validates the asperity model originally proposed by Lay and Kanamori (1981).

Dedication

To Gary, thank you for always encourage me to “go to the factory”, it paid off.

And to volcanoes, and all of those who share the love for understanding them.

Acknowledgements

The text of this dissertation includes reprints of the following previously published material. The co-authors listed in these publications directed and supervised the research which forms the basis for the dissertation.

Chapter 1: Garza-Giron, R., Brodsky, E. E., & Prejean, S. G. (2018). Mainshock-aftershock clustering in volcanic regions. Geophysical Research Letters, 45, 1370–1378. https://doi.org/10.1002/2017GL075738

Chapter 4: Cruz-Atienza, V.M., Tago, J., Villafuerte, C., Wei, M., Garza-Girón, R., Dominguez, L.A., Kostoglodov, V., Nishimura, T., Franco, S.I., Real, J. and Santoyo, M.A., (2021). Short-term interaction between silent and devastating earthquakes in Mexico. Nature communications, 12(1), 1-14. https://doi.org/10.1038/s41467-021-22326-6; Villafuerte, C., Cruz-Atienza, V., Tago, J., Solano, D., Garza-Girón, R., Franco, S., Domínguez, L. and Kostoglodov, V., (2021). Slow slip events and megathrust coupling changes reveal the earthquake potential before the 2020 Mw 7.4 Huatulco, Mexico, event. *Earth Space Sci. Open Archive*, *56*(10.1002). https://doi.org/10.1002/essoar.10504796.3

The work for this dissertation was partially supported by the CONACYT-UC MEXUS fellowship.

I would like to thank and acknowledge the support and work of all the people, groups and organizations that helped me throughout the course of my PhD.

First, I would like to thank my primary advisor, Emily Brodsky, for giving me the life-changing opportunity of coming to UC Santa Cruz to study volcano seismology with her. Thank you for letting me TA for you so many times, it was always a pleasure to watch you teaching class and learning from it. Thank you for putting up with me when I wanted to write my codes in a language unknown to you, for sharing your genius insight on every single plot that I showed you or any idea that I would dare to share with you. Thank you for helping me pursue my passion for field work and for letting me run down to the deepest depths of a seismological rabbit hole when my curiosity urged me to do so. It was not always easy for me to understand that behind every hardship there was a lesson, and I will always be grateful for your mentorship and for pushing my boundaries until I became a scientist. I would like to thank my secondary advisor, Slawek Tulaczyk, for trusting me to work with him and for allowing me to pursue my other professional passion: exploration geophysics. Thank you for having the patience when my obsession with my Okmok project slowed me down in the other projects. It was always an enormous joy to talk about science with you, you are one of the smartest people I have met, always one step ahead to every conclusion. And thank you for helping me realize my long-sought goal to become an Antarctic explorer and letting me proudly fly my Mexican flag in the southernmost continent of the world. I would also like to thank my third advisor and committee member, Thorne Lay. Thorne, it was a privilege to sit down in the same room as you for 6 years and listen to you comfortably explain complicated

topics of seismology. Many times, I found the motivation that I needed to keep going on with my PhD just by having a discussion in the IGPP room and making me feel that what we do matters and that it is extremely interesting. Thank you for always having your door open for us and for turning 5 minutes questions into one hour and a half lectures and thank you for letting me work with you on one of the prettiest projects I have worked on, chasing old paper records and feeling like a true old-school seismologist. Thank you to my committee member Susan Schwartz for all her mentorship and support. You were always the one that managed to put me on the ropes every time I presented my research and catch me on the little details that only an expert observational seismologist would find. Your passion for science and for life outside of the lab is contagious and served me as a model during my PhD years. I would also like to give a special thank you to Max Kaufman, for letting hop on a helicopter and see a glacier for the first time in my life. We were supposed to work together only one day, and you let me work with you for more days in the Cook Inlet and then you invited me to help you in the Aleutian Islands expedition. It was fascinating watching you work and learning from you. Thank you for your friendship and for showing me how a true pro works in the frontlines.

I also want to thank and acknowledge the hard work and mentorship of all my collaborators. Stephanie Prejean and Matt Haney, for sharing their extended knowledge on volcano seismology and guiding me through the "Devil's details" that one must navigate when studying volcanoes in Alaska or elsewhere.

I would also like to thank all the people at AVO, for always treating me well and making me feel like I was a little part of your great family. Thank you to Zack Spica for not only for sharing his valuable friendship and to go with me to the craziest adventures (from the Black Rock desert to the top of active volcanoes in Kamchatsky!), but also for sharing the love for volcano seismology. Thank you to Victor Cruz-Atienza, for letting me collaborate in such a beautiful, complicated, and thorough project that Oaxaca was. Your true passion for understanding is very contagious and motivational. 5 hour-long meetings will hardly ever be so much fun! And an enormous thank you to my best, nerd friend, Carlos Villafuerte. 13 years working together, from our first calculus class to the end of the PhD. I have learned so much from you and I admire you a lot, you are the smartest and most noble person I know.

I would like to thank all of the EPS faculty, it was always great sitting in your classes and talking to you in the hallways, and big thanks to all the EPS graduate students that shared with me this marathonic endeavor, especially to Galen Gorski, who was my academic brother since day zero. Thank you to the EPS department staff, especially to Jennifer Fish and Amy Kornberg, your help with work-related things and your kind personal talks really helped me get through. Thank you to Zack Kornberg and Sabrina Dalbesio for always helping us out with managing the Seismo Lab, and a special thank you to Ed Boring, who's genius always managed to sort out any computer problem that could come up!

Thank you to Peter Webley for providing the plume data for Okmok and for his help explaining how to interpret satellite imagery. I am also grateful to Lingling Ye and Satoko Murotani for taking on the troublesome task to scan the historical WWSSN records at the ERI.

I want to express my massive appreciation and gratitude towards all the Seismo Lab students, postdocs and visiting researchers that shared some time with me while at UCSC. I was always proud of our little family. I felt like every single time I walked into Seismo-coffee my scientifical boundaries were being pushed and talking science every day was everything I hoped for in my PhD. Special thanks to my office mates Esteban Chaves-Sibaja and Travis Alongi, and to Heather Shaddox and Nadav Wetzler, for putting up with me all those years and for thoroughly discussing science until exhaustion wore us out or until you hated me.

Big thank you my Santa Cruz friends (Gary, Susan, Wyeth, Risa, Seth, Mark, Sharon, Larry, Tom, Howard…and many others). Drinking coffee, cooking or being in the ocean with you always brought the calm that I needed when things were not easy and the excitement to live life in such an amazing place.

Finally, I want to acknowledge the unconditional support of my people in Mexico. To my dad, Ricardo, for pushing himself so hard throughout the years to put me and my siblings through school and for being such a role model when it came to wake up in the morning, go do your work passionately, come home late, and then repeat the next day. To my mom, Cecilia, for your infinite patience and

love. For sacrificing everything in your life to stay home with us and raise us, and for always telling me to pursue my own passions and goals. To my siblings Pame and Pato, for their support through the toughest times and always making me feel that home was closer than I though and that I am not as crazy as I think I am. To my best friend Josema, who gave me the money to go to my first AGU and told me to “go get a PhD”, and who has always been a major presence and support in my life since we are 4 years old. And to all of my solid group of friends back home, thank you for you love and support always. To my grandparents, for raising such beautiful extended families. I could not be with some of you until the end, but you always made me know how proud you were of me and that our connection goes beyond this life. And to all my crazy, loving aunts, uncles, and cousins, I am just the luckiest guy in the world to be part of such an amazing clan, los amo a todos!

Chapter 1 – Mainshock-Aftershock Clustering in Volcanic Regions

1.1 Introduction

Seismicity is a ubiquitous feature of active volcanic regions. Earthquakes are some of the prime indicators of magmatic movement and in many cases the most reliable precursors of eruptions (Sparks, 2003). As direct manifestations of the brittle failure of the rocks surrounding a volcanic system, earthquakes provide an indication of the stress state of the crust and insight into its rheological properties. Systems with large differential stresses stored will be prone to failure; those that are unstressed or accommodate differential stresses through viscoelastic or other creep processes will not easily create earthquakes. Furthermore, the propensity to generate small earthquakes can be read as a sign of heterogeneity (Mogi, 1963; Schorlemmer et al., 2005; Wiemer & McNutt, 1997; Wiemer & Wyss, 2002). Therefore, the tendency to generate earthquakes could potentially be used as a probe of the stress and strength state of the volcanic region.

Abrupt changes in the stress field of the crust manifest as earthquake breakouts that follow mainly two characteristic behaviors: swarm-like and mainshock-aftershock sequences (Utsu, 1971). Many studies claim that swarms are more common near volcanoes than elsewhere (e.g., Benoit & McNutt, 1996; Minakami, 1961); however, the commonality of aftershocks near volcanoes, either within swarms or as pure mainshock-aftershock sequences, has not been

well studied. At least one study suggests that earthquake sequences in volcanic and tectonic areas have similar statistical properties, with some swarm-like sequences occurring in nonvolcanic areas (Vidale et al., 2006). Other work also suggested that volcanic sequences might have more in common with tectonic sequences than previously anticipated (Traversa & Grasso, 2010). In this work we follow up on this discussion by utilizing more modern data and a specific definition of mainshock-aftershock clustering to compare the behavior of earthquakes around volcanic and nonvolcanic regions with the goal of getting a better insight into the relationship between earthquake-earthquake interactions and the different processes that cause stress changes in the crust.

1.2 Measuring Mainshock-Aftershock Clustering

Perhaps one of the most diagnostic ways to determine whether earthquakes cluster in mainshock-aftershock sequences or not is the aftershock productivity law (Utsu, 1961). The number of aftershocks in a sequence that follow an earthquake varies as a function of the magnitude of the mainshock. These sequences are well fit by

$$N_{Aft} = K'10^{\alpha(M-M_c)} \quad (1\text{-}1)$$

where α is a constant near 1 (Felzer et al., 2002; Helmstetter et al., 2005; Reasenberg & Jones, 1989), K′ is the averaged aftershock productivity, and M_c is the minimum magnitude above which all earthquakes in the surveyed volume are observed. Here we utilize equation 1-1 to assess the mainshock-aftershock behavior and, for sequences that are well-described by equation 1-1, to

determine the productivity. The definition of mainshock-aftershock clustering in this work is a sequence of earthquakes that is spatially and temporally clustered such that it satisfies equation 1-1. In this sense, our mainshock-aftershock clustering detection algorithm is not designed to test for swarm-like behavior, but rather, it is used to detect which systems favor mainshock-aftershock clustering and which do not as well as to calculate their relative aftershock productivity. This is an important caveat given that even earthquake sequences that are considered as swarms can have mainshock-aftershock sequences within them.

A more complex seismicity model that includes magnitude variation, background rate, and time decay is well established through the epidemic type aftershock sequence (ETAS) model (Ogata, 1988). ETAS in its most commonly implemented form is appropriate for stationary seismicity, which volcanoes may not have. ETAS inversions are also notoriously difficult to stabilize and often require independently setting several parameters (Brodsky & Lajoie, 2013; Traversa & Grasso, 2010). The isolation of just one statistical law, the aftershock productivity law, allows us to ask a more restrictive set of questions of the data without these added complications.

The physical origins of aftershock productivity variations are still unknown (Page et al., 2016). Possible factors include heat flow (Yang & Ben-Zion, 2009) and associated seismogenic crustal thickness, rupture properties (Wetzler et al., 2016), and preexisting stress state (Yamanaka & Shimazaki,

1990). Since several of these factors are expected to affect volcanoes differently than ordinary tectonic fault systems, it might be reasonable to expect a difference in aftershock productivity.

1.3 Practicalities

We use the Japan Meteorological Agency (JMA) seismic catalog for 1998–2016 to measure the propensity of earthquakes to cluster into mainshock-aftershock sequences and aftershock productivity in Japan. This study in many ways revisits the classic work of Mogi (1963), measuring these quantities for the same reason with the benefit of more modern data. We formed subcatalogs for each of the 46 active volcanoes that are constantly monitored by JMA by using hypocenters within 20 km of each vent (Figure 1-1). The 20 km limit is short given that previous work has shown that distal volcano-tectonic events are observed as far as 45 km from the site at which eruptions happen (White & McCausland, 2016). However, this conservative approach better avoids larger tectonic structures that could exist nearby. Even though a much smaller radius may isolate volcanic processes better, our test requires large enough areas to capture statistically significant numbers of earthquakes (below). (Appendix A section A-3 contains an alternative approach to subcatalog definition.) We recognize that small, long-period earthquakes, and other unusual seismicity common at some volcanoes, may not be well represented in the earthquake catalogs used here. Thus, our analysis is relevant only to cataloged seismicity.

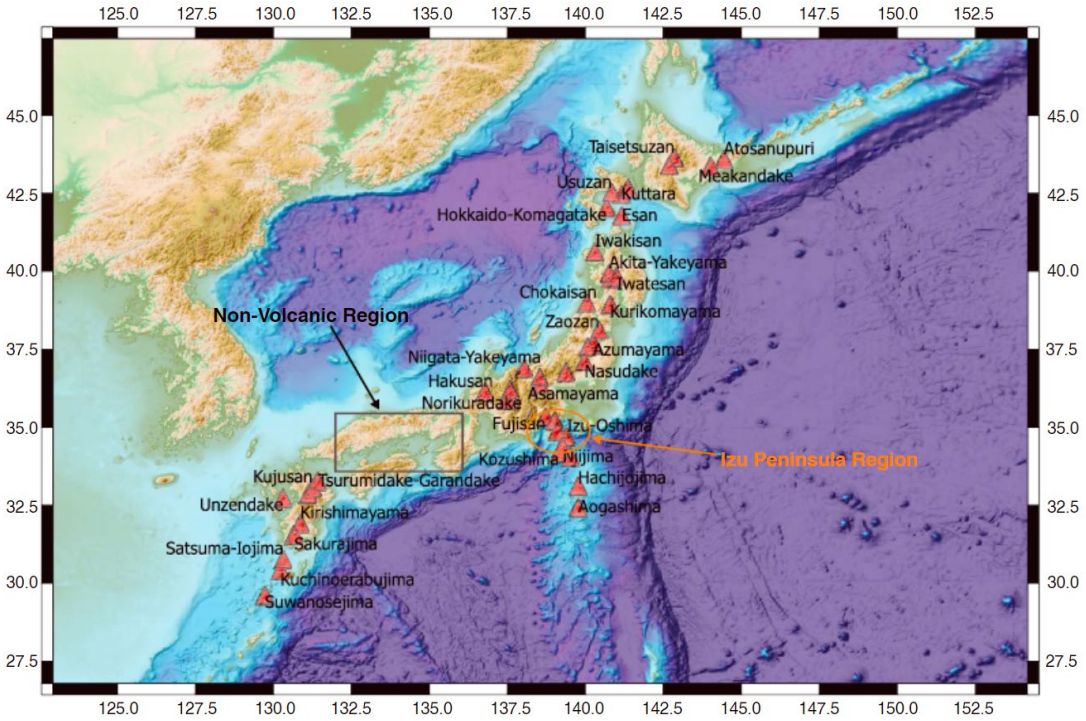

Figure 1-1. Active volcanic regions in Japan. The orange circle shows the highly active Izu Peninsula region, where Miyakejima volcano had a VEI 3 eruption in 2000. The black rectangle shows the Shikoku Island non volcanic region.

To create a comparison data set for nonvolcanic regions, we analyzed the data of the southwest section of Honshu Island, which is characterized by a lack of volcanic activity and the occurrence of large earthquakes such as the 1995 Kobe earthquake with the potential to trigger a substantial number of aftershocks. We divided the region into a grid with 10 km spacing and used the earthquakes within a 20 km radius from each node to estimate the local aftershock productivity (Figure A-4). We used a 15 km depth constraint to limit the study to the crust and avoid the contribution of large interplate earthquakes.

In order to determine mainshock-aftershock sequences, we first define the mainshocks by sorting the events by magnitude from the largest to the minimum magnitude of completeness. The latter is estimated by detecting the maximum curvature of the frequency-magnitude distribution. We let the largest earthquake in the catalog to be the first mainshock in the process. In order to prevent mixing of sequences, we then eliminate from further consideration as potential mainshocks the aftershocks (see definition below), the earthquakes one day before the mainshock and the earthquakes one day after the last aftershock. We repeat the process for the second largest earthquake and so on until there are no events left in the catalog. The aftershocks of each mainshock are those events that occurred within a fixed time window (3 days) after its onset and at a distance less than or equal to 2 times the mainshock fault length. Even though using an estimated fault length for constraining the spatial window helps us parametrize our search based on the earthquake physical properties, the choice of how many times this should be multiplied by and the choice of the time window are completely arbitrary. We did perform tests using different combinations and we selected the ones that gave solutions that were within a common range of values. Fault length is calculated assuming a 3 MPa stress drop and a circular fault (Kanamori & Anderson, 1975). Mainshocks are restricted to within 15 km from the center of the volcanoes so that their accompanying aftershocks are entirely included in the larger search area. Although this earthquake model is clearly simplified, it provides a consistent measure of

affected area for each sequence. The reported relative aftershock productivity values enable comparisons between regions. Sensitivity to the time and space window options is assessed in Appendix A.

1.4 Mainshock-Aftershock Clustering Detection and Goodness of Fit

As mentioned above, we define mainshock-aftershock clustering as those sequences that obey equation 1-1 following a linear trend between mainshock magnitude and the logarithm of the average number of aftershocks. A successful fit has a probability (p value) of the observed correlation coefficient R2 between the N data points of less than 10^{-2}.

However, the observation of such a linear trend emerging from the initial identification is not sufficient to determine whether the apparent mainshock-aftershock clustering stems from temporal clustering. An insidious artifact is possible because we are ordering the mainshocks in a magnitude-dependent hierarchy. The progressive elimination of earthquakes can result in more earthquakes being associated by chance with the first large earthquakes than the smaller earthquakes at the end of the counting process. To solve this problem, we performed a permutation over the time vector of each catalog by randomly resampling the time vector without replacements. We then ran 200 of these time-shuffled subcatalogs through the algorithm and compared the results to the original data (see example in Figure 1-2). To use this shuffling criterion, we require a sufficient number of mainshocks identified (here 3) and a sufficient number of data points with values above the shuffled realizations (here 90%).

Figure A-1 in Appendix A shows an example of a volcanic region that fails the shuffling test.

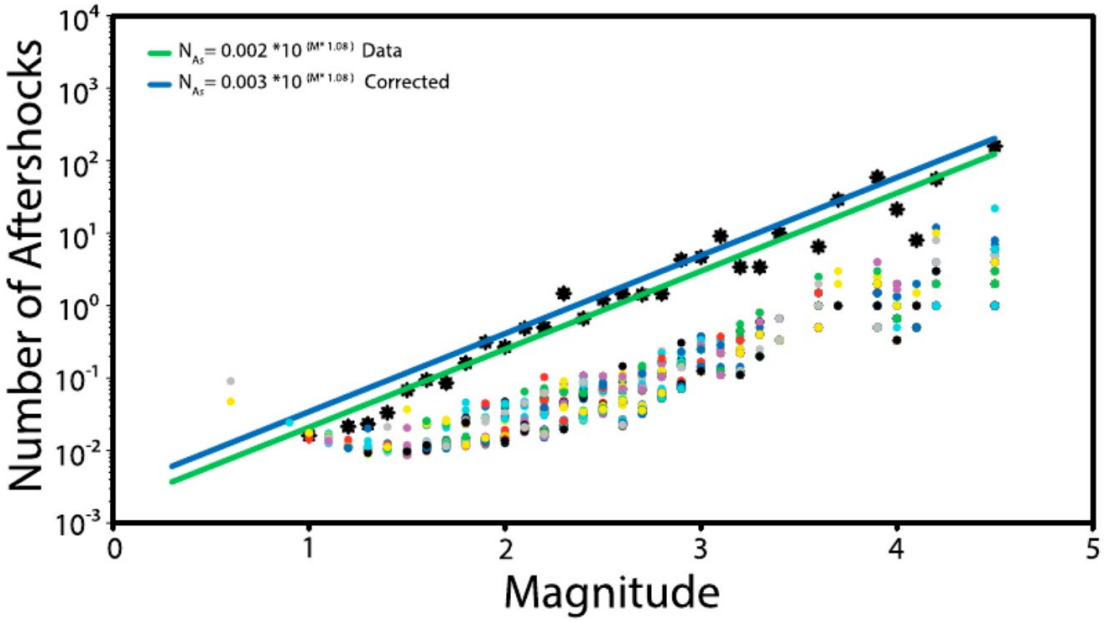

Figure 1-2. Example of aftershock productivity observation (Eq. 1-1) for volcanic region of Ontakesan. The black stars are the data, and the color dots represent the different runs with the shuffled time sequences. We show the linear fit to the data (green) and the adjusted productivity value for the completeness of the catalogue (blue). For Ontakesan most of the data is resolved above the time-shuffled realizations, indicating that high mainshock-aftershock clustering is present in this region.

In summary, to successfully declare that earthquakes in a region cluster in mainshock-aftershock sequences, we require the following: (1) at least 1,000 earthquakes above the completeness magnitude, (2) at least 3 identified mainshocks, (3) the p value of the linear trend $<10^{-2}$, and (4) at least half of the data points (black stars in Figure 1-2) lie above 90% of the shuffled realizations. For this data set, the p value criterion is redundant as all systems that pass the

shuffle test also pass the p value criterion. More stringent criteria are discussed below and in Appendix A section A-4.

1.5 Observations

Out of the 46 volcanic areas, 20 had too few events in their catalog (N < 1,000) for analysis. The lack of seismicity can be due to either incomplete coverage or a genuine paucity of events. We note that our results are not relevant to these low seismicity volcanic systems, and such systems may have earthquakes with different statistical properties.

Only one volcanic region and very few of the non-volcanic regions have sufficient earthquakes but too few identifiable mainshocks for analysis (magenta slices in Figure 1-3). In such systems, either the occurrence of earthquakes is mostly Poissonian or most aftershocks belong to mainshocks of very similar magnitude. These systems fundamentally violate equation 1-1 for the space-time windows considered and are very rare.

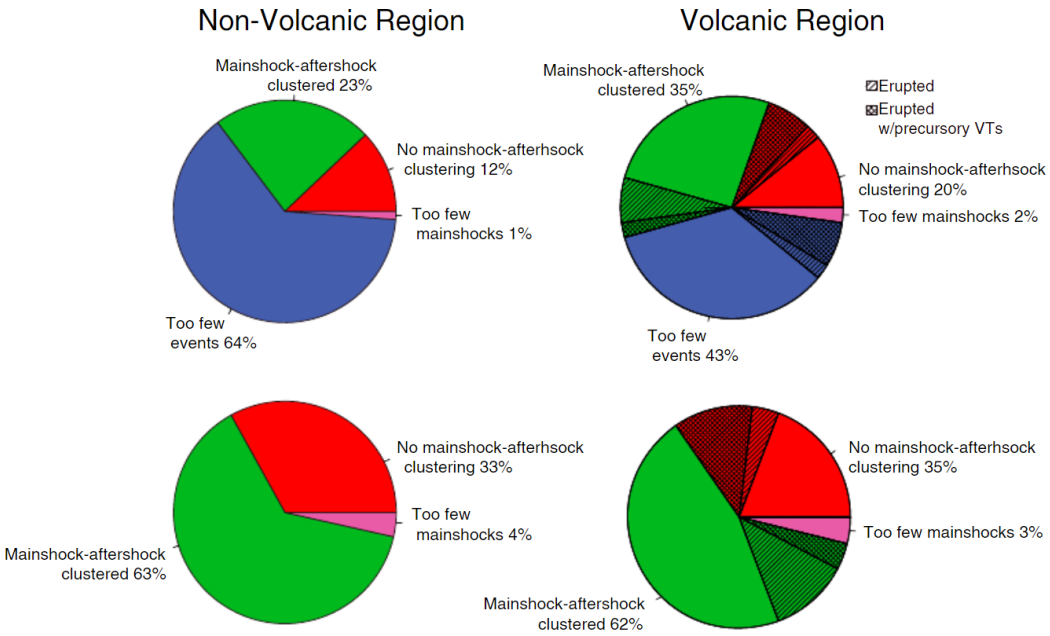

Figure 1-3. Pie chart compiling the results of the 46 volcanic regions (right) and all of the nodes of the non-volcanic region (left). All categories are included in the upper row and the domain is limited to the measurable categories in the bottom row. Blue: Areas with insufficient seismicity (<1000 earthquakes) to study clustering. This category is omitted in the bottom row. Green: Areas that show mainshock-aftershock clustering; Red: Areas that have sufficient total seismicity and identified mainshocks to examine clustering, but failed the time-shuffling test; Magenta: Areas with fewer than 3 identified mainshocks. The hatch slices represent the percentage of volcanoes that have had an eruption since 1998 and the crosshatch areas are the portion of eruptive volcanoes that showed signs of precursory volcano-tectonic events prior to the start of the eruption.

1.5.1 Existence of Aftershock Clustering

Mainshock-aftershock clustering was found in approximately 35% of the 46 volcanic regions and 23% of the non-volcanic grid nodes. If we only consider areas with N ≥ 1,000, 62% of the volcanic regions showed mainshock-aftershock clustering, 35% did not and 4%, which corresponds to only one system (Unzendake), did not have many identifiable mainshocks. For nonvolcanic

regions with N ≥ 1,000, 63% of the grid nodes had mainshock-aftershock clustering, 33% of the nodes did not, and 3% had enough events but not many identifiable mainshocks. Once the data are limited to well-recorded, high seismicity areas, the similarity of the values between environments is very clear (Figure 1-3).

The similarity suggests that a cascading brittle process couples the earthquakes even in the volcanic systems. It appears that a substantial portion of the seismicity recorded at a volcano is not directly indicative of magmatic processes but is a secondary effect stemming from earthquake-earthquake interactions and the accompanying brittle fracture mechanics. If magmatic processes make the mainshock, then the aftershocks are indirectly related to magmatic processes, but the indirect nature of the relationship is important to properly interpreting the seismicity. This inference holds even for the volcanoes that had eruptions during the study period (hatched and cross-hatched regions in Figure 1-3). The existence of an eruption does not result in an overall lack of aftershock clustering in the catalog.

At some volcanoes, aftershock clustering is identified only for certain isolation space and time windows (see Appendix A). However, the proportion of systems that fall into the categories of Figure 1-3 remains similar regardless of window options. Individual systems may have different optimal aftershock windowing parameters depending on the earthquake location accuracy and spatial distribution. However, these differences are not preferentially occurring

in any category. The proportion of systems that favor clustering as mainshock-aftershock sequences is a more robust observation than the identification of aftershock clustering at any single edifice.

Similarly, adjusting the goodness-of-fit measure can affect the number of identified mainshock-aftershock clustered regions in both volcanic and nonvolcanic areas. For example, in Figure A-7, we use a threshold of three-fourth rather than one-half of the data points exceeding 90% of the shuffled random realizations. The stricter criterion results in fewer regions identified as mainshock-aftershock clustered, but the comparability between the volcanic and nonvolcanic regions remains.

This feature is again captured in Table A-1 in Appendix A, which reports the ratio of earthquakes in identified mainshock-aftershock clusters to other events in the catalog. These ratios are between 0.2 and 1.3 with a median of 0.35. The preferred space and time windows miss some aftershocks by design in an attempt to be conservative in the aftershock identification. We conclude that at least one-fourth of the events are part of mainshock-aftershock sequences, which is a satisfactory level for analysis. The fraction of earthquakes in mainshock-aftershock sequence is not a robust statistic for an individual volcano; however, the proportion of volcanoes that are clustered in these types of sequences is.

A common idea shared by the volcano-seismology community is that the response of the country rocks of a volcanic region to a magmatic phenomenon

such as a dike intrusion or the inflation and/or deflation of a magma chamber will be expressed primarily by swarm-like activity, i.e., non-mainshock-aftershock clustered earthquakes of similar magnitudes (e.g., Lu & Dzurisin, 2014; McNutt, 1996; Minakami, 1961). Here we find results consistent with Vidale et al. (2006) in that aftershock sequences are a common property of crustal earthquakes independent of whether they occur in a volcanic or nonvolcanic environment.

1.5.2 Variations in Productivity

In order to assess relative levels of aftershock productivity, we utilize equation 1-1 with the best fit values for K' and α to project the expected number of aftershocks for a magnitude 3 earthquake. The procedure guards against the covariance of the fit parameters by utilizing the model prediction in the best-determined part of the magnitude range. We calculated these values both for volcanic regions where mainshock-aftershock clustering was successfully observed and for the median data set for the non-volcanic regions (Figure 1-4).

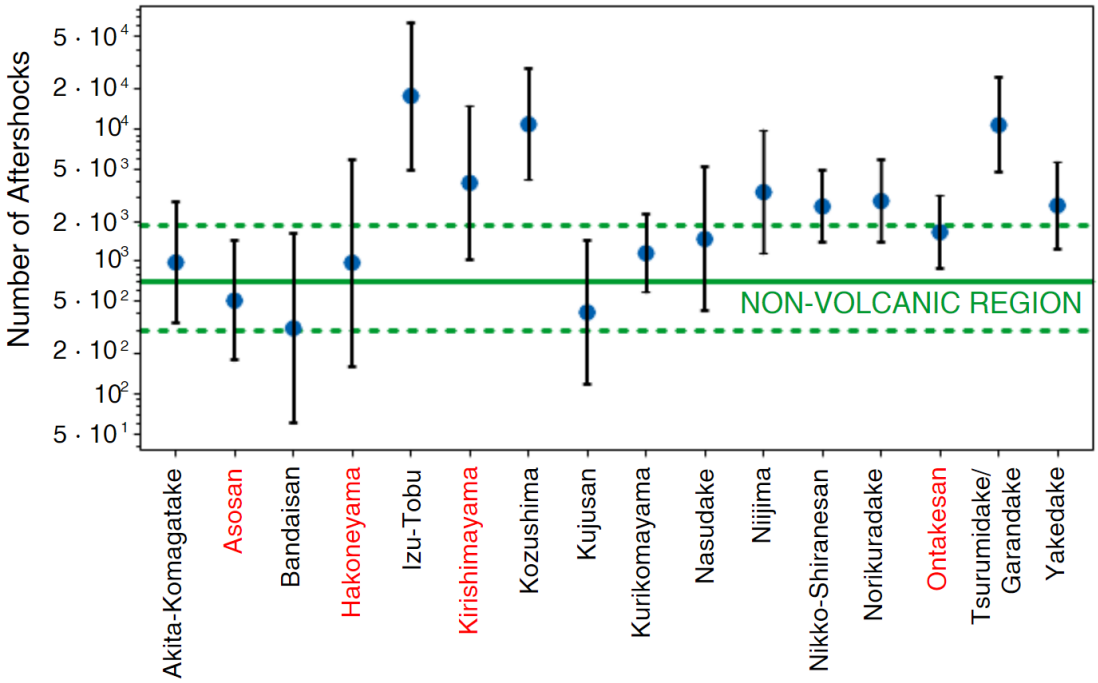

Figure 1-4. Predicted number of aftershocks for a magnitude 3 earthquake in each volcanic region. Error bars show the propagated error of each parameter of the Aftershock Productivity Law into the expected number of aftershocks. The solid line represents the median value of the NAs (M=3) of all the mainshock-aftershock clustered areas of the non-volcanic region and the dashed lines represent the second and fourth quantiles. Volcanoes that have had at least one eruption since 1998 are shown in red. Productivity of most volcanoes seems to be relatively comparable to that of the non-volcanic areas, reinforcing the idea that mainshock-aftershock sequences are pervasive all over the crust.

Of the 17 volcanoes that have measurable mainshock-aftershock clustering, we find that all except three have productivity indistinguishable from the tectonic regions. This agreement reinforces the previous finding that volcanoes with high enough seismicity rates to be included in this study are as aftershock prone as tectonic faults and run contrary to the expectation of aftershock variability with heat flow or seismogenic thickness. Again, the

conclusion does not change if we restrict the study to volcanoes that had eruptions during the study period (red names in Figure 1-4). Eruptive volcano aftershock production generally falls in the same range as the non-tectonic regions.

1.5.3 Specific Cases of Interest and Eruptions

A conspicuous example that deviates from the tectonic values in Figure 1-4 is Kozushima, which is best understood in context of the 2000 eruption at neighboring Miyakejima. About 70 km off the coast of the Izu peninsula lie the Miyakejima, Kozushima, and Niijima volcanoes. On 26 June 2000 seismic activity started to increase rapidly around the southwest flank of Miyakejima volcano as a seafloor eruption began. A dike then intruded ~30 km west-northwest toward Kozushima and Niijima Islands where it developed into bursts of >5,000 events within weeks and where the largest earthquakes of the sequence were observed (Nishimura et al., 2001). Simultaneously, seismicity continued at a lower level on the edifice concurrent with caldera collapse followed by summit eruptions continuing into September 2000 (Geshi et al., 2002).

The mainshock-aftershock clustering detection method used here shows that activity closer to Miyakejima does not cluster in these types of sequences but that the dike-associated earthquakes closer to Kozushima and Niijima do follow a highly productive aftershock triggering pattern (Figure 1-4). The observed lack of aftershock clustering at Miyakejima is consistent with earlier work on the sequence (Traversa & Grasso, 2009); the contrast with Kozushima

and Niijima is a new finding. Previous work has shown that the dike-associated earthquakes appeared to have been triggered by the elastic stresses in the rocks surrounding the dike rather than at the front of the dike only, possibly combined with aseismic transients after the dike stall (Cattania et al., 2017; Passarelli et al., 2015; Toda et al., 2002). It appears that the dike-triggered earthquakes are capable of triggering aftershocks as a secondary effect. Aftershocks can be identified even though the stressing rate is far from constant and individual non-aftershock seismicity bursts can also be identified within the sequence (Cattania et al., 2017). In contrast, the seismicity on Miyakejima that was modulated by both the magma chamber drainage and the piston-like caldera collapse events did not appear to generate secondary aftershocks. One possible explanation for the difference is that the preexisting tectonic faults were oriented more favorably near Kozushima and Niijima. Another possibility is that Miyakejima was unable to store the elastic strain energy required to have triggered brittle failure, that is, aftershocks, whereas the cold, host rock of distant Kozushima and Niijima could respond with brittle failure and abundant aftershocks. The observation hints that the mainshock-aftershock clustering detection algorithm could be used to separate out dike intrusions where sympathetic faults are triggered from other eruptive behavior.

The Miyakejima observations prompt broader questions about whether the mainshock-aftershock clustering behavior on volcanoes generally changes during eruptive periods relative to repose periods. Unfortunately, for all

volcanoes, the catalog data do not allow for an appropriate analysis. In some cases, most of the seismicity belongs to an eruptive sequence (e.g., Miyakejima and Usuzan); in other cases, the eruptions are very quiet and do not produce many earthquakes (e.g., Asosan, Meakandake, and Kirishimayama). For Miyakejima, we more aggressively analyzed the data by dropping the required minimum number of events to 600. In this case, we found no clear differences between the clustering behavior during the 2000 intrusive/eruptive period and neither the complete catalog nor the seismicity that followed December of 2000.

Finally, we examined the connection between ordinary mainshock-aftershock clustering behavior and precursory volcano-tectonic behavior. Precursory volcano-tectonic earthquakes are operationally used as forecast tools but are not ubiquitous and can be difficult to distinguish from ordinary earthquakes in real time. Identifying any pattern of seismicity at volcanoes prone to precursory volcano-tectonic earthquakes would be a benefit both to operational and fundamental volcanology.

We determine whether precursory earthquakes were identified for each eruption in our study period and region by using the National Catalogue of the Active Volcanoes in Japan (Japan Meteorological Agency, 2013), which reports in the text if precursory seismicity was observed, and the type of earthquakes detected for each eruption. We also included the additional case of Hakoneyama, which had a small phreatic eruption on 30 June 2015 preceded by a large number of earthquakes but was not in the time period covered by the bulletins.

We concentrated only on precursory seismicity that was identified by JMA as ordinary earthquakes (volcano-tectonic) and did not consider unusual seismic events such as long period or hybrid earthquakes (Japan Meteorological Agency, 2016; Zobin, 2012).

Eruptive volcanoes with no mainshock-aftershock clustering showed precursory volcano-tectonic earthquakes, whereas most of the volcanoes with mainshock-aftershock clustering did not (see cross-hatching in Figure 1-3). Interpretation must proceed with caution as the data set is small, and the observation is only for three systems out of four in both cases. Nonetheless, while there are cases where precursory seismicity has an obvious cause such as the magma intrusion at Miyakejima, the correlation with a lack of mainshock-aftershock clustering is surprising. Perhaps the rising magma that creates the precursory seismicity is also prone to create more direct earthquakes and fewer secondary aftershocks. The observation suggests that an increase in seismicity on a volcano without mainshock-aftershock clustering might be cause for greater concern than a similar sequence on a volcano that routinely shows mainshock-aftershock behavior.

1.6 Interpretations and Speculations

Differences in clustering behavior have previously been attributed to degrees of heterogeneity (Mogi, 1963). Other explanations are possible. Triggerability in volcanic systems could stem from the abundance of hydrothermal fluids and differences in fluid pressure resulting in low fault

strength (Hill et al., 1993). In addition, differences in openness of the edifice could play a role. If the pressure of magma intrusion and volatile exsolution exerted on the surrounding rocks is not relaxed by giving those fluids an exit from the system, we would expect elastic strain to be accumulated and eventually released through brittle failure.

Another possibility is that the ability to accumulate elastic strain is governed by the rock rheology. The presence of aftershocks indicates that elastic strain energy has been stored in the system and is available to release. Volcanic rocks can be hot or damaged enough that strain is released by creep or viscous flow. In these cases, elastic strain energy would not accumulate, and aftershocks would not exist.

Interestingly, the volcanic systems analyzed in this study do not conform to the above expectation of reduced aftershock productivity. The weakness that is expected to coincide with the high heat flow of volcanoes does not seem to translate into a lack of aftershocks. High heat flow certainly reduces elastic moduli and therefore should affect the overall strength of the system. The observation raises the possibility that the stress required to trigger the faults is also low and therefore able to compensate for the reduced strength. High pore fluid pressure can result in this situation. In that case, the similarity between the resultant productivity in volcanic and tectonic systems is simply a coincidence. A more speculative, and perhaps intriguing possibility is that the fault system adjusts in response to earthquakes to dynamically achieve a steady state

aftershock productivity. Each earthquake perturbs the distribution of stresses on faults in the system. The number of available faults near failure continually responds to the forcing to result in a similar aftershock productivity in a wide range of settings, independent of the local strength.

1.7 Conclusions

We have shown that earthquakes in volcanic regions in Japan cluster into mainshock-aftershock sequences, noting that earthquake swarms can have mainshock-aftershock sequences within them, just as often as or more often than in nonvolcanic regions where most of the seismicity corresponds to crustal tectonic processes. The aftershock production rate in the seismogenic volcanic regions studied seems to be of the same order of magnitude or higher than in the non-volcanic regions. This similarity between the volcanic and nonvolcanic systems suggests that the mechanisms by which earthquakes trigger each other are the same. Even though we were only able to assess the mainshock-aftershock clustering differences between large-scale eruptive periods and the rest of the catalog for one volcano, Miyakejima, in that case, this type of clustering behavior does not change much through time. We speculate that aftershock behavior might imply a preferred aftershock productivity that holds in a variety of systems despite differences in scale and forcing.

The tendency for earthquakes to cluster into different types of sequences may hold information about other properties of the volcanic system. The observation that cataloged earthquakes that are precursory to eruption are

limited to non-mainshock-aftershock-clustered volcanoes comes from a small sample size; however, it suggests that merely the presence of clustering is an important, and understudied, discriminant of volcanic systems.

Chapter 2 – An eruption seen clearly: The co-eruptive seismicity of the 2008 Okmok eruption

2.1 Introduction

The breaking of rocks as manifested by earthquakes is an intrinsic part of volcanic eruptions. Earthquakes are the most readily observable aspect of rock failure and fluid flow during large scale eruptions. Seismicity is one of the most common precursors of eruptions and it often continues after an eruption ends. But what happens in between? How do the earthquakes progress during an eruption? These questions have been studied at length for effusive eruptions, but have been hampered by detection limits during sustained, large-scale explosive eruptions. Explosive eruptions produce seismic waves, as a result surviving, onscale seismograms in the near field are usually covered with continuous waves that obscure individual earthquakes, particularly the low magnitude ones.

Recent advances in seismological processing allow a partial solution to the problem of detecting earthquakes during an explosive eruption by using deep-learning neural networks, fingerprint similarity and template matching (Yoon et al., 2015; Shelley et al., 2016; Chamberlain et al., 2018; Wech et al., 2018, Mousavi et al., 2020). For instance, the transformer neural network is a supervised deep-learning approach that uses a hierarchical attention mechanism that allows it to learn about the features that describe both an event and its phase arrivals simultaneously by presenting to it thousands of pre-classified events and phase-picks. Template matching consists of using previously

detected earthquakes (templates) to scan the continuous data by performing cross-correlations to find new events (detections). Earthquakes of similar geometry that occur close to one another would share a similar travel path, and thus would have a high waveform similarity, which would be reflected with a high normalized cross-correlation value. Fingerprint similarity, on the other hand, is a non-supervised method that allows us to find new events that do not have a parent template in the original catalog by matching any waveform pairs from the windowed, continuous data.

The goal of this research is to identify earthquakes in nearfield records during an extended explosive eruption for the first time. We focus on the 2008 Volcanic Explosivity Index (VEI) 4 eruption of Okmok Caldera as an adequately instrumented volcano where, unusually, most seismic stations survived and produced on-scale recordings for the entire 2-month sequence. By identifying these earthquakes, we will be able to produce a time series of the seismicity and place it in context of the other observations during the eruption. Resolving the full sequence of earthquakes is of particular importance for eruptions like Okmok where the vent structure appears to evolve during the eruption. As will be discussed below, earthquakes provide a window into processes that otherwise are invisible to standard measurements during the eruption.

2.2 The 2008 Okmok Eruption

Okmok is a 10 km wide basaltic-andesitic caldera located on Unmak Island, in the Aleutian Arc of Alaska (Figure 2-1). For over a century, most of the

eruptions at Okmok had their source at an intra-caldera cone (Cone A; Figure 2-1 inset) and were mostly Hawaiian to Strombolian (Coats, 1950; Grey, 2003). The 2008 eruption marked a change in this behavior because of the interactions between magma and water, making new intra-caldera maar-like vents and developing a new tephra cone during a large phreato-magmatic eruption (Larsen et al., 2015). Since the island has a regional-scale tilt towards the northeast, the northern sector is characterized by larger bodies of surface and groundwater, making an approximated $\sim 10^{10}$ kg of water available for the 2008 eruption (Unema et al., 2016).

During the 6 months preceding the eruption, the Alaska Volcano Observatory (AVO) detected only 9 low magnitude earthquakes, giving no sign of obvious precursory activity. Most of the inter-eruptive period seismicity is mainly localized in a geothermal field on the isthmus of Unmak Island inland from Inanudak Bay (Figure 2-1). On July 12, 2008, the seismic network at Okmok recorded the onset of a ~4.5 hour-long earthquake swarm (Johnson et al., 2010) after which explosive activity commenced. The short sequence of precursory earthquakes has been reanalyzed by Ohlendorf et al. (2014) using the AVO catalog events, and the earthquakes originated at approximately 3 km depth beneath the intra-caldera cone known as Cone D (Figure 2-1 inset). The beginning of the eruption was marked by a large-scale sub-plinian explosion that released a ~16 km high dark plume that established the eruption at a VEI 4. This plume was accompanied by more than 12 hours of continuous high-amplitude

seismic eruption tremor (Larsen et al., 2009). Tremor continued at variable levels throughout the 40-day-long eruption and emanated mainly from a new intra-caldera cone (Haney, 2010; Haney, 2014). This new cone, to the north of Cone D and built during the 2008 eruption, was subsequently named Ahmanilix (meaning surprise in the Unangan language). After the initial plume activity continued by opening, and perhaps widening, new vents in a westward alignment from the north-west of Cone D. On July 19, the network recorded high-amplitude sustained tremor that lasted ~20 hours and is thought to be related to the initiation of the temporary drainage of the perennial North Cone D Lake, (hereby called North Lake) (Figure 2-1), which was verified by satellite imagery until August 1 when standing water was observed again at the lake (Larsen et al., 2015). Whether the lake refilled before August 1 is unknown. Moreover, Larsen et al. (2015) report that between July 24 and August 1 the North Vent structure, directly to the north of Ahmanilix, widened and there was an increase in number and size of reflectors observed in SAR images, accompanied by an increase in ash production until August 3, confirmed by AVO staff in the field. From August 3 until August 19, when the last emission of ash was reported and the eruption officially ended, the plumes decreased in number and size.

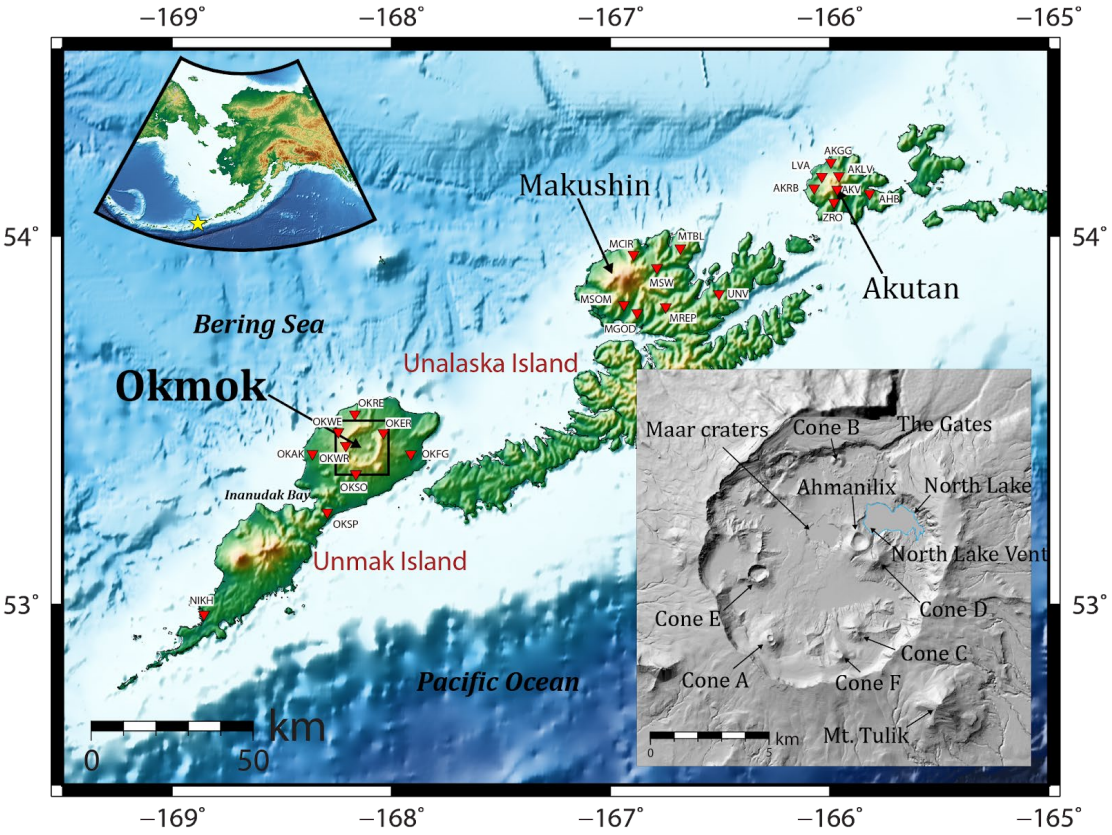

Figure 2-1. Map of the seismic stations (triangles) used for this study with an inset showing the location of the intra-caldera cones and the most important features of Okmok Volcano. Inset corresponds to black rectangle in the larger map.

2.3 Data and methods

Okmok Caldera was relatively well-instrumented at the time of the eruption, although there were some notable outages in some stations. Few large volcanic eruptions have been historically recorded with such a comparable wealth of locally recorded data. On July 12, 2008, Okmok had seven short-period seismometers in addition to two broad-band stations with co-located GPS on the island (OKSO and OKFG). A third GPS station, OKCE, was located inside of the caldera but stopped transmitting data weeks before the eruption started and it was not restarted by AVO staff until September 11, 2008, after the eruption had ended (Freymueller and Kaufman, 2010). Besides this, some of the larger seismic events were recorded as far as Makushin and Akutan volcanoes, which had local seismic networks. With the addition of a station in the permanent Alaska Regional Network (AK) on Unmak and Unalaska Island, this brings the total number of stations within 200 km of Okmok to 8 broad-band and 15 short-period instruments (Figure 2-1).

We used the continuous seismic waveforms records from AVO and the Alaska Earthquake Center during the period of time June-August 2008 to detect, locate and estimate the magnitude of earthquakes and we include 443 events catalogued by AVO during the same time period for our procedure.

2.3.1 Event detection and phase picking

The detection of earthquakes in continuous seismic signals is an essential process for observational seismology. Many novel algorithms have attempted to

overcome the pitfalls of standard procedures such as STA/LTA triggering or the manual inspection of an expert observer using advanced signal processing or deep learning techniques (e.g., Yoon et al., 2015; Kong et al., 2019; Mousavi et al., 2020). However, even these advanced algorithms present some challenges and the reliability of their performance in environments with high noise levels is still unknown. Consequently, we have developed a workflow that allows for the usage of different cutting-edge detection algorithms to benefit from their individual advantages and to counteract the weaknesses that each one of them might present.

We used the newly developed, deep-learning based EQTransformer algorithm (Mousavi et al., 2020) to do a supervised search of earthquakes using the pre-trained model in their package and we have also used the Fingerprint And Similarity Thresholding (FAST) (Yoon et al., 2015) algorithm, which performs an unsupervised search of events by means of reducing the information of waveforms in pre-specified time windows and performing a 2D fingerprint matched filter. We post-processed the signals detected by FAST and selected the phase arrivals manually. Only signals that resembled earthquakes were kept, but no further analysis was made to the others. Because of its unsupervised nature, by using FAST we are aiming to find earthquakes with many different possible sources and that travel different paths. FAST outperformed EQTransformer at detecting earthquakes during the 2008 Okmok eruption.

Finally, we merged the events detected with EQTransformer and FAST with the earthquake catalog provided by AVO to have an initial enhanced catalog. Interestingly, we find that sometimes different algorithms detect the same event but not in all the same channels, the reasons for why this happens are unknown to us and beyond the scope of this work. To have better event locations, we attempt to get the greatest number of channels for each event by merging the repeated events together. We give priority to the AVO catalog over the others since it was already reviewed by expert observers and append the missing channels that the other catalogs might contribute with. The results of the number of earthquakes found by each process and their intersections are shown in Figure 2-2.

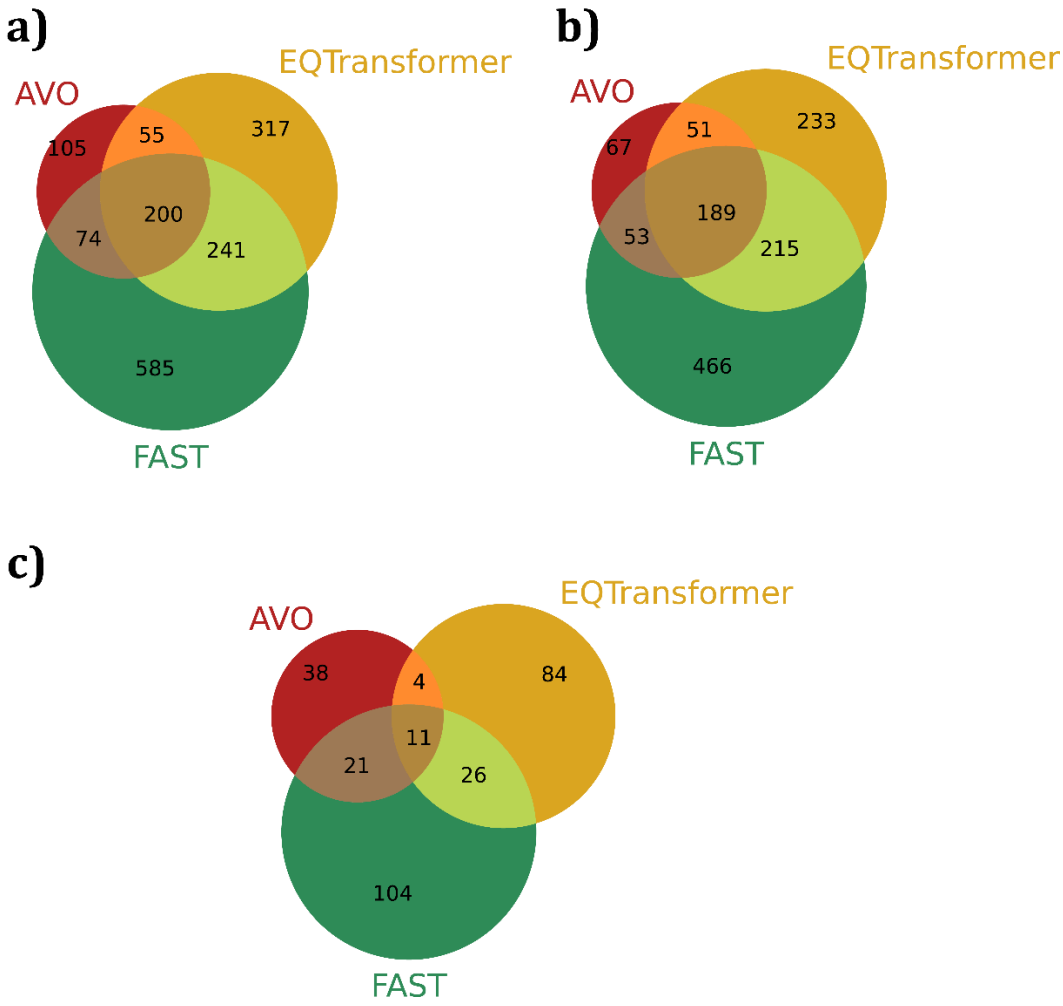

Figure 2-2. Number of earthquakes detected by each method (EQTransformer and FAST) and reported by AVO. Overlapping areas indicate populations of events that were detected by multiple methods. a) All events. b) Events classified as VT. c) Events classified as LP.

Finally, to further enhance our ability to detect earthquakes, we use this initial merged catalog to do template matching using the EQcorrscan package (Chamberlain et al., 2018). More details on the detection, merging and association can be found in Appendix B.

2.3.2 Location and relocation

We calculated the absolute location of all earthquakes with a minimum of 3 stations using the NonLinLoc (NLL) code by Lomax et al. (2001). NonLinLoc estimates the posterior probability density function (PDF) of an earthquake location by using the non-linear, global-search oct-tree importance sampling algorithm (Lomax and Curtis, 2001).

We used a smoothed 1D velocity model for Okmok from Masterlark et al. (2010) and a Vp/Vs ratio of 1.73 to create the travel-time grid necessary for NLL to invert for the locations. We only report the location of the events that had a root mean square error (RMS) less than or equal to 0.3 seconds.

The absolute locations of earthquakes have errors from both the aleatoric uncertainty of the phase picks and the epistemic uncertainty of other factors like the network configuration, the velocity model, and the location process itself. Prior work has used cross-correlation based travel-time differences and the relative location of nearby earthquakes to reduce these errors (Poupinet et al., 1984; Waldhauser and Ellsworth, 2000; Shelly et al., 2013; Shelly et al., 2015).

We follow these precedents by performing a double-difference relocation to our earthquakes using hypoDD (Waldhauser and Ellsworth, 2000) combining as input the travel-time differences from our catalog and the corrected travel-time differences using cross-correlation lags on both P and S phases. Because the seismicity that we are detecting is localized in different areas of Okmok and most likely represent different physical processes, it was impossible to achieve a

stable relocation inversion for all our events using the same parameters. Thus, we divided our data into 4 different principal clusters/groups and adjusted the inversion parameters for each to ensure stable results and then we merged them back together. The way we sectioned our data was as follows: (1) All the earthquakes around the active vents, (2) all the earthquakes in the south sector of the caldera, (3) all the other earthquakes surrounding the caldera and (4) the earthquakes that are located around Inanudak Bay (Figure B-1). The implementation of hypoDD is limited to a small number of layers so we downsampled the velocity model from 126 layers to 12 layers.

To ensure the robustness of our observations, we also relocated our catalog using the more recently published GrowClust code (Trugman and Shearer, 2017), which uses a hybrid relocation/clustering algorithm. For GrowClust we provided only the same cross-correlation based travel-time differences as input, we used the 126 layers smoothed velocity model, and we did not have to sub-divide our data like we did for hypoDD. The results for the GrowClust relocations and the details on the methods used can be found in Appendix B.

2.3.3 Magnitudes

A common approach to estimate the magnitude of detections is based on the ratio of the amplitudes of the detected earthquakes to the earthquakes with a previously estimated magnitude, i.e., the AVO data set (Shelly et al., 2016; Wech et al., 2018). This heuristic procedure works best where the pre-existing local

magnitudes are well-calibrated, which is not the case on this highly attenuating, sparsely instrumented volcano.

Therefore, we used all the data available after template matching to establish a local-magnitude scale inverting for the local attenuation relationship during the time of the eruption and for the specific operating network that we are using. (See Appendix B for full procedure and validation). This customized magnitude scale procedure is similar to that used elsewhere (e.g., Vales et al., 2014; McCausland et al., 2020; Illsley-Kemp et al., 2021).

For Okmok, we applied the procedure using all the earthquakes that were successfully relocated using hypoDD (2089 events). For the near-field locations (< 20 km) we observe a higher attenuation than the one calculated for Southern California. For distances between 20 and 75 km, we see an attenuation curve that does not change dramatically from the one calculated for Southern California. For large distances, however, we find a stronger attenuation, which is expected in an active volcanic arc (Figure 2-3). This attenuation relationship corresponds to values of α and K of -0.442 and -0.01178, respectively, with hypocentral distance R measured in kilometers. Finally, we utilize this newly developed magnitude scale for calculating the magnitude of all 3101 final events.

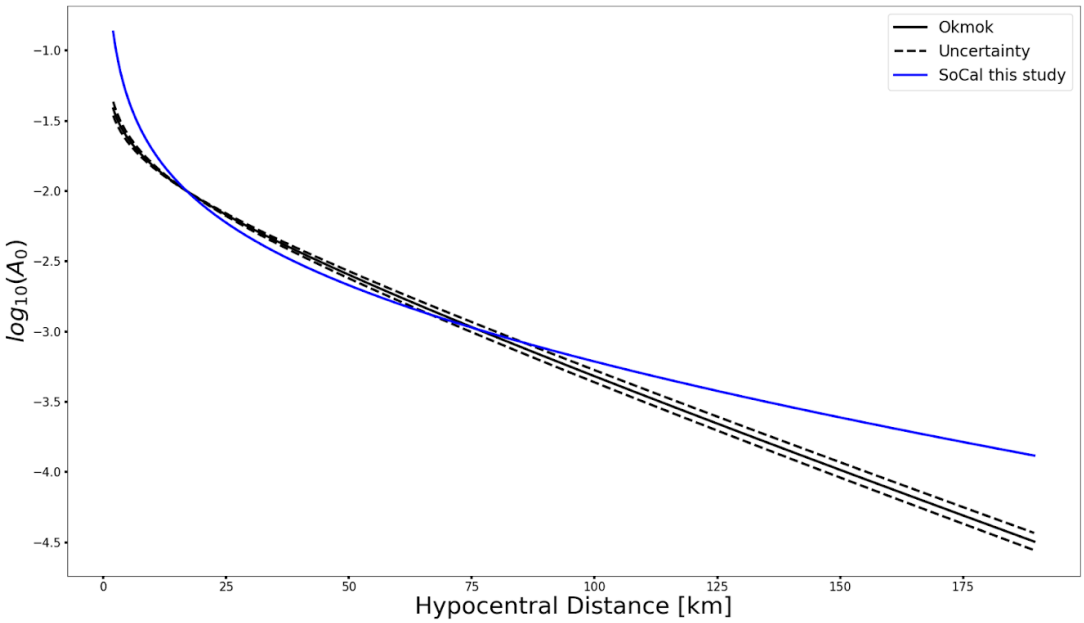

Figure 2-3. Attenuation relationship calibrated for the dataset in this work and its comparison with our results for Southern California , where the attenuation for the standard form of ML is calibrated.

2.3.4 Magnitude distributions

Variations in magnitude distributions are captured by variations in the b-value of the Gutenberg-Richter distributions where the number of earthquakes of magnitude greater than or equal to M is proportional to 10^{-bM}. The b-value is most commonly estimated with a maximum likelihood estimator that requires knowledge of the minimum magnitude at which the detection level is near 100% (Utsu, 1965; Aki, 1965). This sensitivity to the completeness level is problematic for the Okmok data where noise level is constantly changing. Therefore, we utilize the b+ method recently introduced by van der Elst (2021) that uses the inter-event magnitude differences, which follow a distribution of the same functional form as Gutenberg-Richter. The major advantage is that the b+

estimate is that it provides robust measurements of b-values without explicitly requiring an estimate of the completeness magnitude and is not as strongly biased by its value as the maximum likelihood procedure.

The b-value variations require a significance test. Since Van der Elst (2021) proved that the distribution of the differences in magnitudes has the same mathematical form as the distribution of the magnitudes, we calculated the probability that two different b+ values come from the same populations using the Utsu test (Schorlemmer, D., Wiemer, S., & Wyss, 2005; Gerstenberger, M., Wiemer, S., & Giardini, D., 2001; and references thereafter), which was derived for the commonly used b value, to establish the statistical significance of our results. The resulting probability P of randomly obtaining the observed result is

$$P \approx e^{(\frac{-dA}{2}-2)} \quad (2\text{-}1)$$

and the parameter dA is defined by

$$dA = -2N\ ln\ (N) + 2N_1\ ln\ (N_1 + N_2 b_1/b_2) + 2N_2\ ln\ (N_2 + N_1 b_2/b_1) - 2 \quad (2\text{-}2)$$

where N_1 and N_2 are the number of events in groups 1 and 2, respectively, and the total number of events is N, which is equal to N_1+N_2.

2.3.5 Earthquake rates

One of the key questions of this study is when does the overall earthquake rate increase or decrease in context of the overall eruption. The detection methods deployed allow us to ask these questions even during the high noise levels of the eruption. However, at all times noise persists and thus

comparing the observable seismicity rate over time requires a correction for variable detection levels.

We therefore calculate a consistent metric of seismicity rate throughout the eruption in a multi-step process: (1) We compute the completeness magnitude M_c in a moving window of 100 events with 10% overlap by using the maximum curvature method plus a correction of 0.2 to compensate for the common underestimation of M_c (Wiemer and Wyss, 2000). (2) we then count the events above M_c in the window and normalize by its length to obtain an estimate of the observable seismicity rate, (3) we compute the corresponding instantaneous estimate of the b-value using the b+ method of van der Elst (2021) and (4) we extrapolate the observable seismicity rate to a consistent smaller magnitude M_{ref} for all windows. For this study we use $M_{ref} = 0$. This procedure effectively projects a Gutenberg-Richter relationship to magnitude 0 for all time periods and thus corrects for differences in completeness level over time to produce a consistent metric of earthquake rate.

To ensure robustness, we also performed the same procedure using a more conventional maximum likelihood b-value estimate; the results are shown in Appendix B.

2.3.6 Classification

Active volcanoes produce a myriad of different types of signals. Amongst some of the most well studied ones are the volcano-tectonic earthquakes (VT) and the long-period earthquakes (LPs). The former are related to the brittle

failure of rocks and usually contain energy in a broader range of the frequency spectrum, but have the majority of its signal at relatively high frequencies (>5 Hz) (Roman, 2005; Roman & Cashman, 2006; Zobin, 2012). The latter are known for producing energy in the lower band of the spectrum (<5 Hz) and they are related to volumetric deformations related to fluid fill cracks, the resonance in volcanic conduits and/or the brittle failure of magma in the glass transition for magmas with a crystalline andesitic/dacitic composition (Chouet, 1996; Neuberg et al., 2006; Collier and Neuberg, 2006). However, other studies suggest that LP events could be the product of slow ruptures in the unconsolidated or warm materials of volcanoes (Bean et al., 2014; Harrington and Brodsky, 2007).

The seismic waveforms of the cataloged events include both apparent high frequency (i.e., VT) earthquakes and longer-period events with similar magnitudes (Figures 2-5 and B-3). We therefore classified events following a similar procedure to Neuberg et al. (2000), which is based on the frequency content of the signals. The process is as follows: we pre-processed the waveforms by detrending, removing the mean and applying a Hanning taper of 5% to the front and end edges and we removed the instrument response with a pre-filter between 1-20 Hz to stabilize the deconvolution. We obtained the stacked power spectral density (PSD) of the velocity records across all channels and obtained the ratio between the integral of the energy below 5 Hz and the total energy. If an event had 70% or more of its energy below 5 Hz, we classified the event as a long-period earthquake, otherwise we assumed that it is a

volcano-tectonic event. The 70% threshold was chosen given the distribution shown in Figure 2-4 and the overall results presented here are robust independently of the choice of thresholds. Another option for classifying these events is to set a stricter criterion for the ratios using the energy below 3 Hz instead of 5 Hz. We tested this (results in Appendix B) and we found that a similar bimodal distribution of events emerged from the data, confirming that there are two main categories of events in our dataset. For any other frequency threshold, the threshold of percentage should be adjusted according to that distribution. We are aware that there could be other types of events, such as hybrids, that could be reflecting different mechanisms than the ones mentioned above, but performing a more thorough classification of events to achieve a higher order disentangling all of the sources involved during the eruption would require a more sophisticated method (e.g., Buurman, West & Power, 2006; Langer et al., 2016; Malafante et al., 2018).

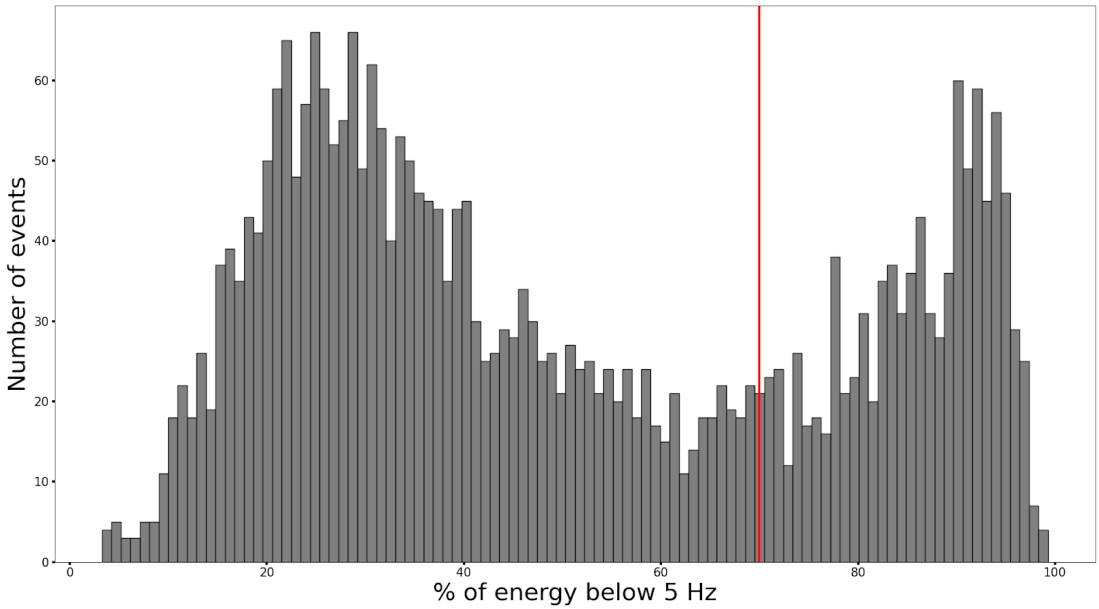

Figure 2-4. Distribution of events given the ratio of energy below 5 Hz. The red vertical line represents the 70% threshold used to classify events. Below this line earthquakes are categorized as VT; above this line they are categorized as LP.

Another potential source of frequency content variation is earthquake size. However, 5 Hz is the expected corner frequency for typical magnitude 3.6 earthquakes with a standard stress drop (Abercrombie, 1995 Figure 2-7). The maximum magnitude of any earthquake recorded is 3.4 and 98.1% of the earthquakes classified as LP have magnitudes < 3.0. Thus, magnitude variation is unlikely to be the source of the LP/VT distinction studied here.

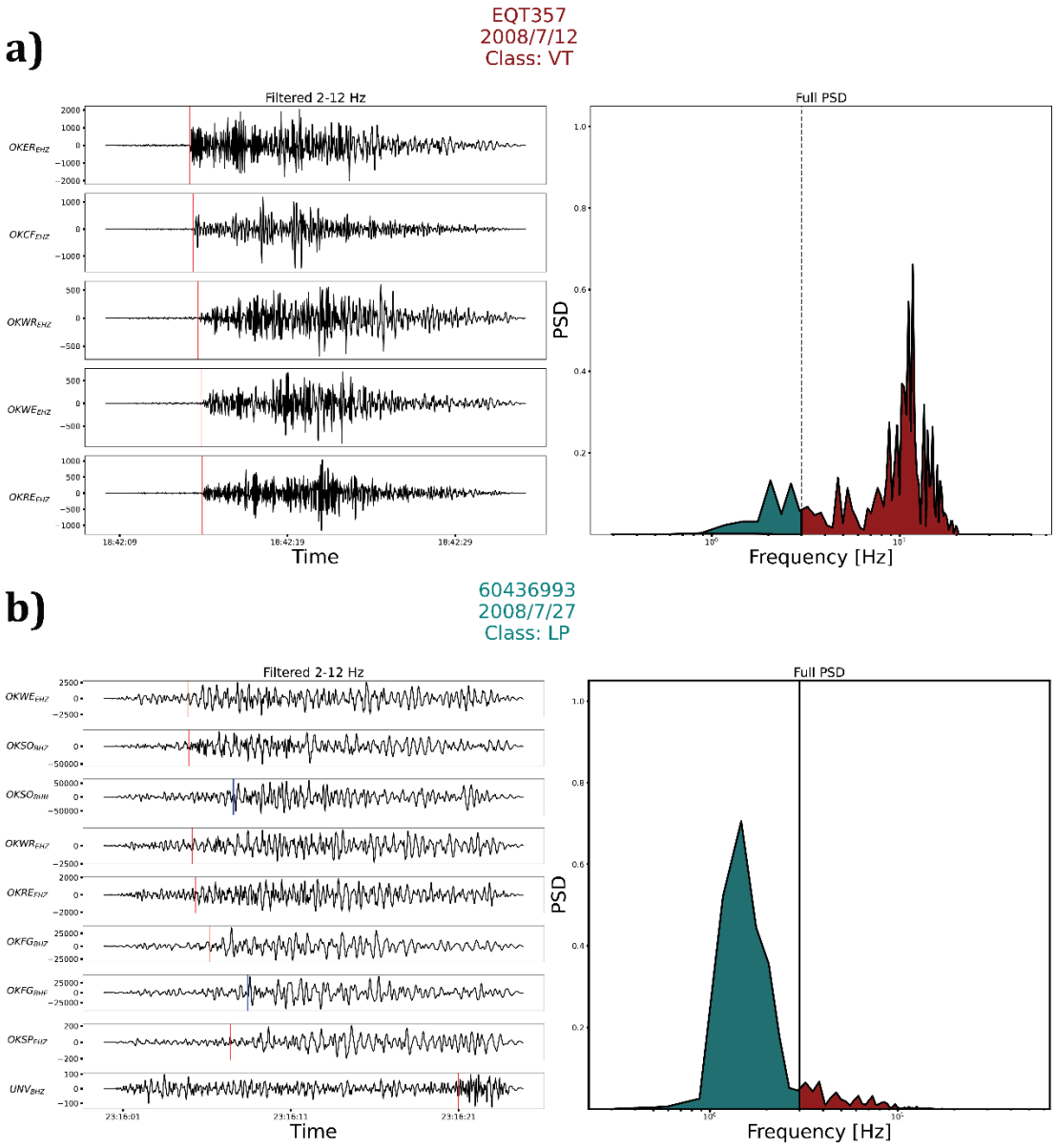

Figure 2-5. Examples of VT (a) and LP (b) classified. The red filled area in the power spectra density shows the integral of the energy above 5 Hz (high frequency energy) and the teal filled area shows the integral of the energy below the 5 Hz threshold (long period energy).

2.4 The sequence of the eruption as shown by the enhanced catalog

2.4.1 Overview

We have expanded the initial co-eruptive catalog of AVO from 443 earthquakes to 3101. The majority of the events provided by the initial detection phase were classified as VT (86% of the events for the AVO catalog, 87% for the events detected by FAST and 91% for the events detected by EQTransformer). The absolute locations of the earthquakes in our enhanced catalog and the comparison to the original AVO locations can be seen in Figure 2-6. Even though we used different algorithms to locate earthquakes (NLL for this work, HYPOINVERSE for AVO), our enhanced catalog shows the same main features that the original AVO catalog had, but it populates other areas and depths that seemed to be completely quiet in the original catalog. For example, Figure 2-6 shows that the AVO catalog already had a good part of the opening sequence underneath the vents, some earthquakes during the eruption mostly at the vents, close to Cone A and a burst to the southeast of Cone D, and very few distributed earthquakes at the end of the eruption. Our catalog shows the same clusters during the same times, but it fills the gaps where the AVO catalog seemed to be depleted of earthquakes (e.g., southeast of the caldera). Most of the newly found events are clustered inside of the caldera, particularly at the 2008 vents and in the south sector. The maximum depth of the events is 16 km, and it is bounded by the inversion grid. The shallowest earthquake located by NLL was at 8m

above sea level, but our search grid expands up to 500m a.s.l., suggesting no detectable earthquakes in higher grounds.

Rounded to the nearest integer, the depth distribution for the NLL locations shows a uniform high density of events from the surface down to 5 km and then it starts decaying gradually. All the depths reported here are referenced to the mean sea level.

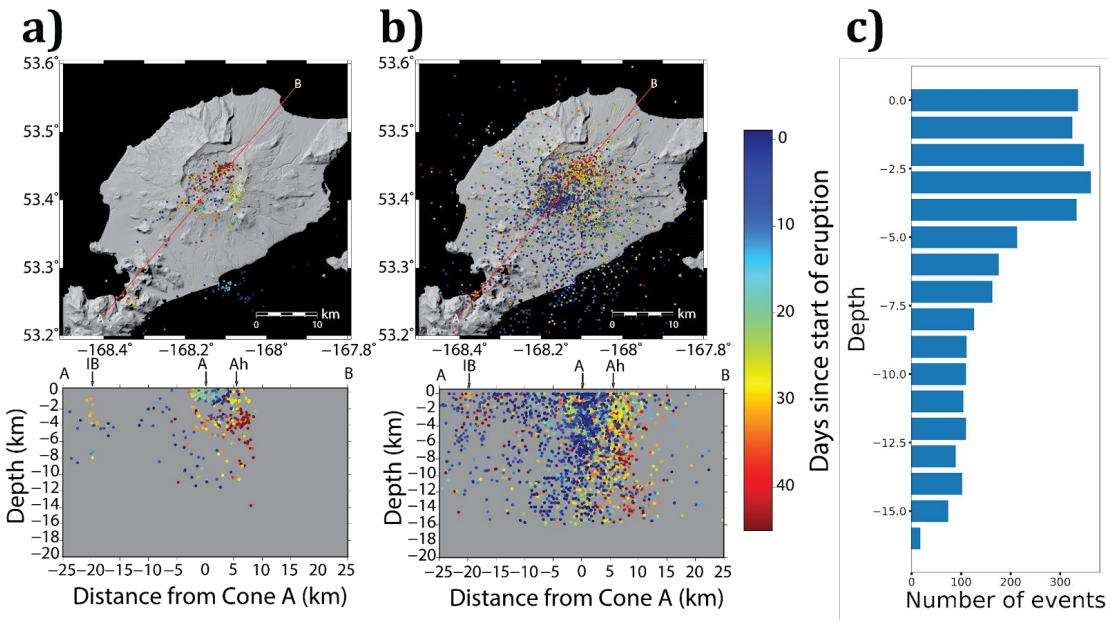

Figure 2-6. a) Original AVO catalog. b) Enhanced catalog located with NLL. c) Depth distribution of the new locations. Width of cross-section = 10km; azimuth = 40°.

The temporal distribution of the magnitudes of our new seismic catalog is shown in Figure 2-7. The most notable feature is the lack of low magnitude events recorded during the course of the eruption and the correlation with an increase in the 1-5 Hz and 5-10 Hz averaged RMS in the broadband stations. The

high co-eruptive noise is the reason the specialized methods of this study were required. They have illuminated nearly an order of magnitude more events than originally recorded, but do not completely solve the problem that the detection of small events is harder during an eruption. Nonetheless, the improved catalog illustrates seismicity rate changes and changes in magnitude distributions that can be investigated with the robust methods discussed above. Another notable feature of Figure 2-7 is that LP events are generally more energetic than VT events throughout the eruptive sequence. This was also observed during the 2007 eruptive sequence of Bezymianny volcano in Russia (Thelen, West, & Senyukov, 2010).

Figure 2-7 alone illustrates a good agreement between the prior chronology of the eruption and the newly enhanced catalog. The observational chronology of the eruption from Larsen et al. (2015) (shaded areas), most of which derive from SAR images and reports from AVO staff that were on-site during the eruption, and the GPS data from Freymueller and Kaufman (2010) both mimic patterns in the enhanced catalog. Examples of this are a prominent burst of earthquakes right after the vents opening/widening phase, and a clear jump in the GPS time-series (previously noted in the original paper) accompanied by a lack of VT earthquakes and a group of moderately large LP events during the time of the North Lake drainage (although the location of these earthquakes are mainly under Cone A). The most interesting thing to us, however, are the events during the middle (peak) of the eruption. The increase

in LP activity (black box in Figure 2-7) matches very well with the periods when Larsen et al. observe the widening of the North vent (see Figure 2-1 for location), and the largest bursts occur before, during and after a period of increased ash content observed in the eruptive plumes. Furthermore, two of the most notable jumps in the GPS data also precede and follow this period of increased ash content, respectively (yellow boxes in Figure 2-7). These bursts of earthquakes will be discussed in more detail below.

Figure 2-7. a) Magnitude of all earthquakes separated by their classification (VTs=red, LPs = turquoise). For context, figure also includes deflation rate as derived by from GPS by Freymueller and Kaufman (2010) (red-line, right-hand axis in matching color) as well as the RMS amplitude on two broadband stations (OKFG and OKSO) to illustrate the level of seismic noise (blue line, right hand axis with matching color). The large spike in RMS on August 7 corresponds to a regional earthquake that was picked up by the network. Shaded background and annotation indicate major periods in the eruption chronology of Larsen et al. (2010). Question marks point at a period where it is unclear if the North Lake was still drained. Key intervals discussed in the text are marked by rectangles: yellow rectangles= change in GPS; Black rectangle= burst of earthquakes under the vents shown in Figure 2-7. The blue line is the average RMS amplitude in the two broadband stations (OKFG and OKSO) measured every 5 minutes. b) Map and cross-sectional view of the relocated VTs (red) and LPs (turquoise). Width of cross-section = 4km; azimuth = 40°. Cross-section arrows: IB=Inanudak Bay; A=Cone A; Ah=Ahmanilix.

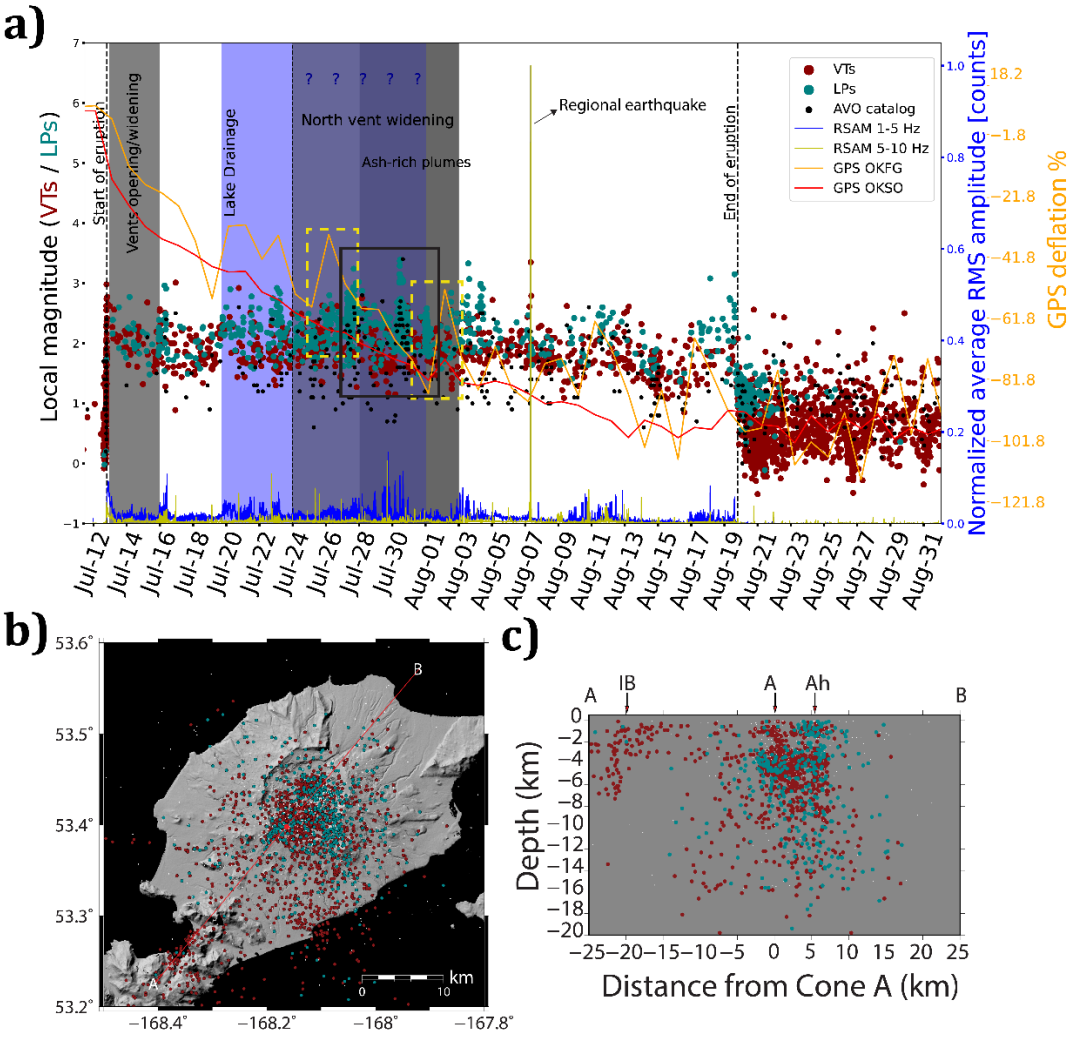
a)
Local magnitude (VTs / LPs)
Normalized average RMS amplitude [counts]
GPS deflation %
Start of eruption
Vents opening/widening
Lake Drainage
North vent widening
Ash-rich plumes
Regional earthquake
End of eruption
VTs
LPs
AVO catalog
RSAM 1-5 Hz
RSAM 5-10 Hz
GPS OKFG
GPS OKSO
b)
c)
Depth (km)
Distance from Cone A (km)
km

Locations

We focus on the earthquakes relocated with hypoDD. (The differences and similarities with the earthquakes relocated with GrowClust are discussed in Appendix B.) Table B-1 summarized the weighted RMS uncertainty reduction obtained with hypoDD. Our values are similar in magnitude to the ones reported by Ohlendorf et al. (2014).

The newly relocated pre-eruptive, co-eruptive and immediately post-eruptive seismicity at Okmok Caldera brings new information about the structures and processes that could have been involved in the beginning, development, and cessation of the 2008 eruption. If we consider the broad seismicity of Okmok Volcano during the eruption (Figure 2-8a), we can see a cone of earthquakes that expands from the surface of the caldera down to a depth of 7 km, below this seismicity starts dipping towards the southeast and continues down to ~16 km following a keel shape. Inside the caldera (Figure 2-8b), most of the earthquakes are located in densely populated clusters underneath intra-caldera cones, including the group of active vents involved in the 2008 eruption, and sparse seismicity in between these clusters and the periphery of the caldera.

A cross-sectional view shows a thin shallow (0-1 km) layer of earthquakes followed by a deeper (3-5 km) and denser cluster. The structural shape of the seismicity resembles in some ways the one presented by Ohlendorf et al. (2014), but we do not observe a dense cluster of earthquakes underneath

the caldera center. In fact, if we take a narrow (2 km) cross section between Cone A and Ahmanilix, our results suggest that there is a bowl-shaped region with almost no earthquakes (either VT or LP) in the central shallow (0-3 km) part of the caldera (Red ellipse in Figure 2-8b). The depths and location of this no-earthquake area roughly matches the location of the deflation source from Lu and Dzurizin (2010).

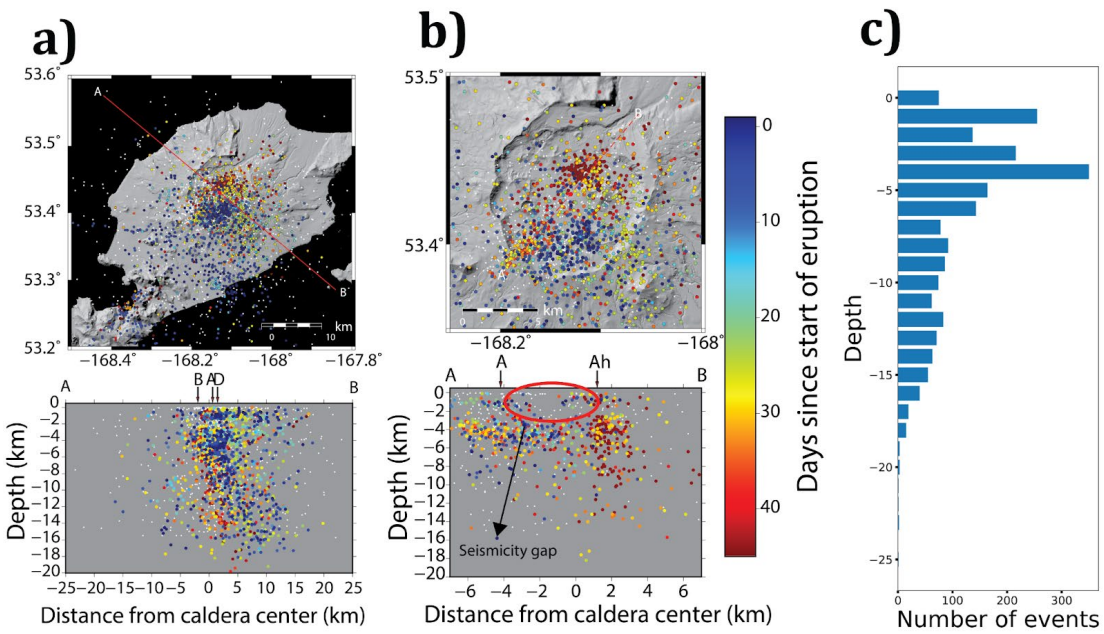

Figure 2-8. Relocated earthquakes using hypoDD (colored) and non-relocated earthquakes (white). a) Broad seismicity and a cross-section trending 130° and a width of 10km. b) Zoom in into Okmok Caldera showing a cross-section trending 40° and a width of 2km. The red ellipse indicates the gap in seismicity at the center of the caldera from 0-3 km depths, which is coincident with the source location from Lu and Dzurisin (2010). c) Depth distribution of all the relocated events. Cross-section arrows: A=Cone A; Ah=Ahmanilix; B=Cone B; D=Cone D.

Seismicity Rate

We utilize the methods discussed above to provide a uniform measure of seismicity rate extrapolated to a consistent magnitude level to account for changes in catalog completeness. Seismicity rates increased gradually during the first ~2 weeks of the eruption, reaching its highest peak on July 29 (vent widening/ash-rich plumes periods). After July 29 the rate had an abrupt drop and, except for an increase towards the end of the eruption, it continued to to decrease until it reached a post-eruptive background rate.

We repeated this procedure using the b value maximum-likelihood estimator and projected the rates to magnitudes M=0, the results are almost identical (Figure B-12).

Figure 2-9 shows the extrapolated seismicity rate for all the events detected and for the VT and LP populations separately. The VT earthquake rate seems to be stable throughout the course of the eruption, showing slight variations during the periods when Larsen et al. report the widening of the North Vent. On the other hand, the LP earthquake rate seems to peak immediately before the ejection of plumes with a higher content of lithics (July 27) and it sustained high levels until August 1 when it saw a drop followed by the ejection of more plumes. After this the LP steadily decreased except for the last burst after the end of the eruption.

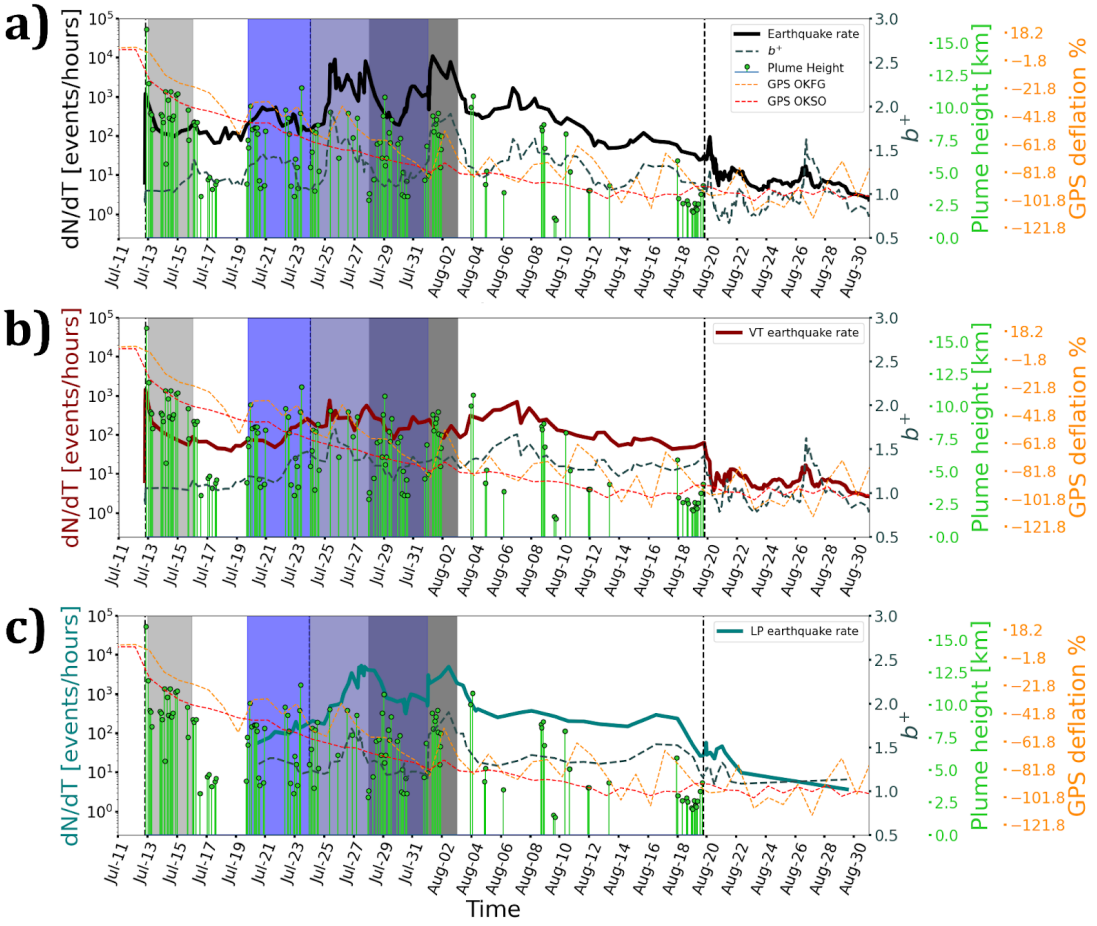

Figure 2-9. Seismicity rate (continuous lines) as the extrapolated number of events >= magnitude 0 based on the local value of b+ (dashed gray line) in a 100 event moving window with 10% overlap. GPS deflation percentage shown for reference (red and orange lines). Plume heights (Larsen et al. 2009) are shown in green. a) All earthquakes. b) VT earthquakes only. c) LP earthquakes only.

Figure 2-9 suggests that the VT earthquake rate is roughly stable throughout the eruption. The LP rate, on the other hand, shows signs of pulsing during the middle of the eruption and it seems to fluctuate according to the periods of plume ejection. More precisely, higher rates of LP events precede the periods where more plumes with ash-rich content are observed. To better illustrate and quantify this observation, we have compared the $\log_{10}$ of the

earthquake rate for each group (all, VTs and LPs) to the number of plumes observed in the same time windows as the earthquakes by cross-correlating them. Because we chose windows of N events (N=100), we simply count the number of plumes that are observed within the time interval from the first earthquake to the last earthquake of the window. Once we have a time series of the number of earthquakes and plumes, we interpolate them to a time series sampled every 4 hours and we remove the mean and trend and apply a 10% Hanning taper to the beginning and end of each of the signals. Finally, we cross-correlate the signals and analyze the cross-correlation value at a zero lag, when the signals have a 100% overlap.

Figure 2-10 shows the results of this procedure. By considering all the events in the eruptive sequence, one could not clearly see the anticorrelation with plume episodes. But after separating the data into VTs and LPs, we can clearly see that the LP events rate is anti-correlated with the plume rate.

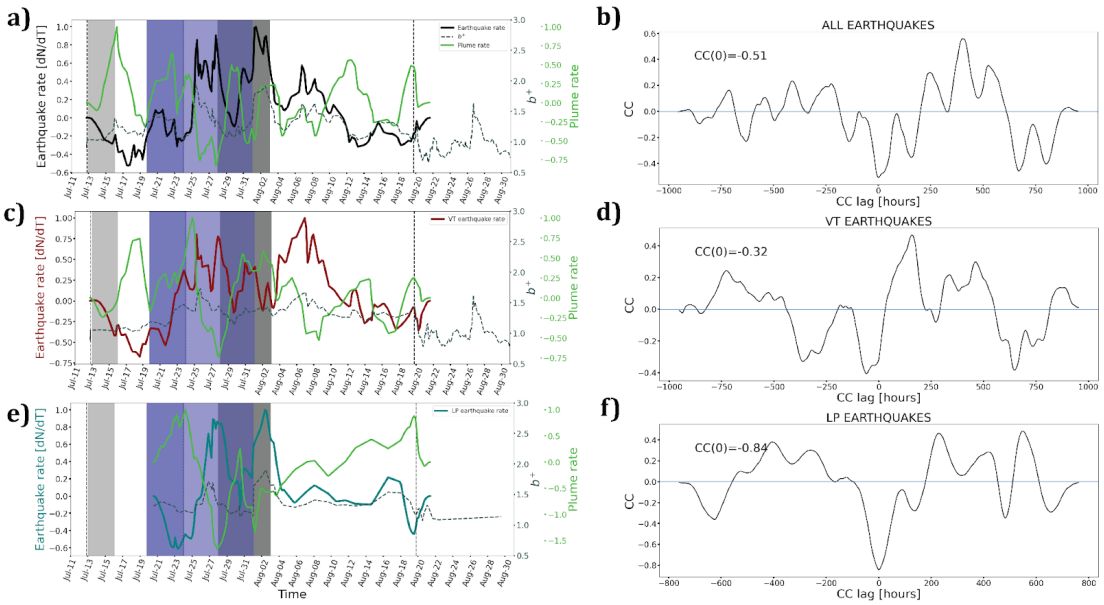

Figure 2-10. Earthquake and plume rate interpolated to an evenly spaced time series sampled every 4 hours. a) All earthquakes, c) VT events only and e) LP events only. Panels b, d and f show the cross-correlation function for the earthquake rate and plume rate shown in a, c and e, respectively. Note that the LP events and the plume rate are anticorrelated at a lag=0.

For further discussion, we separate the caldera into two different sectors: The northern sector (where the eruption developed) and the southern sector (where Cone A and the majority of the large intra-caldera cones are).

2.4.2 Northern sector

The earthquakes that triggered in the north part of the caldera are highly localized in space and time under the active vents. They are characterized by three main populations:

Opening sequence (VTs)

The first population started on July 12 at around 15:00 hours UTC (~4 hours before the eruption which was at 19:43 UTC). All of the earthquakes in

this sequence were classified as VT events. Ohlendorf et al. describe the earthquakes of the opening sequence as a shallow (<6 km) planar feature striking WSW-NNE and dipping to the NNW. Our enhanced catalog illuminates more clearly an elongated structure striking W-E and dipping to the SE down to a depth of ~15 km (Figure 2-11c). The earthquakes are localized underneath the active vents and the adjacent Cone D. The earthquakes that are observed up to three hours before the eruption span the whole dipping structure and they are small in size, but during the last hour the earthquakes started concentrating at shallower depths (3-6km) and the magnitudes were getting progressively larger (Figure 2-11a). Our results also confirm the observations by Ohlendorf et al. on the progression of the earthquakes during the last minutes of the eruption, albeit the direction of the dip of the planar feature that they report differs from our results. Around 10 minutes before the start of the eruption the earthquakes migrated from the region of the eventual vent Ahmanilix towards the deformation source (Figure 2-11d-h). This seismicity migration is in the opposite direction of the eventual magma movement, which presumably came from the deflation source to the vent. The very last events are observed northeast of Ahmanilix in the caldera rim at depths of 9 km and 11 km.

Figure 2-11. Illustration of the VT sequence before the start of the eruption on July 12 19:43 UTC. a) Temporal distribution of magnitudes, b) map view of the sequence and c) cross-sectional view (azimuth=162°). e-h) Same sequence shown with a color scale saturated at 30 minutes before the eruption to show the migration of earthquakes minutes before the eruption start. The azimuth of the cross-sections in g) and h) are 162° and 252°, respectively. Width of cross-sections =3 km. Cross-section arrows: A=Cone A; B=Cone B; D=Cone D.

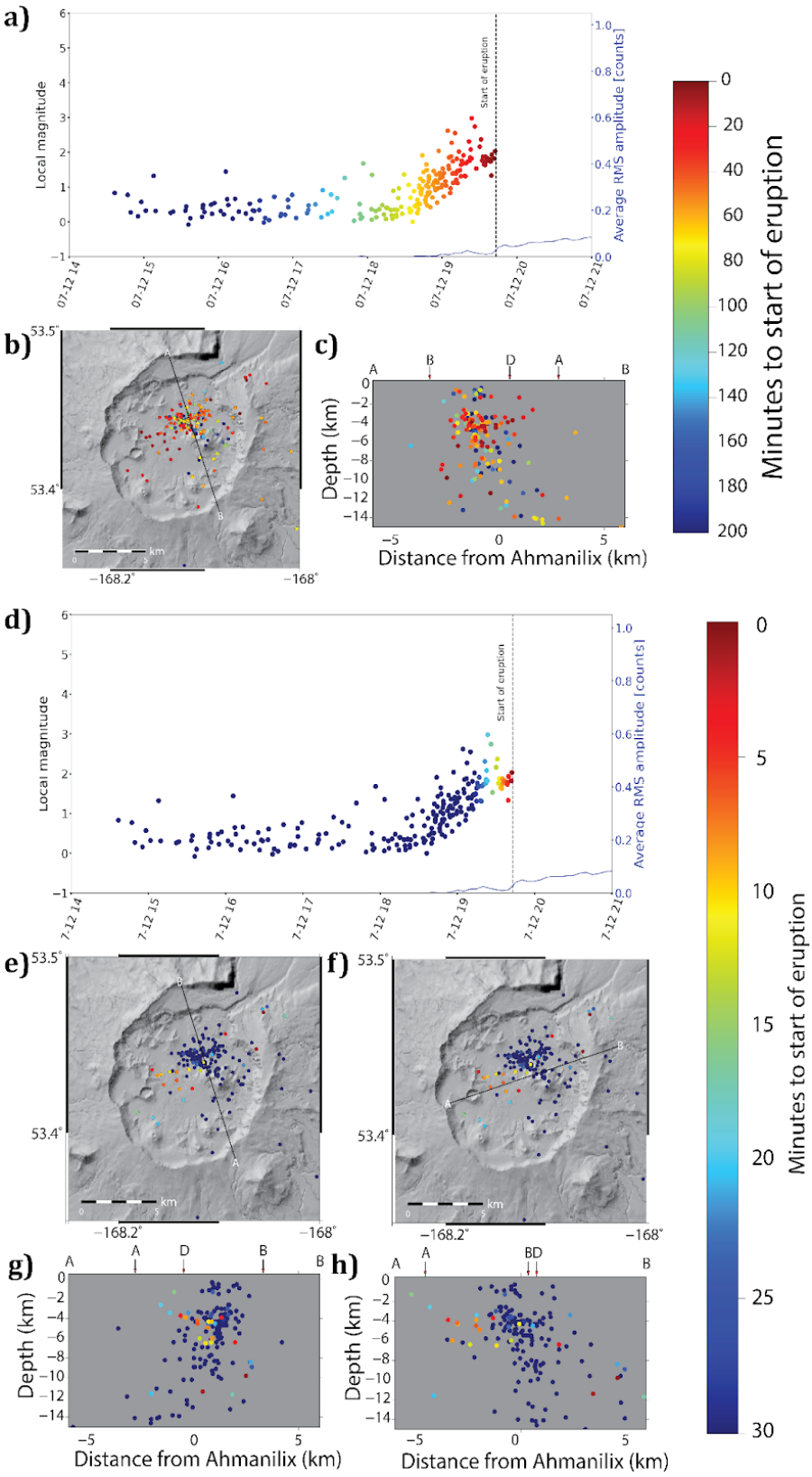
a)
Local magnitude
Average RMS amplitude [counts]
Start of eruption
07-12 14
07-12 15
07-12 16
07-12 17
07-12 18
07-12 19
07-12 20
07-12 21
b)
53.5°
53.4°
−168.2°
−168°
km
c)
A
B
D
A
B
Depth (km)
Distance from Ahmanilix (km)
Minutes to start of eruption
d)
e)
f)
g)
h)
BD

Middle of eruption, July 27-August 1 (LPs)

The middle of the eruption is marked by the most prominent bursts on Figure 2-7 which are also distinguished by a large fraction of LP events. Through this period the seismicity migrated (Figure 2-12). The sequence seems to begin underneath Ahmanilix at 2-5km depths (July 27), then it progresses to the east towards Cone D and it clusters at shallower (~1km) depths (July 30), then it finally migrates east and south towards the caldera wall and Mount Tulik (July 30-August 1).

The first part of the sequence was on July 27, which has more earthquakes than any other day excluding the opening sequence of July 12. The July 27 seismicity had two main bursts, the first between 06:00-12:00 UTC and the second between 16:00-18:00 UTC. The majority of these earthquakes had most of their power at low frequencies, so they were classified as LPs and the observed magnitudes ranged from 2-3. This population is strongly localized underneath Ahmanilix in a region that was previously void of earthquakes (Figure 2-12b).

The sequence is immediately preceded by a slight change in deflation rate which can be seen in the GPS stations at OKSO and OKFG. Interestingly, this burst of LP events happened during a time where SAR images detected the widening of the active vent north of Cone D (called North Vent) and it precedes a period of increased ash content observed in the plumes (Larsen et al., 2015). Observations from MODIS-Terra and MODIS-Aqua corrected reflectance satellite

images, supported by observations from the Advanced Very-High-Resolution Radiometer (AVHRR) (bands 3,4,5) (Figure B-13) and the plume heights reported by Larsen et al. (2009) suggest that, even though there was steam visible in the caldera, clear large emissions of material preceded and followed the earthquakes in this group, but they are not seen during the seismic sequence.

The third burst under the vents was observed on July 30 and lasted from 03:30 to 21:40 UTC. They were also classified as LP events with magnitudes 1.7-3.4 (Figure 2-12). Most of these earthquakes are located under and east of Cone D in a region that was previously relatively quiet seismically.

This burst happened within the periods of the widening of the North Vent and of increase of ash content mentioned above. The burst was also followed by a notable inflationary pulse in the GPS.

Finally on August 1, a group of LP events occurred under the southeast caldera rim extending to Mt. Tulik (see Figure 2-1 for reference). Practically, this group of earthquakes belong to the southern sector of the caldera, but we include them here because they are part of the "middle of the eruption" sequence. These earthquakes were also classified as long-period events and they are slightly smaller in magnitude than the two previous bursts.

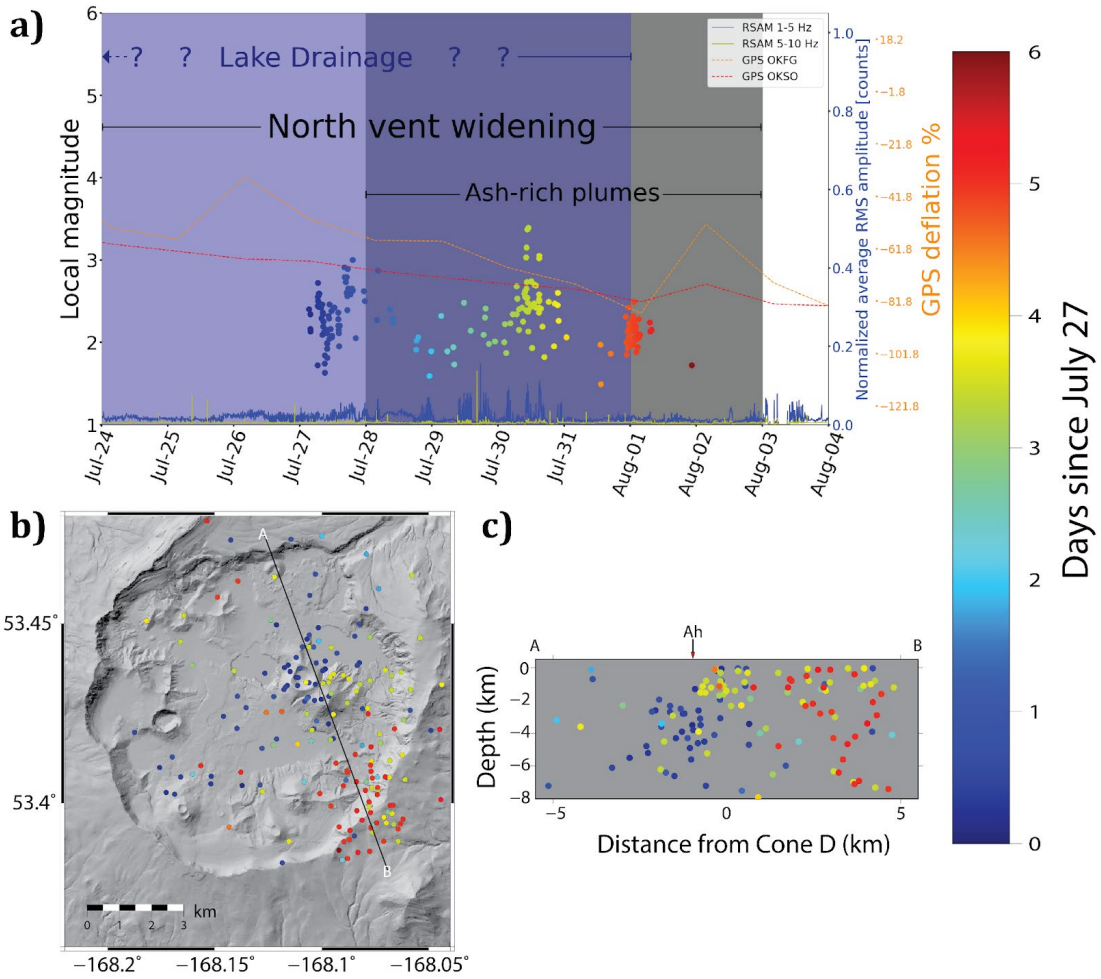

Figure 2-12. a) Magnitudes over time for the LP bursts during the middle of the eruption. b) Map and c) cross-sectional view of the LP earthquakes during the most prominent bursts which occurred from July 27 to August 1 showing the migration pattern. Width of cross-section = 3km; azimuth = 160°. Cross-section arrow: Ah=Ahmanilix.

2.4.3 Southern sector

Cone A (VTs and LPs)

A large number of earthquakes during the eruption are located in the vicinity of Cone A (Figure 2-13), which is the vent that hosted most of the eruptions for more than 100 years. Some of these earthquakes were also noted by Ohlendorf et al. (2014) and are consistent with the results from Johnson et al.

(2010) where they found a multiplet that was persistent throughout years prior to the eruption and where they also noted some activation during the course of the eruption.

Most of the earthquakes in this cluster were classified as VT events, but there were certainly some LP events occurring at this location during the course of the eruption. Interestingly, it is easy to visually separate the earthquakes around Cone A into co-eruptive and post-eruptive. The former are clearly clustered at ~4 km depth southwest of the summit of the cone, whereas the latter start appearing during the very last days of the eruption and they are located west of the cone.

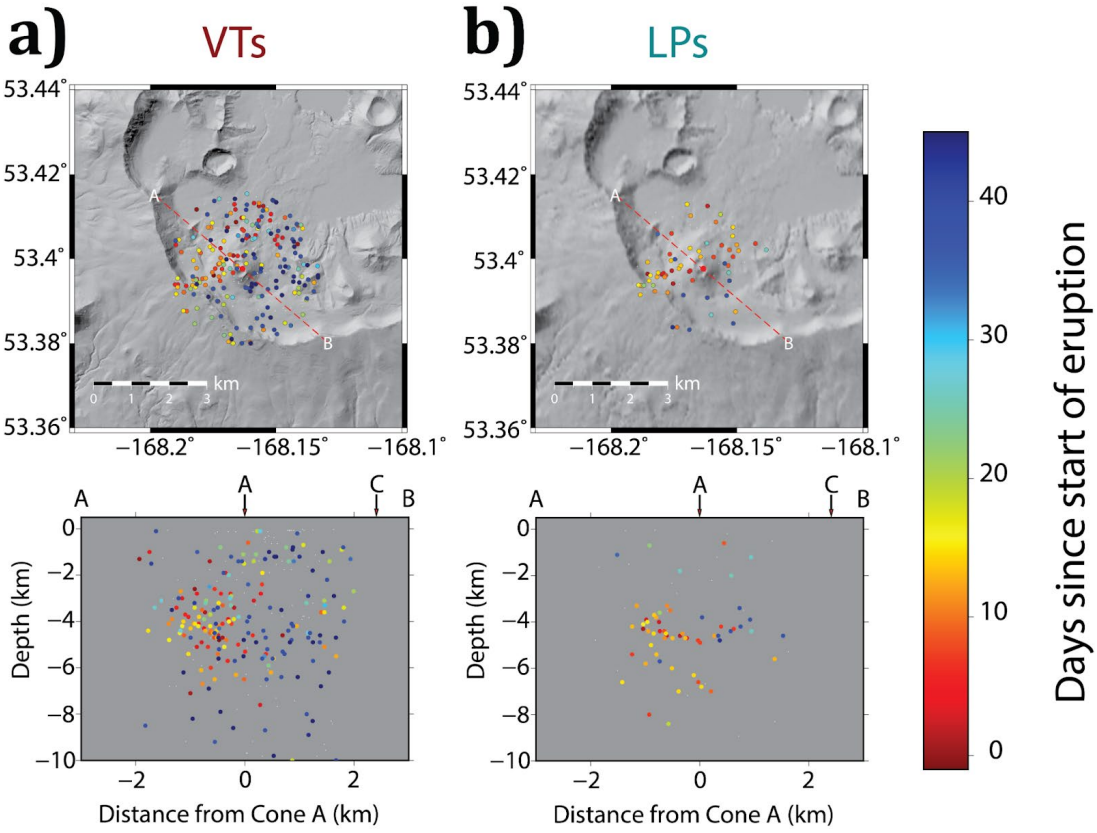

Figure 2-13. Volcano-tectonic events (a) and long-period events (b) localized underneath Cone A, the eruptive vent that hosted the last eruptions in the past 100 years. Cross sectional width = 3 km/azimuth = 130°. Cross-section arrows: A=Cone A; C=Cone C.

End of eruption (mostly VTs)

Instantaneously after the last plume of the eruption was observed, and the RMS of the signal in the two broadband stations on the volcano was reduced, there was a major increase in the number of small earthquakes observed in the southern sector of the caldera and as distributed seismicity all over the southern part of the greater Okmok Volcano and all the way south to the isthmus of Unmak Island. The beginning of this sequence is marked by a burst of LP events

(with some VTs) which winds down after one day to give way to a primarily VT population (Figure 2-7). Inside the caldera, the earthquakes cluster underneath and in between Cone A and Cones E and F. This population represents almost 40% of all the earthquakes that we detected from June 1 to August 31.

2.4.4 Composite measures

Areal Density

An alternative way to visualize the most active areas of the caldera during the eruption is by analyzing the areal density of earthquakes. This metric provides a more quantitative way to define areas of high stress than what one could intuitively derive from looking at the maps presented above. Goebel and Brodsky (2018) used the density decay away from injection wells to classify induced seismicity sequences. Here, we use a variation of their technique by finding the k nearest neighbors of every earthquake and define the areal density as: $\rho = k/\pi(r_{max}-r_{min})$, where r_{max} and r_{min} are the distance of the first and k^{th} event.

To create more insight into the physical processes that triggered VT events versus LP events, we mapped the areal density of each group.

Figure 2-14 reveals that the majority of the events occurred near some of the most relevant intra-caldera cones. The LP event density distributions reinforce the migratory pattern described above showing a high concentration underneath Ahmailix and North Vent and to the southeast of the caldera. However, it is interesting to note that the rest of the LPs during and after the

eruption clustered underneath Cone A. The VT population during and after the eruption is more distributed than the LP population. However, it is highly concentrated in the southern sector underneath Cone A (see section above) and in the proximity of Cone C and Cone F (see Figure 2-1 for reference). Cone C is an asymmetric cone similar in composition to Cone D and its southern face shows signs of hydrothermal alteration. Byers and Brannock (1949) reported seeing Cone C emitting solfataric high-temperature fumaroles in 1946, around 75 years from the date of this publication. The high concentration of VT events in the proximity of this cone and the migration of LP events towards the east of it might be an indication that this hydrothermal system is still active.

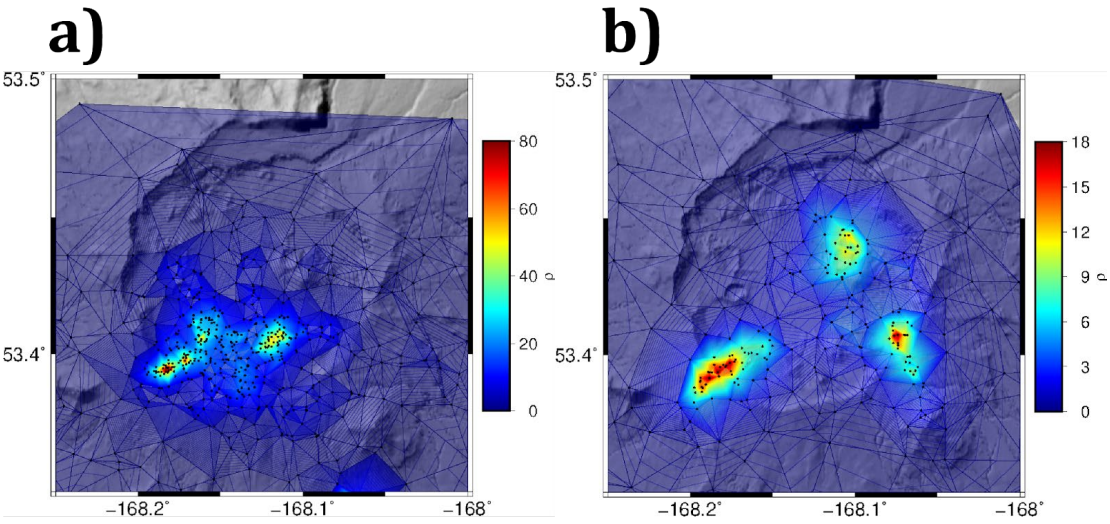

Figure 2-14. Areal density for VT (a) and LP (b) earthquakes with depth < 7km. The density is calculated following the method from Goebel and Brodsky (2018) which uses the k nearest neighbors (10 in this case) from each grid node so that $\rho = k/\pi(r_{max}-r_{min})$, where r_{max} and r_{min} are the distance of the first and k^{th} event.

Earthquake clustering

The cross-correlation of volcanic earthquakes to detect earthquake clusters or multiplets is common practice to understand volcanic processes (e.g., Buurman et al., 2006; Petersen, 2007; Umakoshi et al., 2008; Thelen et al., 2011). Here, we use this technique not with the purpose to find multiplets or families of earthquakes but rather to create more insight into the dynamics of the eruptive process at Okmok. The method that we used is as follows: we used 3 seconds of the waveforms of each event (0.2s before P- 2.8s after P), we processed all our waveforms by removing the mean applying a linear detrending and a 5% Hanning window taper and we filtered all the waveforms between 3-10Hz. Using these waveforms, we created a cross-correlation matrix that allows us to distinguish between the events that are well correlated and the ones that are not. The cross-correlation matrix in Figure 2-15 presents the results of every event cross-correlation to the others. The events are sorted chronologically so low event indices correspond to the starting sequence and high indices correspond to post-eruptive earthquakes. Because of the extreme noise levels during the explosive eruption absolute cross-correlation values between pairs of events are relatively low compared to what is usually observed. However, one can still draw important conclusions from this analysis. By saturating the colors of the matrix to a z value = 3 (3 standard deviations of the mean CC value), we are able to accentuate the data and detect the different clusters much better. For each of the main clusters that stand out, we calculated an epicentral centroid by

using the median latitude and median longitude. Figure 2-15 confirms what our previous observations suggested. There are three main groups in our dataset: pre-eruptive, co-eruptive and post-eruptive. The VT pre-eruptive clusters have their centroid in the active vents. The co-eruptive earthquakes correspond to LP events and their centroids track the migration pattern described above (from Ahmanilix to the southeast caldera rim and Mount Tulik). The last cluster of earthquakes during the eruption clusters near Cone A and the largest post-eruptive earthquake cluster in co-localized.

The short-term runup of seismicity leading up to the eruption (July 12) shows a cluster of well correlated earthquakes from 14:00-18:00 hours UTC and a secondary, not so well correlated, group of earthquakes between 18:00-19:00, before the earthquake migration to the deflation source right before the eruption started which is discussed in a previous section of this paper. The centroid location of these two clusters suggests that the focus of pre-eruptive activity shifted from right underneath the North Vent to Ahmanilix within hours and then it continued to migrate to the southwest towards the deflation source. These observations confirm the pre-eruptive chronology narrated by Ohlendorf et al. (2014) and the existence of the earthquake family to which they refer in their paper.

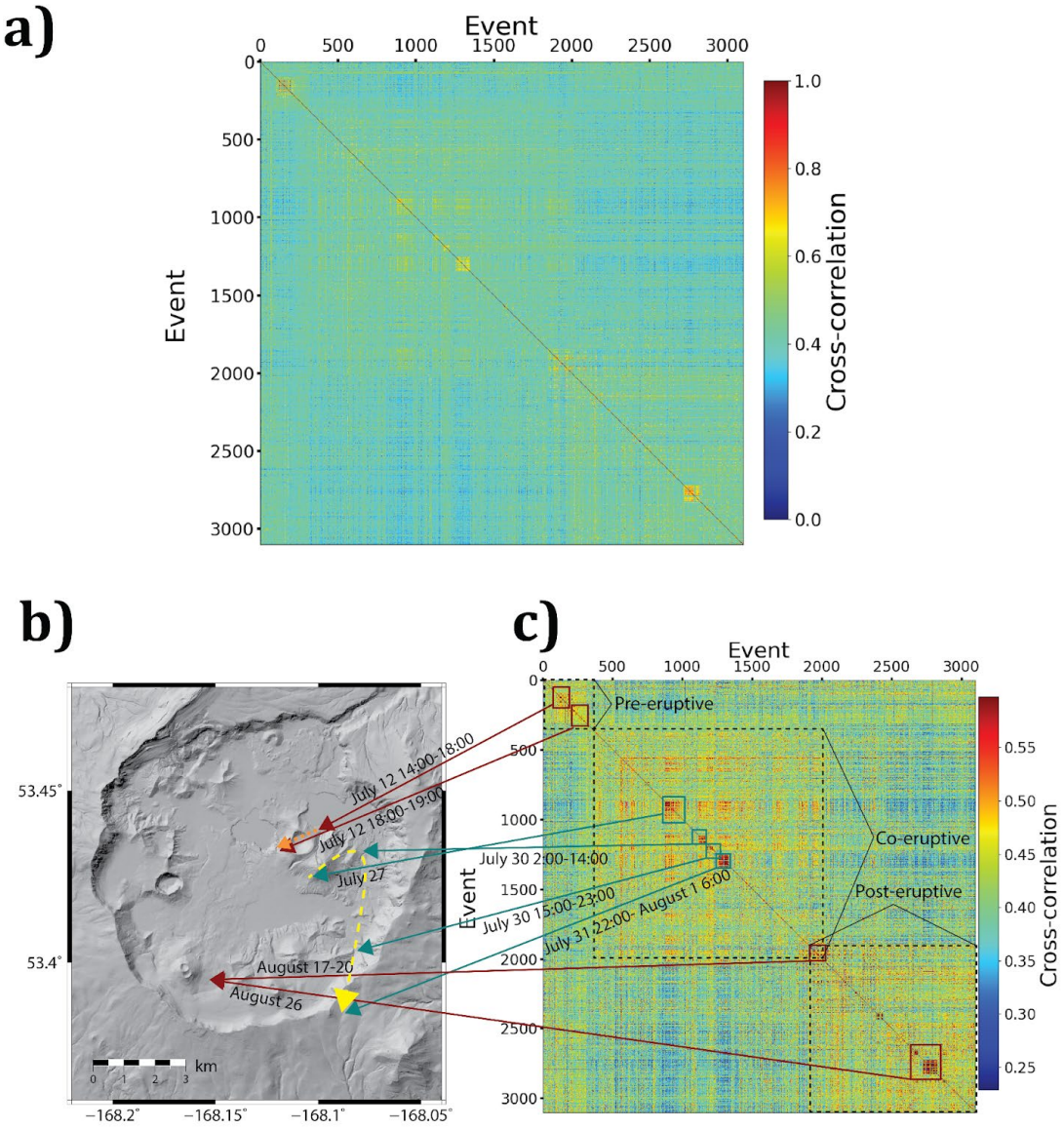

Figure 2-15. Cross-correlation matrix using the full CC scale (a) and the saturated scale at 3 standard deviations (c) showing the main clusters of events and the location of their centroid (b). Turquoise squares/arrows show LP activity. Red squares/arrows show VT activity. Dashed orange arrow shows the suggested precursory VT migration path. Dashed yellow arrow shows the suggested co-eruptive LP migration path. The events are sorted in time.

Frequency-magnitude distribution

Does the abrupt change in magnitudes observed in Figure 2-7 reflect a change in the stressing regime as the eruption evolved? To answer this question we analyzed the frequency-magnitude distribution of the earthquakes by calculating time variations of the newly developed b+ estimator (Van der Elst, 2021) which considers the distribution of the differences in magnitudes instead of the magnitudes themselves. The b-value calculation was also utilized in the seismicity rate extrapolation included in the overview section above, but we have deferred discussion of the b-value specifically until now so as to be able to place it in its eruptive context.

Earthquakes in the opening sequence have a low b+ (0.74) meaning that the stress concentration in the north sector of the caldera was the highest during all the eruptive process (Figure 2-16). Even though the magnitudes of the earthquakes observed during the eruption are the highest, their distribution seems to favor smaller earthquakes, giving a high b+(1.72). Finally, the post-eruptive earthquakes show a lower b+ (1.3) than the co-eruptive period, but higher than the initial sequence, suggesting that the stress was higher than during the course of the eruption. The uncertainties shown in Figure 2-16 were calculated by 300 bootstrap realizations. We also calculated the temporal variations of the b-value using a maximum-likelihood estimation (Utsu, 1965; Aki, 1965) and we could confirm that the main observations are robust and independent of the estimator (Figures B-5 - B-6).

All the 1-P values based on equation 1-1 for all the combinations of pairs of b+ and b values are much lower than the 99% confidence limit, so we conclude that our results are highly statistically significant.

Subdividing our data into pre, co and post-eruptive can help us develop a rough intuition of the eruptive process itself, but we are certainly losing resolution that can tell us about the individual phenomena that actually causes the earthquakes. In an attempt to increase our resolution, we calculated values of b+ in moving windows of 100 events with a 10% overlap. Again, uncertainties were calculated via bootstrapping.

The maximum time difference in our windows (i.e. the time difference between the first and nth earthquakes) was 8.7 days. Once again, our results map into the chronology of the eruption very well (dashed gray lines in Figure 2-9). There is a steady increase in b+ from the start of the eruption that is interrupted right when the North Lake drainage was observed. The b+ values then decrease slightly until the times when the vents widening is reported. The high values during the time of the vent widening are intersected by a large reduction starting at the times when more ash was observed in the eruptive plumes and ending when water was observed standing in the North Lake again. Towards the end of the day on August 2, b+ values started decreasing smoothly until the eruption reached its end and then they went into a large plunge. This large plunge is followed by a recovery in the post-eruptive seismicity but it never reaches the high values that are observed during the eruption.

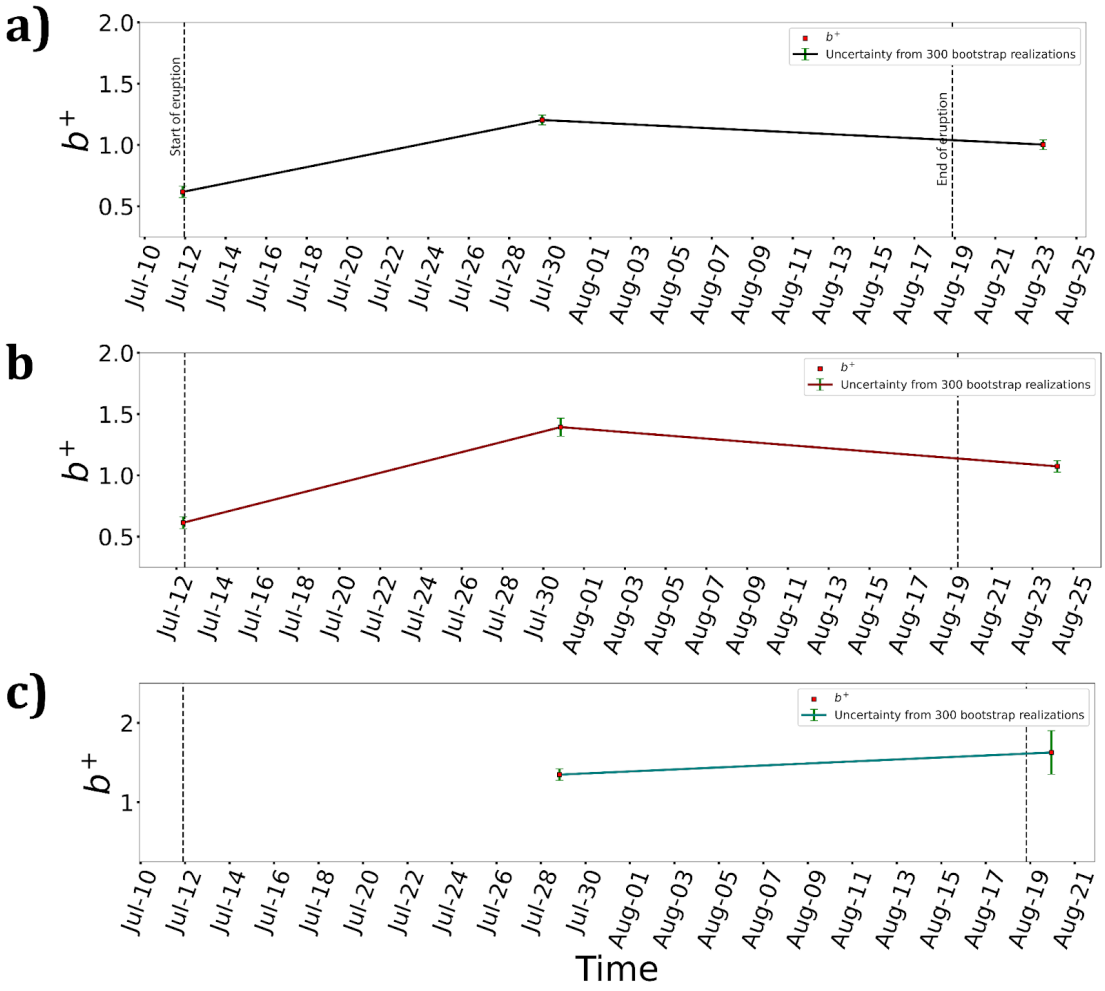

Figure 2-16. Temporal distribution of b+ before, during and after the eruption. a) All earthquakes. b) VT earthquakes only. c) LP earthquakes only. Almost no LP events were detected in the eruption runup.

2.5 Discussion

The fact that our absolute locations map the main features detected by AVO in their original catalog gives us confidence in the location of all our earthquakes. The relocation of the earthquakes shows an improvement in RMS for all the clusters. Below we will give our interpretation of the main features that can be seen using the different relocations (i.e., hypoDD and GrowClust).

2.5.1 Summary of Observations

Observation 1: Absence of seismicity in center of caldera

The center of the caldera shows an absence of any type of seismicity throughout the eruption.

If we only consider the earthquakes during the eruption, we can clearly see the aforementioned bowl of no-seismicity centered in the middle of the caldera at shallow (>3 km) depths bounded by activity underneath the active vents and Cone A (Figure 2-17b). This anomaly matches the location of the shallow magma reservoir suggested by a wealth of other papers (e.g., Mann et al., 2002; Lu et al., 2005; Fournier et al., 2009; Biggs et al., 2010, Haney, 2010; Masterlark, 2010; Lu and Dzurisin, 2010; Albright et al., 2019). However, it does not match the location of the earthquakes that Ohlendorf et al. (2014) relocated in the center of the caldera. We assume that this discrepancy could be due either to the lack of earthquakes in their dataset, even though the misfits of the relocations have a similar order of magnitude in both works, or to the difference in velocity model utilized in each work. If, indeed, there is not a dense cluster of

earthquakes in this location, we intuit that is either because the shallow magma system (which we envision as a network of cracks and pockets filled with magmatic fluids) has been diffusing heat into the rocks that form the matrix of this reservoir, inducing a change in the material properties into a ductile regime or because most of this rocks are actually unconsolidated caldera fill that act more as a granular flow, in both cases being unable to accommodate elastic stresses large enough to trigger even small magnitude earthquakes.

Observation 2: Opening sequence migration

The opening sequence, which is entirely composed of VT earthquakes, extends to depth and is marked by a migration from North Vent to Ahmanilix within hours (Figure 2-15) and after that, within minutes, to the onset of the eruption towards the previously identified center of deformation (Figure 2-11), which is located under the center of the caldera and is distinct from the eruptive vent.

The earthquakes are well located underneath the foci of the eruption at ~4-7km depths. There is only a small cluster of shallow earthquakes underneath the maar craters that could be an indication of more vigorous hydro-magmatic interactions prior to the initial explosions. The time-series of the magnitudes during this runup period show a gradual increase leading to the onset of the eruption, but the magnitude differences and magnitude cumulative distributions functions (Figures B-9 and B-10) suggest that this sequence was cut short by the

opening explosions, resulting in a deficit of the large earthquakes that would have occurred had the eruption been delayed.

The fact that all of these earthquakes have a high frequency content, the increase in magnitudes as the eruption approached and the geometry of that they form, makes us believe that this group is the result of an increase in shear stress in the host rocks as magmatic bodies were supplied with more materials from deeper sources and thus getting rapidly pressurized. The increase of shear stress would cause the brittle failure of the rocks allowing fluids to migrate towards the surface.

Albright et al. (2019) observed that the inflation prior to the eruption at Okmok was mainly lateral and suggested that the 2008 eruption was caused by tensile failure in the magmatic source weeks in advance. Since AVO did not detect any significant shallow earthquakes in the months leading up to the eruption, if such tensile failure in the reservoir happened, it must have occurred slowly and aseismically. Furthermore, Larsen et al. (2013), based on a petrological and geochemical study, concluded that the eruption was triggered by an influx of basaltic magma from a 3-6km depth source, but that it intersected a more evolved andesitic pod of magma underneath Cone D. Then, a possible explanation to reconcile their observations with ours is that magma extended from the center of the caldera to the northern sector without triggering earthquakes until it found the largest groundwater bodies in the caldera, rapidly increasing the pore-pressure in the area triggering hundreds of VT earthquakes

allowing for the contact with the andesitic melt under Cone D. A lack of VT (or LP) events at shallow depths directly underneath Ahmanilix and the North Vent before the eruption started suggests that these vents could have been formed by the blasting of explosions right at the onset of the eruption instead of by fracturing the shallow rocks.

Observation 3: LP events that precede plumes

The most significant co-eruptive seismic sequence occurred nearly half-way through the eruption and initiated a burst of long-period (LP) earthquakes directly under the eruptive vent followed by ash-rich plumes.

The events on July 27 mark the beginning of a key process during the eruption. The evidence is as follows:

- The July 27-August 2 earthquakes under the vents have a predominantly long-period spectral character.
- The events are not well correlated in time with observations of large plumes from satellite images. They are preceded by white plumes, but they are followed by large emissions with a richer ash content (Figure 2-9 and Figure B-13).
- The cross-correlation of LP events rate and plume rates confirm the anti-correlation between the two signals (Figure 2-10).
- The earthquakes are bounded by pulses in the GPS (Figure 2-7)
- They are located underneath Ahamanilix but migrate towards the east and south within days (July 27 to August 1) (Figure 2-11).

- This migration of LP events is followed by tremor migration from the North Vent to the caldera wall to the east on August 2 (Haney, 2014), which was substantiated by the observations of migrating plume sources on August 2 from AVO staff that was on Unmak Island (Larsen et al., 2015)
- During the period from July 27 to August 3, we observed the largest b+ reduction anomaly during the eruption, signaling an increase in magnitudes (i.e., increase in energy) in the earthquakes (Figure 2-9).
- Finally, b+ values (and b values) decrease, but the corrected seismicity rate indicates that there is a spike in earthquake production during those days (Figure 2-9 and B-12).

We start to explain these observations by first noting that pulses in the GPS that interrupt the deflationary trend occur when pressure is allowed to build up in the subsurface of the caldera. The main three pulses are observed after the first observation of drainage in North Lake, and before and during the observations of increase in ash in the ejected plumes. We also note that widening of vents can happen either by explosive blasting or by collapse.

We therefore speculate that the second GPS pulse (July 26-July 27) was due to a partial collapse in one of the main vents (remember that there are no large plumes observed during these days), causing the overpressurization of the trapped fluids and making them migrate through the damaged medium. The

partial decrease in b+ accompanied by a spike in earthquake rate gives testimony of this momentary re-pressurization. The long-period events, then, are not the reflection of slow ruptures or brittle failure in crystal magma, but rather they depict over-pressurized fluid filled cracks (Chouet, 1996; Chouet and Matoza, 2013). Perhaps the magma reservoir to the west and southwest of the vents preclude the fluids to migrate to those regions, and the north is bounded by the vents themselves, so the only place left for the fluids to go is to the east towards Cone D and the caldera wall.

Besides pushing water and gases outward, the overpressurization under the two main active vents (Ahmanilix and North Vent) at some point would also overcome the clogging stress, making large explosions containing water-saturated lithics. Unema et al. (2016) noted that evidence for magma-water interaction increased through the eruption based on analysis of the deposited products. A secondary large pressure pulse on August 1 occurred at the same time as LPs of lower magnitudes are triggered to the southeast of the caldera, signaling another significant clogging episode. The climatic sequence culminates as LPs give way to a migrating high amplitude tremor at the vents and the last large, ash-rich plumes of the 2008 VEI 4 Okmok Volcano eruption are observed. The volcano seemed to have lost most of its eruptive power during this series of events and it began to abate until the last emission was observed on August 19.

Observation 4: VT events in the southern caldera

A distinct population of VT earthquakes maintain a steady rate during the eruption over a large region (Figure 2-8b) and do not follow the deflation rate from the GPS stations. Although the VT earthquakes are more distributed than the LPs, the density maps (Figure 2-14a) and the clustering analysis (Figure 2-15) show that they cluster in the vicinity of Cone A and Cone C. The VT earthquakes under Cone A are the only visible link between the deep (~5 km) cluster of earthquakes and the shallow seismicity (Figure 2-7). A different perspective is provided in Figure 2-13, where we can see that the VT earthquakes occupy most of the southwest flank of Cone A and some of them are co-located with LP events. The co-eruptive VTs have a larger b-value than before or after the eruption (Figure 2-16). This could be indicative of a reduced differential stress state as will be discussed below.

Observation 5: LPs and small earthquakes at the end of the eruption

The cessation of eruptive activity is marked by a sudden burst of long-period (LP) earthquakes which is accompanied and followed by a steady stream of small earthquakes that occur south (and therefore distinct) from the previous concentration of seismicity.

The end of the eruption is marked by an abrupt change in magnitude of completeness, yet a decrease in b+ values, and a jerky but gradual decrease in earthquake rate. Freymueller and Kaufman (2010) discuss the changes in the GPS deflationary trend that started 2-3 weeks after the main ash emissions

(sequence described above). Their main observation was a change in rate in the two GPS stations outside the caldera (OKSO and OKFG), but deflation was still ongoing until late September at least on OKFG, and an instantaneous inflationary signal inside the caldera as recorded by the station OKCE which was repaired by AVO staff after the eruption. They interpreted this as the result of deflation in a deep source and the immediate inflation of a shallow (>2km depth source). The post-eruptive seismic sequence starts with a burst of LP events which is indicative of fluid pressurization. These LPs are accompanied and followed by hundreds of VT events localized in the vicinity of the intra-caldera cones A, C and F and dispersed on the southern flank of the greater Okmok Volcano. We speculate that the earthquakes captured at the end of the eruption are the result of an increase in pressure driven by magma migrating toward the low-pressure shallow zone as the post-eruptive refilling was occurring. The drop in b+ announced that the medium is being re-pressurized as Okmok stayed closed after the last plume was observed.

These previously inaccessible observations show that the co-eruptive LP and VTs are showing distinct behavior, likely signifying distinct processes.

2.5.2 Mechanisms

LP generation

The long-period seismicity that is observed underneath the active vents and Cone D during the middle of the eruption are undoubtedly related to the eruptive process and the immense amount of water accumulated in the

subsurface of this area. The bursts are highly energetic, and their rate is anticorrelated with the rate of plume emissions. Given the timing, location and migration of these low-frequency earthquakes, and their anti-correlation with plumes, our preferred model is a clog and crack mechanism: The open vents become partially clogged, potentially by their own collapse which is also seen in the surface as widening, allowing for pressure to build up in the subsurface and pushing great amounts of fluids into existing cracks causing volumetric changes that translate into the solid medium as low frequency seismic radiation. At some point, the accumulating pressure in the partially clogged system would overcome the clogging stress, triggering explosions that are followed by high, dark plumes and an LP rate reduction. The energetic release would last until most of that pressure has been exhausted, causing the plume rate reduction, re-clogging and triggering of a new LP burst. The last burst of LP events, which occurred after the last plume emissions, possibly reflects the filling of the cracks with magmatic fluids and gases, as well as water, as the system remained permanently clogged and the shallow reservoir started to refill again.

There is, however, another possible explanation for the observed LPs in Okmok that we cannot disregard. This second mechanism would require dividing the LP population into the LPs that are seen directly underneath the vents and the LPs that are seen close to the caldera wall and other intra-caldera cones (A and C). The LPs underneath the vent could be signaling the intrusion of a deeper magmatic dike that is migrating towards the surface (hence the LP

migration and anti-correlation with plumes), whereas the LPs close to the caldera wall could be the reflection of slow slip in patches of the ring fault structure.

Solving this ambiguity would require more data, which we do not have for this eruption. Denser arrays of instrumentation in Okmok Volcano could help better understand the eruptions that will likely happen in the future and the response of the caldera system to it.

VT generation

We interpret the shallowest seismicity in the caldera as events triggered primarily by the pressurization of groundwater in the caldera. The depth at which they occur (0-1 km) coincides with the source of local deformation during the eruption described as a flat-lying tabular source at ~0.5km depth (Lu and Dzurisin, 2010). Also, the only shallow earthquakes in the opening sequence are located under the maar craters, once again indicating magma-water interactions. The elongated "quiet" gap that is seen at ~2-3km depth in the hypoDD relocations cannot be deemed as true because we do not clearly see it in the GrowClust relocations, and most likely is an artifact of the sharper velocity model that we used as input for hypoDD.

From Figure 2-7 we can see that dividing the data into two different groups based on their magnitudes (events with M>=1.6 and M<1.6) makes a clear separation between the events that happened before and after, and during the eruption. Figure 2-17a shows that the pre- and post-eruptive earthquakes

are almost perfectly well divided into the north sector of the caldera (active vents) and the south caldera sector extending to the south flank of the greater Okmok shield volcano, respectively. Furthermore, the temporal distribution of b+ values of VT events (Figure 2-16) suggests that the elastic stresses that have the potential to trigger VT events were lower during the eruption than before and after. Given that we know that the pre-eruptive sequence was triggered by an intrusion and that the GPS station OKCE located inside the caldera (Cone E) showed a re-inflation signal when it was fixed by AVO staff shortly after the eruption ended, we interpret the VT generation as a reflection of the pressure accumulated in the subsurface as a closed and very pressurized system due to the injection of magma (low b+) becoming open as the extraction happens (high b+) and then closed again (low b+). The notion that b values have a stress dependence and that tracking b values over space and time can illuminate changes in the stress field is a common tenet in seismology (Scholz, 1968; Scholz 2015); variations in b values have also been broadly explored in volcanoes (e.g., Bridges and Gao, 2006; Wyss et al., 2001; Garza-Giron, 2014)

The areal density distribution of earthquakes during and after the eruption (Figure 2-14) suggests a very interesting hypothesis. While the eruption was developing in the northern sector of the caldera, hundreds of earthquakes were being triggered under Cone A and its surroundings, including Cone C. If we exclude the opening sequence and consider only the co and post-eruptive earthquakes, the areal density map shows that, even though the largest

earthquakes happened at the vents, most of the seismic activity was being triggered in the south. Cone A had been the active vent during the past 100 years before the 2008 eruption, and Cone C is the most hydrothermally altered cone inside the caldera and it was seen producing fumaroles ~75 years ago. The high production of triggered earthquakes around these areas during the 2008 eruption might imply that even though the northern sector was seeing a large-scale extraction process during the eruption, the rocks in the southern sector were being subject to loading. Whether these earthquakes were triggered by changes in injection (or extraction) of fluids, or simply by the changes in the stress-field as the caldera floor subsided during the eruption and subsequently inflated in the post-eruptive stage, remains unknown. Nevertheless, this observation does imply that the rocks around Cone A and Cone C are very subject to brittle failure and possibly mark de limits of the shallow magma reservoir.

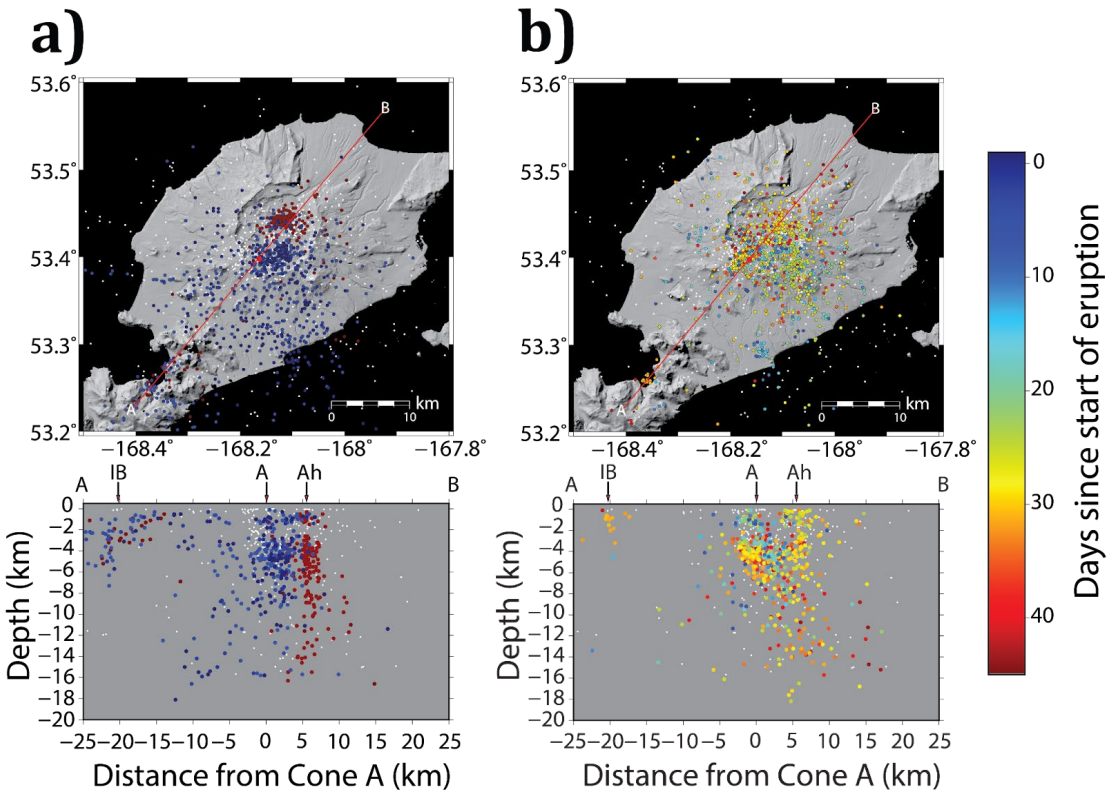

Figure 2-17. a) Pre and post eruptive events. b) Co-eruptive events. Cross sectional width = 3 km/azimuth = 40°.

2.5.3 Caveats

The dramatic change in magnitude of completeness before, during and after the eruption is a peculiar observation and its meaning is a difficult problem to resolve. Even during the days when the RMS was very low during the eruption (e.g. August 13-17), we could not detect many small (<M1) magnitude earthquakes. Thus, even though it is likely that an increase in ambient noise is responsible for the lack of detection of small earthquakes during the span of the whole eruption, there is a possibility that there were just no small events while the system was open. The magnitudes of the original AVO catalog (black points

in Figure 2-4) are also affected by this bias, although their magnitudes seem to be systematically smaller than the ones calculated by us.

2.6 Conclusions

By leveraging the advantages of modern earthquake detection methods, we have enhanced the seismic catalog of a long-lived explosive eruption. The co-eruptive LP and VTs are showing distinct behavior, likely signifying distinct processes. LPs are strongly localized in space and time and directly precede, but are not concurrent with, mass ejection in contrast with the steady, widely distributed VTs. Together the seismicity is illuminating how an eruption begins, evolves, and ends, which is a major goal of volcanology (National Academies, 2017).

The opening sequence extends to depth and is marked by a migration from the North Vent towards the previously identified center of deformation, which is located under the center of the caldera and is distinct from the eruptive vent. This seismic migration is consistent with magma recharge from depth into a chamber 2-3 hours before the eruption.

The eruption then evolved through a series of opening and closing cycles that showed a distinctive pattern of seismicity that we term clog-and-crack. High levels of seismicity rate half-way through the eruption disclose a series of migratory long-period (LP) earthquakes that started with a burst directly under the eruptive vent, followed by ash-rich plumes, and continued to the east and southeast with two other main bursts that were also followed by dark plumes. The rate at which

these long-period earthquakes occurred is anti-correlated with plume rates. Repeated injection, opening and reclosing is a major feature of the eruption's progression.

The eruption also involved a distinct population of VT earthquakes maintain a steady rate over a large region on the southern side of the caldera. These co-eruptive VTs have a larger b-value than before or after the eruption, suggesting that the extraction process induced lower levels of stress in the caldera than the pre and post-eruptive injection. The presence of these events over a wide swath of the caldera and their absence in a bowl in the central caldera that is likely less brittle is evidence that the presence or absence of VTs can be controlled by structure rather than the location of the stressing. In this case, the different structures in the volcano respond differently to a fairly distributed, steady forcing.

The end of the eruptive activity is marked by a sudden burst of LP earthquakes which is accompanied and followed by a steady stream of small earthquakes that occur south (and therefore distinct) from the previous concentration of seismicity. Given the association of LP events with the previous pressurization episodes it is possible that the end of the eruption was marked by another intrusion that failed to reach the surface and thus sealed the system.

An overriding theme is the repeated closure with clogged vents, as signaled by the localized LPs and subsequent opening with eruptive plumes. Even the closure of the eruption appears to have been a variation of this cycle. The high-speed

evolution of the vent and pressurization of the rock can be seen through these previously inaccessible observations have provided new clarity into the stages of the Okmok eruption.

Chapter 3 – Geothermal heat-flux mapping in the McMurdo Sound using air-borne transient electro-magnetics

3.1 Introduction

Geothermal heat flux (GHF) reflects tectonic and volcanic history of the upper crust and lithosphere (e.g., Damiani et al., 2014; Begeman et al., 2017). In Antarctica, where there is paucity of constraints on GHF (Davies, 2013), climate sensitivity of polar ice sheets and glaciers may be dependent on the magnitude of heat input from beneath them (e.g., Pollard et al., 2005; Seroussi et al., 2017). Geothermal heat flux in Antarctica is generally described as having continental-scale variations, with the West Antarctic ice sheet having higher values (>40 mW/m^2) than the East Antarctic ice sheet (<40 mW/m^2) (e.g., Shapiro and Ritzwoller, 2004; Pollard et al., 2005). However, it has also been shown that regional variations in GHF can be large (Fisher et al., 2015; Begeman et al., 2017).

Burton-Johnson et al. (2020) reviewed the limitations of the various methods used in Antarctica to constrain GHF. Some of these limitations have to do with shallow penetration of tools used to determine the vertical temperature gradient and with the very localized nature of such measurements. By reviewing previous studies that calculated GHF from borehole measurements and adding a high-quality measurement from an Antarctic Drilling Program (ANDRILL) borehole close to McMurdo station, Morin et al. (2010) showed that, on a regional scale, there is some variation in the spatial distribution of GHF in the

McMurdo Sound. However, their study was limited in resolution due to the sparsity of the data, which came from a small number of deep boreholes drilled into marine sequences and bedrock found at the bottom of the McMurdo Sound. Nonetheless, along with the relatively well-studied region of the Antarctic Peninsula (e.g., Burton-Johnson et al., 2017), the McMurdo region offers the best opportunity to study the regional variability of GHF in Antarctica and its relationship to tectonic and volcanic history. This is mainly thanks to the fact that several GHF measurements were made here on land and in the McMurdo Sound (e.g., Decker and Buecker, 1982; Morin et al., 2010).

More recently, Foley et al. (2020) presented a method for mapping 10-km-scale variations in GHF on the western flank of Mount Erebus in Ross Island, Antarctica, using electrical resistivity obtained from air-borne transient electromagnetics (ATEM). Variations in the electrical resistivities of rocks and soils are chiefly dominated by porosity and the ionic content of the water that saturates them. Previous ATEM surveys in the McMurdo Dry Valleys (MDV)(Figure 3-1) have shown the presence of conductive layers underlying resistive zones interpreted as brine saturated fluids under caps of ice or permafrost (Dugan et al., 2015a; Mikucki et al., 2015; Foley et al., 2016). In this work, we follow up on the finding of these previous GHF and ATEM studies and extend the approach of Foley et al. (2020) to a regional scale by applying their GHF mapping technique to a new data set that covers ~2,000 km of TEM data in the McMurdo Sound, Antarctica, with the goal of acquiring more information on

the variability of heat flux in a polar region surrounded by active volcanism and its implications on ice sheets dynamics.

3.1.1 Tectonic Setting

The McMurdo Sound is located in the South Victoria Land of West Antarctica, and it is a product of the extensional regime of the Victoria Land Basin (VLB), which is a 150 km wide half-graben and represents a local structure of the greater West Antarctic Rift System (Cooper et al., 1987; Henrys et al. 2008). The most recent extensional sequence started in the late Cenozoic giving rise to the Terror Rift (McGinnis et al., 1985; Fielding et al., 2006), which is associated with young alkalic volcanism, and it is bounded by the active volcanoes Mount Melbourne at Cape Washington in the north and Mount Erebus in Ross Island in the south, although the complete southern extension is unknown (Cooper et al., 1987). The primary tectonic characteristics of the McMurdo Sound are the Transantarctic mountains to the west, the Erebus volcanic complex to the east and the Discovery volcanic complex to the south, the southern striking half-graben structure and east-west striking transform faults (Figure 3-1) (Kyle, 1990; Wilson et al., 2007; Johnston et al., 2008).

3.2 Data and methods

3.2.1 2018 Antarctica Airborne Electromagnetic Survey

We use the data from a 2018 airborne transient electromagnetic survey in the McMurdo Sound. Overall, the survey collected ~2000 km of flight lines (black lines in Figure 3-1) focusing on the McMurdo Dry Valleys, their coastal

ranges, and an area outside of McMurdo station where the Ross Ice Shelf meets the sea-ice. Since high conductivity layers close to the surface, as well as induced polarity (IP) effects (e.g., Garwood Valley) make it difficult for the SkyTEM system to accurately sample the deeper subsurface (Grombacher et al., 2021), we only used resistivity profiles of places where such effects were not present and where we could distinguish a clear boundary between the resistive permafrost (or ice) and the conductive sub-permafrost groundwater systems. These profiles are shown as green lines in Figure 3-1.

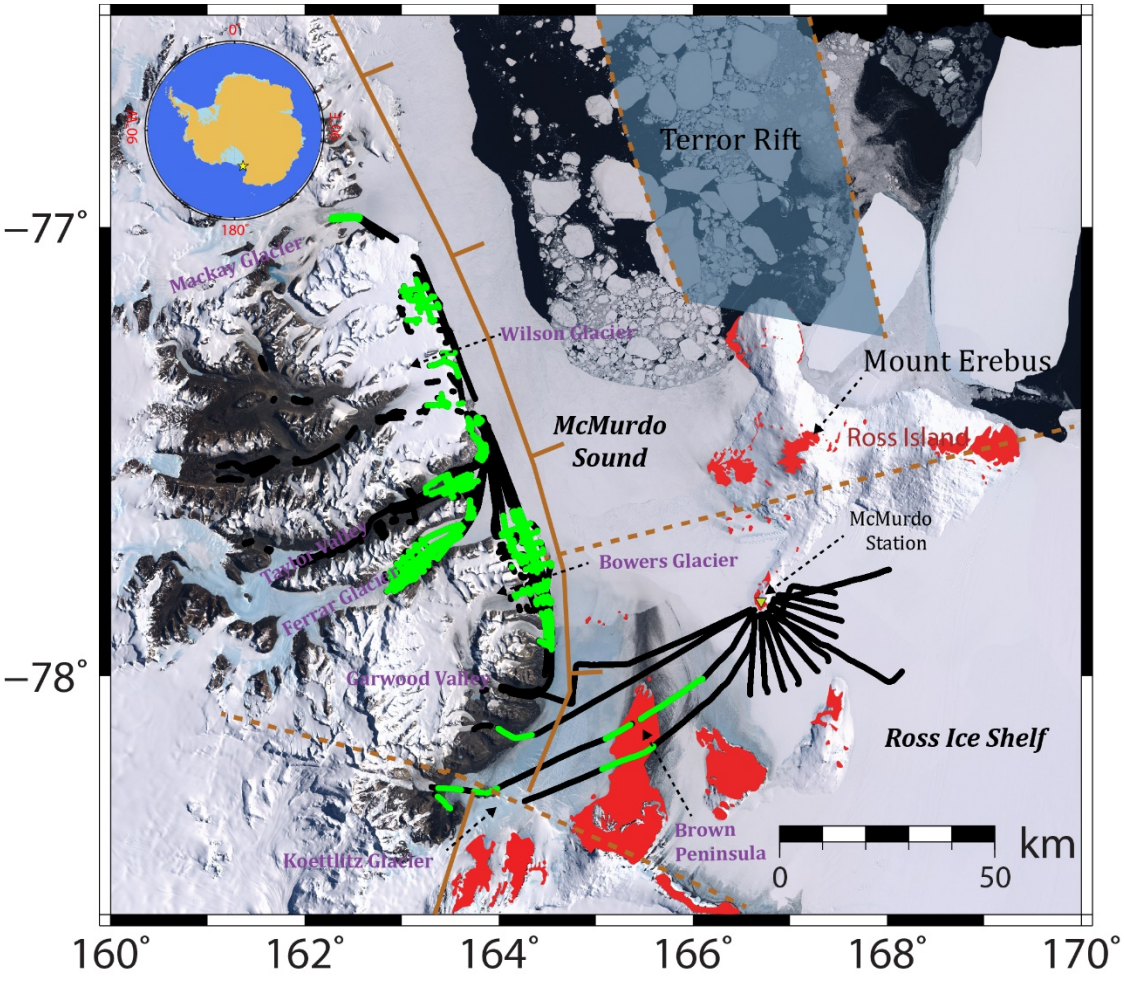

Figure 3-1. Map of the 2018 SkyTEM survey in the McMurdo Sound, Antarctica. Black lines show the path of all the flight lines of the survey (~2000 km). Green lines show the data used in this study. Red patches indicate the mapped McMurdo Volcanic Group (Kyle and Cole,1974; Kyle 1990). The main tectonic features are the McMurdo Sound rift basin which is tectonically bounded by an east dipping fault to the west and a transform fault to the south (RL) and it is crossed by the Ross Fault (Wilson et al., 2007; Johnston et al., 2008).

The SkyTEM system (Sørensen and Auken, 2004) is an airborne time-domain electromagnetic sensor and its functionality can be summarized as follows: Electric pulses of up to ~100 Ampere are sent through a transmitter coil which induces a magnetic field that propagates vertically. A dual high-moment/low-moment transmission allows for good resolution at both shallow and deep penetration depths. The magnetic field travels through the subsurface inducing Eddy currents in conductive materials which in turn induce a secondary magnetic field with a time decay proportional to the conductivity of the material, which is measured by a receiver coil mounted on the stern of the transmitter coil frame. This gives us information about the apparent conductivity as a function of time, which is then inverted to obtain vertical profiles of the distribution of conductivities in the subsurface. The inversions are performed using a 1D layered model with a smooth gradient and laterally constrained by using information of the nearest neighbors along the flight-line. All of the data was processed and inverted by the Antarctica Airborne Electromagnetics team (ANTAEM) at the University of Aarhus, Denmark. The final product is a geoelectric image that reflects the resistivities of the materials in the subsurface (e.g., Figure 3-2). More details on the functionality of the SkyTEM system can be found in Sørensen and Auken (2004) and Foley et al. (2016).

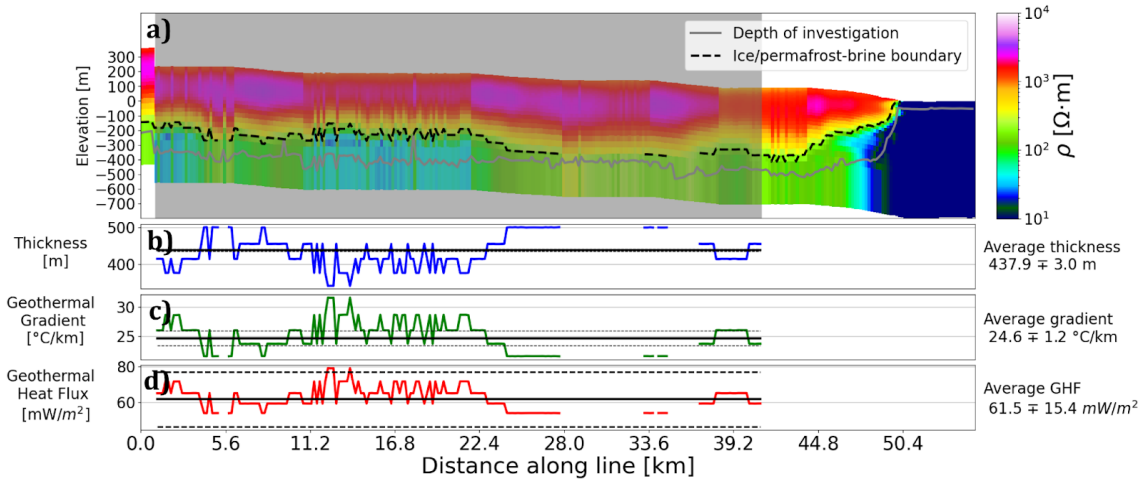

Figure 3-2. a) Resistivity profile at Bowers Glacier, ~50 km inland from the shore. The gray line represents the depth of investigation, and the black dotted line is the calculated resistivity boundary. b) Thickness profile. c) Calculated geothermal gradient along the profile. d) Calculated geothermal heat flux. Black lines in b), c) and d) represent the mean of each measurement.

3.2.2 Geothermal gradient and GHF

Geothermal heat flux (GHF) is the heat flow rate per unit area of Earth's surface. It can be calculated as the product of the geothermal gradient and thermal conductivity. This mathematical expression stems from Fourier's Law (equation 3-1):

$$GHF = -k\frac{dT}{dZ} \quad (3\text{-}1)$$

For our purposes dT is the difference between mean annual temperature at the surface and the temperature at the bottom of the permafrost/ice while dZ is the permafrost thickness, and k is the thermal conductivity of permafrost (Foley et al., 2020).

Our method focuses on making estimates of the different parts of this equation based on ATEM and climate data. We pay particular attention to the

error propagation of each parameter/variable to track the uncertainty of our final GHF estimates. A more detailed description of the process followed to estimate the different components of equation 3-1 is outlined below. As all approaches to estimating GHF, ours is necessarily associated with uncertainties (e.g., Burton-Johnson et al., 2020). However, its advantage is that it can provide regional-scale GHF estimates that are based on a geothermal gradient evaluated over the entire depth of the permafrost, here hundreds of meters (Foley et al., 2020).

3.2.2.1 Permafrost thickness

A steady-state permafrost layer thickness is directly dependent on GHF (Osterkamp and Burn, 2003). We use the results of the inversions from the ATEM survey to find the geoelectric boundary between ice or permafrost (resistive) and the liquid-phase brines underneath them (conductive) (e.g., Foley et al., 2016; Myers et al., 2021). For each of the profiles marked in Figure 3-1, we selected areas that were at least a permafrost thickness away from the coast and that did not show any obvious spurious artifacts. We manually reviewed each one of them to ensure that we had a long enough distance along a line with reliable data to perform our calculations and culled out the ones that did not. Furthermore, we developed an algorithm that automatically detects this boundary by finding the first vertical occurrence of a resistivity value between 30-200 [ohm m], since this has been the range of resistivities at which conductive brines have been detected before (Foley et al., 2016). We then

calculate the elevation difference between this boundary and the elevation of the surface to get the thickness of the resistive layer. To avoid the 3-dimensional thermal effects of the contact between permafrost and the warmer ocean on the shore (Lachenbruch, 1957; Foley et al, 2020), we select areas that are at least a few permafrost thicknesses away from the coastline (shaded region in Figure 3-2). Finally, we use the standard error of the mean (SDM) along the profile to quantify the uncertainty on the average permafrost thickness for each profile.

3.2.2.2 Temperature differences

Since we do not have information from Automatic Weather Stations (AWS) everywhere where the SkyTEM collected data, for the surface temperature we use the monthly 2m air temperature from the ERA5-Land reanalysis data set.

ERA5 dataset represents the fifth iteration of ECMWF (European Center for Medium-Range Weather Forecasts) global climate hindcasting derived by combination of climate data assimilation and climate simulations (Hersbach et al, 2020). With its global coverage, high temporal resolution, and relatively high spatial resolution of 31 km this dataset may prove particularly useful for research in polar regions such as Antarctica, where long-term climate observations are geographically sparse and often temporally discontinuous (Lazzara et al, 2012). A recent study found encouraging agreement between ERA5 output and AWS data from 13 stations located in the southern section of Antarctic Peninsula (Tetzner et al., 2019).

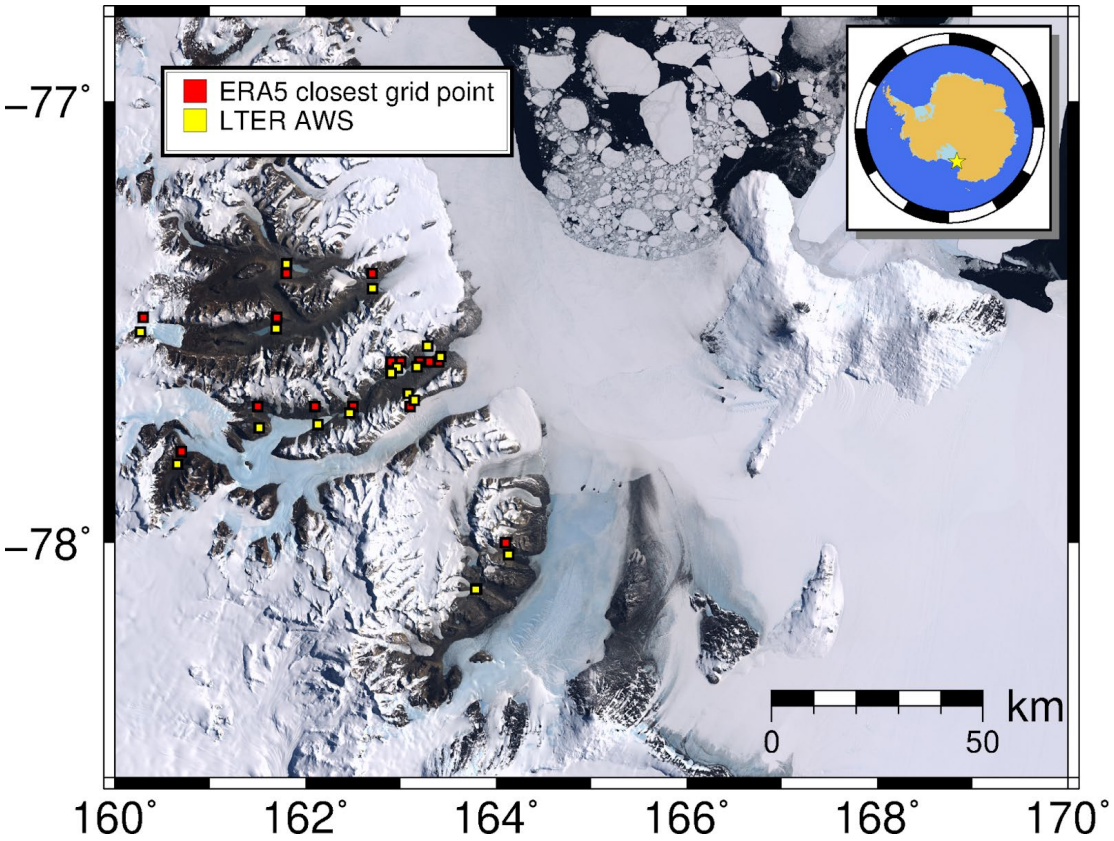

Figure 3-3. Map of the McMurdo Dry Valleys region showing the location of the automatic weather stations (AWS) managed by LTER and their corresponding closest ERA5 grid node.

To assess the reliability of the reanalysis data in the McMurdo Sound, we perform a comparison between monthly 2-meter air and ground temperatures reported in the ERA5 dataset and the daily surface temperature (2m temperature) recorded at 17 AWS (Figure 3-3) managed by the McMurdo Dry Valleys Long Term Ecological Research Project (LTER) since 1992, although some of the stations have been reporting data only since 1986 (Doran et al., 2002). We compare the AWS data to the monthly ECMWF ERA5 climate reanalysis surface temperature data. For each LTER AWS, where daily 2-meter air temperature data was available, we ran a 30 day moving average filter with

0% overlap to obtain monthly time series. The ERA5 grid node used in comparisons to each individual AWS was selected by minimizing the haversine distance between each AWS and all the nodes in the reanalysis grid. Finally, we interpolated both time series to a regular monthly sequence The time series for the ERA5 node data were truncated to match the periods where data was available at their corresponding AWS. We report the mean temperature for the span of each time series and the standard error of the mean for each sample.

Furthermore, we compare the two data sets by analyzing the correlograms and performing a linear regression. Figure 3-4b shows an example of this comparison. We report the squared correlation coefficients (R2) as a metric of the goodness of fit and the p-values from the F-statistic to assess the level of statistical significance.

Table C-1 summarizes the results of our comparison. Even though some of the largest differences in the mean between the AWS station and the closest ERA5 grid node are observed for stations at high altitudes (e.g., Beacon Valley and Mt. Fleming) there are other stations at relatively high altitudes that report a smaller bias (e.g., Friis Hills) and conversely, the Taylor Valley AWS station is not at a high altitude, but it does report a significant bias. The only station where the ERA5 average temperature was warmer than the corresponding AWS was located at Lake Vida, in Wright Valley.

Figure 3-4a illustrates the comparison of AWS and ERA5 monthly temperature time series for one of 17 locations used in this study (Lake Hoare)

over the time span of two decades. The cold bias is clearly visible and persistent throughout the time period covered by the AWS data. The monthly temperature mismatch is particularly large during the summer months, when observations indicate actual temperatures were up to +10°C higher than ERA5 temperatures (e.g., Figure 3-4b). Over the rest of the year the mismatch shrank to the range of 2-6°C. Figure 3-4b suggests that there is a strong seasonal influence in the relationship between the data sets. During the austral Winter and Summer seasons the temperatures are generally more clustered together, systematically being closer correlated during the Winter and diverging during the Summer. The Spring and Fall seasons show a hysteresis pattern that is repeated over all the comparisons, suggesting a seasonal dependence in the correlation. As the environment warms up during the Spring months the ERA5 temperatures are higher above the best fit line, and it starts getting colder during the Fall the temperature lies below the best fit line. These seasonal biases may ultimately be helpful in revealing what climate processes must be better represented in the ERA5 reanalysis to eliminate the strong observed temperature bias.

We found that the temperatures reported by the global climate reanalysis are, on average, 5.34 ∓ 0.76 °C colder than the temperatures recorded at the permanent weather stations.

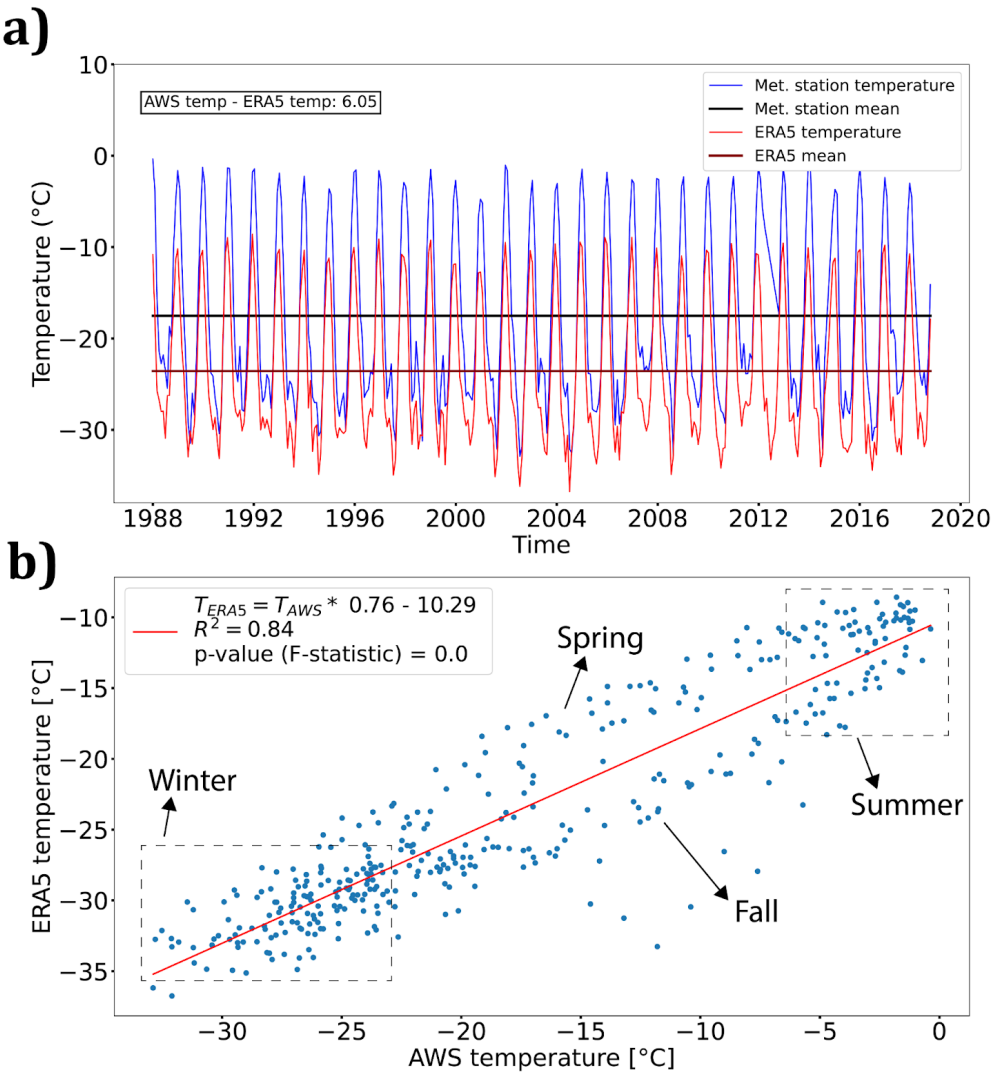

Figure 3-4. a) Comparison of the monthly averaged surface temperature time series recorded at station Lake Hoare (HOEM) (blue) and the values from the closest grid node of the ERA5 reanalysis (red). b) Correlogram showing the best fit line to the relationship between the AWS temperatures and the reanalysis temperatures. Note the seasonal variation in the relationship.

For each profile that was processed we calculated the latitude and longitude of the middle point and found the nearest node of the ERA5 model grid by minimizing the haversine formula. Whenever the closest grid node was on the ocean, we continued looking for the next closest point and so on until the closest overland node was identified. The surface temperature from each node extends from 1981 to 2020 and the values that we report as Ttop are calculated using the mean of the monthly values and corrected for the cold bias by adding 5.34 ∓ 0.76°C.

For the permafrost bottom, because our profiles are close to the ocean, we make the assumption that the conductive layer that we find underneath the permafrost is close in composition to seawater and we use the constant value of the freezing temperature of -2 +/- 0.1 °C as T_{bott}.

3.2.2.3 Thermal conductivity (k)

Since GHF is directly proportional to thermal conductivity, the choice of values for k are important to make the right measurement of the spatial distribution of GHF. We do not have laboratory-derived measurements for thermal conductivity across the coastal range of the MDV. However, previous work has shown that the permafrost that constitutes the bulk of the shallow layers in this area, the subxerous climatic zone, is ice-cemented permafrost that is constantly losing ice to the atmosphere by evaporation (Bockheim et al., 2007; Quinn et al., 2010). Furthermore, McKay et al. (1998) calculated a thermal conductivity value of 2.5 ∓ 0.5 W m-1 K-1 for ice-cemented permafrost by fitting

a thermal model to long-term temperature variations in the Asgard range. Thus, by assuming that the ice-cemented permafrost in the higher altitudes of the Asgard Range is similar to the permafrost located in the coast of the Dry Valleys, we can expect that the thermal conductivity value of $k = 2.5 \mp 0.5$ W m^{-1} K^{-1} is appropriate for this study. The only exception that we make is for the data points in the Brown Peninsula where we know that the lithology corresponds to phonolitic basalts, and we assigned a value of $k = 2 \mp 0.1$ W m^{-1} K^{-1} after Foley et al. (2020).

3.2.3 Error propagation

For each profile we assigned the average GHF value to the coordinates of the center. As described above, we start by using the SDM of the estimated permafrost thicknesses and from there we propagate the error of each of the parameters described above accordingly. In order to keep track of the uncertainties of each data point in our final interpretation, we performed a weighted interpolation where the size of the interpolated block around each point depends on the propagated uncertainty of the heat flux calculation. Furthermore, we include the values of the thermal gradients/GHF reported in other studies that are within our study region. Whenever one of these data did not have a reported uncertainty, we assigned an uncertainty equivalent to 10% of its value.

3.3 Observations/Results

Figure 3-2 shows an example of the results obtained from applying our workflow to a resistivity profile. For the other profiles please see Appendix C. A comparison between the automatically delineated bottom of the permafrost and a few manually chosen boundaries confirm that our method works well and it's reliable for the majority of the transects of our profiles. Moreover, by manually inspecting and selecting the useful part of the transects with the well estimated thicknesses we ensure that we are reducing the uncertainty of our results.

After disregarding profiles where a high data quality was not guaranteed, we successfully calculated the geothermal heat-flux values for 33 profiles. By adding the observations of the previously published results and using the highest value in the complete data set as a data point for Mount Erebus, our data totals 40 observations (Table C-2). This unprecedented data set provides a new way to analyze regional scale variations in geothermal heat-flux in polar regions.

Figure 3-5 shows the main results of our study. Because GHF values depend directly on the choice of thermal conductivity, it is convenient to visualize the variability of thermal gradients at the same time as the changes in heat-flux. The maximum and minimum calculated values for thermal gradients are 21.5 ∓ 0.9 °C/km and 52.6 ∓ 1.9 °C/km respectively, and the maximum and minimum values of GHF are 53.8 ∓ 13.1 mW/m^2 and 164 ∓ 16.4 mW/m^2 respectively. The maximum value for both the thermal gradient and GHF for the region were 79.7 ∓ 18 and 164 ∓ 18 from Risk and Hochstein (1974).

The GHF in the McMurdo Sound region shows an interesting pattern of local variability, confirming the results from Morin et al. (2010) while at the same time populating the region with more than 5 times the number of observations. The highest values for both GHF (>90 mW/m^2) and thermal gradient (>45 °C/km) are observed in the eastern portion of the region, where the recent Cenozoic active volcanoes are. The southern volcanic province of Mount Discovery (i.e., Brown Peninsula) shows more moderate values. For the western section of our area of study, the Dry Valleys coastal ranges, we find that the values of thermal gradient are the lowest of the region, especially for the data points that are in the Bowers and Wilson piedmont glaciers which are in close proximity to the coast. Because of the differences in thermal conductivities used across the region, by looking at the GHF spatial variation the more subtle thermal gradient differences in the Dry Valleys accentuate, showing that a higher heat-flux value is present inland.

Without taking into account differences in thermal conductivity, the region as a whole seems to have a differential thermal gradient that goes from high values in Ross Island to lower values in the Dry Valleys.

Figure 3-5. Map of the thermal gradient (a) and geothermal heat flux (b) variation in the McMurdo Sound region. The data points from this study are shown as open circles. Data points from other studies are shown as closed circles. Note that the highest values for both measurements are in the vicinity of the McMurdo Volcanic group (red areas).

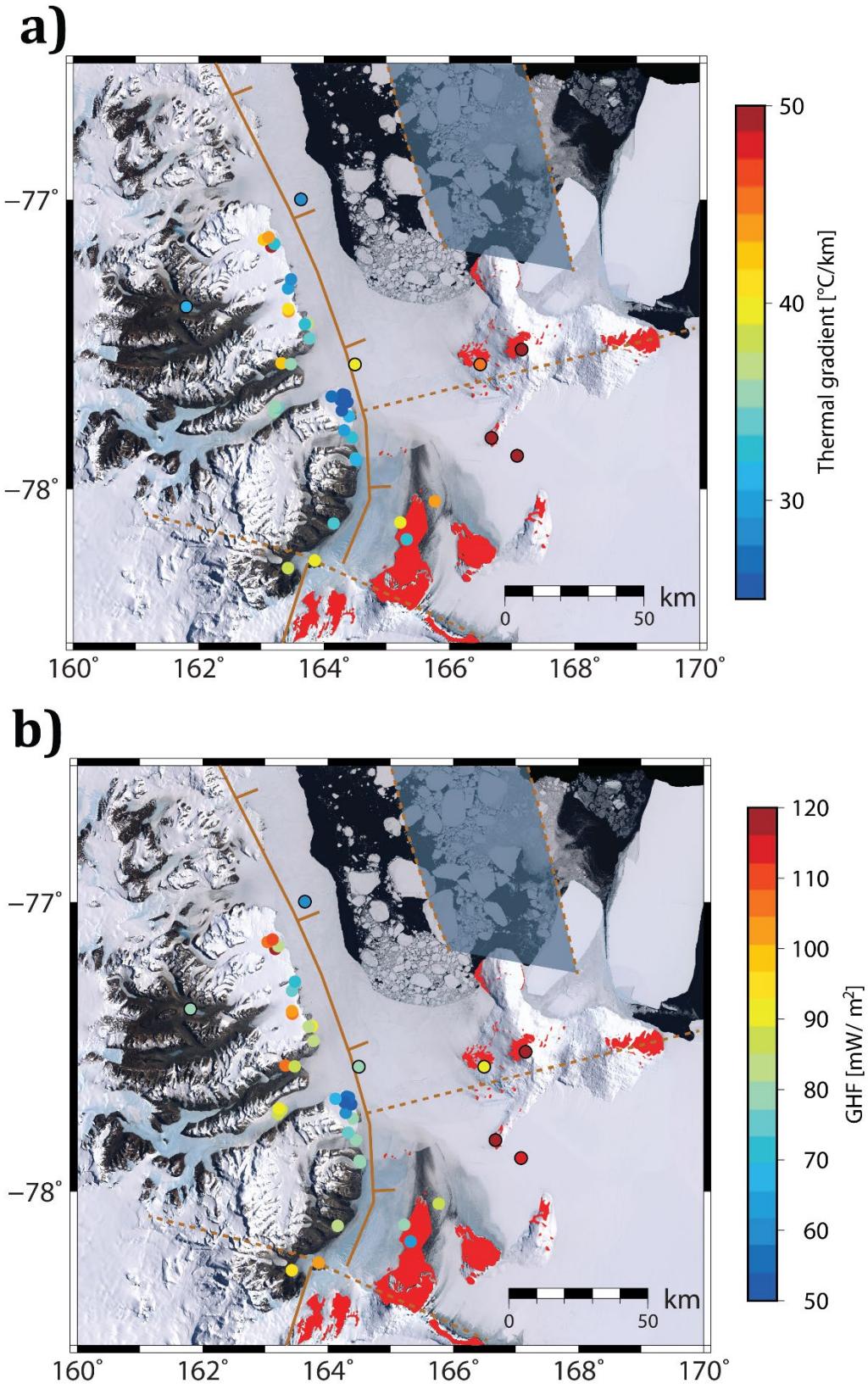
a)
−77°
−78°
160°
162°
164°
166°
168°
170°
km
0
50
50
40
30
Thermal gradient [°C/km]
b)
−77°
−78°
160°
162°
164°
166°
168°
170°
km
0
50
120
110
100
90
80
70
60
50
GHF [mW/ m²]

3.4 Discussion

Our results for the temperature comparison between the AWS stations and the ERA5 data differ significantly from the findings reported by Tetzner et al. (2019) for the Southern Antarctic Peninsula - Ellsworth Land region. For that region there is slight colder bias of the ERA5 surface temperatures close to the coast (-0.51°C $\mp$ 0.74) and a warm bias in the mountain range escarpment (+0.14°C $\mp$ 0.72). These small biases had implications for using the reanalysis data where there is no AWS coverage, which represents most of Antarctica. However, the magnitude of the overall cold bias that we find (averaged of all differences) is more than an order of magnitude larger (5.33 $\mp$ 0.76 °C) and seems to be systematic. Furthermore, we find no clear topographic dependence on the temperature differences for AWS and ERA5 data, even though the highest differences are indeed in two high altitude areas, Beacon Valley and Mount Fleming. The large summer undershoot of ERA5 output (e.g., Figure 3-2) may be a particularly significant problem given the fact that warm summer temperatures determine the annual melt rate of snow, glaciers, and permafrost in Antarctica. Modeling of snow or ice melting driven by ERA5 temperatures (e.g., Costi et al., 2018) with a strong cold bias, as observed in our study region, will result in a significant underestimate of melt. Although the ERA5 reanalysis is an outstanding source of global climate measurements, the discrepancy between our results and those obtained by Tetzner et al. (2019) suggests that

secondary observations should be used to test the reliability of the ERA5 dataset in different polar regions.

The spatial variations of geothermal heat-flux and thermal gradient in the McMurdo Sound indicate that the sources of heat coming from the ground do not only vary at continental scales, but rather that they can also vary by a factor of 3 at a local scale. Overall, the thermal structure of this region is congruent with the local geology and tectonics. The comparison of the thermal gradient and GHF maps suggests that the main control of variability in the system is not the differences in thermal conductivity.

The highest values of GHF are found in the vicinity of Ross Island, where the most active Cenozoic volcanism has taken place and where one of the most active volcanoes in the world (Mount Erebus) is located. The volcanism in the southern edge of the region is older than the still active Mount Erebus by ~10Ma (Kyle, 1990), so observing lower values for this area compared to the eastern portion of the region is sensible.

Also, even though we still have few data points in the middle of the grid where the ocean is, the values reported by White (1989) off Ferrar Glacier using the CIROS-1 Drillhole data matches the values in the center of the grid that we find for Brown Peninsula, strengthening the tectonic dependence of the spatial distribution of GHF, as these data points lie along the western edge of the extensional structure that constitutes the McMurdo Sound.

The lowest values of heat-flux and thermal gradient are observed in the western portion of the region in the Dry Valleys coastal ranges. The Dry Valleys are a transverse extension of the Transantarctic Mountain Range that were carved by retreating glaciers as active volcanism and uplift of the range occurred ~5Ma (Armstrong, 1978). The most notable volcanic features that have been mapped in this area are located in the Wright and Taylor valleys and they are mostly composed of chains of scoria cones which are a product of short-lived eruptive periods (Wilch et al., 1993). Furthermore, the stratigraphy of the southwest portion of the Dry Valleys which include the Koettlitz Glacier and Walcott Glacier also include basaltic flows that have been dated at ~15Ma and ~5Ma using K-Ar dating (Armstrong, 1978). Interestingly, the GHF and thermal gradient local variations within the western portion of the McMurdo Sound show higher values in the Wright and Taylar Valleys compared to the piedmont Glaciers that bound them at the coasts (e.g., Bowers Glacier and Marble Point). Moreover, the data points that are closest to Walcot Glacier also show a higher value compared to Bowers Glacier. These local variations in GHF, even at the ~10km scale, could be explained by the localization of cooling lava bodies that are still diffusing heat into the overlying permafrost, causing it to thaw at the bottom and showing a thinner resistive layer in our data. Begeman et al. (2017) proposed that the high GHF variations observed in the West Antarctic Ice Sheet can be explained by magmatic intrusions and/or the advection of heat by fluids migrating through the crust. The effect of heat transportation via the advection

of fluids in convective systems near oceanic rifts has also been shown by Fisher et al., (1990). Our regional scale spatial distribution of geothermal heat-flux shows that, even though the Dry Valleys show signs of localized variation that can be explained by cooling volcanic bodies, the largest anomalies are present where the current volcanism is happening, which is in agreement with the mechanism proposed by Begeman et al., (2017). The major volcanoes along Ross Island lie along a system of fractures separated at 120° (Kyle, 1990), similar to the distribution of other theolytic basalt volcanoes such as the Mauna Loa, Kilauea and Mauna Kea system. Rocks in the vicinity of magmatic bodies are prone to fracturing due to the relief of thermoelastic effects (Warren and Latham, 1970), and seismicity in volcanic regions are known to produce greater amounts of microfractures due to this effect (McNutt, 2005; Garza-Giron, 2014). In Ross Island, the major system of fissures combined with the potentially dense distribution of micro-fractures at depth provide an excellent system of pathways for hot fluids to migrate to the surface, creating a convecting system. Thus, it is expected to observe higher values of geothermal heat flux in this area compared to its surroundings, where the potential effect of volcanism in the surrounding rocks is purely conductive.

Finally, the east-west variability in thermal gradients observed in our results could be a sign of the effect of the extensional regime of the Terror Rift, although a caveat to this hypothesis is that the data in the middle section of the region is still very sparse due to the lack of observations in the ocean bottom.

3.5 Conclusion

By using a regional scale airborne transient electromagnetic survey in the McMurdo Sound, we have increased the number of geothermal heat-flux determinations in the region by a factor of 5. Our results show that the only area clearly exhibiting high GHF (>100 mW/m^2) is Ross Island, a site of geologically young and ongoing volcanic activity. This is consistent with inference of Begeman et al. (2017) that the vertical advection of heat into the crust with volcanic intrusions may be responsible for high magnitude GHF 'hot spots' in Antarctica. At the same time, geologically recent tectonic extension appears to have some impact on GHF. The GHF measurements from the western portion of the Terror Rift, the coastal ranges of the McMurdo Dry Valleys, show the lowest GHF values (e.g., 60-70 mW/m^2), but they also depict local variations within the study area possibly related to cooling magma bodies from >∼5Ma, while the rift-shoulder uplift to the west is typified by somewhat higher values (80-90 mW/m^2). The regional compilation of GHF constraints combined with our new data further reinforces the conjecture that areas of high GHF in Antarctica will generally be associated with Cenozoic volcanic and magmatic activity while tectonic history has comparatively smaller impact on GHF distribution (Begeman et al., 2017). These lessons from the best studied part of Antarctica may aid further improvements of a continent-wide GHF dataset.

Chapter 4 – Repeating large earthquakes in the Oaxaca subduction zone, Mexico, and their implication for the asperity model

4.1 Introduction

Subduction zones are convergent boundaries where a colder and denser plate underthrusts a younger and more buoyant plate. Large earthquakes along these boundaries are characterized by different degrees of heterogeneity in their rupture process and slip distributions (e.g., Lay and Kanamori, 1981; Lay et al., 1982; Astiz et al, 1988). An important question is the persistence of slip distributions over repeated earthquakes (e.g., Thatcher, 1989; Schwartz, 1999). The issue of slip patch persistence is difficult to address given the typically long-time interval between repeated rupture of a given region in large earthquakes and the rapidly decreasing information about prior ruptures the further back in time that they occur. Recent advances have shown that the degree of heterogeneity in the rupture process of an earthquake can be inferred by measuring the ratio of the radiated energy of the event calculated from the observed moment rate function (MRF) and the calculated minimum radiated energy for a comparable seismic moment and duration source (i.e., the smoothest solution) (Ye et al., 2018). This powerful tool is useful to elucidate differences in fault slip processes along subduction margins and to understand the evolution of each individual earthquake. However, the requirement of good quality seismic records to estimate a reliable MRF and the space-time distribution of slip makes it difficult to assess the level of heterogeneity of

historic ruptures and thus inhibits the ability to compare the rupture process of large, repeated earthquakes that can shed light into the earthquake cycle of the region.

Another topic of long-term interest has been the nucleation process of large earthquakes and its association with the aforementioned fault heterogeneity. The most popular models to explain the initiation of large earthquakes involve observations of foreshocks (Dodge et al., 1996). Whether foreshocks are the result of aseismic slip on the fault plane or of an increase in stress that triggers a cascading process that ends up loading the mainshock by static-stress transfer has been a topic of debate (e.g., Mignan, 2014). The great 2011 M_w9.1 Tohoku-Oki earthquake in Japan and the M_w8.1 2014 Iquique earthquake in Chile provided extraordinary data sets from which it has been determined that both earthquakes were preceded by foreshocks that appear to have been triggered by aseismic slip on the megathrust interface (Kato et al., 2012; Obara and Kato, 2016; Ruiz et al., 2014; Socquet et al., 2017).

Large earthquakes in southeast Mexico have historically been characterized as ruptures with relatively simple localized slip distributions that give rise to simple teleseismic waveforms (Chael and Stewart, 1982). However, at least one study has suggested that, for two of these large earthquakes, such a simplistic model is a spurious artifact from using long-period WWSSN teleseismic records to assess them (Tajima, 1984). Recently, two large megathrust earthquakes have ruptured in Oaxaca with excellent observations to

constrain their source processes. The data also provide insights into the triggering of large earthquakes. These recent earthquakes provide an excellent opportunity to study their relation with previous ruptures which occurred in the 1960s and were well-recorded by WWSSN stations, providing insights into the slip history of the area and the implications for the degree of heterogeneity on the plate boundary.

In this Chapter, we present the results of research on the nucleation process of the 2018 Mw7.2 Pinotepa Nacional earthquake (hereinafter referred to as Pinotepa earthquake), and comparison with the prior 1968 M_s7.1 earthquake, which, as it will be shown, ruptured the same large-slip patch, or asperity with relatively high confidence.

4.1.1 The asperity model and world-wide observations

The rupture complexity of large, shallow earthquakes in subduction zones around the Pacific Ocean can be characterized to first order using the asperity model (Lay and Kanamori, 1981). The premise of this model is that megathrust boundaries are segmented along strike with possibly persistent localized regions that accumulate and abruptly release elastic strain over time. Differences in frictional properties and interface coupling, among other factors, may control the rate of the cyclic rupturing of each of these segments (idem; Ruff, 1992; Kanamori and Brodsky, 2004).

There are regions in the world where large earthquakes seem to have involved multiple localized high-slip zones in a single rupture giving rise to very

complicated teleseismic P waveforms, suggesting a heterogeneous distribution of asperities (e.g., Kurile Islands, Lay and Kanamori, 1981; Schwartz and Ruff, 1987). In some cases, historical records suggest that, at times, the segmentation along strike of major subduction zones is overcome by synchronized accumulation of elastic stress in all the asperities, releasing the cumulative stored energy in great magnitude earthquakes that exceed the moment release of separate failures of individual asperities (e.g., Kanamori and McNally, 1982; Suárez and Albini, 2009). In the Nankai Trough, Ando (1975) suggested that the different rupture areas of the 1946 Nankaido, 1944 Tonankai and 1854 doublet in Ansei, could have ruptured all together in the 1707 Hoei earthquake. Sykes et al. (1981) collected historical records that hint at the possibility that the 1788 and 1847 earthquakes in the Alaska-Aleutian Arc broke the same segment of the 1938 Shumagin Islands earthquake and could have breached the Shumagin gap. The megathrust in this area has recently ruptured again with a M_w7.8 earthquake in June 2020 west of the 1938 rupture (Liu et al., 2020; Ye et al., 2021) and a M_w8.2 earthquake in July 2021 occurred in the same area as the 1938 earthquake. In South America, the 1906 earthquake ruptured the separate source regions of the 1942, 1958 Ecuador and 1979 Colombia earthquakes (Kanamori and McNally, 1982; Beck and Ruff, 1984; Mendoza and Dewey, 1984) and the 1942 region ruptured in 2016 in a M_w7.8 earthquake (Ye et al., 2016). Also, the 1746 Peru earthquake extends the length of the 1940, 1966 and 1974 earthquakes (Beck and Ruff, 1989; Beck and Nishenko, 1990). Lay et al. (2005)

showed that the Great Sumatra-Andaman M_w9.1 earthquake of 2004 ruptured the same area as other previous large earthquakes that triggered in 1861, 1881 and 1941.

These examples provide evidence that the rupture process of the megathrust interface may be generally compatible with the asperity model, but the variation in global subduction zones, as well as the timing of the earthquakes, suggests that there could be dynamic interactions among distinct frictional patches and with the rest of the subducting system. It is difficult to analyze complex ruptures to establish persistence of large-slip patch asperities over multiple ruptures (e.g., Nagai et al., 2001; Tilmann et al., 2016; Ye et al., 2016; Kobayashi et al., 2020; Ye et al., 2021). Park and Mori (2007) analyzed events along the New Britain trench and argued that asperities from five great earthquakes are not persistent in this area. What is required is repeated rupture of large events with relatively simple source processes that are well recorded and precisely located; this motivates consideration of the Mexico subduction zone which has relatively short recurrence times for major earthquakes. Recent ruptures will have had proximate prior ruptures with numerous well-calibrated seismic recordings that allow direct comparisons of seismic recordings.

4.1.2 The Oaxaca subduction zone, Mexico

In southeastern Mexico (Figure 4-1), the subduction of the Cocos plate under the North American plate along the Middle-America Trench is characterized by the occurrence of M7 class thrust earthquakes that have

average repeat times between 32 and 56 years (Singh et al., 1981). For example, the 2012 M_w7.5 Ometepec (state of Oaxaca) earthquake (U.N.A de Mexico, 2013) ruptured the same area as the 1982 doublet (Ms6.9 and Ms7.0) (Astiz and Kanamori, 1984) and at least three other prior earthquakes (1890 Ms7.3, 1937, Ms7.5 and 1950 Ms7.3) (idem). On February 16, 2018, a M_w7.2 earthquake occurred under Pinotepa Nacional, Oaxaca, breaking an area that had previously ruptured in 1968 (M_w 7.3) (Chael and Stewart, 1982) and probably in 1854 and 1890 (Suarez et al., 2020). This event was part of a sequence of large earthquakes and slow-slip events (SSE) that provided a wealth of geodetic and seismic data and that allows for a thorough investigation of the nucleation process. The interaction between large earthquakes and SSEs and its relationship with the initiation of the Pinotepa earthquake will be described in more detail below.

Finally, the Pinotepa earthquake was followed by the June 23, 2020, M_w7.4 Huatulco earthquake (also referred to as La Crucecita earthquake), which had a slip area that overlaps with the area covered by the aftershocks of the 1965 (M_w 7.5) earthquake (Chael and Stewart, 1982) and which had probably ruptured previously in 1801 and 1870 (Suarez et al., 2020). In 1978 an earthquake, with M_s7.8 struck the region of Puerto Escondido, Oaxaca, which is situated in between the 1965 and 1968 earthquakes, and this region, which previously ruptured in an apparently similar event in 1928 (Hjorleifsdottir et al., 2013) is considered to be a good prospect for future rupture within a decade or

two. Furthermore, Suarez and Albini (2009) suggest that the M8.6 1787 earthquake that took place in this region ruptured the entire shallow portion of the megathrust, putting the southeastern Mexican subduction zone in the category of the asperity model where intermittently a great event can occur by a cascade of discrete asperities when conditions are favorable.

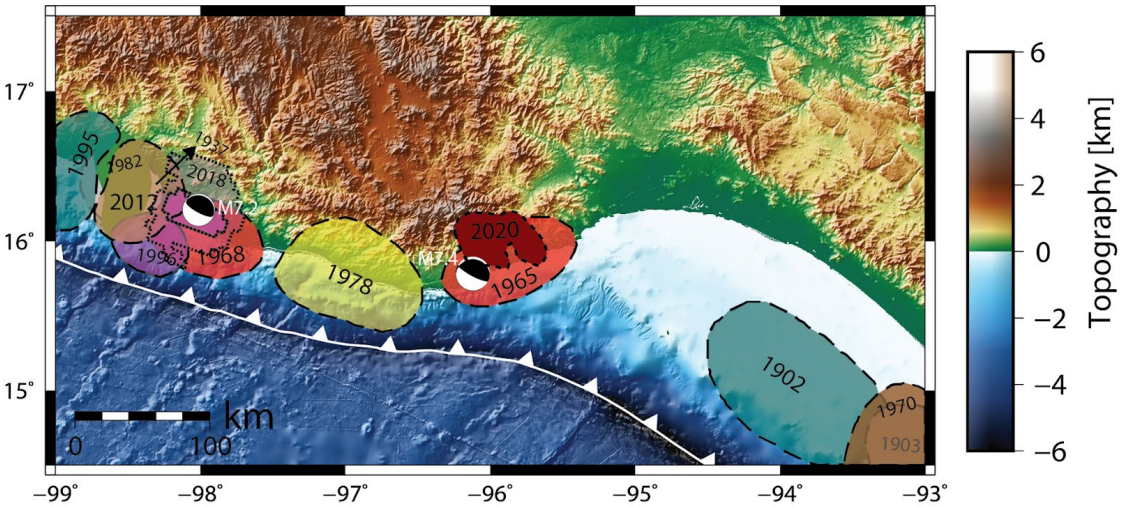

Figure 4-1. Map of the study region showing the rupture zones of historic earthquakes (inferred from the distribution of aftershocks) and the M_w7.2 Pinotepa and M_w7.4 Huatulco earthquakes epicenters and focal mechanisms from the Global CMT database. The dark red patch shows the rupture area of the Huatulco earthquake from the geodetic inversions of Villafuerte et al. (2021). The magenta patches show the rupture area and high slip regions of the 2018 Pinotepa event obtained by Mendoza and Martinez-Lopez (2021) from teleseismic body waves inversions.

4.2 The interaction between silent and devastating earthquakes in Mexico

The most recent earthquakes in the Oaxaca region, 2018 and 2020, are part of an intricate story of causal events and have been studied in depth by Cruz-Atienza et al. (2021) (Figure 4-2) and Villafuerte et al. (2021).

The full sequence of events can be summarized as follows:

1. On September 8, 2017, the great M_w8.2 intraplate Tehuantepec earthquake entirely ruptured the Cocos slab in the megathrust region with strong rupture directivity toward Oaxaca (Ye et al., 2017; Melgar et al., 2018; Suarez, 2021).
2. Before the Tehuantepec earthquake, spontaneously triggered Slow Slip Events (SSEs) were developing in the states of Guerrero (G-SSE1) and Oaxaca (O-SSE1) (blue patches in Figure 4-2A).
3. The dynamic stresses induced by the passing of the strong long-period seismic waves of the Tehuantepec earthquake triggered acceleration of the SSE in Oaxaca, making it expand bilaterally as well as updip (green and yellow patches in Figure 4-2A).
4. On September 19, 11 days after the Tehuantepec earthquake and on the 32nd anniversary of the devastating M_w8.0 1985 Michoacan earthquake, a M_w7.1 normal fault intraslab earthquake ruptured at the boundary between the states of Morelos and Puebla (~120 km from downtown Mexico City), causing the collapse of 44 buildings and severely damaging another 600 (Singh et al., 2018). It is proposed that this earthquake could have been triggered by the effects of the SSE in Guerrero (Cruz-Atienza et al., 2021).
5. On February 16, 2018, a M_w7.2 earthquake on the megathrust boundary beneath Pinotepa Nacional, Oaxaca, triggered in the same area as the August 2, 1968, Ms7.1, M_w7.3 earthquake,

enhancing the damage in nearby villages and in Mexico City. The postseismic slip of this event spanned the coseismic slip area as well as the downdip portion of the plate interface and it seemed to have propagated to the west towards Guerrero (Figure 4-2B).

6. About one year later, in March 2019, a second SSE started downdip from the Pinotepa earthquake (O-SSE2) and it lasted until October 2019. This SSE extended to the west to the border between the states of Guerrero and Oaxaca and to the east to the downdip portion of the Ms7.8 1978 Puerto Escondido earthquake zone (Figure 4-1).
7. In January 2020, a third SSE (O-SSE3) started in the downdip (30-40 km) portion of the Pinotepa earthquake and extended, again, to the east towards the 1978 earthquake zone.
8. Finally, on June 23, 2020, a M_w7.4 interplate thrust event triggered in the vicinity of the town of Huatulco, Oaxaca, coinciding spatially with a August 23, 1965 Ms7.6, M_w7.5 earthquake.

This intriguing series of tectonic events yielded a wealth of data that have allowed thorough study of the interaction between slow and fast rupturing events in the Mexican subduction zone. Cruz-Atienza et al. (2021) showed that the acceleration of the SSE downdip from the Pinotepa earthquake contributed to its nucleation process.

The main evidence that the M_w8.2 Tehuantepec earthquake caused rippling effects that contributed to the triggering of the 2018 M_w7.2 Pinotepa earthquake stems from geodetic inversions and can be explained with three key points:

- The dynamic stress induced by the passing of the seismic waves of the M_w8.2 Tehuantepec earthquake caused the spontaneous SSE that was already occurring in Oaxaca to accelerate and expand bilaterally (Figure 4-2A).
- Due to this development of the SSE to the north, the Coulomb Failure Stress changes (CFS) in the hypocentral region of the Pinotepa earthquake increased by ~200 kPa reaching values up to ~400 kPa before the triggering of the earthquake (Figure 4-7a, b).
- The plate interface coupling (PIC) (interplate slip rate/plate convergence rate) in the hypocentral region increased during this period (see reduction of interplate slip rate in Figure 4-7b), but the area to the north of the hypocenter saw 1-2 cm of slip due to the penetration of the SSE (Figure 4-7a).

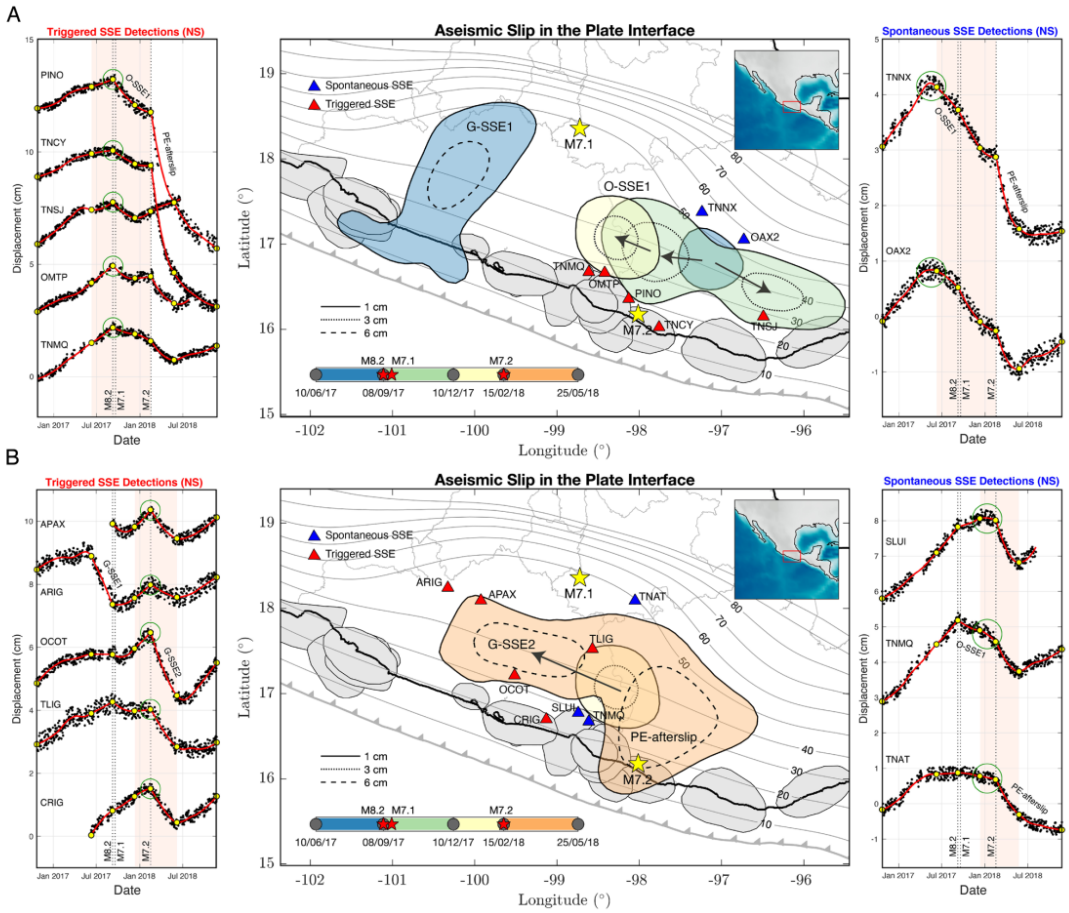

Figure 4-2. Evolution of the plate interface aseismic slip (SSEs and afterslip) during the earthquake sequence (separated in two parts) and representative GPS time series (north-south components). The first part (panel A) before the M7.2 Pinotepa earthquake and the second part (panel B) after the earthquake. Pink shaded rectangles encompass the GPS windows (yellow dots) that were slip-inverted in the central maps (color areas) for each panel. Blue triangles show GPS stations where we observe spontaneously initiated or preexistent SSEs at the time of earthquakes (right panels, green circles), while red triangles show the stations where we observe triggered SSEs also at those times (left panels, green circles). Notice the abrupt reversal of the deformation pattern in the left panels (from north to south, green circles) right at the time of the M_w8.2 Tehuantepec and M_w7.2 Pinotepa earthquakes. Gray contours show iso-depths (in kilometers) of the 3D plate interface and gray shaded regions the rupture areas of historical earthquakes. (From Cruz-Atienza et al., 2021)

GPS data inversions allow us to have the capability to observe the phenomena that contribute to the nucleation process at a macro-scale. However, it is impossible to resolve smaller scale processes, such as the migrating foreshocks observed before the 2011 M_w9.1 Tohoku-Oki earthquake (Kato et al., 2012), that might also shed light into the nucleation process using such methods. To address this problem, we applied a single station matched filter technique to enhance the seismic catalog of the Mexican National Seismological Service (SSN) using the closest station (~20 km) to the epicenter of the earthquake.

4.2.1 Method

The template-matching process for finding earthquakes in the hypocentral region of the Pinotepa earthquake considers only the waveforms on the three channels of station PNIG, the closest site to the earthquake epicenter (21 km, Figure 4-3).

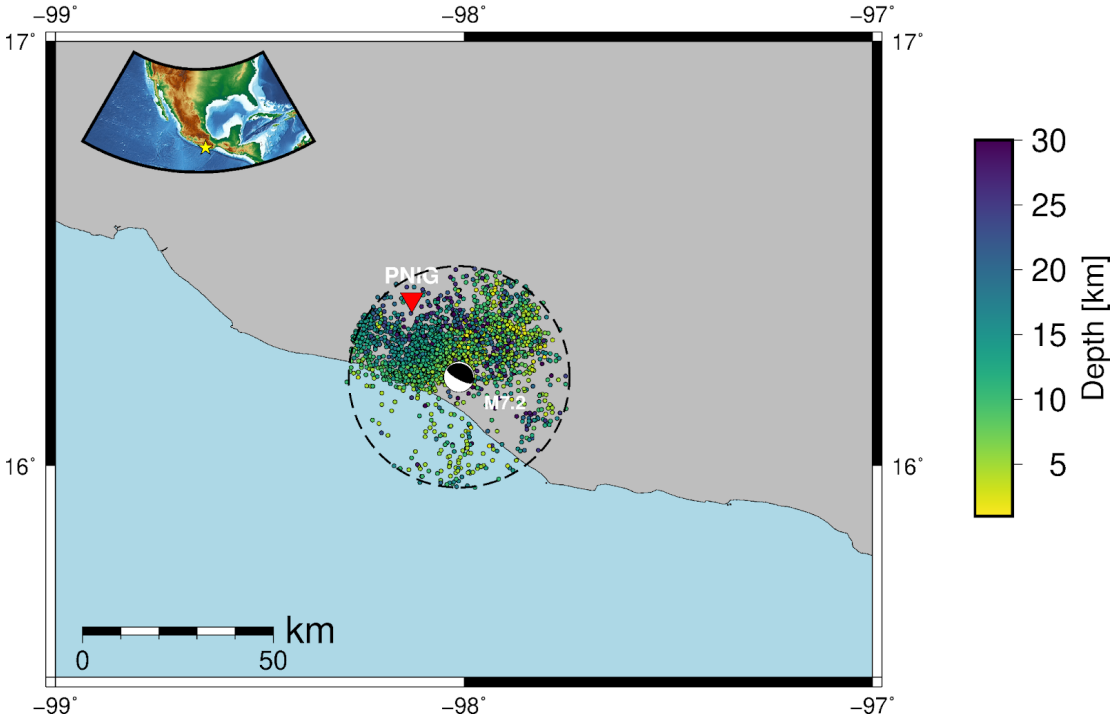

Figure 4-3. Epicentral location of the SSN earthquakes that were used as templates. Only earthquakes within 30 km of the M7.2 Pinotepa event hypocenter were taken into account for the study. The location of station PNIG is shown as an inverted red triangle.

For generating the templates, we selected 4105 events from the SSN catalog in the period between March 1, 2017, and March 31, 2018. The waveforms were cut 0.2 s before the P-phase arrival and 0.5 s after the S-phase arrival and filtered using a zero-phase Butterworth bandpass filter with corner frequencies at 3 Hz and 12 Hz. The template matching was performed using the Python package EQcorrscan (Chamberlain et al., 2018) and the detection threshold was set to 0.9 of the average cross-correlation values in the three channels, which guarantees not only that the detections come from the same place as the templates, but also that our local catalog does not include any false-positives.

Single-station detections have proved to be a powerful tool to find earthquakes that are small and located close to certain stations, but that are too attenuated to be detected at farther stations given high cross-correlation thresholds (Huang and Beroza, 2015). Furthermore, a visual inspection of hundreds of waveforms helped us verify that the timing and the relative amplitudes of the P and S waves in the three components are very similar to the parent templates, guaranteeing that the detected signals are, indeed, earthquakes that share a common hypocentral location as the template events (Figure 4-4). We kept only the best-correlated detections in windows of 10s.

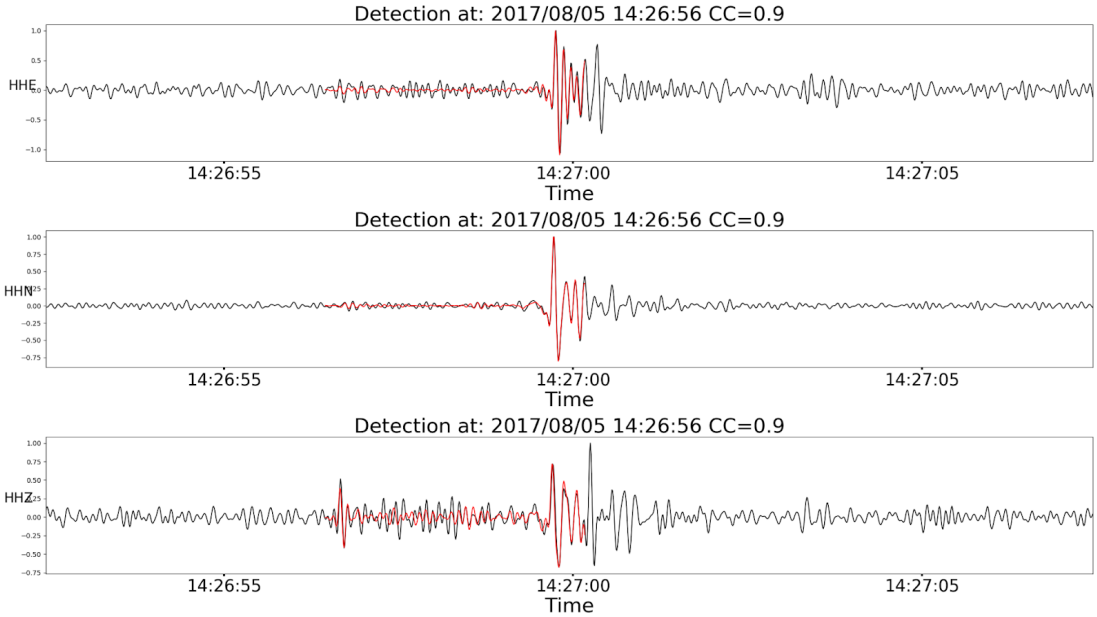

Figure 4-4. Example of a detection with an average cross-correlation value of 0.9. The agreement between the normalized amplitude and polarity between the template and the detection in the three channels gives us confidence that the detection followed the same path from the source to the station as the template.

In order to assign a magnitude to all detections that is in agreement with the magnitude of the templates (i.e., the cataloged magnitude), we determined an attenuation relationship specific to PNIG using a variation of the magnitude calibration method presented in Chapter 2 of this dissertation. Instead of inverting for the magnitudes and the attenuation relationship parameters at once, we used the cataloged magnitudes from the SSN for events with signal-to-noise ratio (SNR) greater or equal to 5 and inverted only for the geometric spreading, attenuation, and station correction parameters from horizontal displacement records (mm), effectively using waveform data to calibrate a relationship to the cataloged earthquakes. To obtain the displacements, we integrated velocity records in the bandwidth of 3–12 Hz. The resulting attenuation relationship and the comparison of the magnitudes calculated with this method and the cataloged magnitudes for the templates are shown in Figure 4-5.

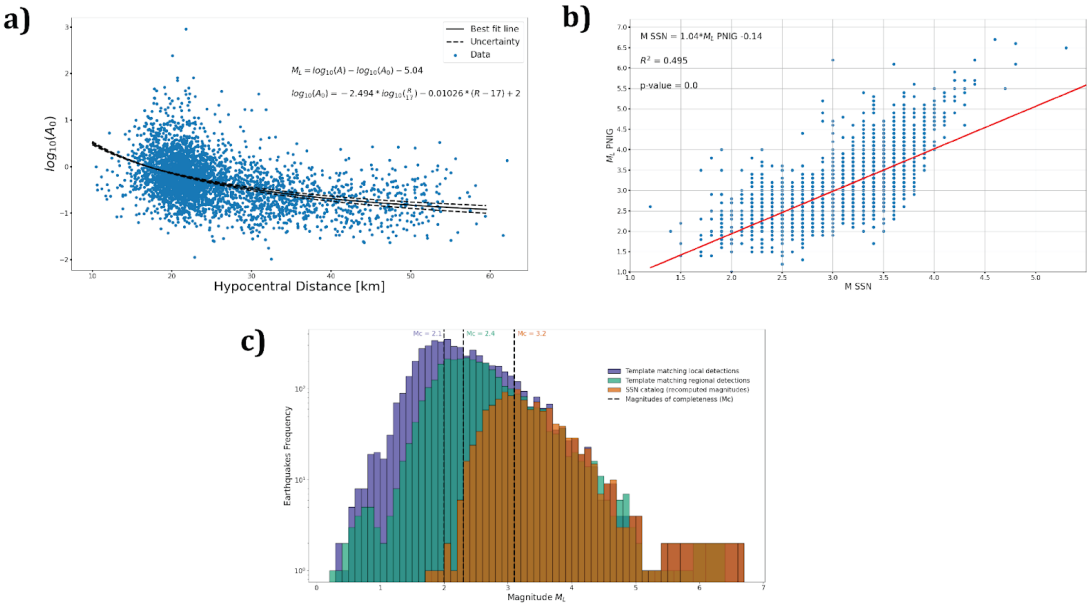

Figure 4-5. Magnitude estimation for the template-matching detected earthquakes and final catalog comparison. (a) Attenuation relationship calculated on the horizontal components (geometric mean) of PNIG and magnitude scale. (b) Correlation between recomputed magnitudes using the PNIG station and the magnitudes reported by the SSN. (c) Earthquake frequency distributions for the template matched catalog using the closest station PNIG (blue), three stations of the regional network (green) and the catalog provided by the SSN (brown).

4.2.2 Template matching results

We detected 5064 events which represent a 350% detection increase, as compared with the 1125 earthquakes reported by the SSN in the same period within a 30 km hypocentral radius of the M7.4 hypocenter. Additionally, we integrated these events with the results of a secondary template matching approach which utilizes three regional stations and 394 events that were previously identified as repeaters. The details of this method are provided in Cruz-Atienza et al. (2021). The repeater earthquakes template matching method yielded 3156 events. We integrated all the detections, from both methods, into a

single catalog avoiding duplicate events and our final earthquake catalog comprises 5977 events, which represents a 431% increase from the original catalog. Figure 4-5 shows the frequency-magnitude histograms for both our template matching detections and the SSN catalog, where the cutoff completeness magnitudes correspond to 2.1, 2.4, and 3.2, for local detections (method described here), repeater earthquakes detections, and the SSE catalog, respectively.

Since the secondary method one uses nine seismic channels (i.e., the three components of three stations) at a regional scale, its detections very likely correspond to events with hypocentral locations close to those of the templates that lie, all of them, within 30 km from the Pinotepa earthquake hypocenter. Thus, we used these detections for relatively large events to check how well method two, which only considers local records at PNIG (i.e., the three-component detections), detected earthquakes within such hypocentral vicinity. Figure 4-6 shows a Venn diagram for all catalogs where we see that 72% of regional detections were also found using only local records.

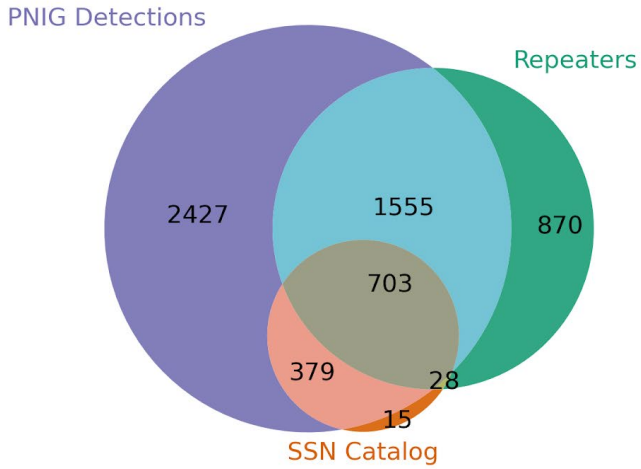

Figure 4-6. Venn diagram showing the relationship of the number of events of each catalog. The intersections are calculated by finding common events in time (events within 10 seconds of each other).

Figure 4-7c shows the seismicity rate (number of earthquakes every 21 days) of the template matched catalog for all events above the M2.1 completeness level and within 30 km of the hypocenter of the Pinotepa earthquake. Starting after the M_w8.2 Tehuantepec earthquake and the evolution of the SSE north of the hypocenter of the Pinotepa earthquake, the seismicity had a steady increase in rate reaching numbers of ~1.5 times the background level before the earthquake happened. This seismicity density map (inset in Figure 4-7a) and the earthquake rate of the enhanced catalog correlate in space and time, respectively, with the increase in CFS in the hypocentral region. The combined observations (high IPC, high CFS and high seismicity rate) suggest that there were small stress concentrations around the nucleation patch that were being triggered prior to the earthquake by increases in CFS due to the long-range

loading of the SSE to the north, and not by aseismic slip as it is commonly suggested (Kato et al, 2012; Kato et al, 2016; Kato and Ben-Zion, 2021).

Figure 4-7. Coulomb Failure Stress (CFS), Plate Interface Coupling (PIC), and seismicity rate evolution before the Pinotepa earthquakes in the vicinity of its hypocenter. (a) 15-month cumulative CFS on the plate interface and spatial evolution of the O-SSE1 (1 cm slip solid contours and 3 cm slip dashed contours). The density of the template matching earthquake detections is shown in the inset (i.e., of the precursor seismicity). Gray contours show iso-depths (in kilometers) of the 3D plate interface and the green triangles show the broadband seismic station PNIG. (b) Temporal evolution of the CFS change and the interplate slip rate averaged within a 20 km radius from the Pinotepa earthquake hypocenter (dotted circle, panel a) along with the associated standard deviations (vertical bars). (c) Seismicity rate evolution for template matched events ($M > 2.1$) within a distance $R = 30$ km from the Pinotepa earthquake hypocenter. (Taken from Cruz-Atienza et al., 2021)

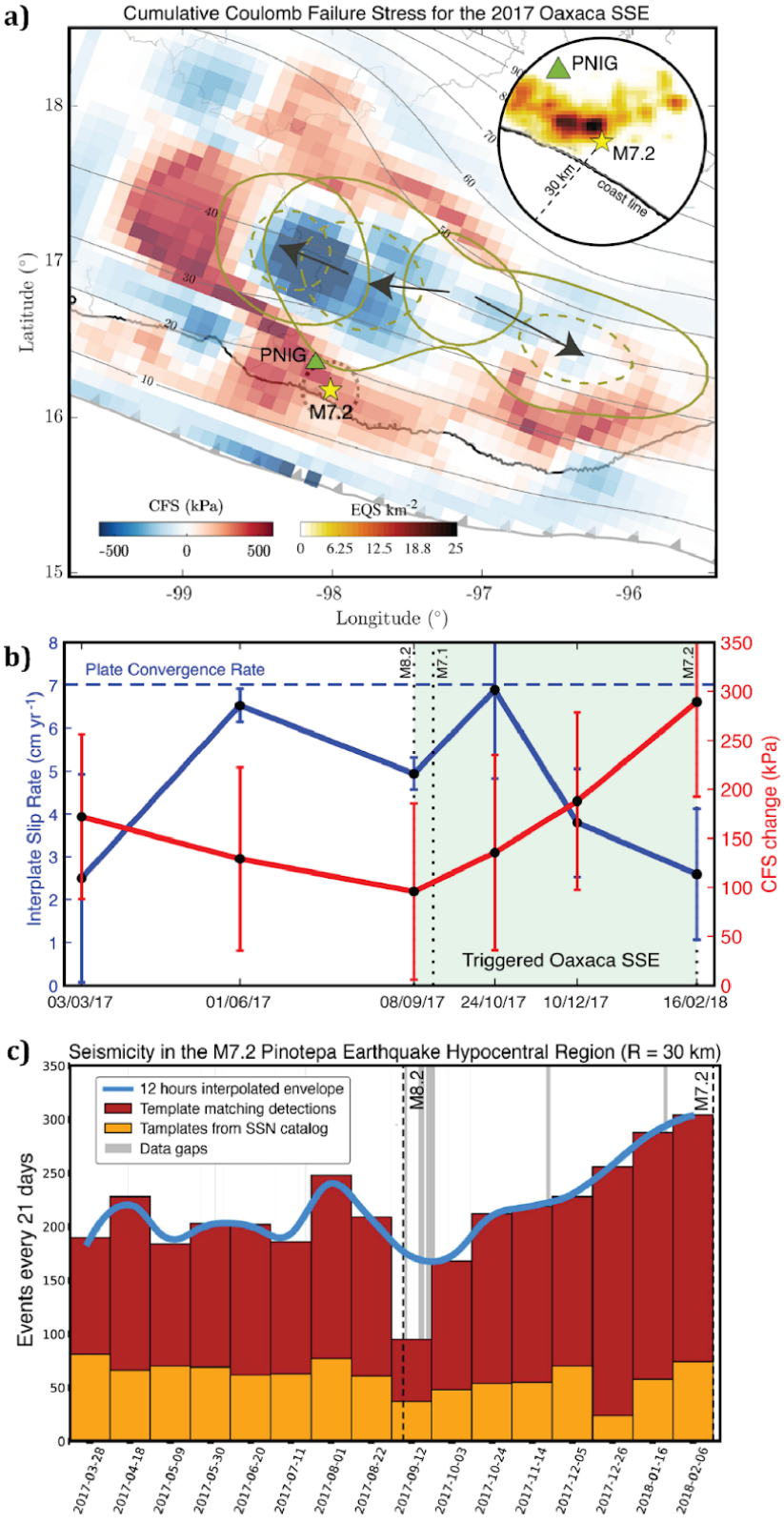
a)
Cumulative Coulomb Failure Stress for the 2017 Oaxaca SSE
PNIG
M7.2
30 km
coast line
Latitude (°)
Longitude (°)
CFS (kPa)
-500
0
500
EQS km-2
0
6.25
12.5
18.8
25
b)
Plate Convergence Rate
M8.2
M7.1
M7.2
Interplate Slip Rate (cm yr-1)
CFS change (kPa)
Triggered Oaxaca SSE
03/03/17
01/06/17
08/09/17
24/10/17
10/12/17
16/02/18
c)
Seismicity in the M7.2 Pinotepa Earthquake Hypocentral Region (R = 30 km)
12 hours interpolated envelope
Template matching detections
Templates from SSN catalog
Data gaps
Events every 21 days
M8.2
M7.2
2017-03-28
2017-04-18
2017-05-09
2017-05-30
2017-06-20
2017-07-11
2017-08-01
2017-08-22
2017-09-12
2017-10-03
2017-10-24
2017-11-14
2017-12-05
2017-12-26
2018-01-16
2018-02-06

4.3 Comparison of the 1968 M_s7.1 and 2018 M_w7.2 earthquakes

By the time the 1965 and 1968 earthquakes occurred in Mexico, the World-Wide Standardized Seismograph Network (WWSSN) was already operating with over 100 stations around the world. The WWSSN was deployed in the decade of the 60's as a response to the preparation for the nuclear test ban treaty in 1963 and the first station was installed in the U.S. Coast and Geodetic Survey Albuquerque Seismological Laboratory in October 1961 (Oliver and Murphy, 1971). The two main types of seismometers that were used for the WWSSN network were the Benioff-type variable-reluctance short-period seismometers (electromechanical instruments which operate with a transducer attached to the frame of the instrument on one end and a pendulum on the other (Benioff, 1955) and the long-period Press-Ewing type seismometers (Press et al., 1958), which basically uses the same principle of a stable vertical pendulum using a zero-length spring (i.e. a spring that does not move if an external force is not applied to it) designed by LaCoste (1934) and used in the LaCoste-Romberg gravimeters. The first long-period seismometers operated with a period of 30s and then they were reduced to 15s in the mid-1960s to improve stability (Peterson and Hutt, 2014).

A basic WWSSN station consisted of three-component seismometers connected to a galvanometer with a mirror in it. As the mirror of the galvanometer moved, the light from a lamp mounted on a photographic recorder

drum in a darkroom reflected from it, focusing on the photographic paper and leaving the record behind as the drum turned (Petterson and Hutt, 2014). This light beam was deflected periodically to purposely leave time ticks on the paper that represented one minute. Each minute in time spanned either 15 mm or 30 mm of distance in the paper depending on the rotation rate of the drum.

The availability of teleseismic records of the 1965 and 1968 earthquakes present an excellent opportunity to compare with the records of the 2020 and 2018 earthquakes, respectively, and provide new insights into their repeating nature. However, since the WWSSN records for the 1968 are more numerous, more clearly visible, and more viable for digitization than for the 1965 earthquake, and since the study of the 2018 Pinotepa earthquake sequence is included in this work, we focus our analysis on the comparison between the 1968 and 2018 Pinotepa earthquakes. A previous study showed preliminary comparisons between the waveforms of repeated earthquakes in the Mexican subduction zone recorded by a Wiechert instrument in Uppsala Sweden (Hjörleifsdóttir et al., 2016). They found that for the Oaxaca region, particularly for the Ometepec area, seismic waveforms of repeated historical earthquakes were almost identical, whereas waveforms of repeated historical earthquakes in other parts of the Mexican subduction zone were not very similar. They interpreted the similarity between waveforms as indicative of persistent asperities, but with only one station in a stable part of the radiation pattern it is difficult to ensure that the slip is truly similar (different large events that are not

co-located along the arc produce very similar waveforms at WWWSSN station ESK, as shown by Chael and Stweart (1982). (Figure 4-10b).

4.3.1 Method

We used scanned copies of the 1968 vertical component P waves from the 70 mm (filmchip) or 35mm (reel) film for all WWSSN stations available from the repository of the Japan Earthquake Research Institute at the University of Tokyo. We digitized the waveforms (Figure 4-8) using the time tick marks of each record to do the appropriate scaling of time and amplitudes. We only digitized records that had at least ~150 seconds of a clearly visible P wave trace. For each of these records, we searched for a co-located modern station with available broad-band waveforms from the 2018 Pintotepa earthquake. Whenever we could not find a co-located station, we searched for the nearest modern station within a 1000 km radius (~⅔ of a wavelength). Searching for all available data, we had a total of 13 potential pairs of stations. Three of the modern station records were too noisy or inadequate for comparison, leaving us with 10 pairs of stations.

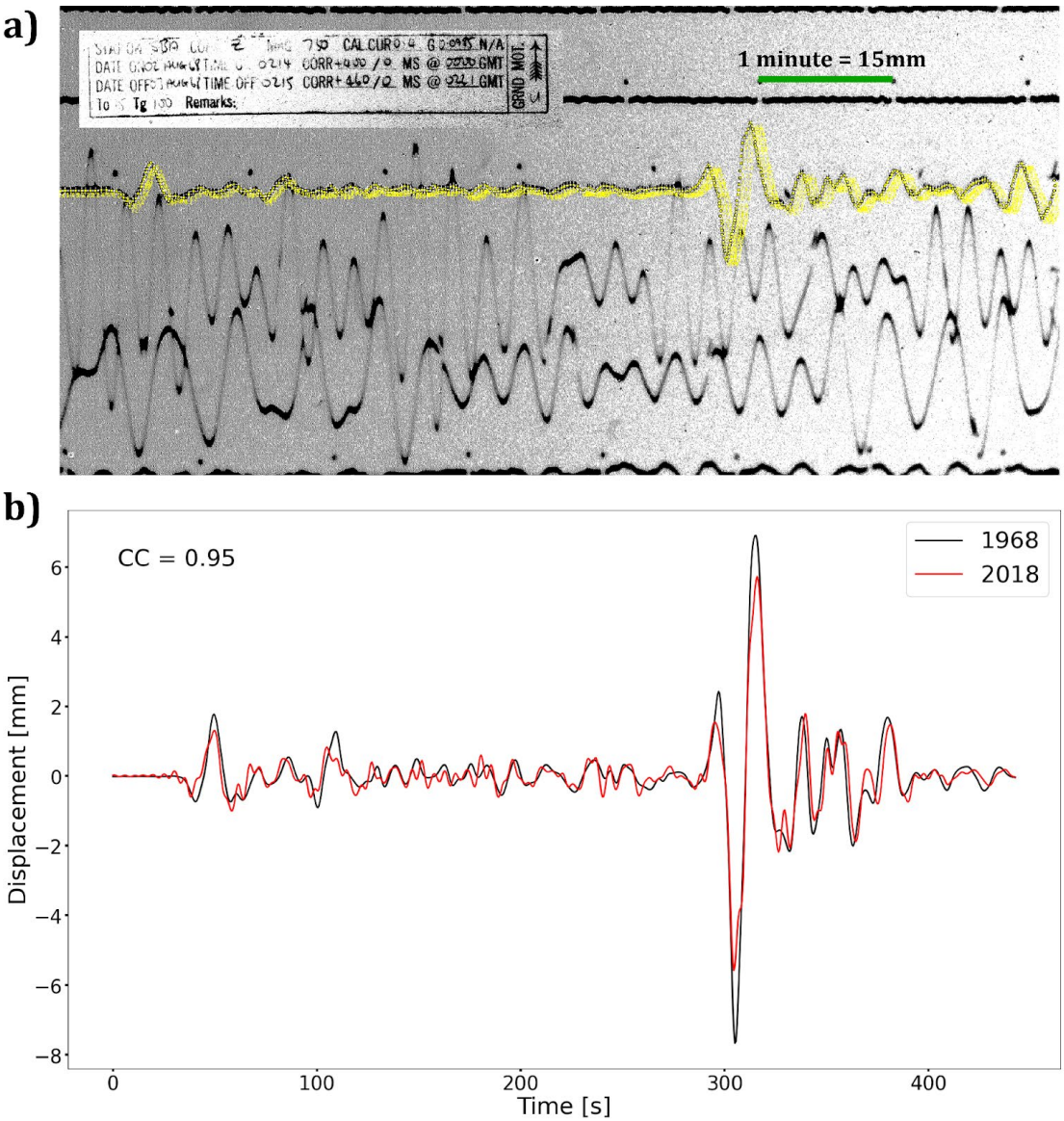

Figure 4-8. (a) Example of the digitization process for the 1968 earthquake recorded at the WWSSN Scott Base, Antarctica station (SBA) and (b) its comparison with the vertical component for the 2018 Pinotepa event (red) recorded at the same location, after conversion to WWSSN instrument response. The inset in (a) shows the record information and the green line shows an example of the scaling factors used.

The processing of the modern waveforms was as follows: we demeaned and detrended our signals and applied a 10% Hanning taper to each end. We removed the instrument response by applying a pre-filter with corner

frequencies at 100, 20, 2 and 1 seconds to stabilize the deconvolution. Then we convolved the signals with the instrument response of the WWSSN long-period stations (Peterson and Hutt, 2014) and applied a magnification correction according to the matching WWSSN record. For example, the magnification for the record at the SBA station is 750 (see Figure 4-8a inset). Finally, we removed the mean and linear trend for both records, old and new, and filtered the waveforms using a low-pass Butterworth filter with a cut-off frequency at 10 seconds to remove digitization errors from the older records. After we processed all the data, we performed a time-domain normalized cross-correlation between the waveforms of the 2018 and 1968 earthquakes and obtained the maximum cross-correlation values.

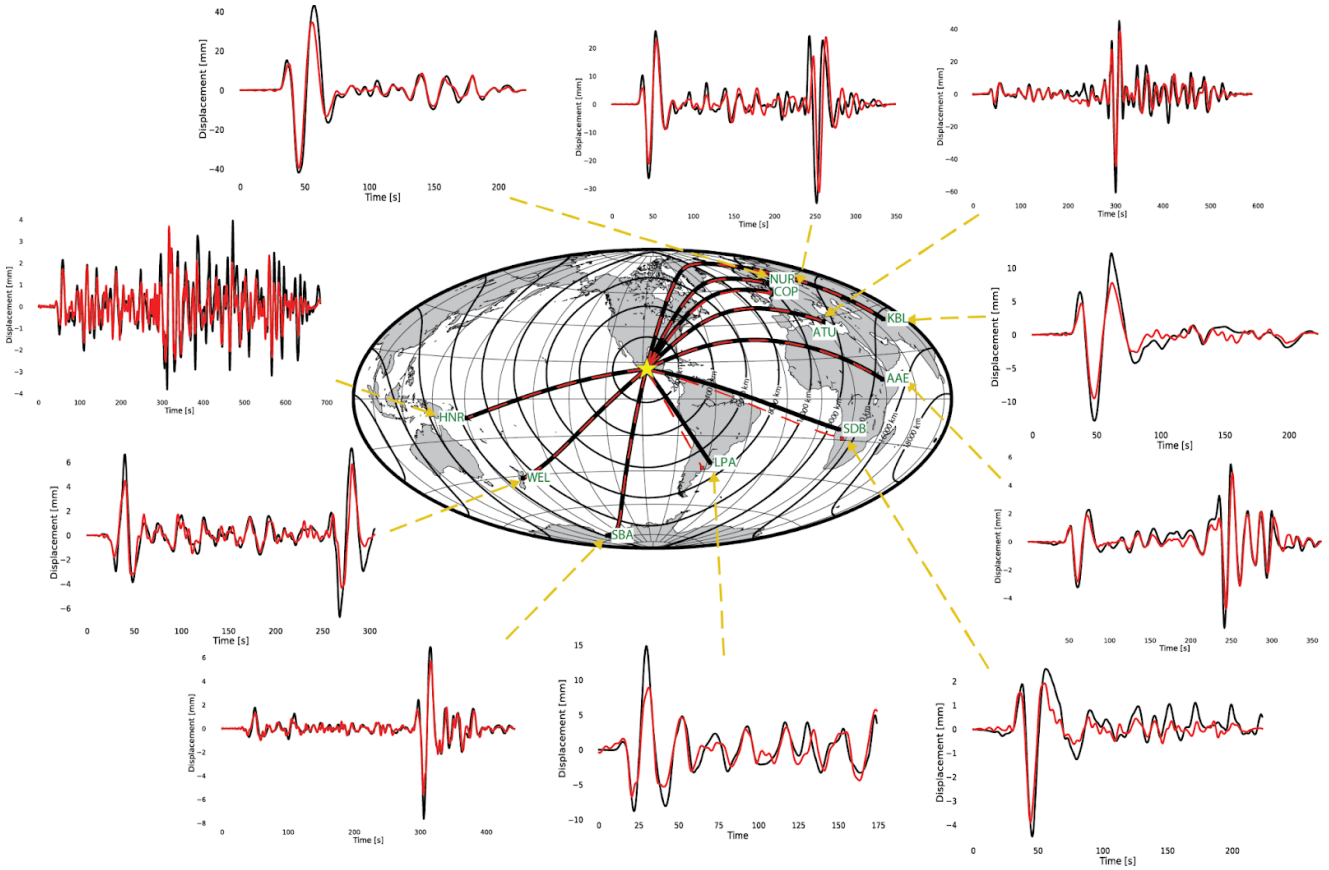

Figure 4-9. Results of the comparison between the 10 1968 WWSSN records and their corresponding modern record. The black solid lines in the map show the great circle distance between Pinotepa Nacional and the WWSSN stations. Red dashed lines in the map show the great circle distance between Pinotepa Nacional and the modern stations. Black and red waveforms correspond to the 1968 and 2018 records, respectively. The amplitude of the waveforms are in units of displacement (mm).

4.3.2 Comparison results

Figure 4-8 shows an example of the digitization process and comparison between the waveforms of the two earthquakes recorded at a co-located station in Scott Base, Antarctica. The rest of the stations and their azimuthal distribution are shown in Figure 4-9 and in more detail in Appendix D. Overall, the comparison between the records from the 1968 and 2018 earthquakes in Oaxaca shows an outstanding agreement between the signals for the two events. The azimuthal coverage of stations is relatively good except for the NW quadrant where we do not have any stations (Figure 4-9). The maximum normalized cross-correlation value for any pair was 0.99 for the co-located stations in Kabul, Afghanistan, using ~200 seconds of the waveforms. The minimum cross-correlation value is 0.77 for the 1968 WWSSN record at COP (Copenhagen, Denmark) compared to the 2018 earthquake record at RGN (Ruegen, Germany) located 137 km away. Some of the short-length (~200s) comparisons that were made for stations at long distances (>500km) showed a good visual agreement with each other and had high cross correlation values (e.g., LPA, SDB). Figure 4-9 illustrates the azimuthal distribution of the stations and the waveform comparison between the two events. A table with the summary of the results is provided in Appendix D.

4.4 Discussion

The results presented here add important evidence that support the common understanding that the subduction zone in southeast Mexico is

characterized by well-defined frictional asperities that tend to fail in similar ruptures over multiple cycles.

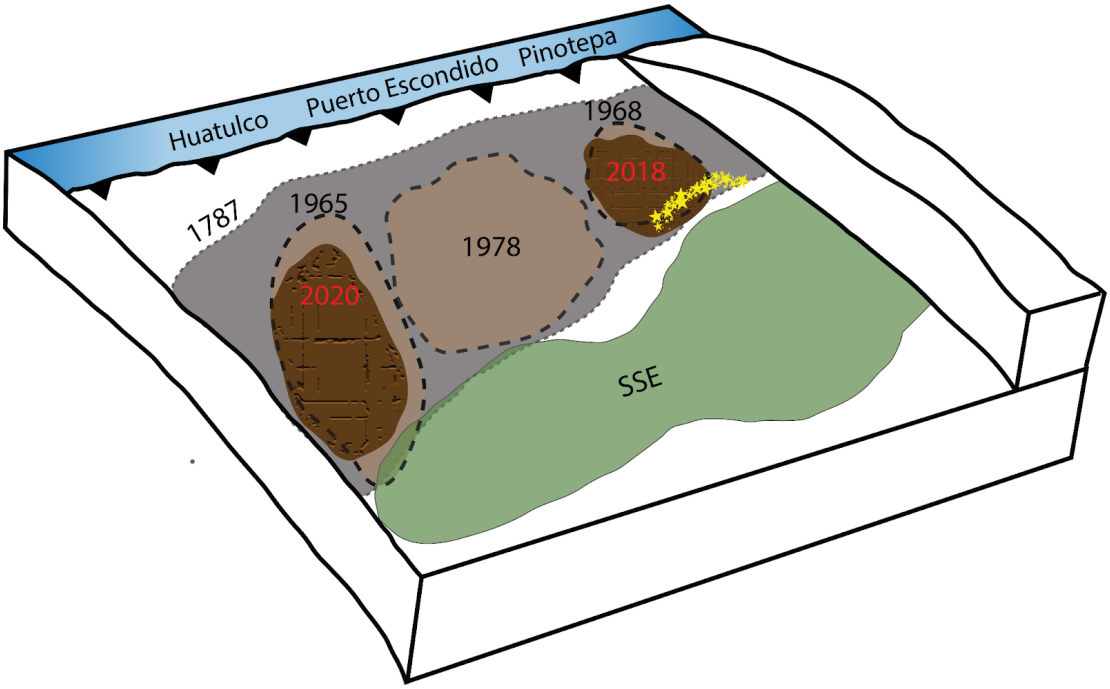

Figure 4-10. Conceptual model of the slip history in the subduction zone of Oaxaca, Mexico. The dark brown textured patches represent the 2018 M_w7.2 Pinotepa earthquake and the 2020 M_w7.4 Huatulco earthquake. The light brown solid patches with black dashed contours represent the 1965, 1968 and 1978 earthquakes. The gray solid patch with dashed contours represents the 1787 M_w8.6 earthquake proposed by Suarez and Albini (2009). The green solid patch represents the area of maximum extent of the O-SSE1 slow slip event. The stars next to the 2018 rupture patch represent the foreshocks that had an increasing rate before the large earthquake.

The fact that the increase in seismicity rate in the hypocentral region of the 2018 Pinotepa earthquake correlates in space and time with an increase in CFS and with an increase in interplate coupling suggest that the preparatory stage of this earthquake does not involve aseismic slip in the vicinity of the nucleation patch prior to the event. Instead, we suggest that the slow slip event that accelerated and propagated bilaterally and updip, due to the dynamic stress

changes induced by the passing of the M_w8.2 Tehuantepec earthquake waves, loaded the megathrust on a large scale. The long-range forcing of the SSE in the hypocentral region caused an increase in coupling of the already critically loaded frictional asperity, as well as an increase in CFS which triggered a cascade of events that developed until the frictional strength of the main slip patch was exceeded, rupturing in a M_w7.2 earthquake (Figure 4-10).

The teleseismic body wave waveform comparison between the 1968 Ms7.1 and the 2018 M_w7.2 presented in this work is the most comprehensive data set for comparing historical earthquakes that occurred in a given place as it consists of at least 10 long (>200s) records at stations with a good azimuthal distribution from the source. This comparison shows remarkable similarity between the two earthquakes in the passband of >10 s. The displacement amplitudes for the 1968 earthquake are systematically slightly larger than the 2018 earthquake, suggesting that the former could have been a larger magnitude event. However, the reliability of this observation is hard to assess given that not all the stations are perfectly co-located and differences in amplitude could be due to local effects.

The only way we could expect to see such similarity between signals at different azimuths is if indeed both events ruptured essentially the same area with a similar distribution of stress and the same frictional properties, and if they happened at the same depth and traveled the same path to the stations. Chael and Stewart (1982) showed the focal mechanisms of the 1965, 1968 and

1978 Oaxaca earthquakes, as well as a comparison between their body waves as recorded in the WWSSN station in Eskdalemuir, Scotland (Figure 4-11). They noticed that the waveforms of these events were very similar and could all be modelled by a very simple trapezoidal source time function with durations of ~16 seconds. They suggest that these earthquakes broke different smooth frictional asperities and that the differences in calculated moment for each could be explained by differences in the amount of slip that each earthquake had rather than the fault area. The focal mechanism for the 1968 earthquake is almost identical to the focal mechanism published by the Global CMT for the 2018 Pinotepa earthquake.

The sources for the 2018 Pinotepa earthquake and the 2020 Huatulco earthquake have been modeled by different organizations and authors. Most of these models agree on a simple, smooth MRF that suggests a homogeneous distribution of stress in the fault plane. Examples of this are shown in (Figure 4-12). Here, we show the moment rate function of the 2018 Pinotepa earthquake obtained from the SCARDEC Source Time Functions Database (Valle and Douet, 2016) (Figure 4-12a) and the solutions of the 2018 and 2020 earthquakes reported by the USGS (Figure 4-12b,c). We could not find the 2020 earthquake solution in the SCARDEC database at the time this dissertation was written. For comparison, Figure 4-12d shows the source time function of the 2019 M_w7.1 Ridgecrest earthquake in California, which had a particularly complicated MRF. Note the simplicity of the source time functions of the Oaxaca events compared

to the Ridgecrest event, which is of a comparable moment magnitude. The good visual and quantified correlation between the 1968 and 2018 earthquakes agrees with the notion of Chael and Stewart of simple fault models for the Oaxaca earthquakes. One must evaluate shorter period information to evaluate the suggestion by Tajima (1984) that in detail the 1968 earthquake involved a somewhat complex rupture process.

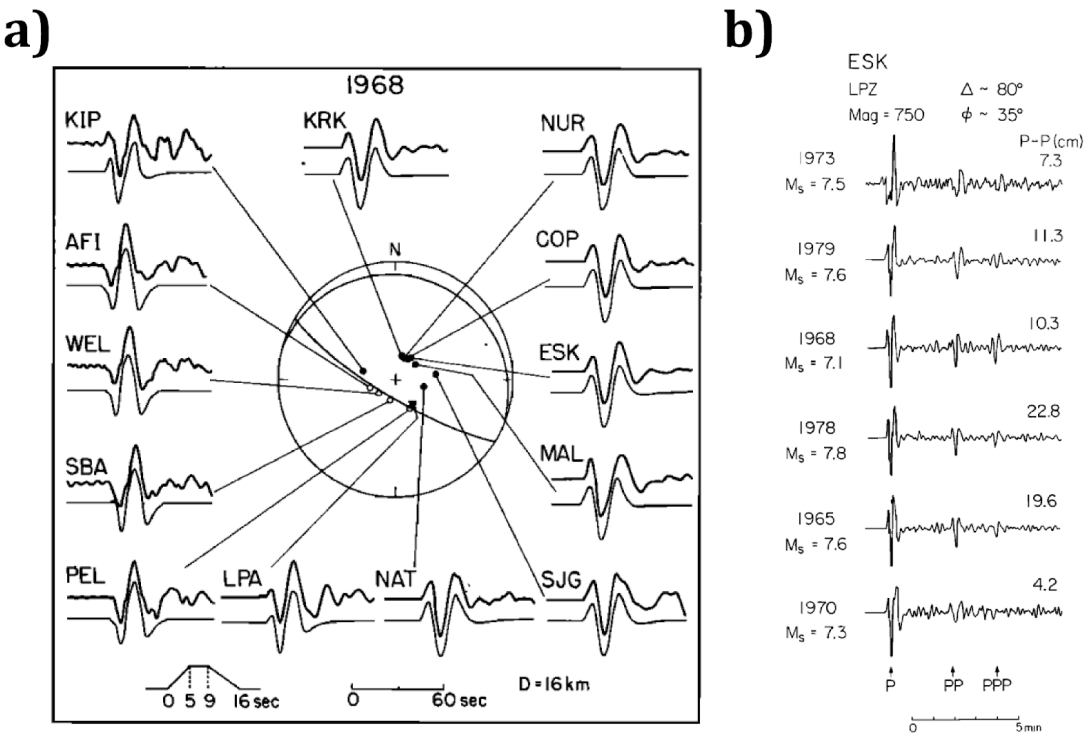

Figure 4-11. (a) WWSSN observed (heavy, upper lines) and synthetic (below) P waves for the 1968 Oaxaca event. The focal mechanism in the center was determined from P wave first motions and surface wave data. The synthetic waveforms were generated using the source mechanism, the time function and the depth shown. (b) Vertical long-period WWSSN seismograms of P, PP and PPP waves recorded at Eskdalemuir, Scotland (ESK). The 1965, 1968, 1978 and 1979 earthquakes show a higher level of simplicity compared to the 1970 Chiapas and 1973 Colima earthquakes. (From Chael and Stewart, 1982).

Another interesting observation from these solutions is that the MRF of the 2018 Pinotepa and 2020 Huatulco earthquakes from the USGS solutions is

that they both have a very similar duration, which translates into a similar rupture area, assuming a constant rupture velocity for both events. On the USGS website the maximum slip for the Pinotepa earthquake was 0.8 meters, whereas the maximum slip for the Huatulco earthquake was 7.5 meters. This difference in slip explains the difference in total moment release for earthquakes and may be related to the observations by Chael and Stewart that the 1965 records are larger than those for the 1968 earthquakes. This provides some evidence that the 1968 and 2018 earthquakes and the 1965 and 2020 earthquakes ruptured the same frictional asperity, respectively (Figure 4-10).

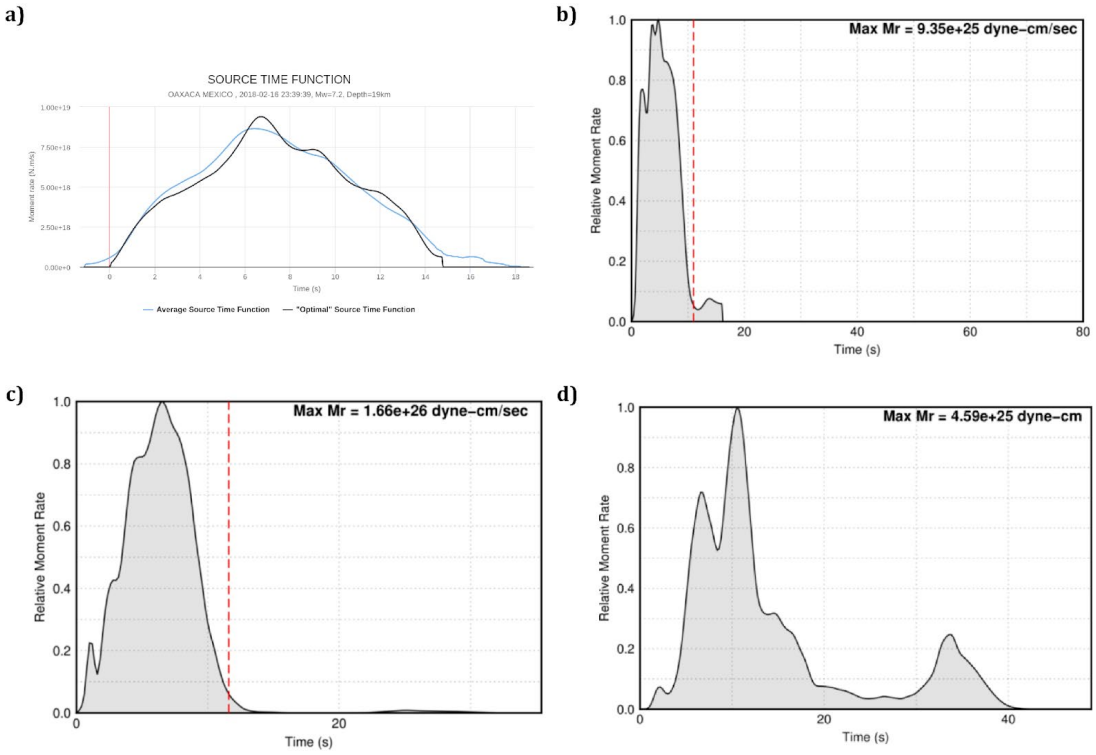

Figure 4-12. Moment rate functions (MRF). (a) MRF from the SCARDEC database for the 2018 Pinotepa earthquake. (b) MRF from the USGS for the 2018 Pinotepa earthquake. (c) MRF from the USGS for the 2020 Huatulco earthquake. (d) MRF from the USGS for the 2019 Ridgecrest earthquake. Notice how the moment rate function for the Ridgecrest earthquakes shows more complexity than those of the Oaxaca earthquakes.

One last piece of evidence for the existence of individual, well defined frictional asperities in Oaxaca stems from the results of Villafuerte et al. (2021). They observed that neither the O-SSE3 nor the postseismic slip of the 2020 Huatulco earthquake penetrated the zone of the aftershock area of the 1978 Puerto Escondido earthquake (Figure 4-13). Furthermore, the same work and Cruz-Atienza et al. (2021) show that this region remained fully coupled during the whole 2017-2020 sequence of events. We interpret their results as indicating a strongly coupled area representing the frictional asperity that ruptured in the large Ms7.8 Puerto Escondido earthquake and that this strong pinning point

belongs to the same system of well-defined frictional boundaries that characterize the Mexican subduction zone.

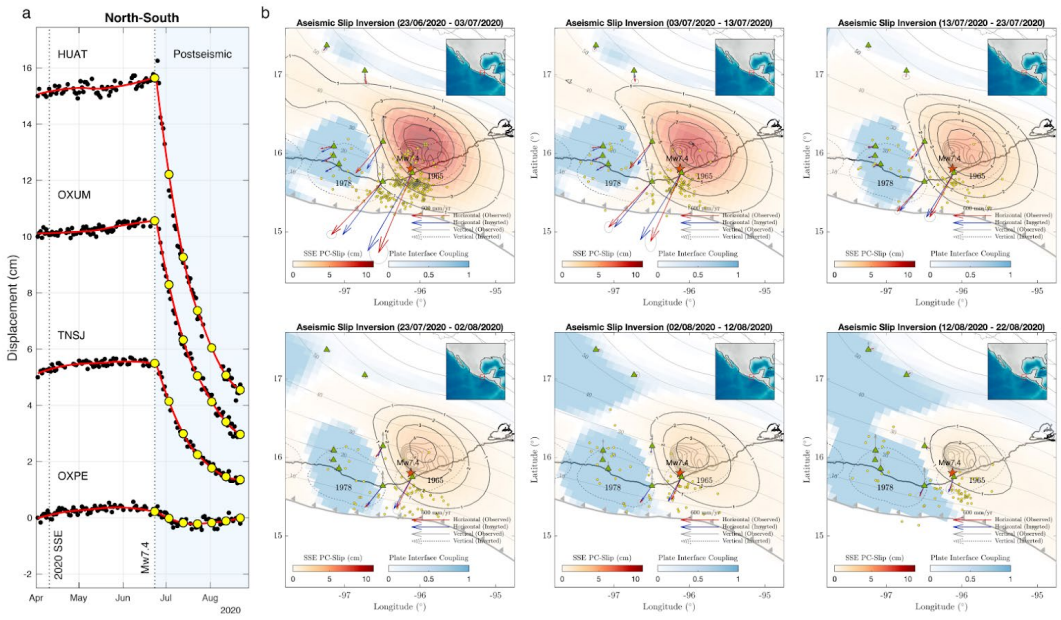

Figure 4-13. GNSS inversions of the 9-month deformation period prior to the June 23, 2020, M_w 7.4 Huatulco earthquake. (a) North-south GNSS time series in 5 selected stations. Yellow dots indicate the beginning and end of the four time-windows used for the slip inversions shown in b-e, and red dashed lines depict the inter-SSE displacement trend during the interface decoupling phase. (b-e) Inverted slip in the plate-convergence (PC) direction for all time windows. Slip contours are in centimeters. Red and yellow stars indicate the epicenters of the Huatulco and 2018 Pinotepa (M_w 7.2) earthquakes, respectively. Dashed regions are the aftershock areas of historic interplate earthquakes. Gray ellipses around the arrow tips are represent one standard deviation of the observed displacements. (f) Average and standard deviation (vertical bars) of the plate interface coupling (PIC) and relaxing slip in the region where the 2020 SSE developed (i.e., within the dotted black circle in b-e). (From Villafuerte et al., 2021)

4.5 Conclusions

We applied a template matching technique to enhance the detectability of microseismicity preceding the 2018 M_w7.2 Pinotepa Nacional earthquake in Oaxaca, Mexico. Our results showed that the seismicity rate steadily increased following the occurrence of the M_w8.2 Tehuantepec earthquake, and the acceleration of a slow slip event downdip, up to the onset of the Pinotepa earthquake. This increase in seismicity rate was accompanied by an increase in Coulomb Failure Stress changes in the hyocentral region as well as an increase in intraplate coupling. Our results suggest that the hypocentral region of the 2018 earthquake was loaded at a mesoscale by the SSE, triggering a cascade of events that led to the nucleation of the earthquake. This observation contrasts with the observations of foreshocks triggered by aseismic slip preceding other large earthquakes.

We also compared the teleseismic body wave records of the 1968 and 2018 earthquakes in Oaxaca. Our results show that the seismic waveforms of these events are almost identical over a wide range of azimuths and suggest that the principal rupture mechanism in the subduction zone of Oaxaca is compatible with a discrete persistent asperity model as proposed by Lay and Kanamori (1981). These observations are relevant to understanding the relationship between silent and devastating events in Mexico and the predictability of the latter.

Appendices

Appendix A – Supplemental Information for Chapter 1

Introduction

This supplementary material shows the figures of an example of a non-clustered aftershock productivity relationship, the sensitivity tests for the different combinations of space and time windows, a supporting figure for the results of the non-volcanic region studied and a table with the expanded contents of Figure 1-3 and the results for an alternative goodness of fit threshold.

Section A-1

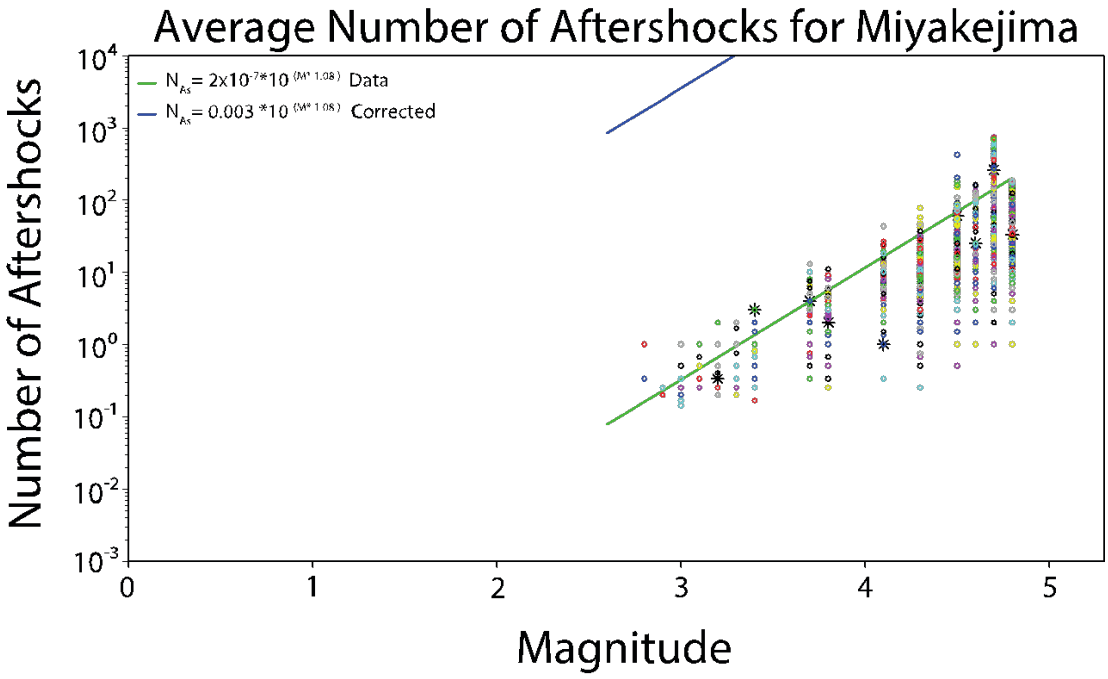

Figure A-1. Example of a volcanic system that fails the time-shuffling test. The black stars are the data, and the color dots represent the different runs with the shuffled time sequences. We show the linear fit to the data (green) and the adjusted productivity value for the completeness of the catalogue (blue). For Miyakejima the observed number of apparent aftershocks in each magnitude bin is not distinguishable from the time-shuffled realizations, indicating that mainshock-aftershock clustering is not robustly present in this region.

Section A-2

Sensitivity to space and time windows

We investigated a range of space and time windows in order to assess the robustness of our results. The results should be compared to the results in the main text that used a time window of 3 days and aftershocks search radii of 2 times the fault length of each mainshock seem to be stable compared to the other trials. The minimum size of space-time windows is restricted by the overall activity level. Windows must be large enough to capture a statistically significant number of events for many regions. The maximum size is restricted by the background rate. Windows must be small enough that they isolate the systems of interest. As illustrated in Figures A-2 and A-3, these conditions can be satisfied by a range of space-time windows. The key results are not changed by any windows within this range. We detect no significant changes in the ratio of mainshock-aftershock clustered vs not-mainshock-aftershock clustered areas in either the non-volcanic regions or the volcanic regions for the full range of space-time windows and not just a specific set.

Even though the major conclusion that earthquakes in volcanic systems trigger as much, or more, aftershocks sequences than tectonic crustal earthquakes seems to hold, there are some peculiar variations detected for individual cases. As shown in both Figure A-2 and Figure A-3 mainshock-aftershocks clustering in systems such as Fujisan, Iwatesan and Izu-Oshima seemed to be turned on or off given the choice of space-time windowing

sensitivity of these particular systems suggests that those individual results be viewed with caution.

Definition of Non-Volcanic Region

Figure A-4 shows the grid used to define the non-volcanic region. Each node was treated the same way as each volcanic summit in the volcanic regions, i.e., earthquakes were collected around each node and mainshock-aftershock clustering evaluated following the same algorithm as the volcanic regions.

Figure A-2. Time-windows sensitivity tests for: a) 1 hour, b) 5 hours, c) 12 hours, d) 1 day and e) 3 days, using a fixed space window of two times the fault length.

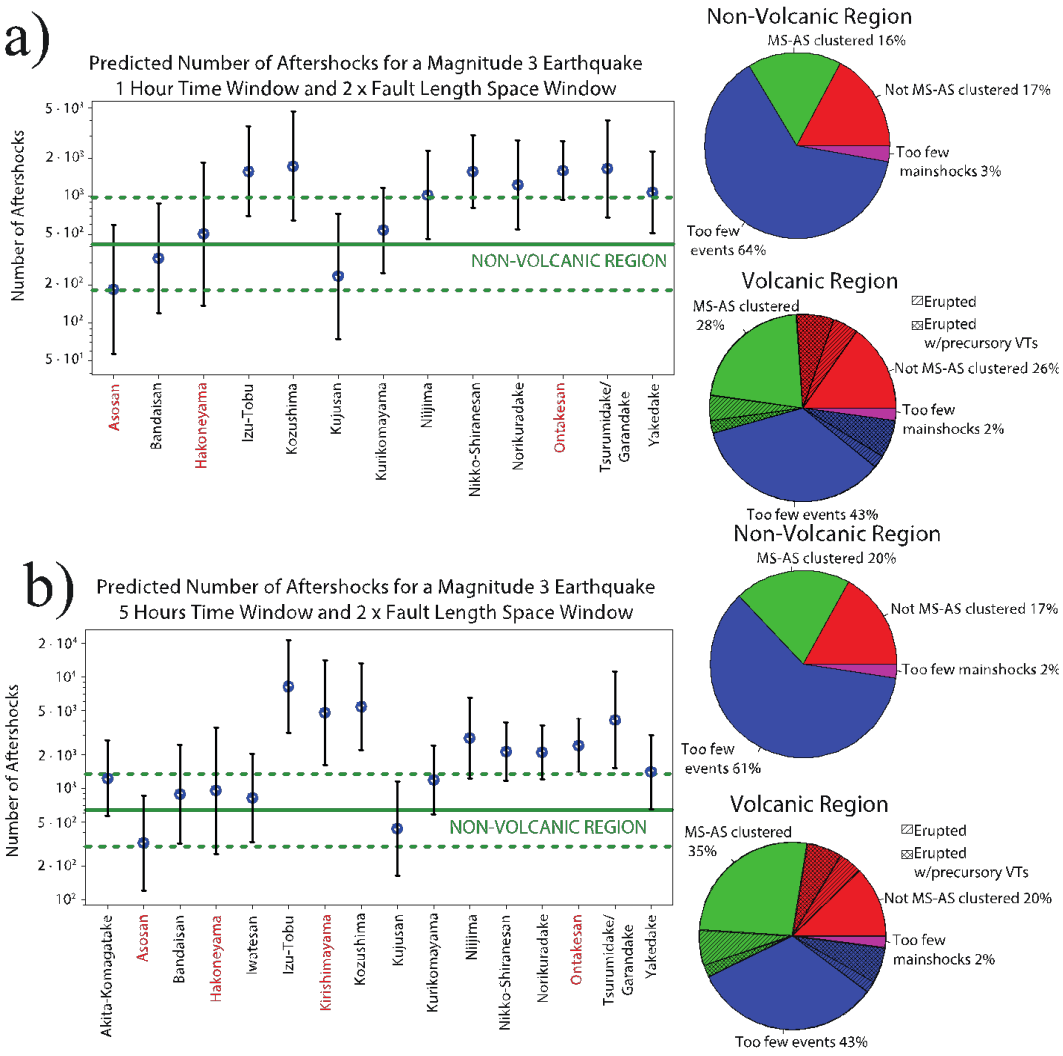
a)
Predicted Number of Aftershocks for a Magnitude 3 Earthquake
1 Hour Time Window and 2 x Fault Length Space Window
Number of Aftershocks
NON-VOLCANIC REGION
Asosan
Bandaisan
Hakoneyama
Izu-Tobu
Kozushima
Kujusan
Kurikomayama
Nijima
Nikko-Shiranesan
Norikuradake
Ontakesan
Tsurumidake/ Garandake
Yakedake
Non-Volcanic Region
MS-AS clustered 16%
Not MS-AS clustered 17%
Too few mainshocks 3%
Too few events 64%
Volcanic Region
MS-AS clustered 28%
Erupted
Erupted w/precursory VTs
Not MS-AS clustered 26%
Too few mainshocks 2%
Too few events 43%
b)
Predicted Number of Aftershocks for a Magnitude 3 Earthquake
5 Hours Time Window and 2 x Fault Length Space Window
Number of Aftershocks
NON-VOLCANIC REGION
Akita-Komagatake
Asosan
Bandaisan
Hakoneyama
Iwatesan
Izu-Tobu
Kirishimayama
Kozushima
Kujusan
Kurikomayama
Nijima
Nikko-Shiranesan
Norikuradake
Ontakesan
Tsurumidake/ Garandake
Yakedake
Non-Volcanic Region
MS-AS clustered 20%
Not MS-AS clustered 17%
Too few mainshocks 2%
Too few events 61%
Volcanic Region
MS-AS clustered 35%
Erupted
Erupted w/precursory VTs
Not MS-AS clustered 20%
Too few mainshocks 2%
Too few events 43%

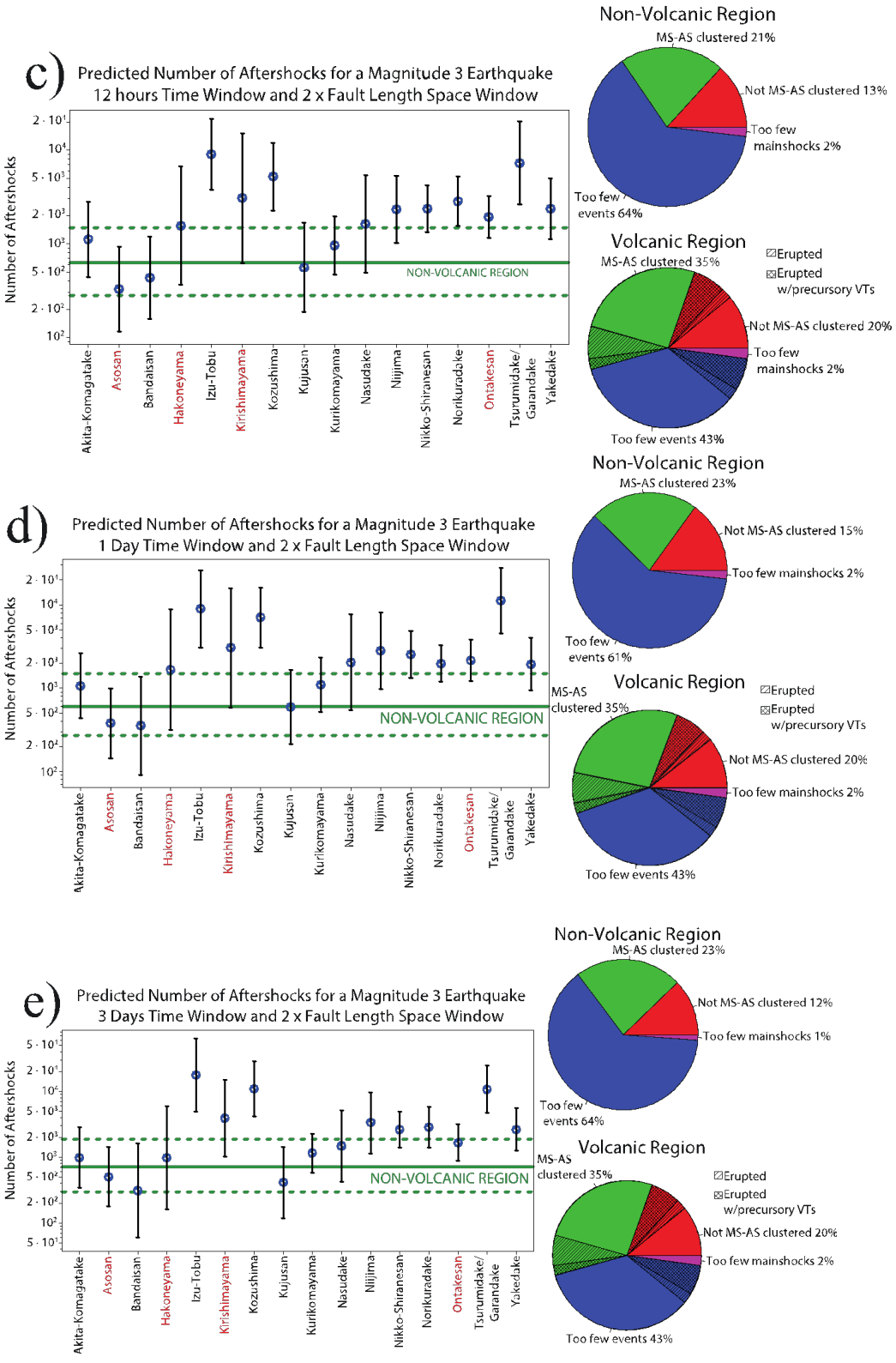
c)
Predicted Number of Aftershocks for a Magnitude 3 Earthquake
12 hours Time Window and 2 x Fault Length Space Window
Number of Aftershocks
NON-VOLCANIC REGION
Akita-Komagatake
Asosan
Bandaisan
Hakoneyama
Izu-Tobu
Kirishimayama
Kozushima
Kujusan
Kurikomayama
Nasudake
Nijima
Nikko-Shiranesan
Noriuradake
Ontakesan
Tsurumidake/ Garandake
Yakedake
Non-Volcanic Region
MS-AS clustered 21%
Not MS-AS clustered 13%
Too few mainshocks 2%
Too few events 64%
Volcanic Region
MS-AS clustered 35%
Erupted
Erupted w/precursory VTs
Not MS-AS clustered 20%
Too few mainshocks 2%
Too few events 43%
d)
Predicted Number of Aftershocks for a Magnitude 3 Earthquake
1 Day Time Window and 2 x Fault Length Space Window
Number of Aftershocks
NON-VOLCANIC REGION
Akita-Komagatake
Asosan
Bandaisan
Hakoneyama
Izu-Tobu
Kirishimayama
Kozushima
Kujusan
Kurikomayama
Nasudake
Nijima
Nikko-Shiranesan
Noriuradake
Ontakesan
Tsurumidake/ Garandake
Yakedake
Non-Volcanic Region
MS-AS clustered 23%
Not MS-AS clustered 15%
Too few mainshocks 2%
Too few events 61%
Volcanic Region
MS-AS clustered 35%
Erupted
Erupted w/precursory VTs
Not MS-AS clustered 20%
Too few mainshocks 2%
Too few events 43%
e)
Predicted Number of Aftershocks for a Magnitude 3 Earthquake
3 Days Time Window and 2 x Fault Length Space Window
Number of Aftershocks
NON-VOLCANIC REGION
Akita-Komagatake
Asosan
Bandaisan
Hakoneyama
Izu-Tobu
Kirishimayama
Kozushima
Kujusan
Kurikomayama
Nasudake
Nijima
Nikko-Shiranesan
Noriuradake
Ontakesan
Tsurumidake/ Garandake
Yakedake
Non-Volcanic Region
MS-AS clustered 23%
Not MS-AS clustered 12%
Too few mainshocks 1%
Too few events 64%
Volcanic Region
MS-AS clustered 35%
Erupted
Erupted w/precursory VTs
Not MS-AS clustered 20%
Too few mainshocks 2%
Too few events 43%

Figure A-3. Space windows sensitivity tests for: a) 0.5 times the fault length, b) 2 times the fault length, c) 3 times the fault length, d) 4 times the fault length and e) 5 times the fault length, using a fixed time window of 3 days.

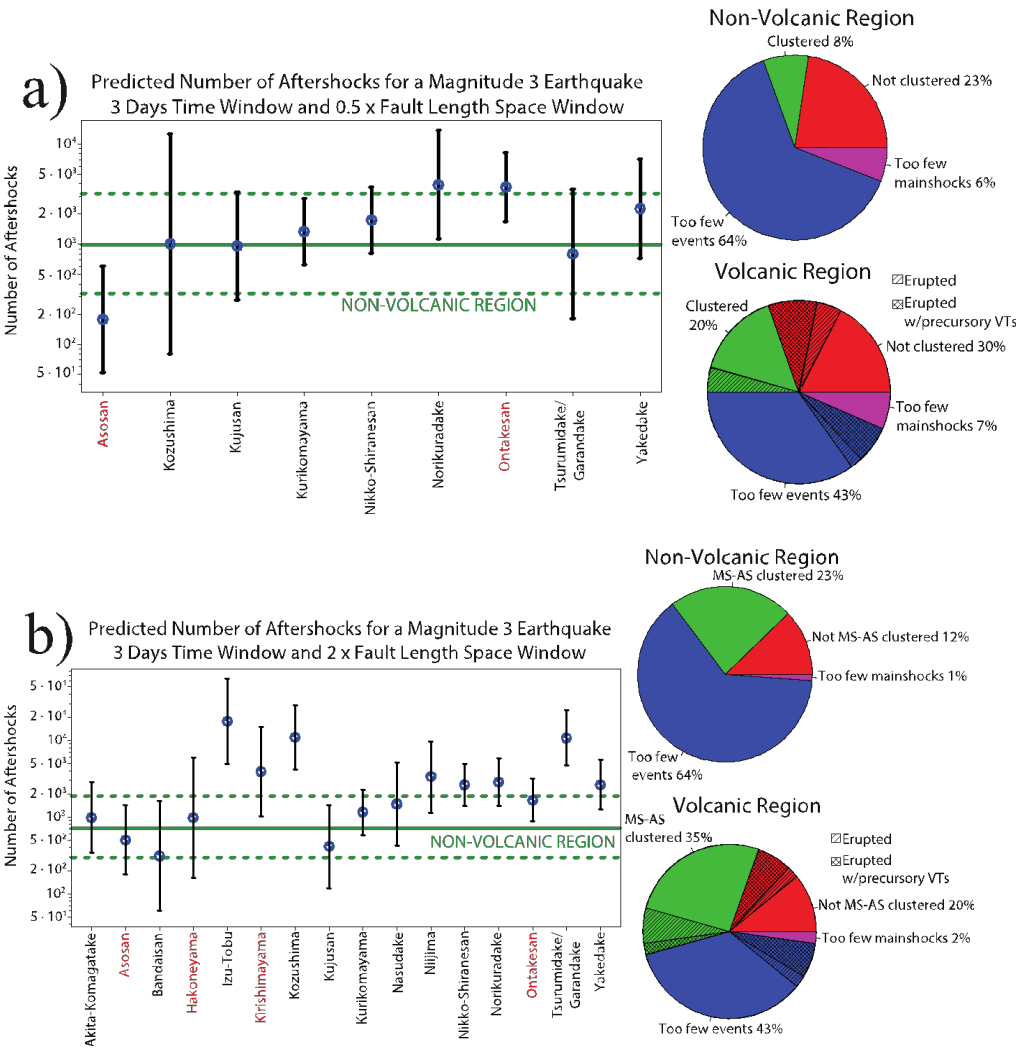
a)
Predicted Number of Aftershocks for a Magnitude 3 Earthquake
3 Days Time Window and 0.5 x Fault Length Space Window
Number of Aftershocks
NON-VOLCANIC REGION
Asosan
Kozushima
Kujusan
Kurikomayama
Nikko-Shiranesan
Norikuradake
Ontakesan
Tsurumidake/ Garandake
Yakedake
Non-Volcanic Region
Clustered 8%
Not clustered 23%
Too few mainshocks 6%
Too few events 64%
Volcanic Region
Erupted
Erupted w/precursory VTs
Clustered 20%
Not clustered 30%
Too few mainshocks 7%
Too few events 43%
b)
Predicted Number of Aftershocks for a Magnitude 3 Earthquake
3 Days Time Window and 2 x Fault Length Space Window
Number of Aftershocks
NON-VOLCANIC REGION
Akita-Komagatake
Asosan
Bandaisan
Hakoneyama
Izu-Tobu
Kirishimayama
Kozushima
Kujusan
Kurikomayama
Nasudake
Nijijima
Nikko-Shiranesan
Norikuradake
Ontakesan
Tsurumidake/ Garandake
Yakedake
Non-Volcanic Region
MS-AS clustered 23%
Not MS-AS clustered 12%
Too few mainshocks 1%
Too few events 64%
Volcanic Region
MS-AS clustered 35%
Erupted
Erupted w/precursory VTs
Not MS-AS clustered 20%
Too few mainshocks 2%
Too few events 43%

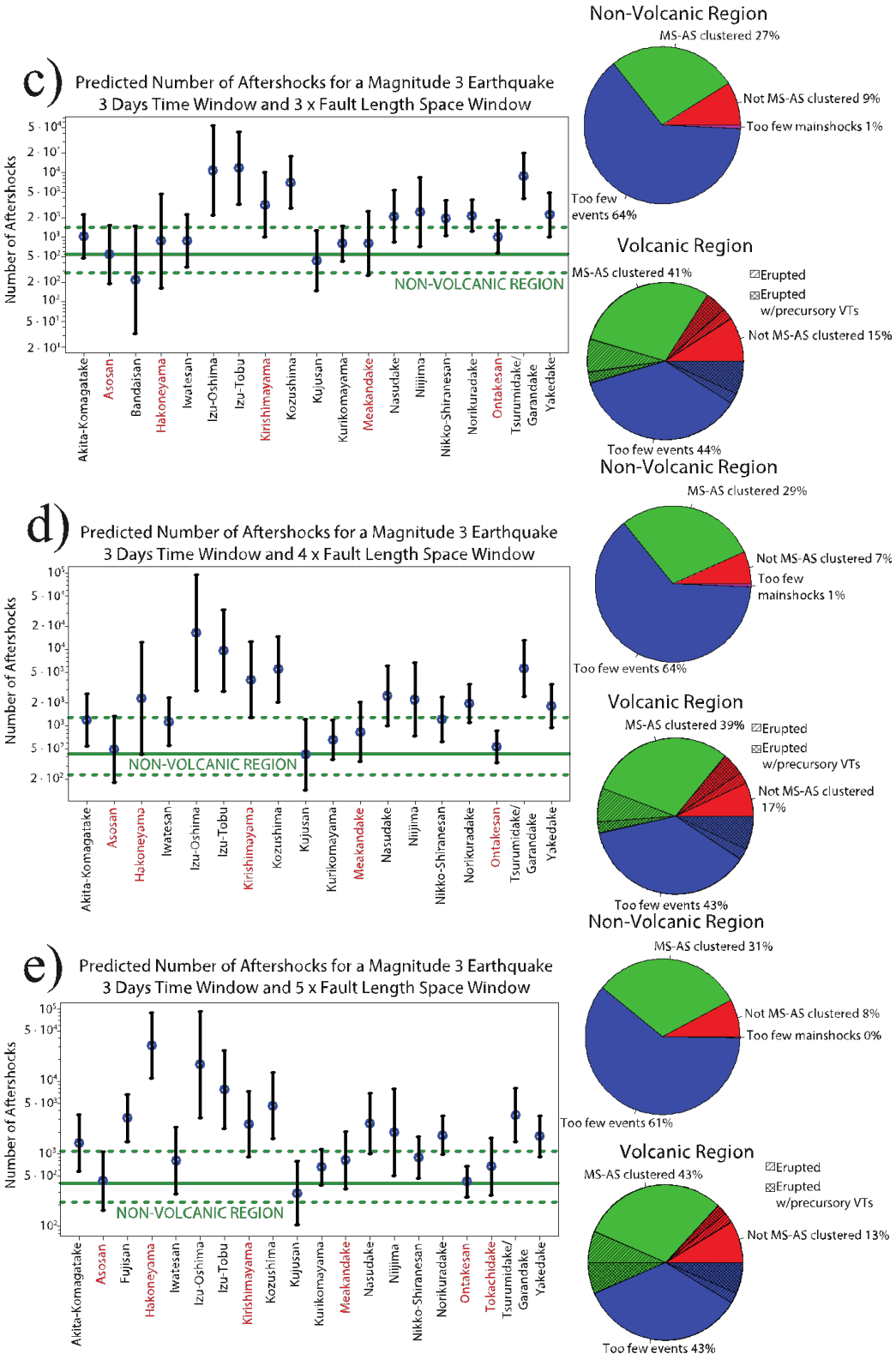
c)
Predicted Number of Aftershocks for a Magnitude 3 Earthquake
3 Days Time Window and 3 x Fault Length Space Window
Number of Aftershocks
NON-VOLCANIC REGION
Akita-Komagatake
Asosan
Bandaisan
Hakoneyama
Iwatesan
Izu-Oshima
Izu-Tobu
Kirishimayama
Kozushima
Kujusan
Kurikomayama
Meakandake
Nasudake
Niijima
Nikko-Shiranesan
Norikuradake
Ontakesan
Tsurumidake/
Garandake
Yakedake
Non-Volcanic Region
MS-AS clustered 27%
Not MS-AS clustered 9%
Too few mainshocks 1%
Too few events 64%
Volcanic Region
MS-AS clustered 41%
Erupted
Erupted w/precursory VTs
Not MS-AS clustered 15%
Too few events 44%
d)
Predicted Number of Aftershocks for a Magnitude 3 Earthquake
3 Days Time Window and 4 x Fault Length Space Window
Number of Aftershocks
NON-VOLCANIC REGION
Akita-Komagatake
Asosan
Hakoneyama
Iwatesan
Izu-Oshima
Izu-Tobu
Kirishimayama
Kozushima
Kujusan
Kurikomayama
Meakandake
Nasudake
Niijima
Nikko-Shiranesan
Norikuradake
Ontakesan
Tsurumidake/
Garandake
Yakedake
Non-Volcanic Region
MS-AS clustered 29%
Not MS-AS clustered 7%
Too few mainshocks 1%
Too few events 64%
Volcanic Region
MS-AS clustered 39%
Erupted
Erupted w/precursory VTs
Not MS-AS clustered 17%
Too few events 43%
e)
Predicted Number of Aftershocks for a Magnitude 3 Earthquake
3 Days Time Window and 5 x Fault Length Space Window
Number of Aftershocks
NON-VOLCANIC REGION
Akita-Komagatake
Asosan
Fujisan
Hakoneyama
Iwatesan
Izu-Oshima
Izu-Tobu
Kirishimayama
Kozushima
Kujusan
Kurikomayama
Meakandake
Nasudake
Niijima
Nikko-Shiranesan
Norikuradake
Ontakesan
Tokachidake
Tsurumidake/
Garandake
Yakedake
Non-Volcanic Region
MS-AS clustered 31%
Not MS-AS clustered 8%
Too few mainshocks 0%
Too few events 61%
Volcanic Region
MS-AS clustered 43%
Erupted
Erupted w/precursory VTs
Not MS-AS clustered 13%
Too few events 43%

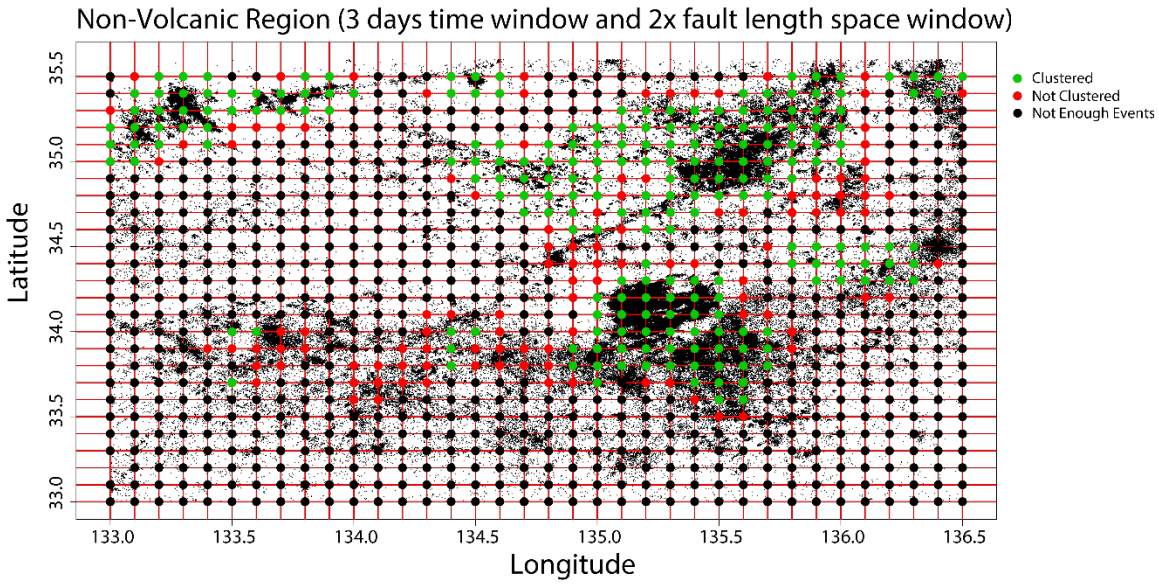

Figure A-4. Map of non-volcanic region. The nodes of the grid represent the center of each of the 20 km radius areas where mainshock-aftershock clustering was analyzed. The green nodes represent areas where clustering is present, red nodes are areas where no significant manishock-aftershock clustering was detected, and black nodes are the areas with low earthquakes density. Earthquakes in the region since January 1998 are shown in the background.

	Name	M_c	N ($M \geq M_c$)	Ms-As Clustering	Erupted since 1998	Precursory VTs	N_{As} (M=3)	α	K' X 10^{-3}	N_{aft}/N_{non}
1	Adatarayama	0.2	488	N/A	NO	NO	N/A	N/A	N/A	N/A
2	Akita-Komagatake	0.6	2567	YES	NO	NO	1026	1.0	4.4	0.78
3	Akita-Yakeyama	0.7	3825	NO	NO	NO	N/A	0.91	13.8	0.43
4	Aogashima	3.1	5	N/A	NO	NO	N/A	N/A	N/A	N/A
5	Asamayama	0.5	186	N/A	NO	NO	N/A	N/A	N/A	N/A
6	Asosan	0.4	6339	YES	YES	NO	502	0.90	12.5	0.35
7	Atasanopuri	0.8	379	N/A	NO	NO	N/A	N/A	N/A	N/A
8	Azumayama	1.1	461	N/A	NO	NO	N/A	N/A	N/A	N/A
9	Bandaisan	0.9	22129	YES	NO	NO	311	0.81	48.5	0.05
10	Chokaisan	0.8	74	N/A	NO	NO	N/A	N/A	N/A	N/A
11	Esan	1.0	570	N/A	NO	NO	N/A	N/A	N/A	N/A
12	Fujisan	0.5	2295	NO	NO	NO	N/A	1.14	3.3	0.59
13	Hachijojima	2.3	123	N/A	NO	NO	N/A	N/A	N/A	N/A
14	Hakoneyama	0.3	5992	YES	YES	YES	971	0.99	7.5	0.29
15	Hakusan	0.6	759	N/A	NO	NO	N/A	N/A	N/A	N/A
16	Hokkaido-Komagatake	0.7	503	N/A	YES	YES	N/A	N/A	N/A	N/A
17	Iwakisan	0.8	524	N/A	NO	NO	N/A	N/A	N/A	N/A
18	Iwatesan	0.7	2023	YES	NO	NO	N/A	0.99	5.5	0.95
19	Izu-Oshima	0.8	2953	NO	NO	NO	N/A	1.21	8.5	0.27
20	Izu-Tobu	0.5	17135	YES	NO	NO	14927	1.39	2.3	0.77
21	Kirishimayama	0.5	4587	YES	YES	NO	3902	1.20	4.9	0.50
22	Kozushima	1.7	9338	YES	NO	NO	10825	1.34	9.7	0.32
23	Kuchinoerabujima	0.8	496	N/A	NO	NO	N/A	N/A	N/A	N/A
24	Kujusan	0.4	8985	YES	NO	NO	410	0.86	21.4	0.32
25	Kurikomayama	0.6	30281	YES	NO	NO	1148	1.02	5.6	0.20
26	Kusatsu-Shiranesan	0.4	1558	NO	NO	NO	N/A	1.16	4.8	0.44

27	Kuttara	1.3	322	N/A	NO	NO	N/A	N/A	N/A	N/A
28	Meakandake	0.5	1535	NO	YES	YES	N/A	0.98	7.6	0.81
29	Miyakejima	2.6	2072	NO	YES	YES	N/A	1.14	166.7	0.28
30	Nasudake	0.5	4456	YES	NO	NO	1469	1.05	6.2	0.77
31	Niigata-Yakeyama	0.8	1384	NO	YES	NO	N/A	0.96	14.1	0.35
32	Niijima	1.6	7107	YES	NO	NO	3324	1.17	12.9	0.24
33	Nikko-Shiranesan	0.5	15353	YES	NO	NO	2593	1.14	6.6	0.26
34	Norikuradake	0.3	17977	YES	NO	NO	2847	1.15	3.5	0.25
35	Ontakesan	0.2	24017	YES	YES	NO	1653	1.07	3.2	0.16
36	Sakurajima	0.6	972	N/A	YES	YES	N/A	N/A	N/A	N/A
37	Satsuma-Iojima	1.3	127	N/A	NO	NO	N/A	N/A	N/A	N/A
38	Suwanosejima	2.0	420	N/A	YES	NO	N/A	N/A	N/A	N/A
39	Taisetsuzan	0.6	330	N/A	NO	NO	N/A	N/A	N/A	N/A
40	Tarumaesan	1.0	831	N/A	NO	NO	N/A	N/A	N/A	N/A
41	Tokachidake	0.1	1532	NO	YES	YES	N/A	0.72	11.2	0.92
42	Tsurumidake-Garandake	0.6	4432	YES	NO	NO	10687	1.34	4.0	1.15
43	Unzendake	0.5	1601	N/A	NO	NO	N/A	1.14	166.7	1.15
44	Usuzan	2.0	866	N/A	YES	YES	N/A	N/A	N/A	N/A
45	Yakedake	0.4	15613	YES	NO	NO	2632	1.14	9.1	0.48
46	Zaozan	0.9	512	N/A	NO	NO	N/A	N/A	N/A	N/A

Table A-1. Contents: Number of earthquakes equal or larger than the magnitude of completeness; mainshock-aftershocks clustering detection; volcano erupted since 1998; precursory volcano-tectonic earthquakes preceding eruption, predicted number of aftershocks produced by a magnitude 3 earthquake. The colors in each row refer to the category to which each volcano belong to in Figure 1-3. Note: When we lower the minimum number of events after completeness threshold to N ≥ 800, the results for Sakurajima, Tarumaesan and Usuzan show that there is no mainshock-aftershocks clustering behavior for these regions.

Section A-3.

In this section of the Supplementary Material, we present the overall results using a different approach to selecting the seismicity around a volcanic center or a node in the non-volcanic region.

In this method, we allow earthquakes that are farther than 15km away from the center to be mainshocks. If the aftershock radius of the mainshock (2 times the fault length) exceeds the 20km boundary, we allow it to go beyond such limit to search for aftershocks. The reason to include the 15km boundary limit for mainshocks in the main analysis is that the earthquakes that we have rarely exceed fault lengths of 2-3km, so by restricting them to the first 15km, we avoid a possible deficiency in aftershocks. In this other approach, we allow any earthquake to be a mainshock and by extending the catalog beyond the 20km boundary we also avoid the aftershock deficiency problem. The results of this section show that the major results of the paper are robust to this detail of mainshock-aftershock selection procedure.

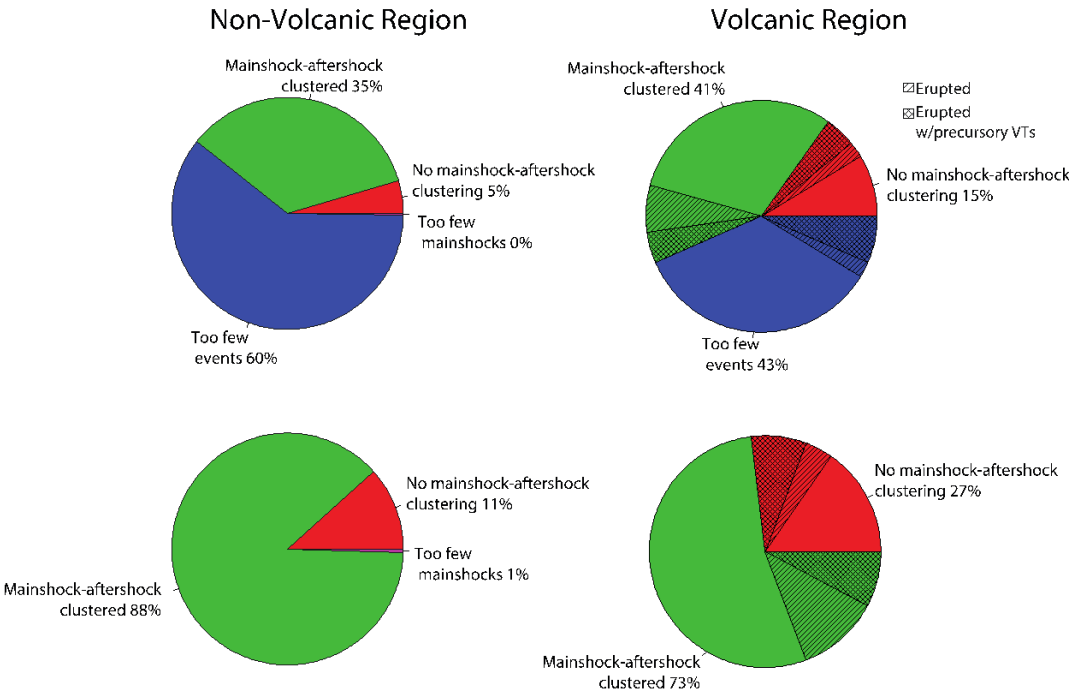

Figure A-5. Pie chart compiling the results of the 46 volcanic regions (right) and all the nodes of the non-volcanic region (left) for a selection method that allows mainshocks to occur beyond the 15km boundary. All categories are included in the upper row and the domain is limited to the measureable categories in the bottom row. Blue: Areas with insufficient seismicity (<1000 earthquakes) to study clustering. This category is omitted in the bottom row. Green: Areas that show mainshock-aftershock clustering; Red: Areas that have sufficient total seismicity and identified mainshocks to examine clustering, but failed the time-shuffling test; Magenta: Areas with fewer than 3 identified mainshocks. The hatch slices represent the percentage of volcanoes that have had an eruption since 1998 and the crosshatch areas are the portion of eruptive volcanoes that showed signs of precursory volcano-tectonic events prior to the start of the eruption.

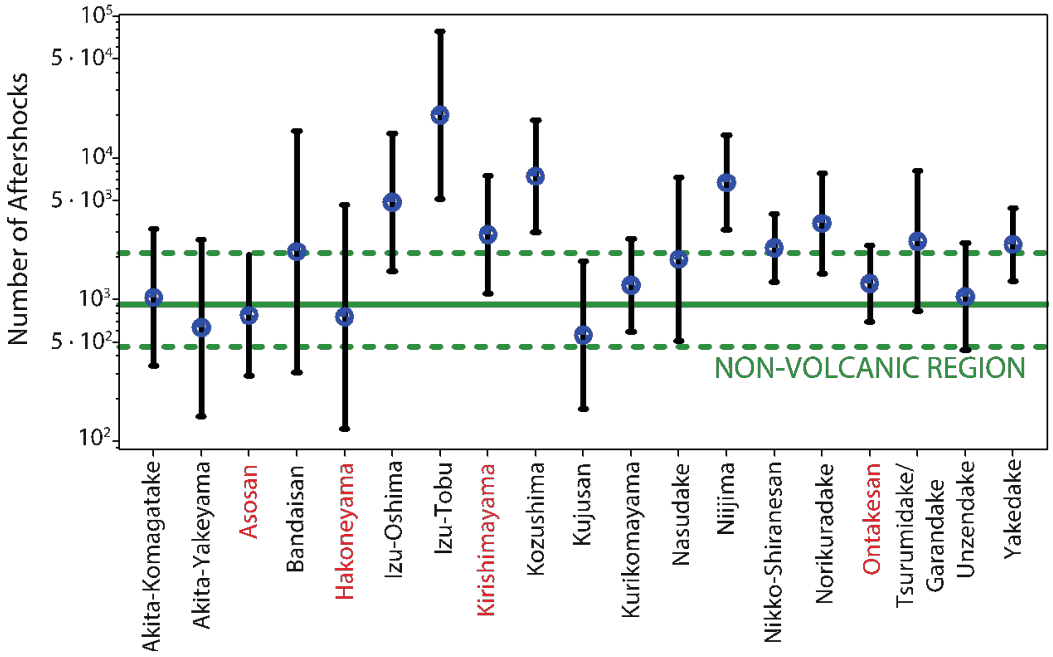

Figure A-6. Predicted number of aftershocks for a magnitude 3 earthquake in each volcanic region using the selection method described above . Error bars show the propagated error of each parameter of the Aftershock Productivity Law into the expected number of aftershocks. The solid line represents the median value of the NAs (M=3) of all the mainshock-aftershock clustered areas of the non-volcanic region and the dashed lines represent the second and forth quantiles. Volcanoes that have had at least one eruption since 1998 are shown in red.

	Name	M_c	N ($M \geq M_c$)	Ms-As Clustering	Erupted since 1998	Precursory VTs	N_{As} (M=3)	α	K' X 10^{-3}	N_{aft}/N_{bck}
1	Adatarayama	0.2	488	N/A	NO	NO	N/A	N/A	N/A	N/A
2	Akita-Komagatake	0.6	2567	YES	NO	NO	1040	1.0	3.7	0.55
3	Akita-Yakeyama	0.7	3825	NO	NO	NO	634	0.93	14.6	0.25
4	Aogashima	3.1	5	N/A	NO	NO	N/A	N/A	N/A	N/A
5	Asamayama	0.5	186	N/A	NO	NO	N/A	N/A	N/A	N/A
6	Asosan	0.4	6339	YES	YES	NO	775	0.96	9.5	0.19
7	Atasanopuri	0.8	379	N/A	NO	NO	N/A	N/A	N/A	N/A
8	Azumayama	1.1	461	N/A	NO	NO	N/A	N/A	N/A	N/A
9	Bandaisan	0.9	22129	YES	NO	NO	2188	1.11	21.6	0.11
10	Chokaisan	0.8	74	N/A	NO	NO	N/A	N/A	N/A	N/A
11	Esan	1.0	570	N/A	NO	NO	N/A	N/A	N/A	N/A
12	Fujisan	0.5	2295	NO	NO	NO	N/A	1.11	3.2	0.45
13	Hachijojima	2.3	123	N/A	NO	NO	N/A	N/A	N/A	N/A
14	Hakoneyama	0.3	5992	YES	YES	YES	761	0.96	6.1	0.22
15	Hakusan	0.6	759	N/A	NO	NO	N/A	N/A	N/A	N/A
16	Hokkaido-Komagatake	0.7	503	N/A	YES	YES	N/A	N/A	N/A	N/A
17	Iwakisan	0.8	524	N/A	NO	NO	N/A	N/A	N/A	N/A
18	Iwatesan	0.7	2023	NO	NO	NO	N/A	1.01	4.5	0.79
19	Izu-Oshima	0.8	2953	YES	NO	NO	4868	1.23	4.6	0.30
20	Izu-Tobu	0.5	17135	YES	NO	NO	20063	1.43	1.4	0.67
21	Kirishimayama	0.5	4587	YES	YES	NO	2882	1.15	3.6	0.40
22	Kozushima	1.7	9338	YES	NO	NO	7426	1.29	11.4	0.20
23	Kuchinoerabujima	0.8	496	N/A	NO	NO	N/A	N/A	N/A	N/A
24	Kujusan	0.4	8985	YES	NO	NO	562	0.91	16.8	0.24
25	Kurikomayama	0.6	30281	YES	NO	NO	1269	1.03	4.8	0.21

26	Kusatsu-Shiranesan	0.4	1558	NO	NO	NO	N/A	1.27	1.7	0.17
27	Kuttara	1.3	322	N/A	NO	NO	N/A	N/A	N/A	N/A
28	Meakandake	0.5	1535	NO	YES	YES	N/A	1.02	5.0	0.81
29	Miyakejima	2.6	2072	NO	YES	YES	N/A	1.78	53.3	0.16
30	Nasudake	0.5	4456	YES	NO	NO	1928	1.09	5.1	1.22
31	Niigata-Yakeyama	0.8	1384	NO	YES	NO	N/A	1.41	1.7	0.42
32	Niijima	1.6	7107	YES	NO	NO	6693	1.27	9.8	0.19
33	Nikko-Shiranesan	0.5	15353	YES	NO	NO	2327	1.12	6.4	0.17
34	Norikuradake	0.3	17977	YES	NO	NO	3460	1.18	3.6	0.22
35	Ontakesan	0.2	24017	YES	YES	NO	1305	1.04	4.4	0.15
36	Sakurajima	0.6	972	N/A	YES	YES	N/A	N/A	N/A	N/A
37	Satsuma-Iojima	1.3	127	N/A	NO	NO	N/A	N/A	N/A	N/A
38	Suwanosejima	2.0	420	N/A	YES	NO	N/A	N/A	N/A	N/A
39	Taisetsuzan	0.6	330	N/A	NO	NO	N/A	N/A	N/A	N/A
40	Tarumaesan	1.0	831	N/A	NO	NO	N/A	N/A	N/A	N/A
41	Tokachidake	0.1	1532	NO	YES	YES	N/A	0.84	6.6	0.34
42	Tsurumidake-Garandake	0.6	4432	YES	NO	NO	2587	1.14	7.1	0.76
43	Unzendake	0.5	1601	YES	NO	NO	1053	1.01	6.1	0.32
44	Usuzan	2.0	866	N/A	YES	YES	N/A	N/A	N/A	N/A
45	Yakedake	0.4	15613	YES	NO	NO	2460	1.13	8.7	0.40
46	Zaozan	0.9	512	N/A	NO	NO	N/A	N/A	N/A	N/A

Table A-2. Results of alternative mainshock selection method. Contents: Number of earthquakes equal or larger than the magnitude of completeness; mainshock-aftershocks clustering detection; volcano erupted since 1998; precursory volcano-tectonic earthquakes preceding eruption, predicted number of aftershocks produced by a magnitude 3 earthquake. The colors in each row refer to the category to which each volcano belongs to in Figure 1-3.

Section A-4

The major tool of mainshock-aftershock clustering detection in this work is the time-shuffling test. Therefore, the threshold of number of datapoints which need to exceed the shuffling realizations is the most important quantity used to determine goodness of fit. In the main results we present a minimum threshold of 1/2 of the data being above 90% of the shuffling realizations. Here we utilize a threshold of ¾ of the data being above 90% of the time-shuffled trials. Figure A-7 shows that fewer systems pass the more stringent criteria, however, the stringency affects the non-volcanic and volcanic regions equally. The ratio of mainshock-aftershock clustered regions to non-mainshock-aftershock clustered regions is the same for the non-volcanic and volcanic regions, just as in the results of the main text.

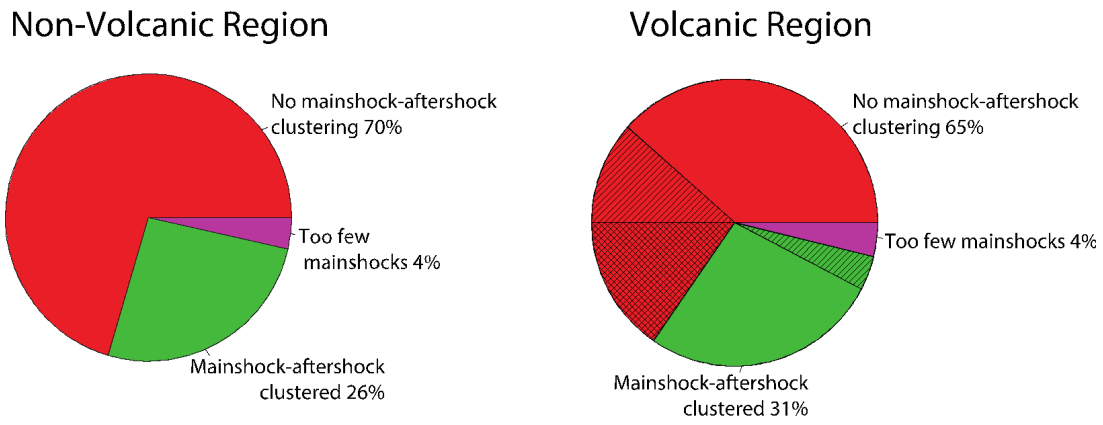

Figure A-7. Pie chart compiling the results of the 46 volcanic regions (right) and all the nodes of the non-volcanic region (left) using a shuffling test criterion of 0.75. The areas of insufficient seismicity are omitted. Green: Areas that show mainshock-aftershock clustering; Red: Areas that have sufficient total seismicity and identified mainshocks to examine clustering but failed the time-shuffling test; Magenta: Areas with fewer than 3 identified mainshocks. The hatch slices represent the percentage of volcanoes that have had an eruption since 1998 and the crosshatch areas are the portion of eruptive volcanoes that showed signs of precursory volcano-tectonic events prior to the start of the eruption.

Appendix B – Supplemental Information for Chapter 2

Event detection and phase picking

The first part of the procedure consists in creating individual earthquake catalogs using the seismicity that is already known in the region, i.e., the AVO earthquake catalog for the 2008 Okmok eruption (Power et al., 2019), enhanced by two novel earthquake detection algorithms.

The first algorithm is EQTransformer (Mousavi et al., 2020), which is a supervised deep learning-based algorithm which uses an attention mechanism to detect earthquakes and perform phase picks and by using the pre-trained model provided in their package, we can be assured that most of the earthquakes that are detected by the transformer will look like common brittle failure events found all around the world.

The second is the Fingerprint and Similarity Thresholding (FAST) (Yoon et al., 2015) algorithm which is an unsupervised system based on data reduction and fingerprint matching. The process utilized by FAST is as follows: the continuous seismic time series is presented as a spectrogram, from which the data is divided into time windows. Then, a 2D Haar wavelet transform is performed on each one of these windowed spectral images to get their wavelet representation, from which the k most anomalous coefficients, i.e., the k coefficients that deviate the most from the median value of the N coefficients, are extracted. By doing so, one is essentially eliminating the noise of the data (most

common values of the Haar wavelet coefficients), while extracting the most characteristic features of each window. For further data compression, all N-k coefficients that are not kept are represented with 0, and the remaining k Haar wavelet coefficients are represented by keeping only their sign, so that the negative values are all represented with -1 and the positive values with 1. Moreover, the new, vastly compressed images are turned into a binary fingerprint by transforming all the -1,0 and 1 into their binary representation. Finally, the similarity search is performed by using a min-wise independent permutation (Min-Hash) algorithm that applies a "hashing" function to map the sparse binary fingerprints into vectors of integers, called Min-Hash signatures. The normalized number of integers in common for two different fingerprints results in their similarity estimate. For more details on the FAST method please refer to Yoon et al (2015) and Bergen and Beroza (2019).

We then use the resulting earthquakes of each catalog and make a global merge by identifying which events correspond to individual detections and which events are repeated in different catalogs. In order to have better event locations, we attempt to get the greatest number of channels for each event by merging the repeated events together. We give priority to the AVO catalog over the others since it was already reviewed by expert observers and append the missing channels that the other catalogs might contribute with.

Besides the disparity of performance between these detection procedures, we also have differences in the way the phase arrivals were selected.

For the AVO and FAST catalogs, the picks were manually selected by expert seismologists, whereas the EQTransformer algorithm assigns a phase-pick via its hierarchical attention mechanism. Even though, in general, both the expert picks and the automatic picks from the deep-learning algorithm yield good estimates, a manual inspection of the merged events showed errors in some of the phase picks. To ensure a high data quality, we manually inspected all the events form the merged catalog and when an erroneous phase pick was found we first attempted to fix it using the automatic kurtosis picker of the PhasePApy package (Chen and Holland, 2016) and if a solution for the phase arrival could not be found, we manually picked the arrival ourselves.

Finally, to further enhance our ability to detect earthquakes, we use this initial merged catalog to do template matching using the EQcorrscan package (Chamberlain et al., 2018). Because of high levels of noise and attenuation expected during a volcanic eruption, and because of the low number of stations in the network, which translates to a lack of guarantee to have all channels available for each template, we opt to do template matching at individual channels, and we then associate the detections.

Template matching and association

Template matching

We processed all day-long waveforms by applying a linear detrending, removing the mean of the data, applying a Hanning taper of 5% in each end of the waveform and using a bandpass Butterworth filter between 5 and 12 Hz. To

make the templates we selected windows of 3 seconds around the P wave (0.2s before P- 2.8s after P) and whenever it was available 2 seconds around the S wave (0.2s before S - 1.8s after S). We used 0.6 as the absolute cross-correlation value threshold for all detections and scanned individual channels parallelly using EQcorrscan. This procedure yielded millions of individual detections.

Association

Because the matched filter routine was performed over individual channels, we used an associator to bind individual detections into a complete event.

The first step in the association process was to link horizontal components to their corresponding vertical component for all 3 channel stations. To do this, we clustered detections by their parent template and sorted them in time. If a vertical arrival was followed by a pair of horizontal arrivals within a prescribed time window (5 seconds for this dataset) they were associated together.

For the events association, we clustered all the available detections, which included the pre-associated 3 component detections, again by their parent template and sorted them in time. In this case, however, we use a lookup table that is based on the move-out of all the channels of each parent template as a guide to link up individual detections; if two detections, at different channels, have a time difference shorter than or equal to the move-out of those channels for the parent template +/- 1 second, we associated them together. We repeated

this process over all the available detections for all parent templates and finally we identified which events were repeated and kept only the one with the highest average cross-correlation value across all channels.

Because of the lack of a dense seismic network, we cannot guarantee that the parent template of the strongest detection had all channels available, and this could lead to missing out channels that had the detection recorded. To sort this out, we scanned over the detections that corresponded to the same event looking for all available channels and appended the missing ones to the strongest detection in the group. We considered this an important step to help us have better location accuracy.

Quality control

After the template matching and the association steps, we had a list of 114,092 potential events that were detected and associated using completely automated processes and that had at least 3 individual associated channels. However, as with all automated processes, there are many drawbacks to this procedure. For example, the seismic network that was deployed and stayed transmitting during the 2008 Okmok eruption did not have enough coverage to detect earthquakes in all Unmak Island. Also, every individual algorithm that was used to detect and associate required the input of thresholding parameters that are informed but arbitrary choices.

Our goal was to find a balance between extracting most of the information as possible from a sparse network while keeping a certain quality

control that guarantees, with its inherent caveats, that the final results at least do not depend on a lack of data.

To this end, we embarked on an attempt to both automatically and visually filter out potentially bad detections and to keep only the best. Visual inspection of thousands of events made us decide that there were too many false positive detections with an average cross-correlation value smaller than 0.7 to be able to hand-pick true positives from this category, so we eliminated all of these detections which represented 95.3% of the bulk of our initial list, leaving us with 5356 remaining events. Since volcanic eruptions can produce noise levels at a wide range of frequencies, it is very likely that even random noise can correlate well with templates and make it to a final event. To prevent against this, we scanned over the individual channels of each event and calculated a signal-to-noise (SNR) ratio using 5 seconds of the event waveform and 5 seconds of noise preceding the earthquake, if the SNR did not exceed 1.5, we eliminated the channel from the event, and if the respective event did not have at least 3 channels after this elimination, it was taken out of the final list. Only 3569 events passed this stage of the quality control procedure.

Finally, we visually inspected all the final 3569 events. We manually removed conspicuous or clearly erroneous channels from each event and whenever we suspected that the phase arrivals assigned by template matching were incorrect, we re-calculated them using the same steps as for the parent templates, i.e. using an automatic kurtosis picker and/or manually assigning the

pick. As a caveat, we acknowledge that even a visual inspection of the phase picks does not guarantee an extremely accurate location of these small magnitude events, the wide distribution of frequency content and signal-to-noise ratios for each individual earthquake can make it difficult for a seismologist to make the right decision at selecting the first arrivals.

After removing the events that lost most of their channels from these processes, we had a list of 3464 revised events. After locating the events and calculating a magnitude (see main text), we had a total number of 3101 events.

Location and relocation

For the relocation process, we follow a method similar to that of Waldhauser and Schaff (2008). We performed time-domain cross correlations to all pairs of events using both 0.5- and 1-seconds windows around the P and S phases. The start of the window was 0.2 seconds before the phase pick and 0.3 and 0.8 seconds after for each respective window. The waveforms were pre-processed and filtered between 3 and 15 Hz. The conditions for a pair or events to be considered for relocation were: (1) Events must be within 5 km of each other using the initial absolute location. (2) Events must have at least three stations in common. (3) The cross-correlation lag difference between the two different windows (0.5s and 1s) must be within 4 samples, which translates into maximum errors of approximately 600 meters for P waves traveling at the maximum speed in our velocity model (7.414 km/s) and using the stations with

the lowest sampling rate (50 Hz). (4) The maximum corrected travel-time difference between a pair of events is less than or equal to 1 second.

As described in the main text, it was impossible to find a set of input parameters to hypoDD that yielded good results from the inversion for all events (i.e., the condition number was either too high or too low). Therefore, we separated our data into 4 different subsets (Figure B-1): (1) Events in the active vents, (2) events in the southern sector, (3) events in the Inanudak Bay (Hotsprings Cove) area, (4) all the other events. By partitioning our data this way, we were able to find the input parameters that yielded good results for each subset.

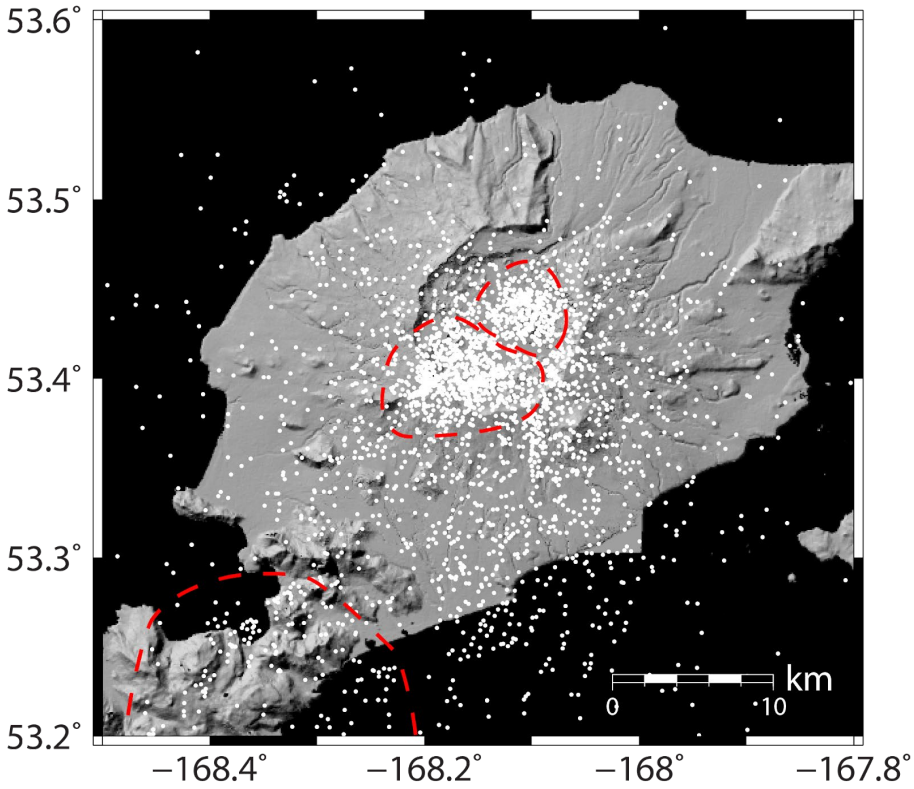

Figure B-1. Map of seismicity showing the (4) subsets of data for which we ran hypoDD separately.

Cluster/Area	Number of events	Absolute cc RMS [s] (initial/final)	Weighted cc RMS [s] (initial/final)	Absolute ct RMS [s] (initial/final)	Weighted ct RMS [s] (initial/final)
Vents	347	0.3510/0.1774	0.3304/0.1084	0.3291/0.1819	0.3044/0.1322
South of Caldera	682	0.2847/0.0064	0.2676/0.0042	0.2535/0.1354	0.2378/0.1022
Others Caldera	1394	0.3777/0.0631	0.3720/0.0354	0.3532/0.1627	0.3470/0.1184
Inanudak Bay area	168	0.2551/0.1083	0.2175/0.0923	0.2390/NaN	0.2008/NaN
Average over all clusters	N/A	0.3171/0.0888	0.2967/0.060	0.2937/0.16	0.2725/0.118

Table B-1. Results of residuals for the relocations of individual clusters of earthquakes and the average residual.

Classification

In the main text of this paper, we discuss the classification procedure that we followed to separate high-frequency events (VTs) to low-frequency events (LPs) based on their spectral content. Here, we show the results of the distribution of percentage of energy below 3 Hz as opposed to the 5 Hz used in the main text. Even though the shape of the distribution is not kept the same as in Figure 2-4, a bimodal distribution is still clearly visible. If we were to classify events following this thresholding scheme, we would also have to adjust the threshold of percentage of energy below 3 Hz (~50-60%) to separate both distributions. We tested this scheme and we found that the results discussed in this work do not depend on the thresholds used in the classification procedure.

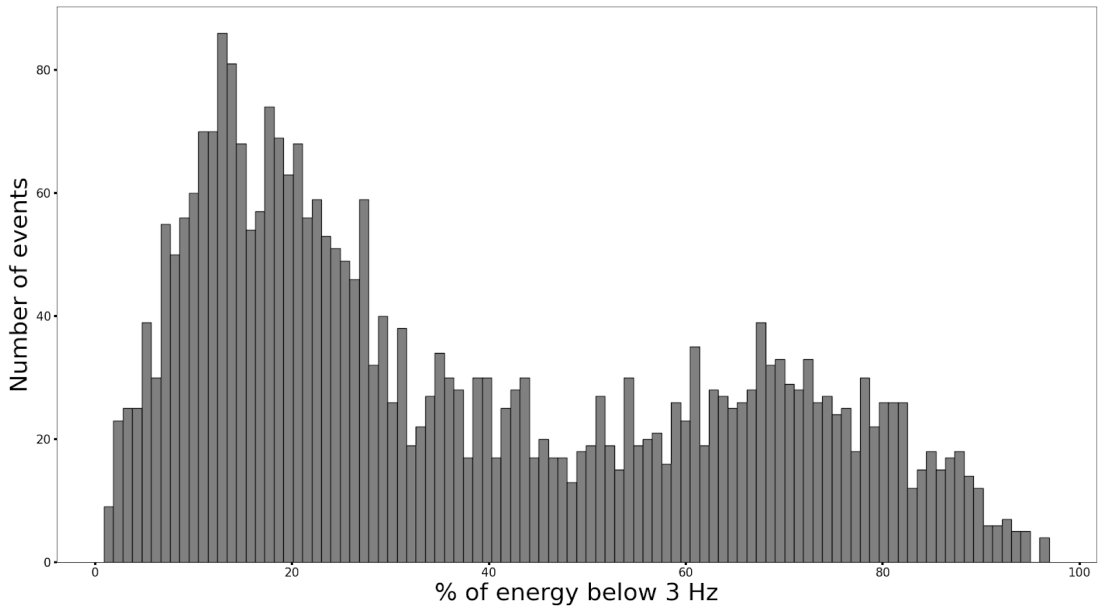

Figure B-2. Distribution of events given the ratio of energy below 3 Hz.

Another pitfall to our classification, as discussed in the main text, is that larger events generally have a lower corner-frequency, meaning that they have more power in the low-frequency part of the spectrum. We have inspected hundreds of events (VTs and LPs) of the same magnitude, and we conclude that the classification does not have a magnitude dependence. Here we show an example of two earthquakes with magnitudes ~M_L2.3 during the same time period of the eruption that were classified in the different groups based on their frequency content. Even though the VT earthquakes still show the influence of the long-period eruptive noise, their higher frequency content compared to the LP events that we detect/classify is indicative of brittle failure ruptures.

Figure B-3. Examples of VT (left) and LP (right) classified events. a) and b) are events detected by AVO only; c) and d) were detected by EQTransformer only, and e) and f) were detected by FAST only. The colored lines in the power spectra density (PSD) of each plot shows the contribution of the vertical component of each individual station to the stacked PSD (black line). Note that **t**he long-period events are clearly depleted of high frequencies compared to the VT earthquake.

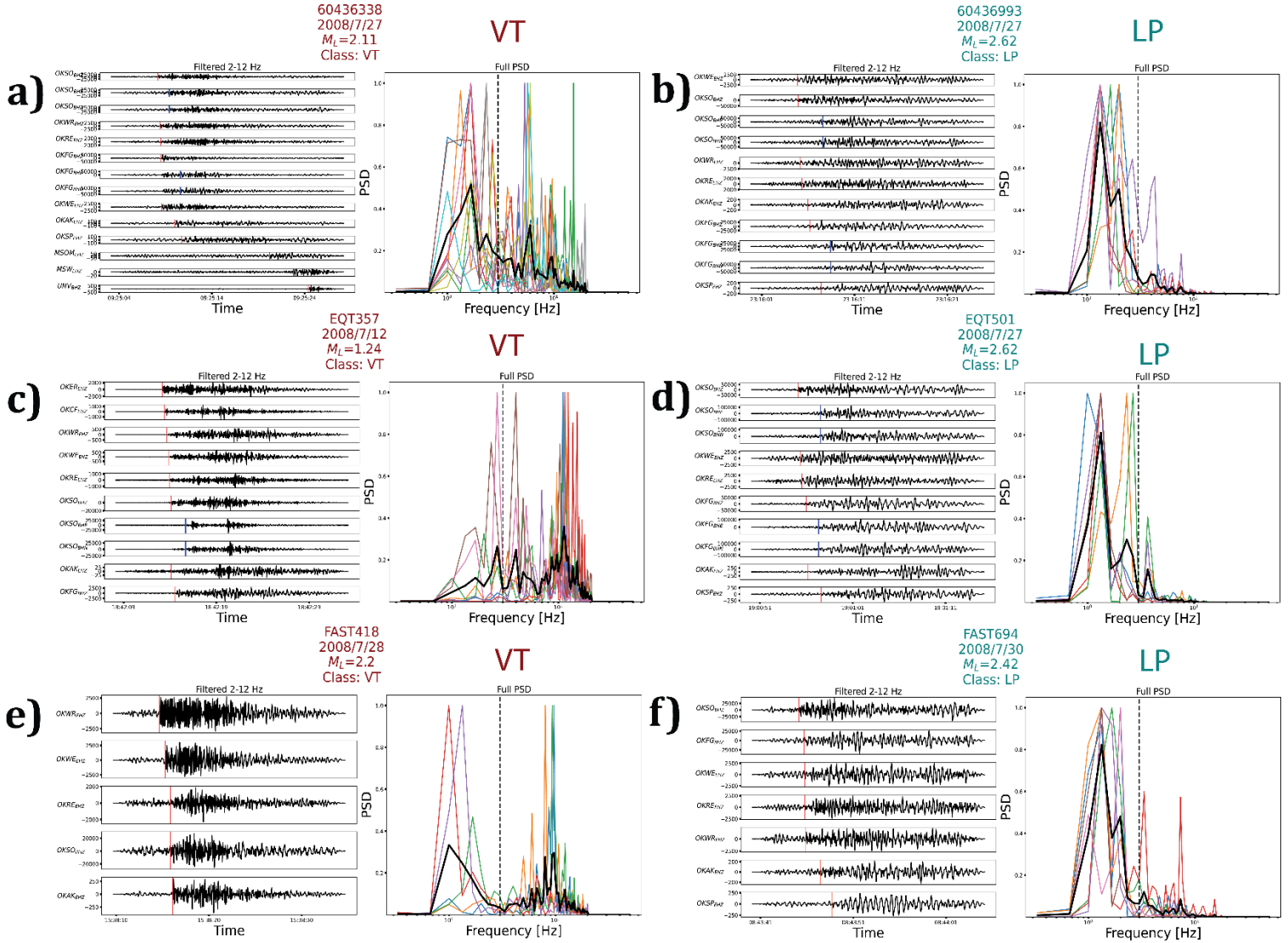
a)
60436338
2008/7/27
M_L=2.11
Class: VT
VT
Filtered 2-12 Hz
Full PSD
Time
Frequency [Hz]
PSD
b)
60436993
2008/7/27
M_L=2.62
Class: LP
LP
Filtered 2-12 Hz
Full PSD
Time
Frequency [Hz]
PSD
c)
EQT357
2008/7/12
M_L=1.24
Class: VT
VT
Filtered 2-12 Hz
Full PSD
Time
Frequency [Hz]
PSD
d)
EQT501
2008/7/27
M_L=2.62
Class: LP
LP
Filtered 2-12 Hz
Full PSD
Time
Frequency [Hz]
PSD
e)
FAST418
2008/7/28
M_L=2.2
Class: VT
VT
Filtered 2-12 Hz
Full PSD
Time
Frequency [Hz]
PSD
f)
FAST694
2008/7/30
M_L=2.42
Class: LP
LP
Filtered 2-12 Hz
Full PSD
Time
Frequency [Hz]
PSD

Local magnitude calibration

We followed the procedure prescribed by Richter (1935) and the corrections noted by Hutton and Boore (1987) so that a M_L=3 earthquake has a 10mm amplitude at a 17 km hypocentral distance on a Wood-Anderson instrument:

$$M_L = (A) - (A_0) + dM_L \qquad \text{(E.B.1)}$$

where

$$(A_0) = \alpha\left(\frac{R}{17}\right) + K(R - 17) - 2 \qquad \text{(E.B.2)}$$

and

A=peak-to-peak Wood-Anderson amplitude /2 (note that this is different than just the zero-to-peak amplitude)

R = Hypocentral distance in km

α = Geometric spread factor

K = Attenuation factor

dM_L=Station correction

To find the unknown parameters of these expressions, we arrange our equations so that:

$$(A) + 2 = M_L + \alpha\left(\frac{R}{17}\right) + K(R - 17) - dM_L \qquad \text{(E.B.3)}$$

We inverted Eq 3. to solve for M_L, K and dM_L using a generalized linear least squares (Miao and Langston,2007; Menke, 2018).

We systematically process all the earthquake waveforms in the vertical components available at all stations by windowing between 0.5 seconds before the P arrival time and 10 seconds after or 0.5 seconds before the onset of the next event, whichever occurred first. Even though it is true that the original local magnitude derived by Richter for Southern California uses horizontal components instead of vertical components, which are generally lower in amplitude, as pointed out by Kanamori et al. (1993) this does not really matter because the differences between using vertical or horizontal components for the inversion would be taken by the station correction free parameter.

We applied a linear detrend, a Hanning taper and performed the full deconvolution of the instrument response applying a bandpass pre-filter between 1-20 Hz (range at which the response of all the instruments available is flat) and lastly convolving the signal with the response of a Wood-Anderson instrument. The displacement response of the Wood-Anderson instrument that we used is based on the one reported by Bormann and Dewey (2012) in the *New Manual of Seismological Observatory Practice 2* of the International Association of Seismology and Physics of the Earth's Interior (IASPEI), which includes the magnification correction from 2800 to 2080 reported by Uhrhammer and Collins (1990).

We tested our code using the same procedure on all the waveforms available for the cataloged events between November 1, 2018-November 30, 2018 in Southern California, where comparison to the tabulation and

relationships given by Richter (1958) and Kanamori et al. (1993) are possible and the waveform data was provided by the Southern California Earthquake Data Center (SCEDC). In this case, however, we did use a magnification value of 2800 since it was the one used by Richter and Kanamori et al. This 1-month period has a comparable number of earthquakes to the Okmok dataset. As shown, in Figure B-4, the comparison is excellent with the resulting inverted attenuation relationship matching well the previously determined attenuation function.

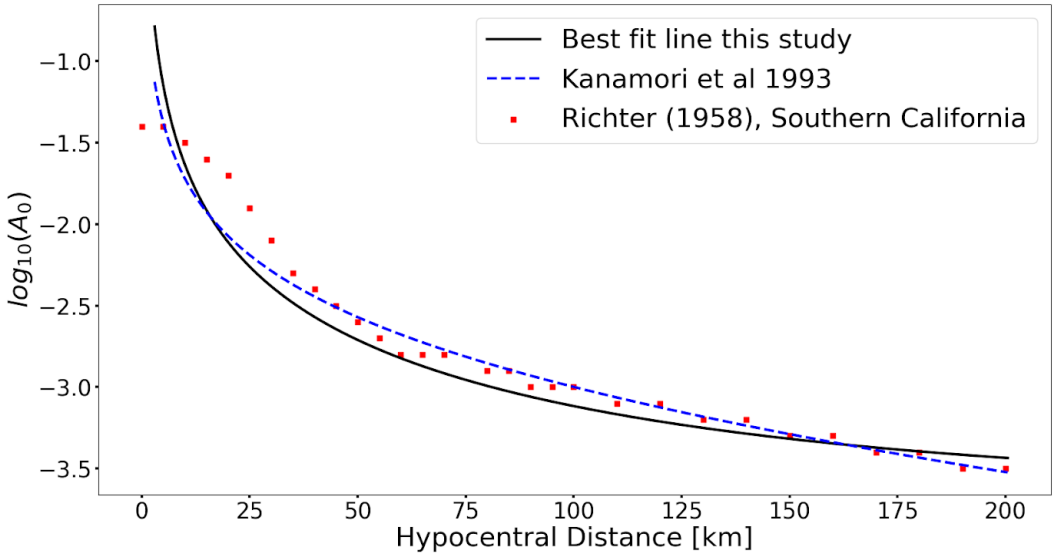

Figure B-4. Attenuation relationship validation for Southern California using the data of November 2018. For comparison, the curves provided by Richter (1958) and Kanamori et al. (1993) are included to represent the standard solution.

Locations/Relocations

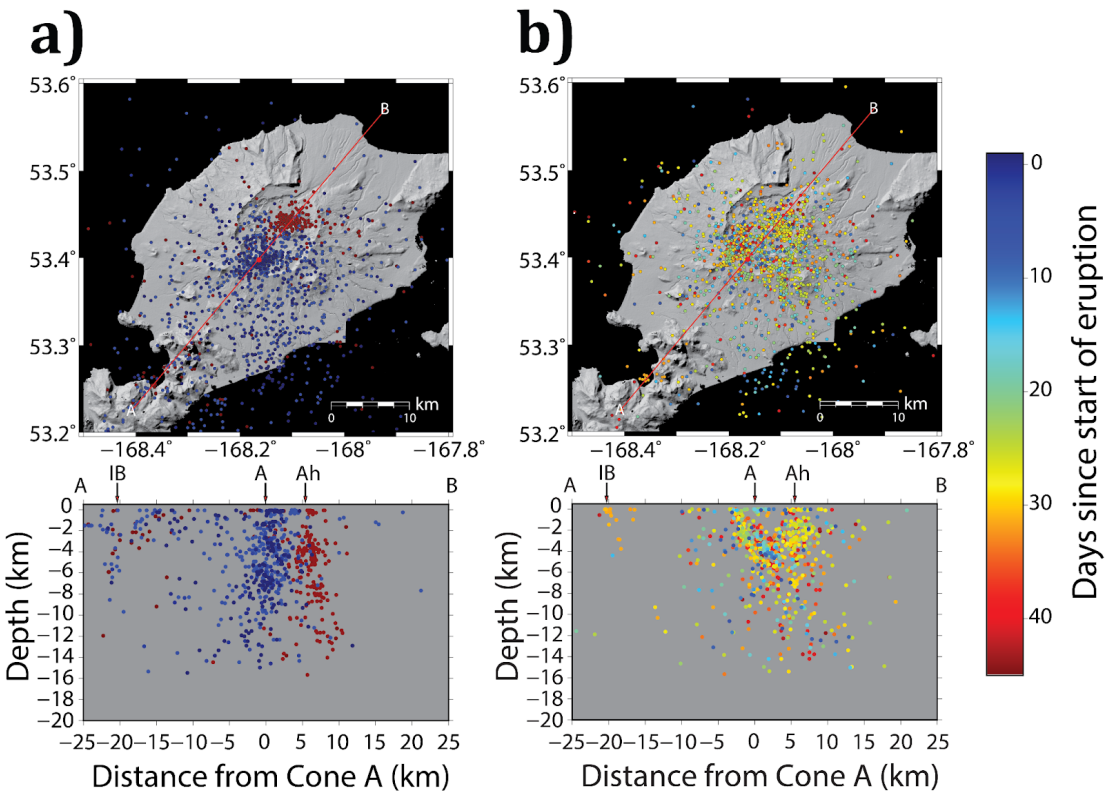

Figure B-5. NonLinLoc located earthquakes separated based before and after the eruption (a) and during the eruption (b).

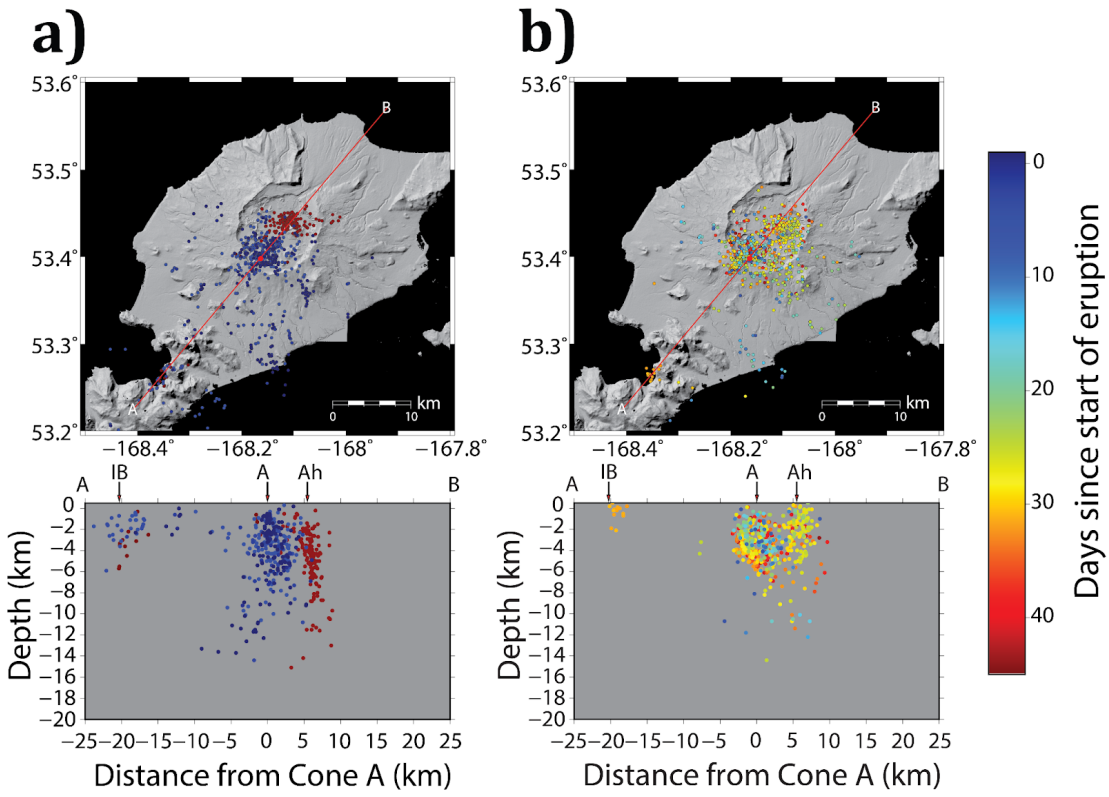

Figure B-6. GrowClust relocated earthquakes separated based before and after the eruption (a) and during the eruption (b).

Middle of eruption

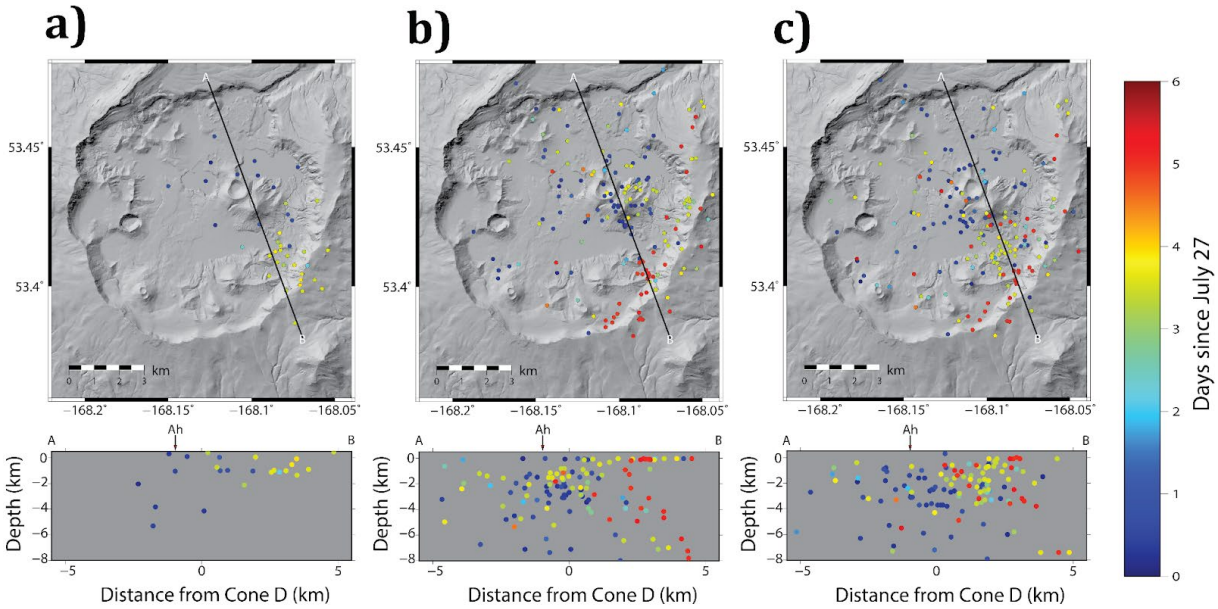

Figure B-7. AVO (a), NonLinLoc (b) and GrowClust (c) locations for the July 27-August 3 LPs sequence.

Frequency-magnitude distributions

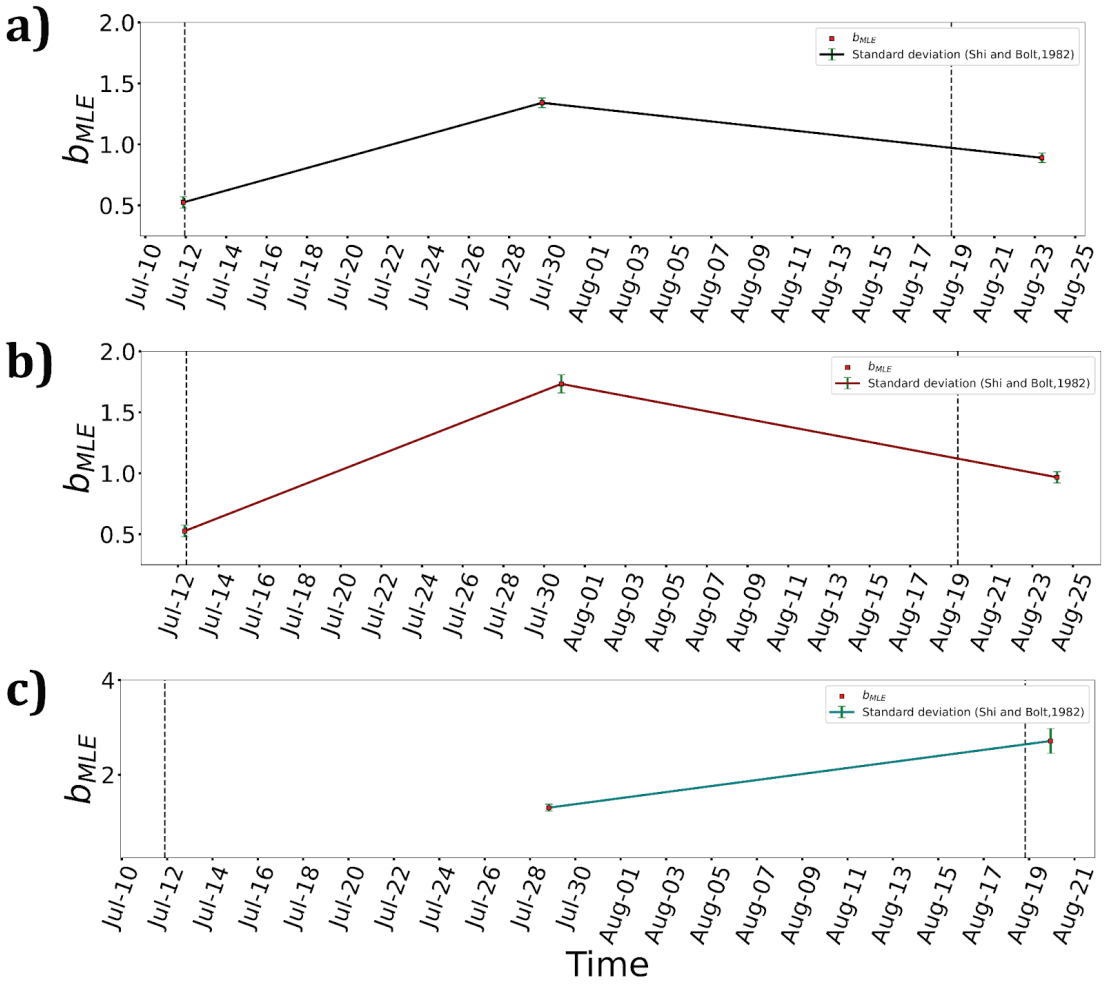

Figure B-8. Before, during, after calculation of b values using the maximum-likelihood estimate. a) All earthquakes. b) VT events only. c) LP events only.

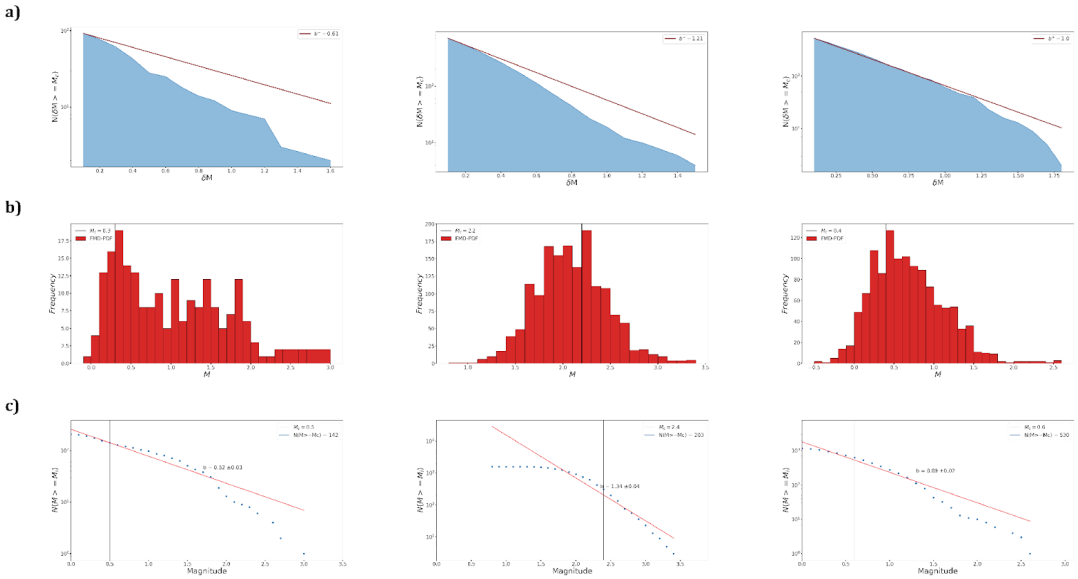

Figure B-9. a) b+ before, during and after the eruption for all earthquakes. b) Probability distribution functions for the magnitude of earthquakes before, during and after the eruption for all earthquakes. c) Gutenberg-Richter relationship (cumulative distribution function of earthquakes) and b values calculated with the maximum-likelihood method before, during and after the eruption for all earthquakes.

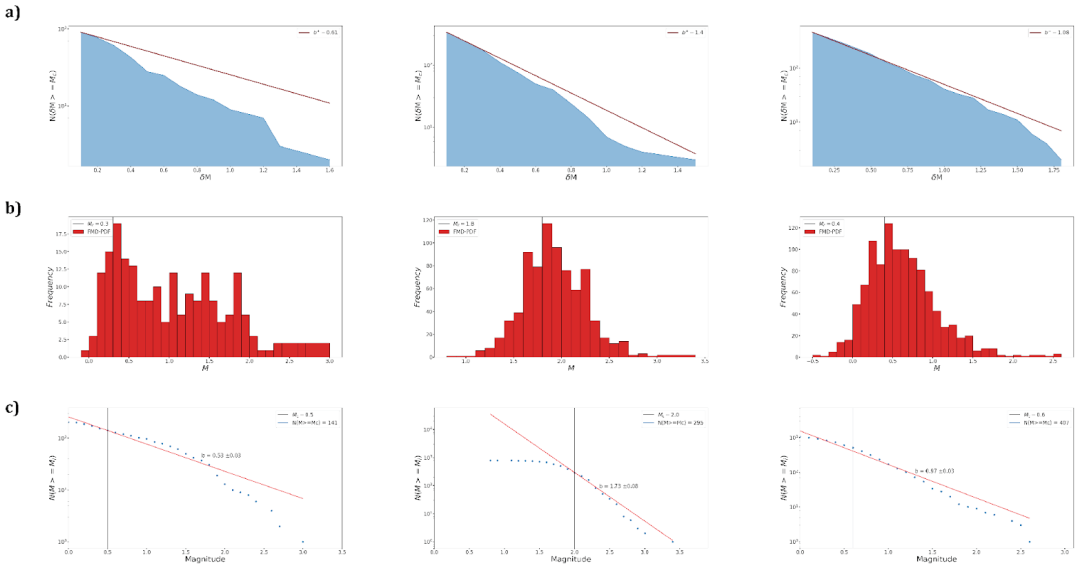

Figure B-10. a) b+ before, during and after the eruption for VT earthquakes only. b) Probability distribution functions for the magnitude of earthquakes before, during and after the eruption for VT earthquakes only. c) Gutenberg-Richter relationship (cumulative distribution function of earthquakes) and b values calculated with the maximum-likelihood method before, during and after the eruption for VT earthquakes only.

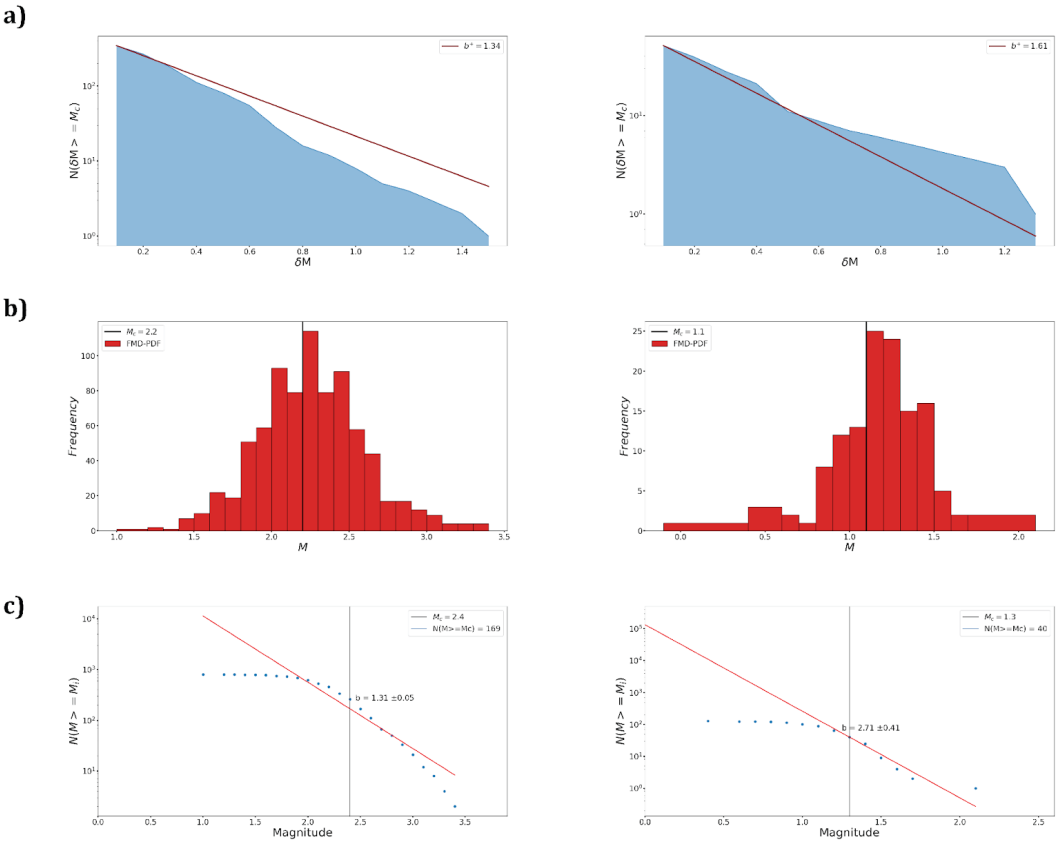

Figure B-11. a) b+ before, during and after the eruption for LP earthquakes only. b) Probability distribution functions for the magnitude of earthquakes before, during and after the eruption for LP earthquakes only. c) Gutenberg-Richter relationship (cumulative distribution function of earthquakes) and b values calculated with the maximum-likelihood method before, during and after the eruption for LP earthquakes only.

Seismicity rate estimated using b values (maximum-likelihood estimate)

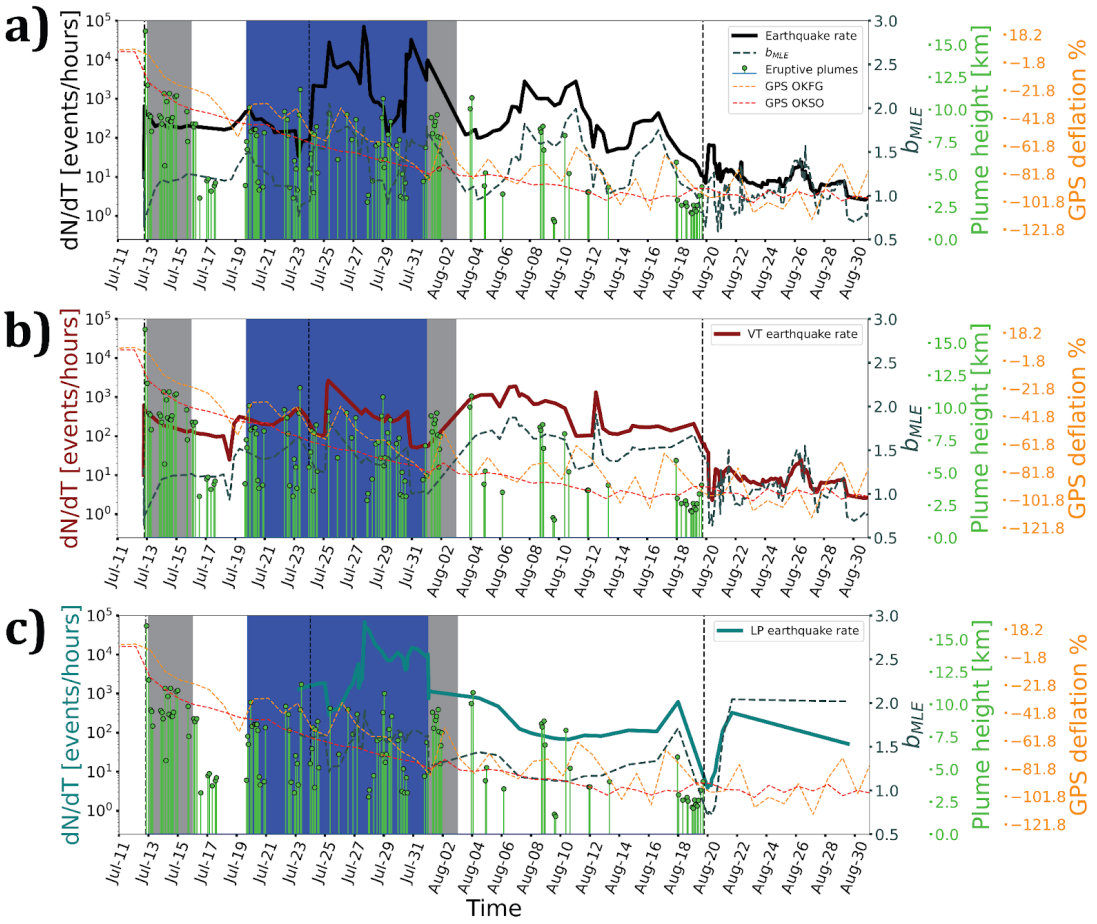

Figure B-12. Seismicity rate (continuous lines) as the extrapolated number of events >= magnitude 0 based on the local value of b values using the maximum-likelihood method (dashed gray line) in a 100-event moving window with 10% overlap. GPS deflation percentage shown for reference (red and orange lines). Plume heights (Larsen et al. 2009) are shown in green. a) All earthquakes. b) VT earthquakes only. c) LP earthquakes only.

Plume data from satellite observations

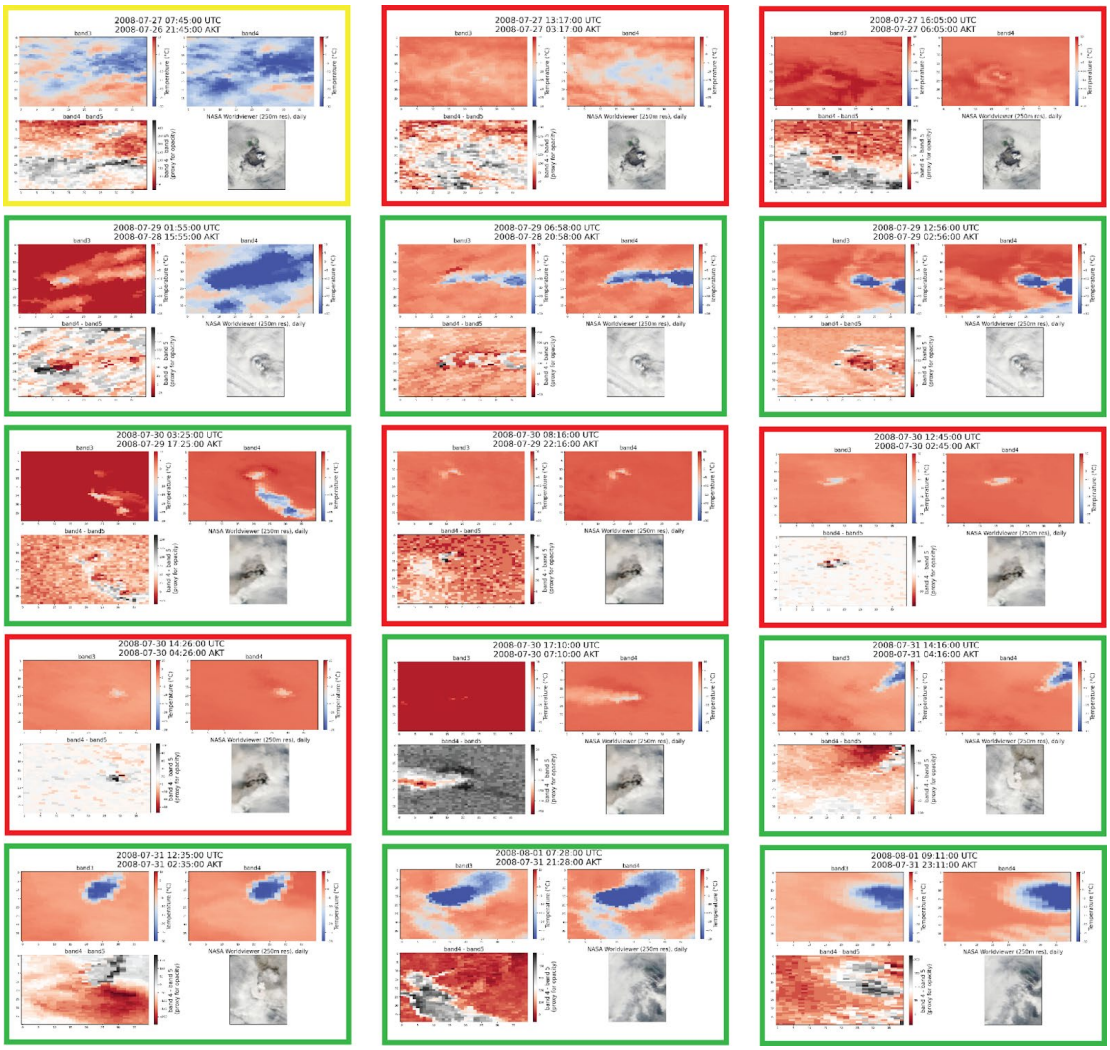

Figure B-13. Observations from July 27 to August 1 from the Advanced Very-High-Resolution Radiometer (AVHRR) (bands 3,4,5) and MODIS-Terra and MODIS-Aqua corrected reflectance satellite images. The images of July 29 are shown as an example of what we would expect to see during a time of the ejection of a significant plume. On July 27 (during the LP bursts) the plume signal was so weak that one can even see the silhouette of Okmok Volcano. Red frames indicate that no plume is observed, green frames indicate that a plume is observed, and orange frames indicate times where the observation of plumes (or lack of) is unclear.

Appendix C – Supplemental Information for Chapter 3

Comparison of the monthly averaged surface temperature time series recorded at the Automatic Weather Stations (AWS) and the values from the closest grid node of the ERA5 reanalysis.

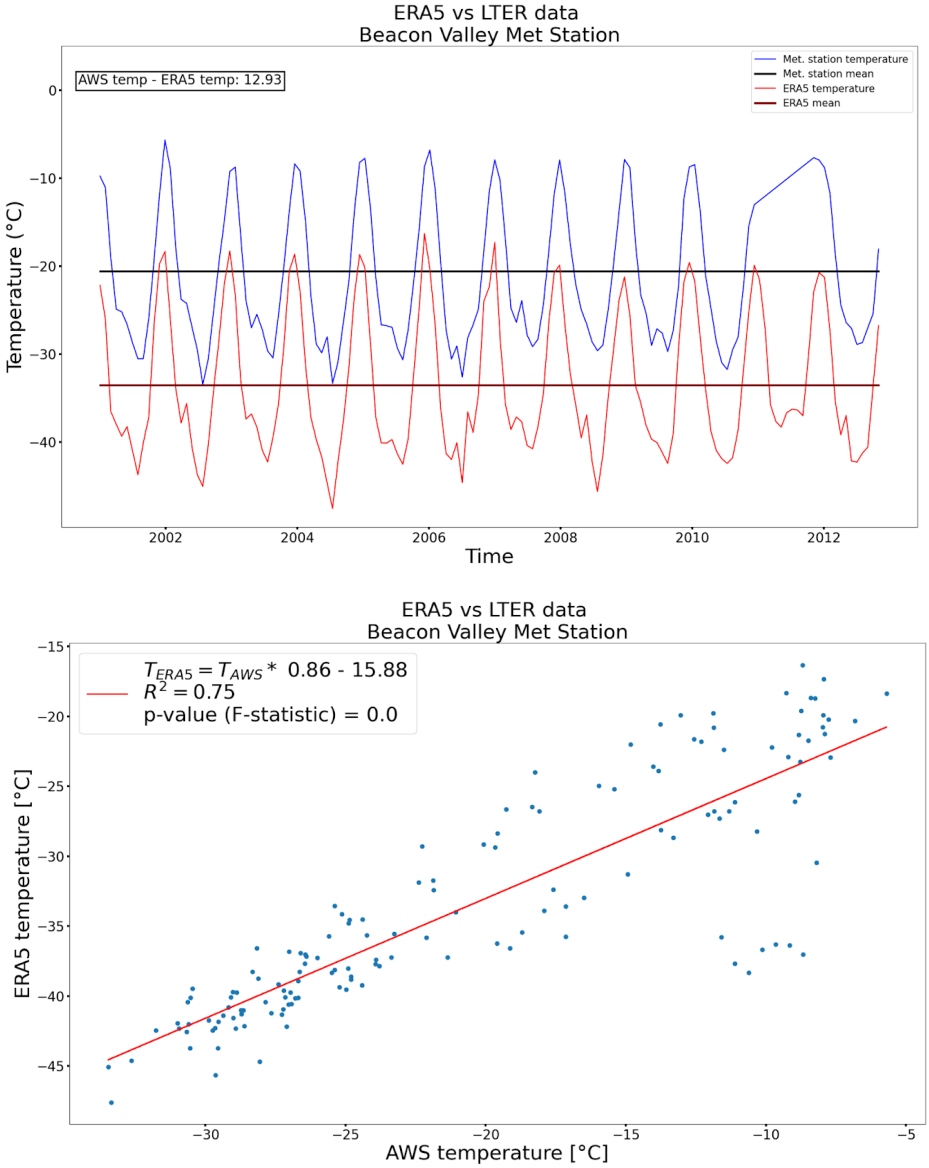

Figure C-1. Beacon Valley. Top: Time series for station Beacon Valley (BENM) (blue) and the values from the closest grid node of the ERA5 reanalysis (red). Bottom: Correlogram.

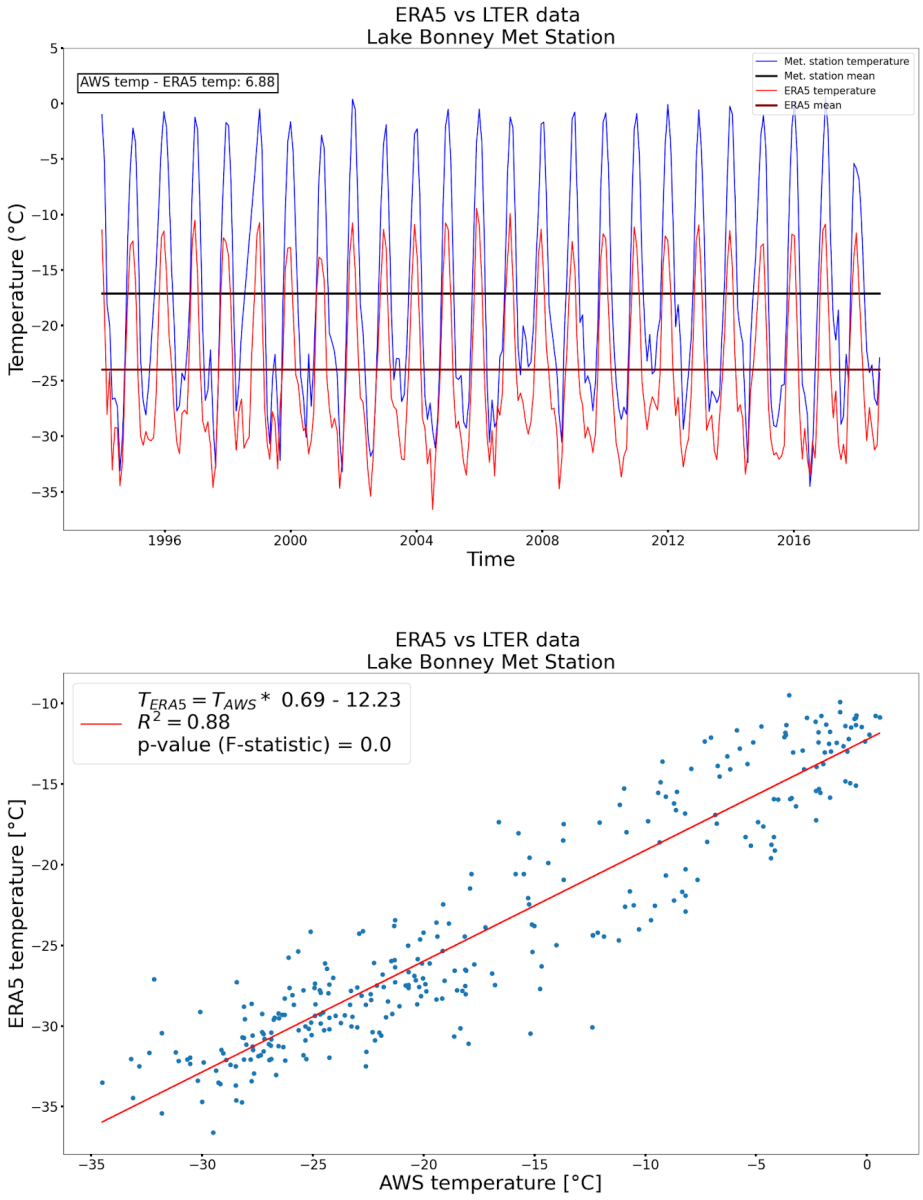

Figure C-2. Lake Bonney. Top: Time series for station Lake Bonney (BOYM) (blue) and the values from the closest grid node of the ERA5 reanalysis (red). Bottom: Correlogram.

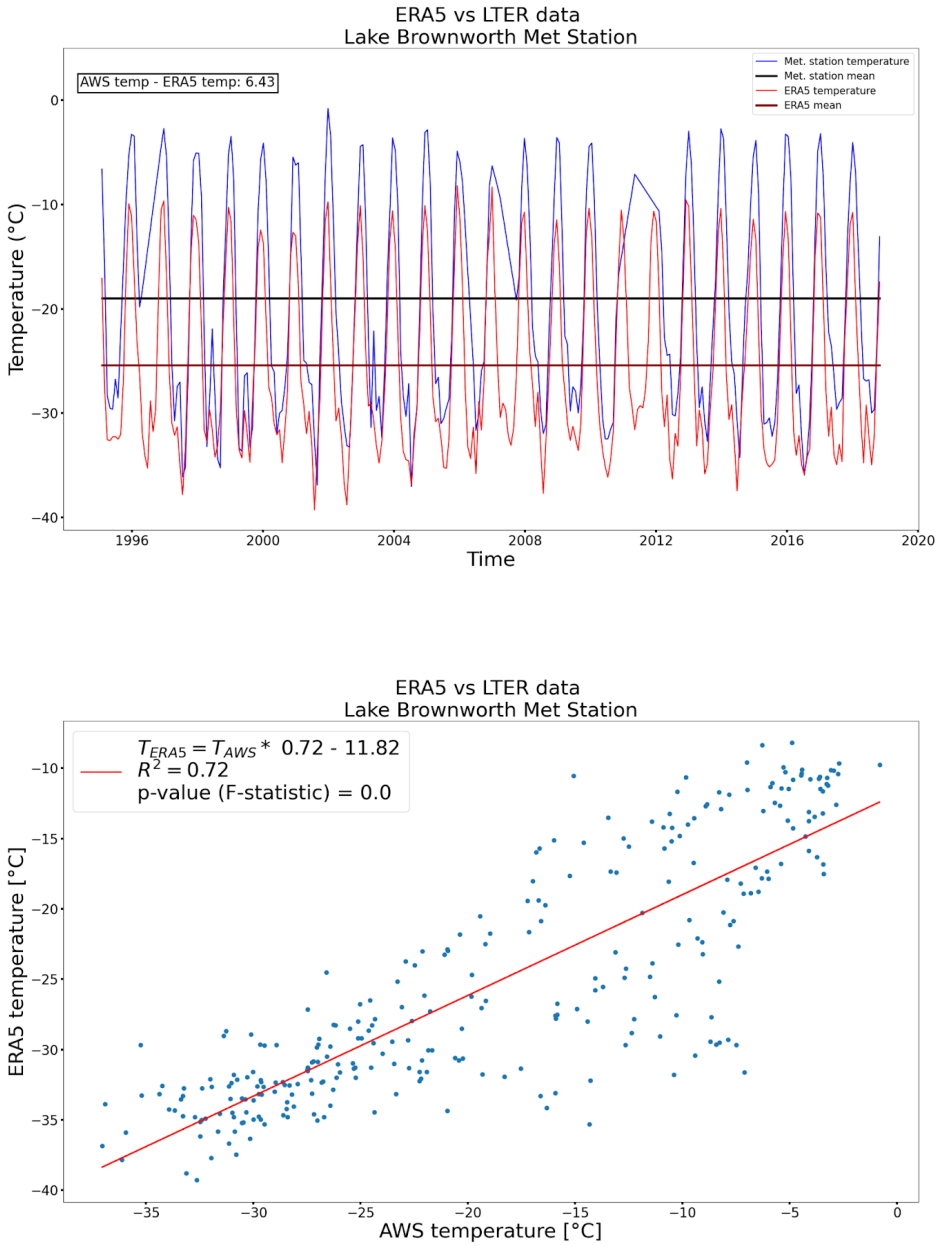

Figure C-3. Lake Brownworth. Top: Time series for station Lake Brownworth (BRHM) (blue) and the values from the closest grid node of the ERA5 reanalysis (red). Bottom: Correlogram.

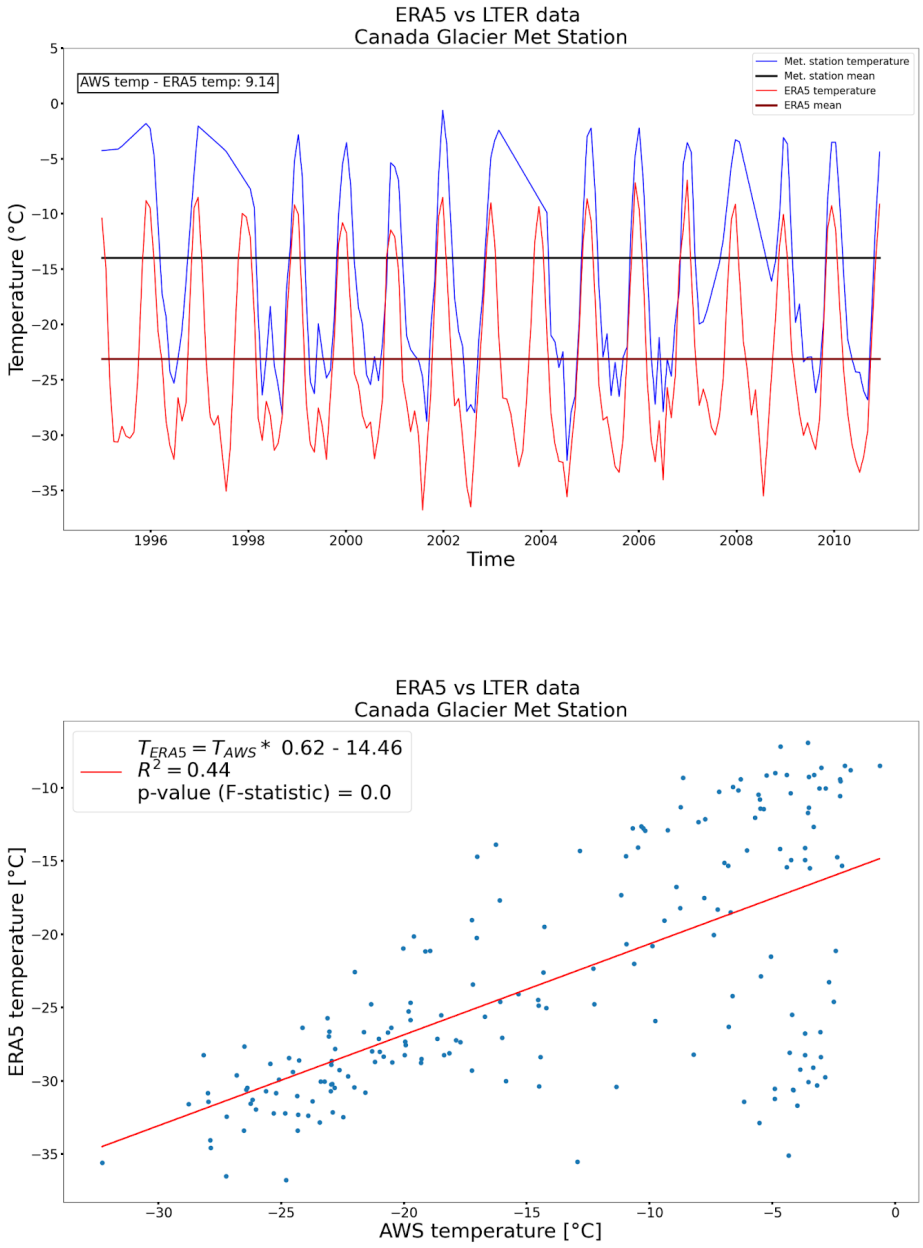

Figure C-4. Canada Glacier. Top: Time series for station Canada Glacier (CAAM) (blue) and the values from the closest grid node of the ERA5 reanalysis (red). Bottom: Correlogram.

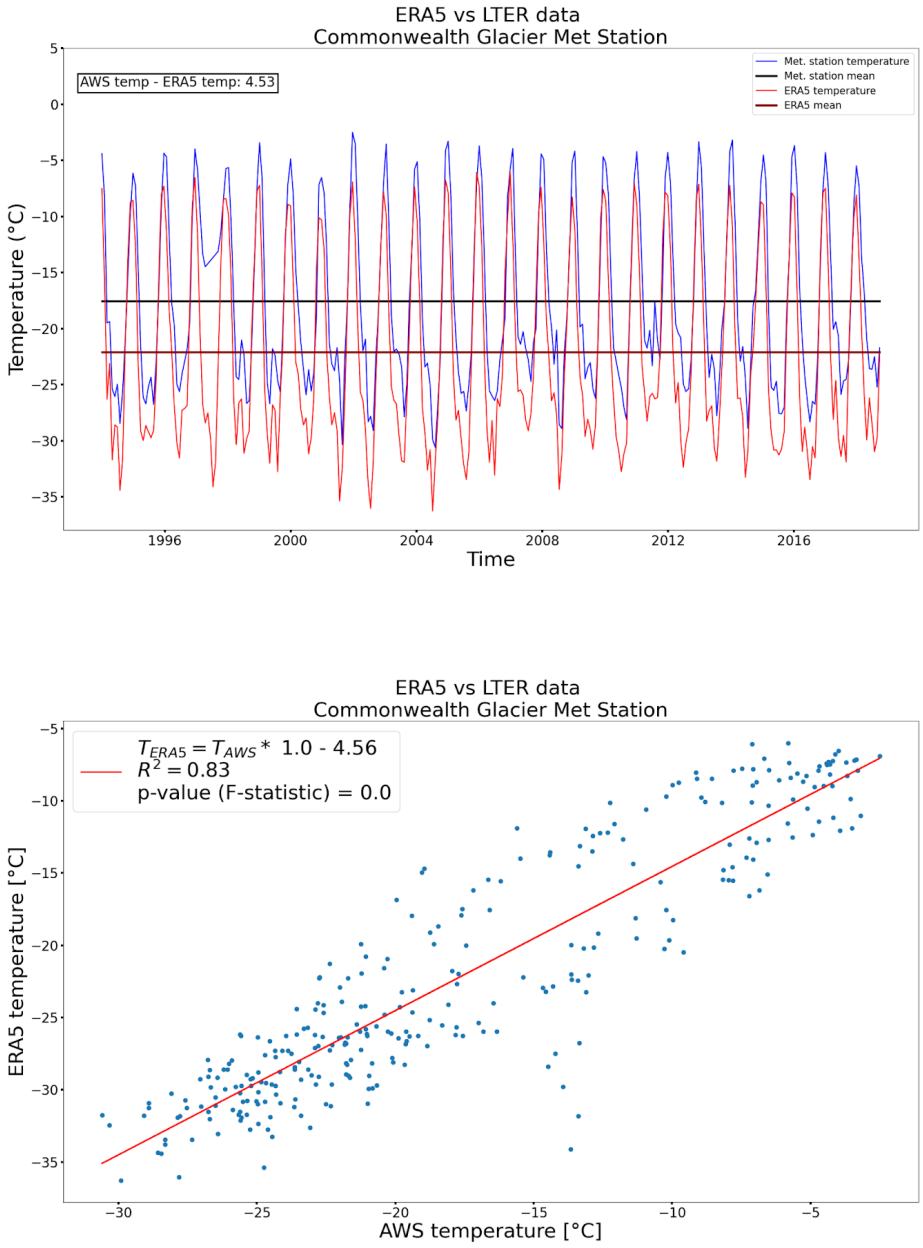

Figure C-5. Commonwealth Glacier. Top: Time series for station Commonwealth Glacier (COHM) (blue) and the values from the closest grid node of the ERA5 reanalysis (red). Bottom: Correlogram.

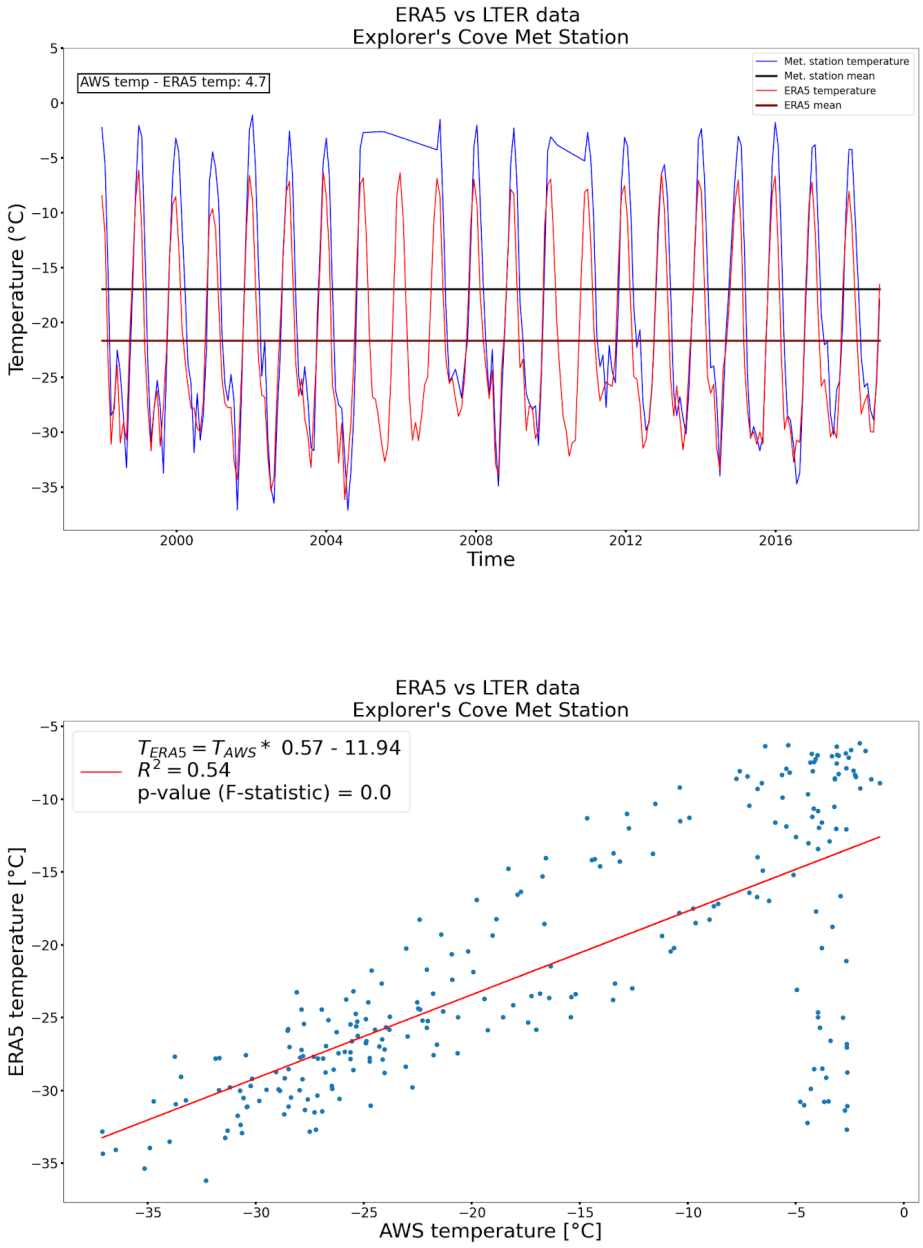

Figure C-6. Explorer's Cove. Top: Time series for station Explorer's Cove (EXEM) (blue) and the values from the closest grid node of the ERA5 reanalysis (red). Bottom: Correlogram.

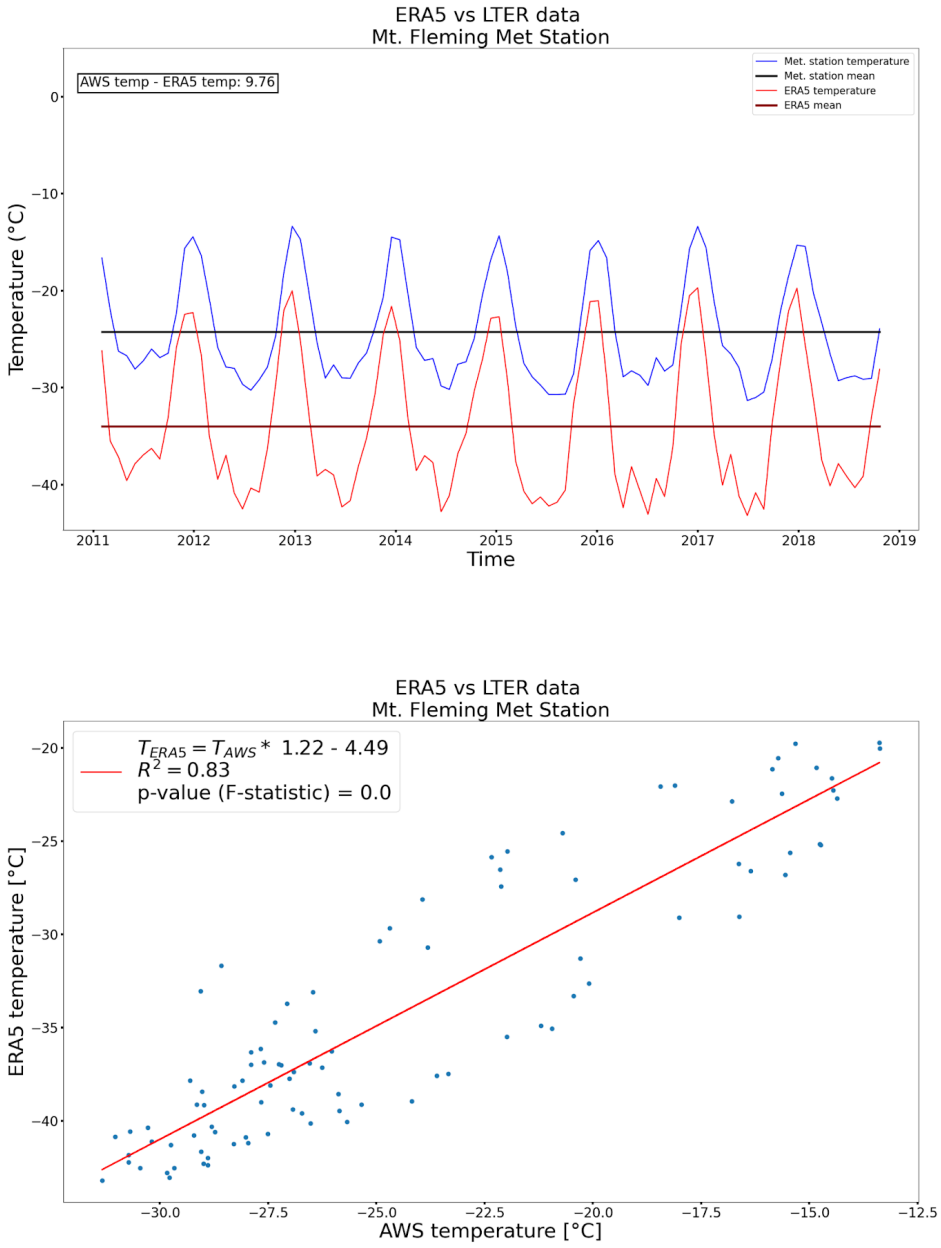

Figure C-7. Mount Fleming. Top: Time series for station Mount Fleming (FLMM) (blue) and the values from the closest grid node of the ERA5 reanalysis (red). Bottom: Correlogram.

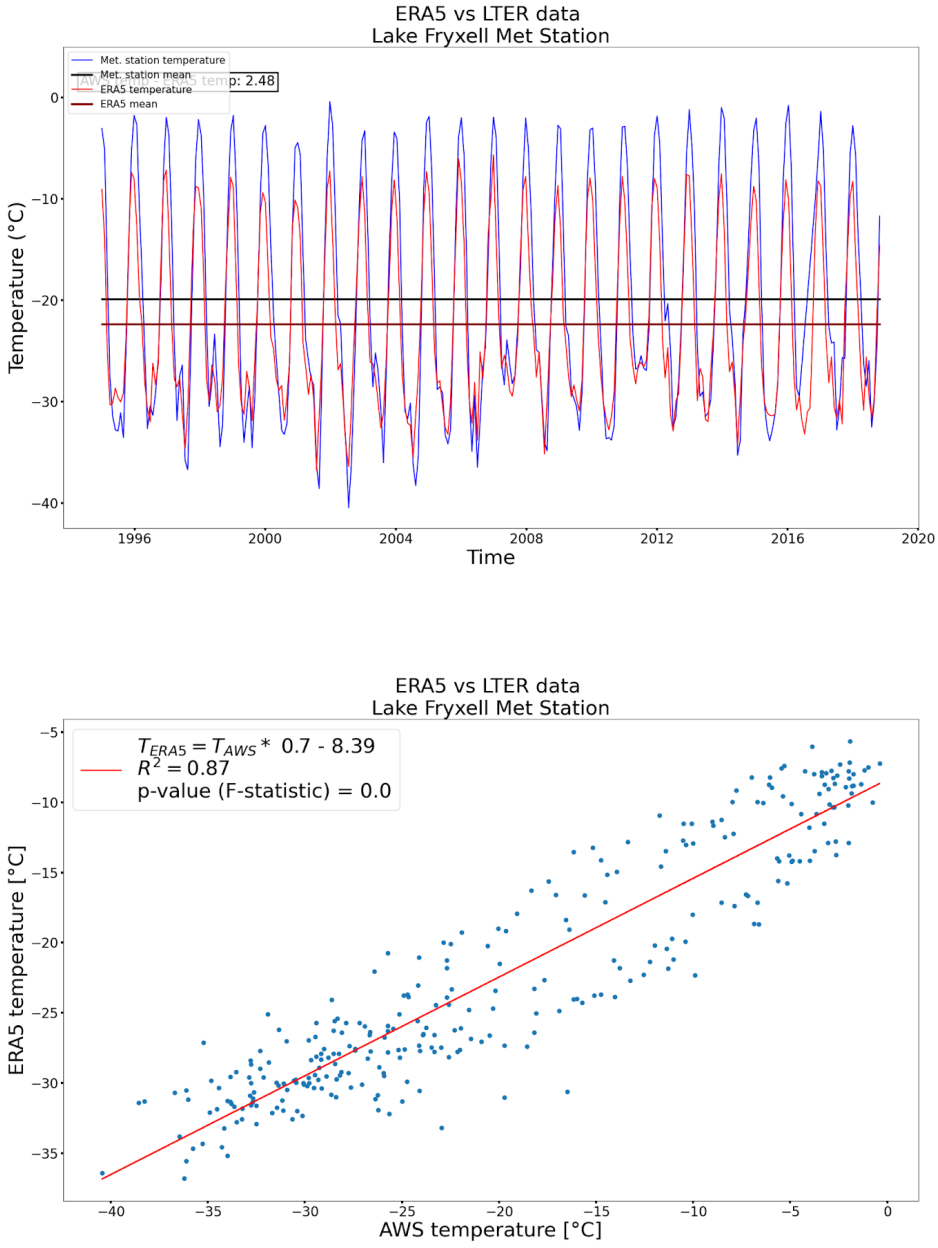

Figure C-8. Lake Fryxell. Top: Time series for station Lake Fryxell (FRLM) (blue) and the values from the closest grid node of the ERA5 reanalysis (red). Bottom: Correlogram.

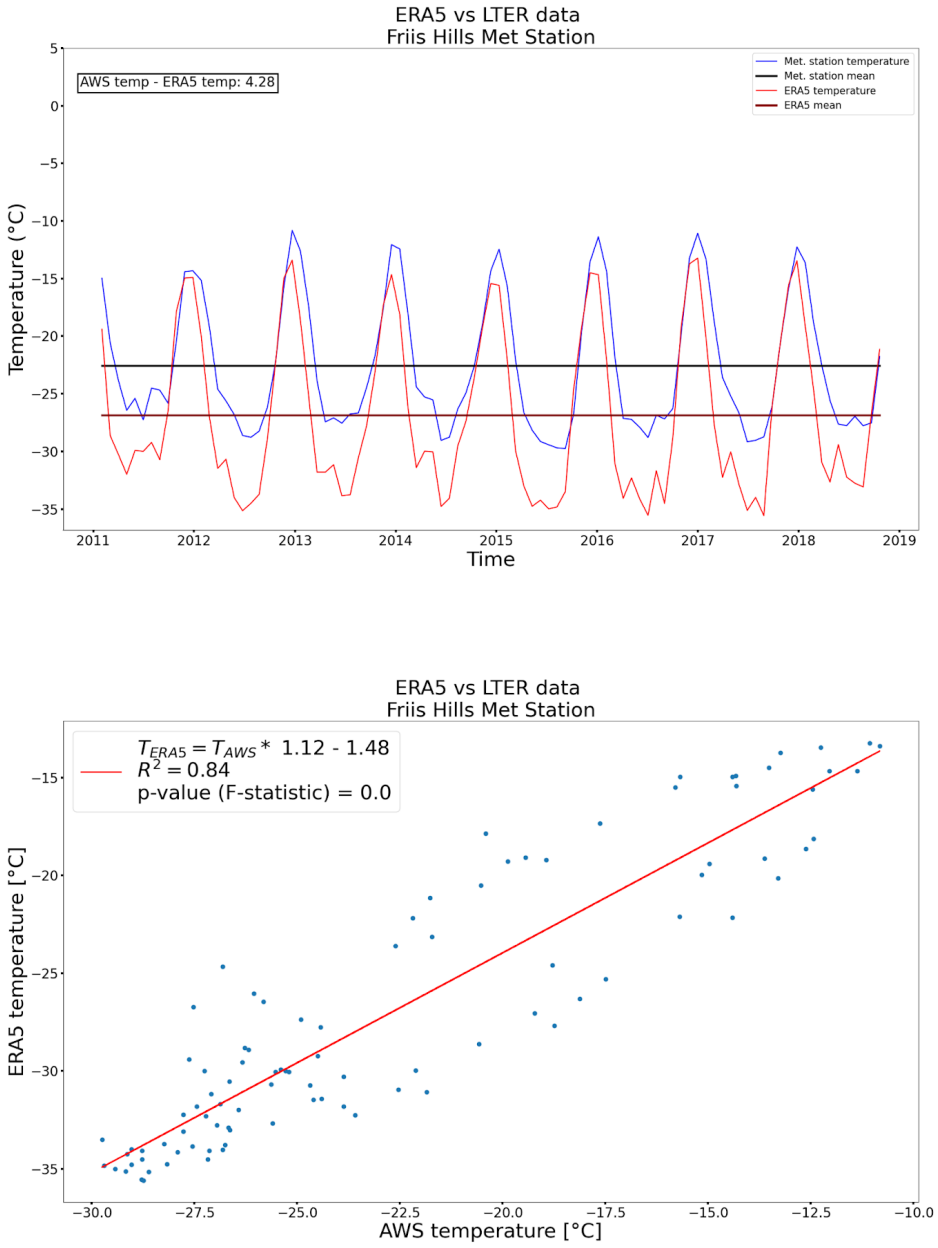

Figure C-9. Friis Hills. Top: Time series for station Friis Hills (FRSM) (blue) and the values from the closest grid node of the ERA5 reanalysis (red). Bottom: Correlogram.

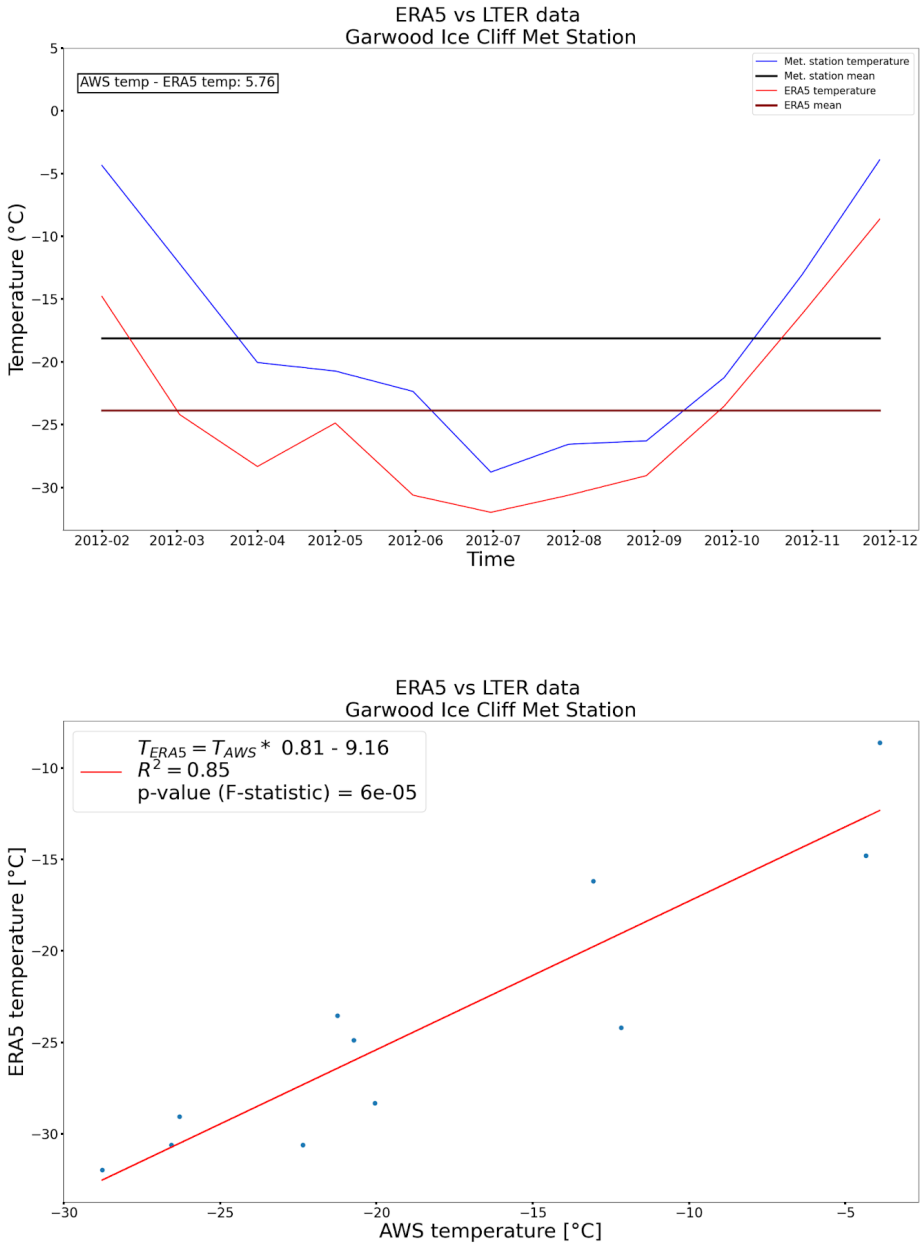

Figure C-10. Garwood Ice Cliff. Top: Time series for station Garwood Ice Cliff (GAFM) (blue) and the values from the closest grid node of the ERA5 reanalysis (red). Bottom: Correlogram.

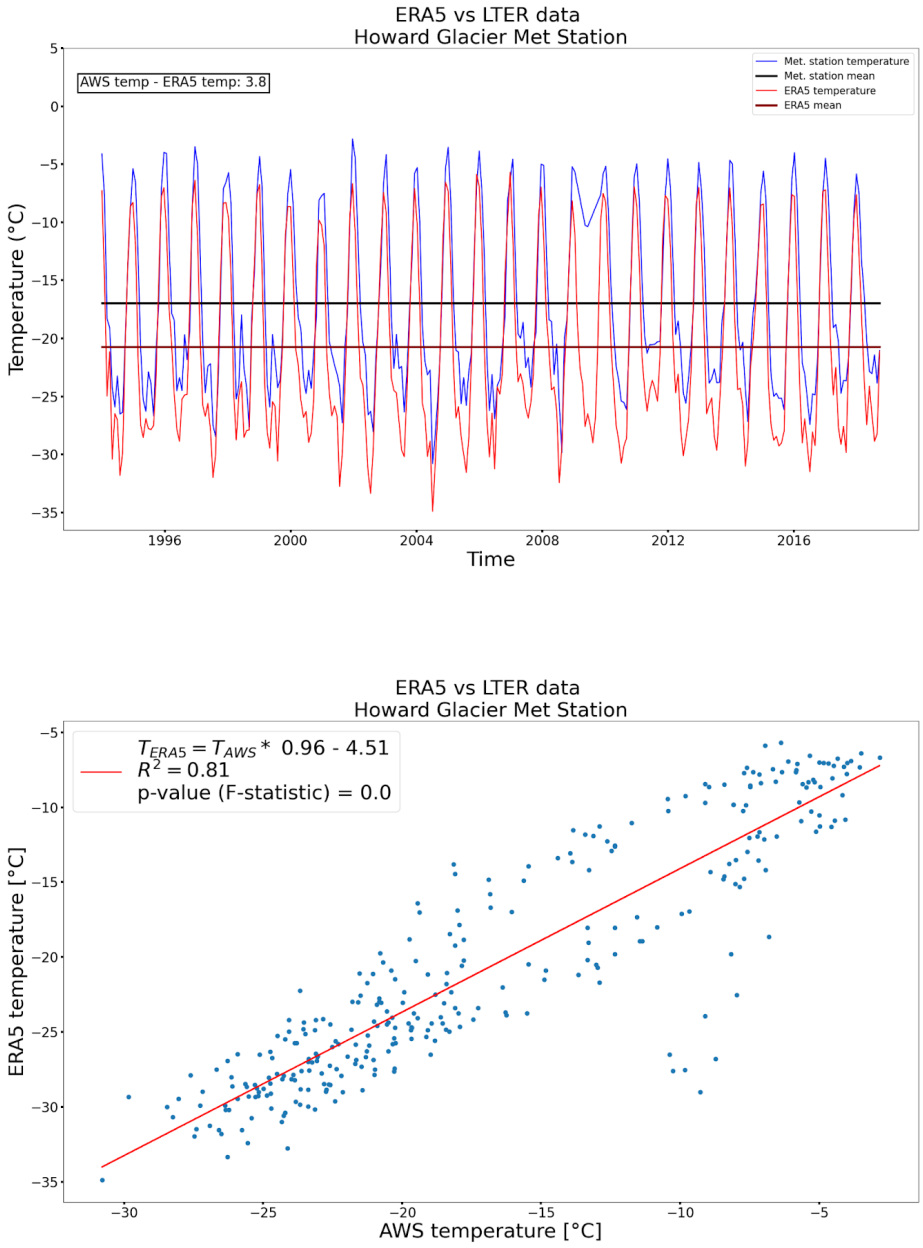

Figure C-11. Howard Glacier. Top: Time series for station Howard Glacier (HODM) (blue) and the values from the closest grid node of the ERA5 reanalysis (red). Bottom: Correlogram.

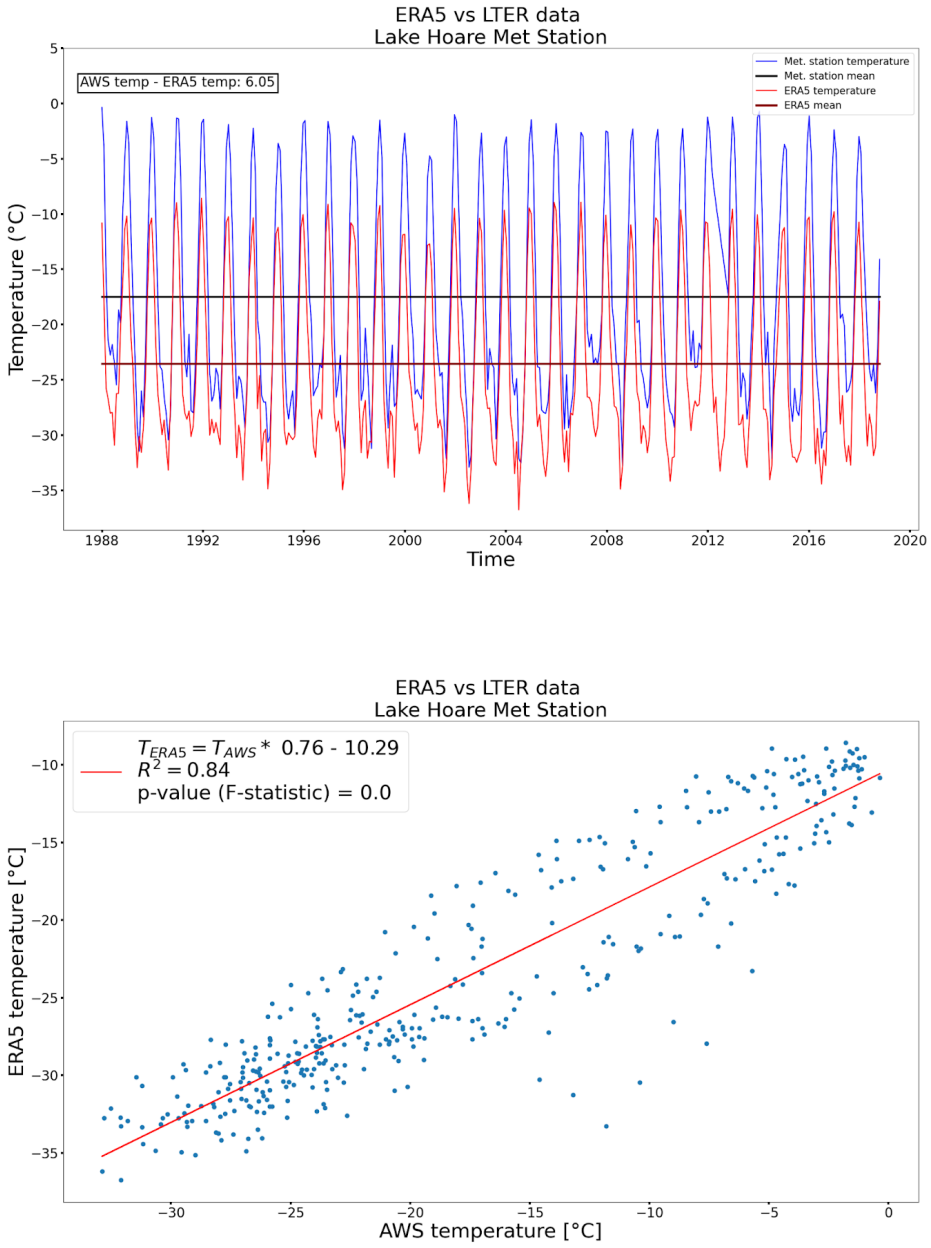

Figure C-12. Lake Hoare. Top: Time series for station Lake Hoare (HOEM) (blue) and the values from the closest grid node of the ERA5 reanalysis (red). Bottom: Correlogram.

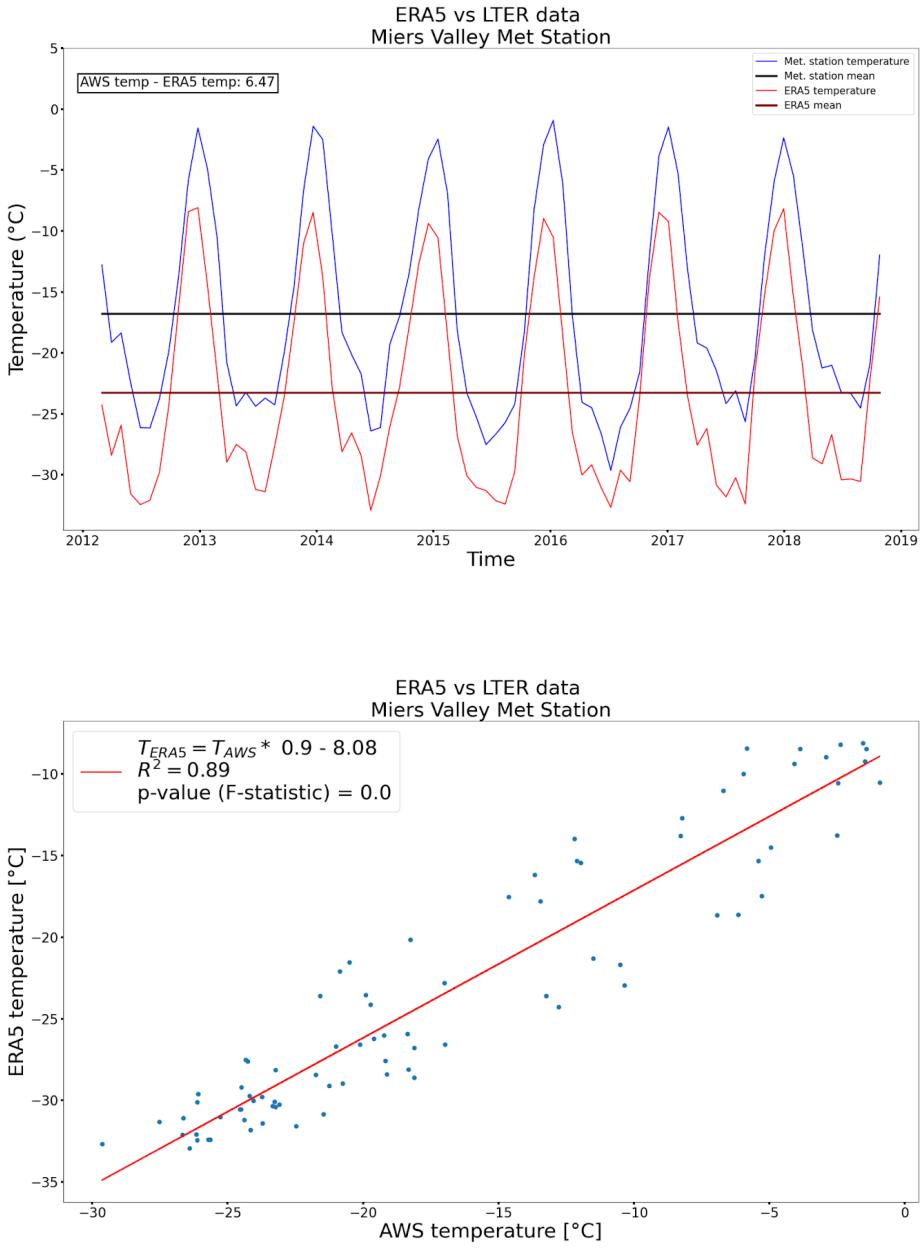

Figure C-13. Miers Valley. Top: Time series for station Miers Valley (MISM) (blue) and the values from the closest grid node of the ERA5 reanalysis (red). Bottom: Correlogram.

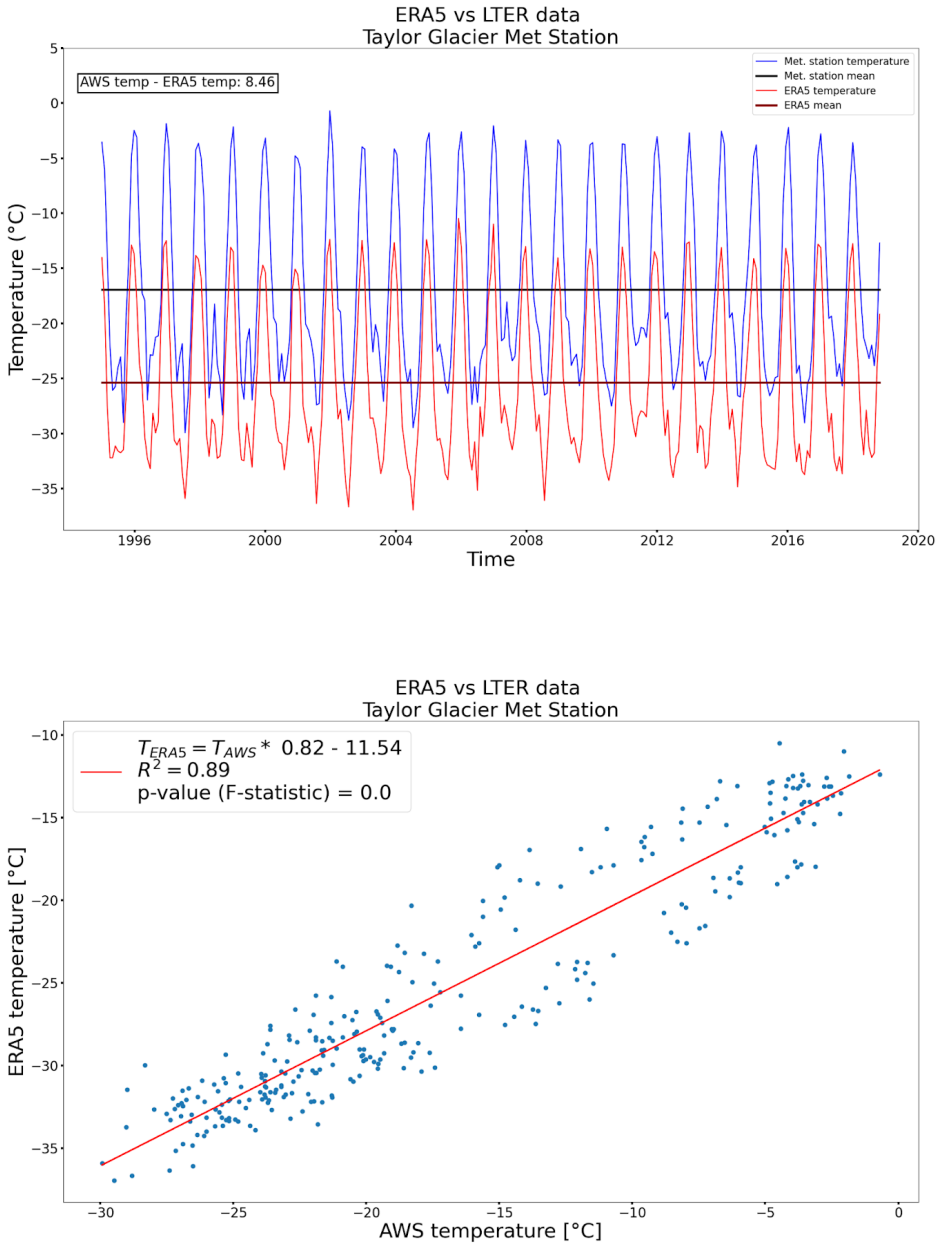

Figure C-14. Taylor Valley. Top: Time series for station Taylor Valley (TARM) (blue) and the values from the closest grid node of the ERA5 reanalysis (red). Bottom: Correlogram.

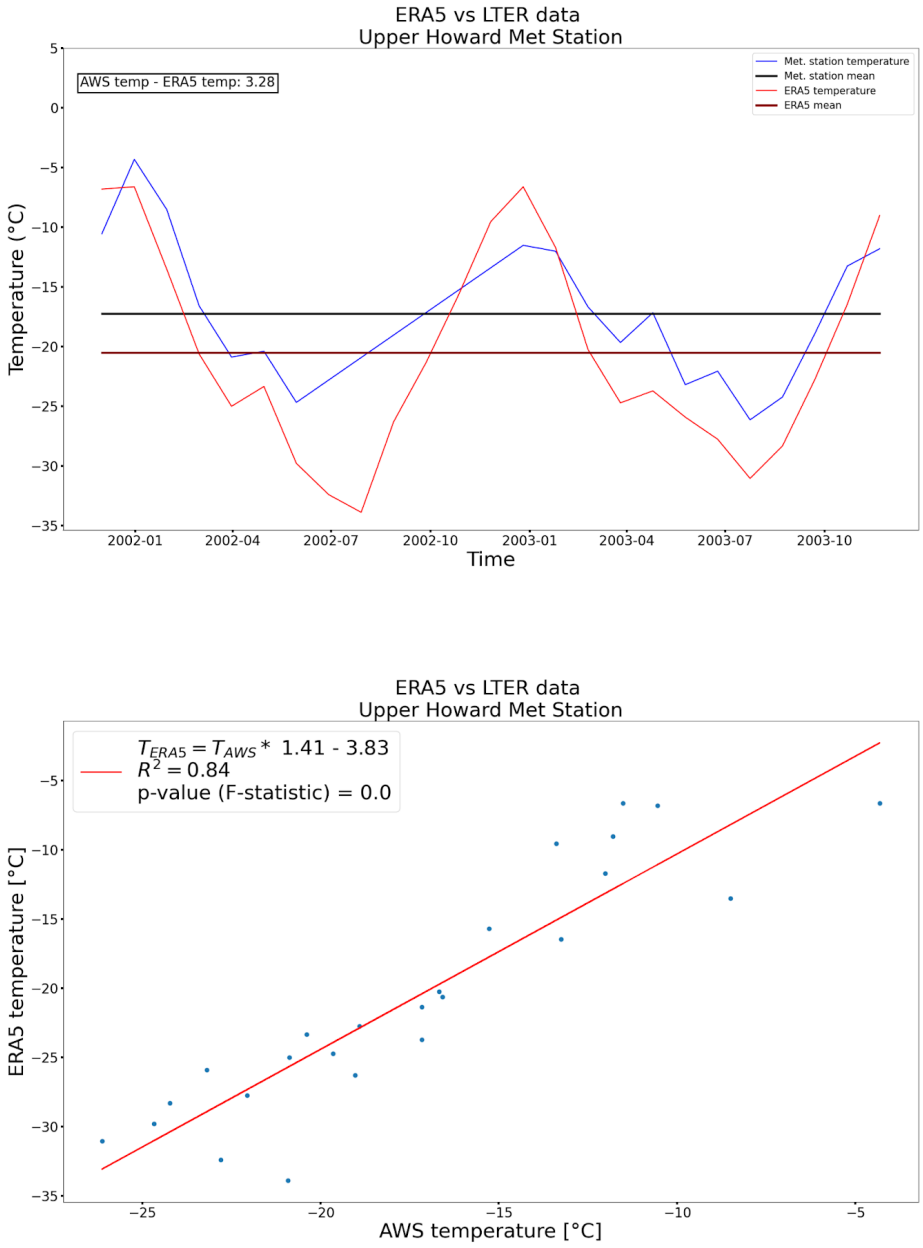

Figure C-15. Upper Howard. Top: Time series for station Upper Howard (UHDM) (blue) and the values from the closest grid node of the ERA5 reanalysis (red). Bottom: Correlogram.

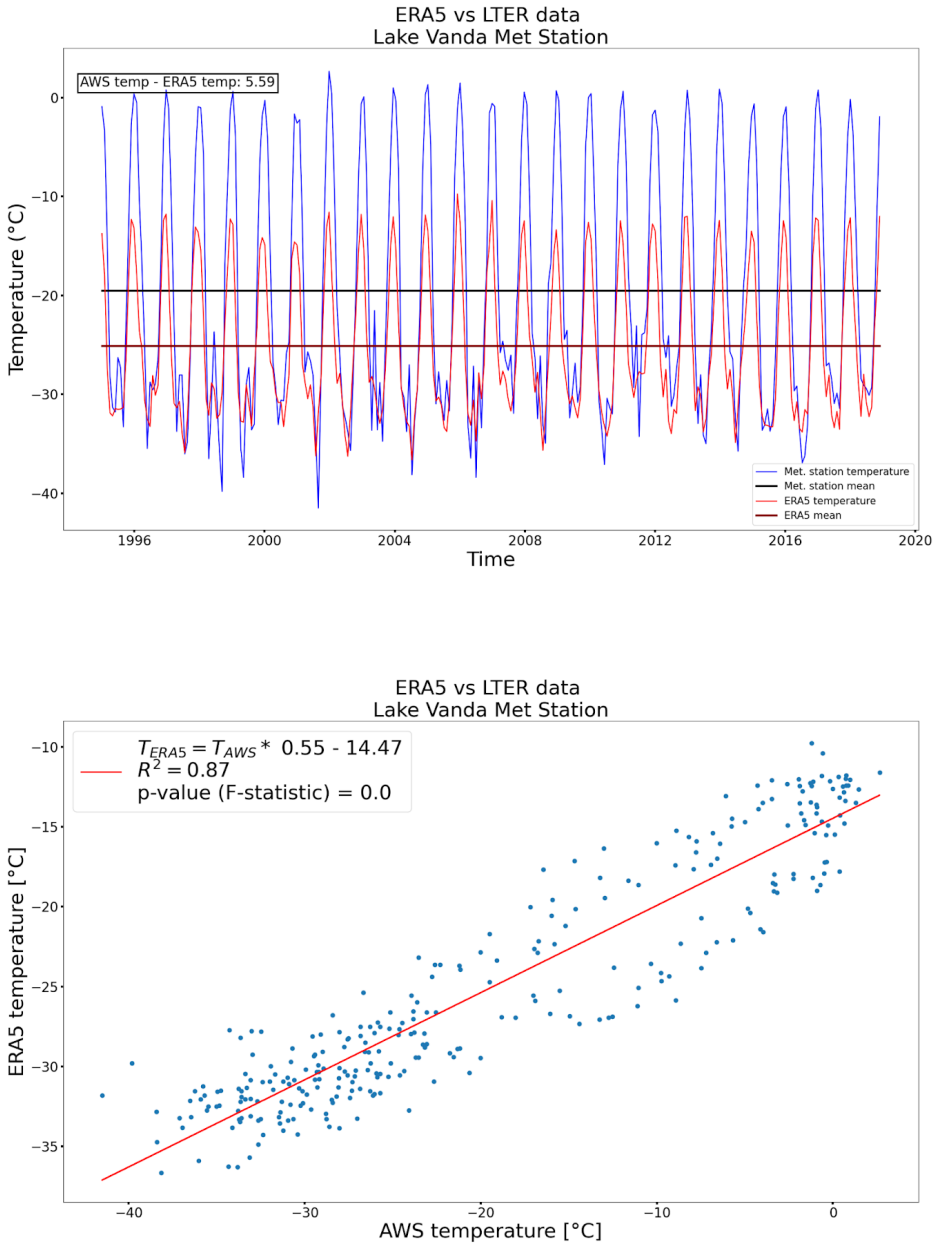

Figure C-16. Lake Vanda. Top: Time series for station Lake Vanda (VAAM) (blue) and the values from the closest grid node of the ERA5 reanalysis (red). Bottom: Correlogram.

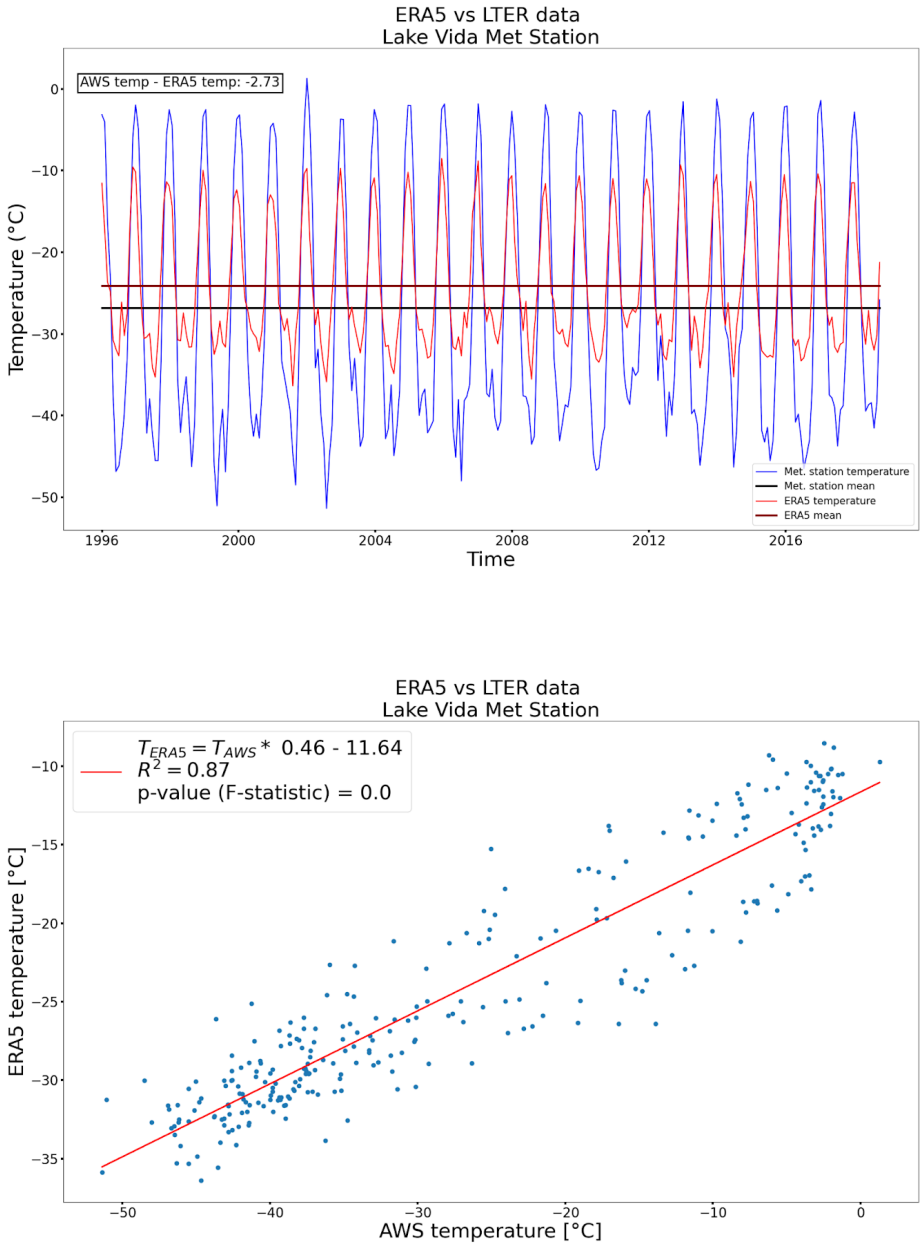

Figure C-17. Lake Vida. Top: Time series for station Lake Vida (VIAM) (blue) and the values from the closest grid node of the ERA5 reanalysis (red). Bottom: Correlogram.

Table C-1. List of available AWS in the McMurdo Sound region and the comparison with the closest node in the grid of the ERA5 reanalysis.

AWS Location name	AWS ID	Latitude	Longitude	Elevation (m.a.s.l.)	Distance to closest ERA5 node (km)	AWS data date range	Average 2m air temperature @ AWS	Average 2m air temperature @ ERA5 node	AWS_{mean_temp}-$ERA5_{mean\_temp}$
Beacon Valley	BENM	-77.828	160.6569	1176.0	3.27	2000-12-11 - 2012-11-19	-21.48 ∓ 0.7	-33.39 ∓ 0.69	11.91 ∓ 1.39
Lake Bonney	BOYM	-77.7147	162.4646	64.0	1.84	1993-12-08 - 2018-10-09	-17.26 ∓ 0.61	-23.85 ∓ 0.43	6.59 ∓ 1.04
Lake Brownworth	BRHM	-77.4344	162.7036	279.0	3.83	1995-01-23 - 2018-11-10	-19.94 ∓ 0.66	-25.28 ∓ 0.52	5.34 ∓ 1.18
Canada Glacier	CAAM	-77.6133	162.9644	264.0	1.71	1994-12-18 - 2011-01-05	-16.36 ∓ 0.72	-22.93 ∓ 0.61	6.57 ∓ 1.33
Commonwealth Glacier	COHM	-77.5646	163.2823	290.0	3.96	1993-12-06 - 2018-10-30	-17.69∓ 0.47	-21.94 ∓ 0.51	4.25 ∓ 0.98
Explorer's Cove	EXEM	-77.5887	163.4175	25.0	1.32	1997-12-05 - 2018-11-23	-18.97 ∓ 0.7	-21.51 ∓ 0.55	2.54 ∓ 1.25
Mt. Fleming	FLMM	-77.5327	160.2714	1870.0	3.7	2011-01-22 - 2018-11-11	-24.2 ∓ 0.58	-33.84 ∓ 0.76	9.65 ∓ 1.34
Lake Fryxell	FRLM	-77.6113	163.1701	19.0	1.45	1994-12-12 - 2018-11-19	-19.78 ∓ 0.7	-22.22 ∓ 0.51	2.44 ∓ 1.21

Friis Hills	FRSM	-77.7474	161.5162	1591.0	5.28	2011-01-04 - 2018-11-06	-22.56 ∓ 0.63	-26.69 ∓ 0.75	4.13 ∓ 1.38
Garwood Ice Cliff	GAFM	-78.0259	164.1315	51.0	2.97	2012-01-24 - 2012-12-19	-16.66 ∓ 2.79	-23.49 ∓ 2.28	6.84 ∓ 5.07
Howard Glacier	HODM	-77.6712	163.0773	472.0	3.25	1993-12-04- 2018-10-31	-17.18 ∓ 0.44	-20.6 ∓ 0.47	3.42 ∓ 0.91
Lake Hoare	HOEM	-77.6254	162.9005	77.0	2.82	1987-11-25 - 2018-11-29	-17.61 ∓ 0.51	-23.53∓ 0.42	5.92 ∓ 0.93
Miers Valley	MISM	-78.1011	163.7877	51.0	0.31	2012-02-11 - 2018-11-06	-16.69 ∓ 0.97	-23.1 ∓ 0.91	6.41 ∓ 1.88
Taylor Glacier	TARM	-77.74	162.1314	334.0	4.51	1994-12-05 - 2018-11-05	-16.9 ∓ 0.5	-25.23 ∓ 0.43	8.34 ∓ 0.93
Upper Howard	UHDM	-77.686	163.145	N/A	1.89	2001-11-28 - 2003-12-24	-16.56 ∓ 1.49	-20.15 ∓ 1.73	3.59 ∓ 3.22
Lake Vanda	VAAM	-77.5257	161.6913	296.0	2.87	1994-12-08 - 2018-12-07	-19.58 ∓ 0.75	-24.96 ∓ 0.44	5.38 ∓ 1.19
Lake Vida	VIAM	-77.3778	161.8007	351.0	2.47	1995-12-08 - 2018-11-14	-26.68 ∓ 0.96	-23.93 ∓ 0.48	-2.74 ∓ 1.44

Resistivity profiles used for the GHF estimation

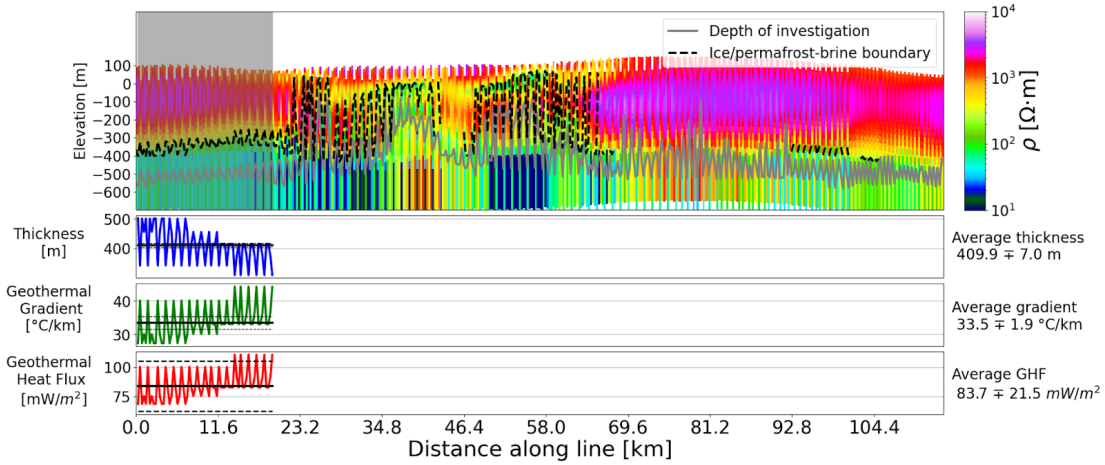

Figure C-18. Resistivity profile at Cape Bernacchi.

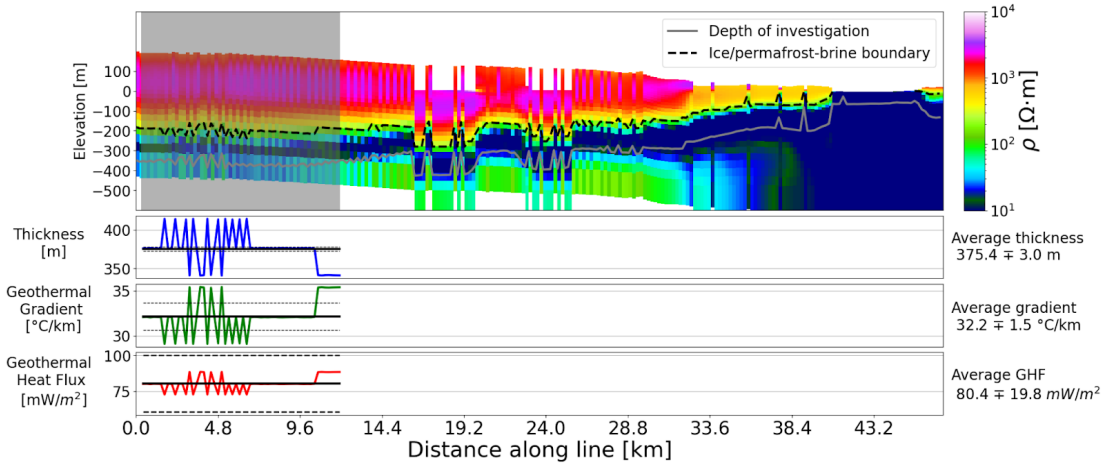

Figure C-19. Resistivity profile at Blue Glacier 1.

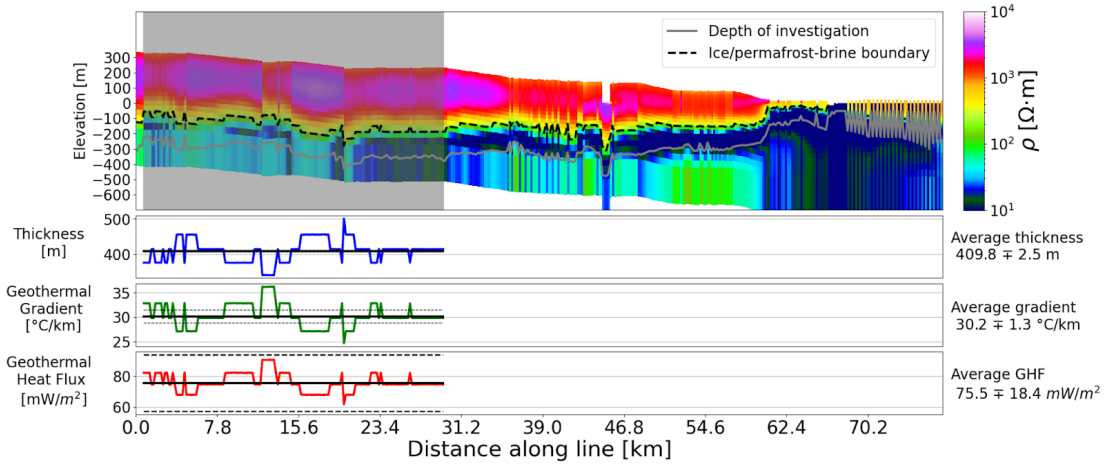

Figure C-20. Resistivity profile at Blue Glacier 2.

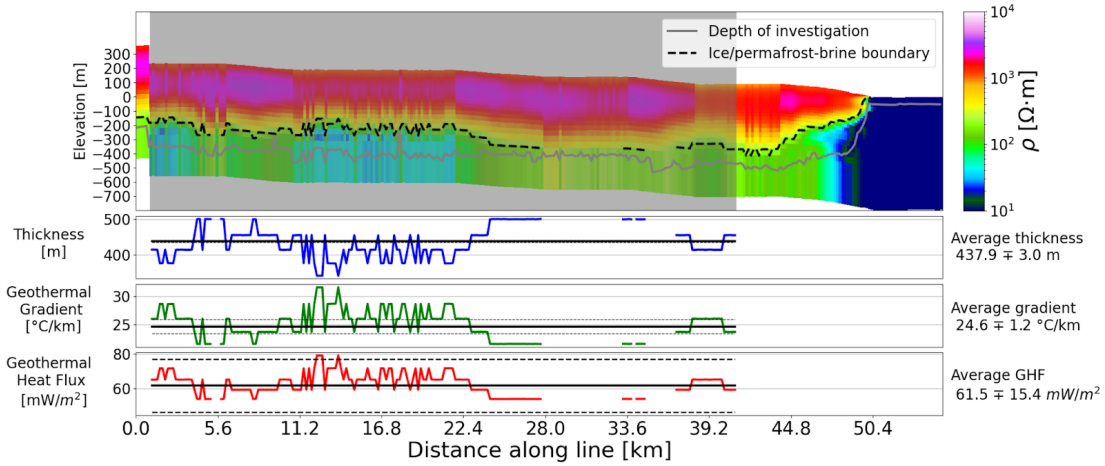

Figure C-21. Resistivity profile at Bowers Glacier 1.

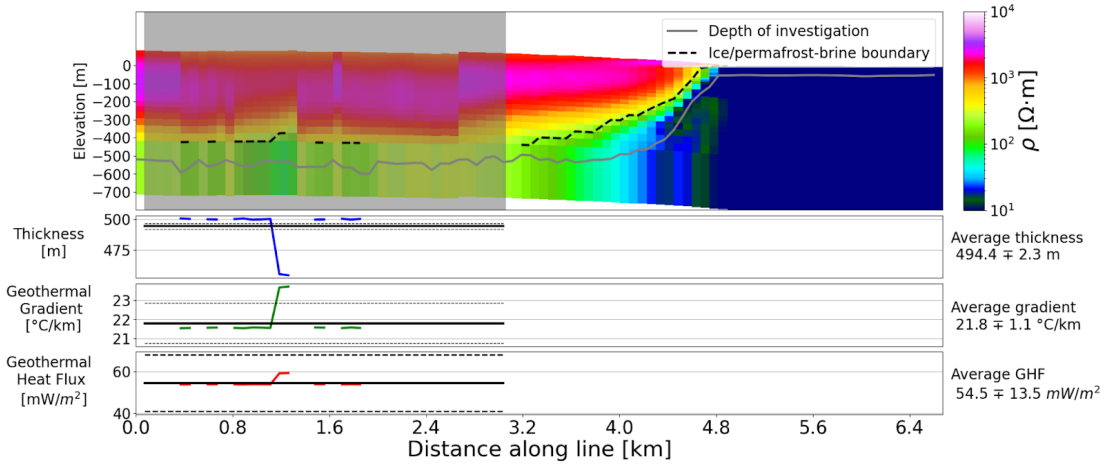

Figure C-22. Resistivity profile at Bowers Glacier 2.

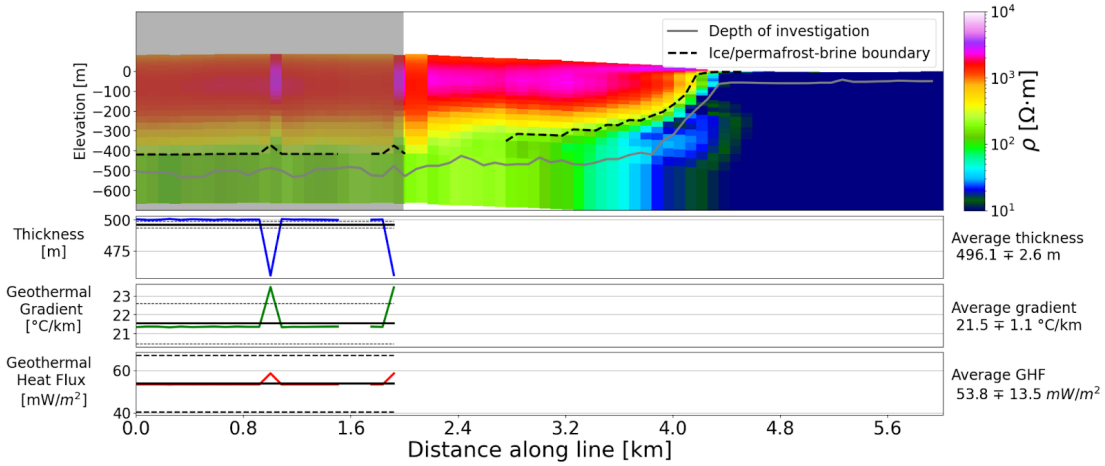

Figure C-23. Resistivity profile at Bowers Glacier 3.

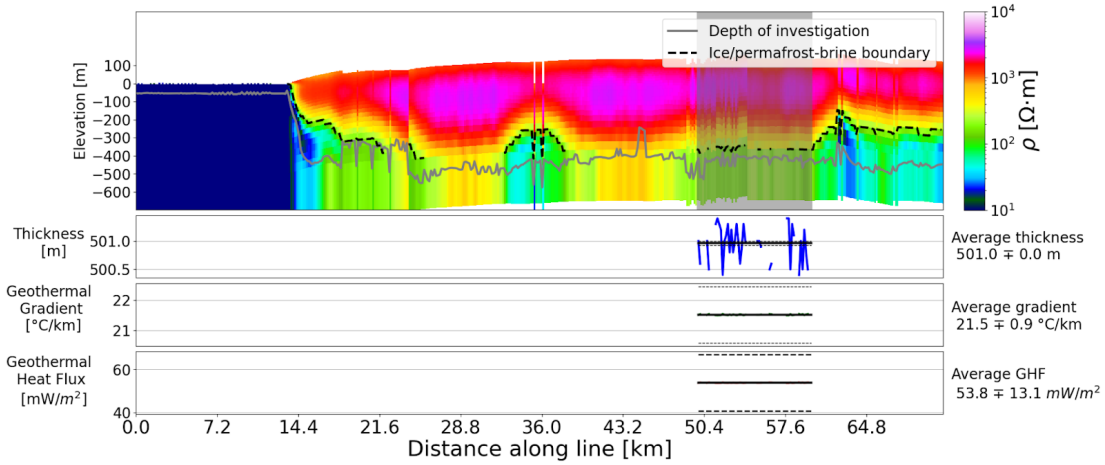

Figure C-24. Resistivity profile at Bowers Glacier 4.

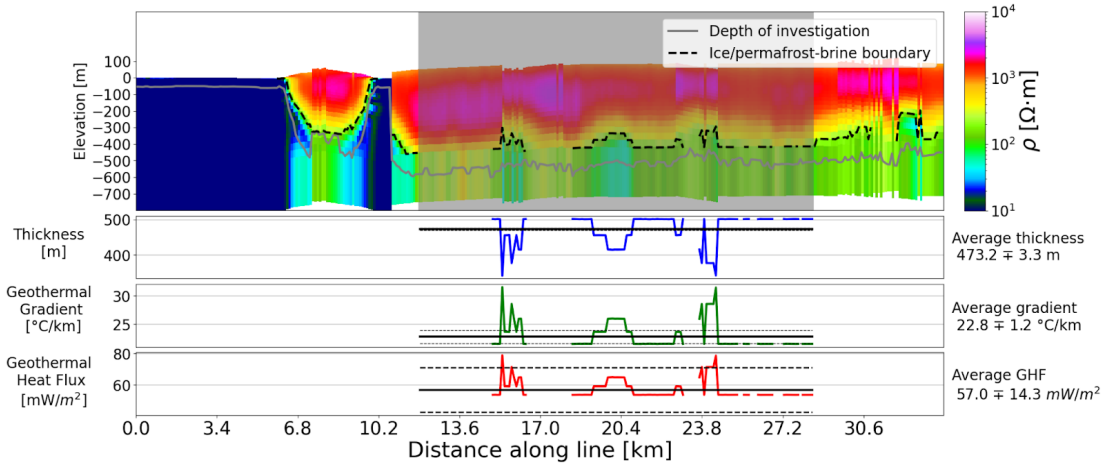

Figure C-25. Resistivity profile at Bowers Glacier 5.

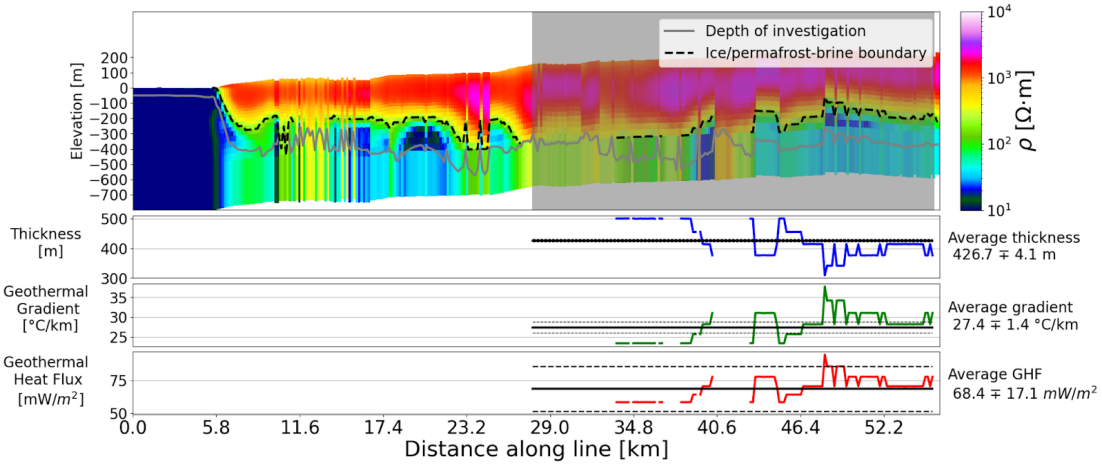

Figure C-26. Resistivity profile at Bowers Glacier 6.

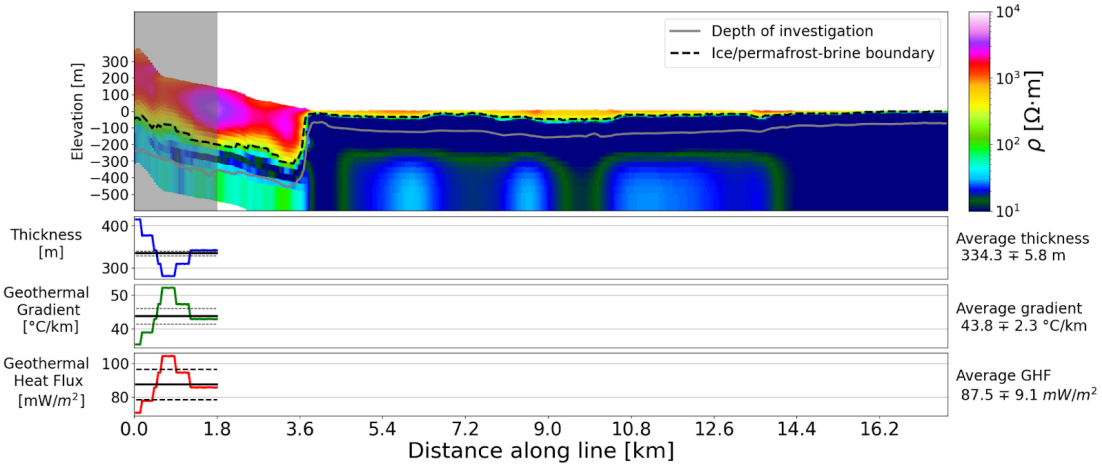

Figure C-27. Resistivity profile at Brown Peninsula 1.

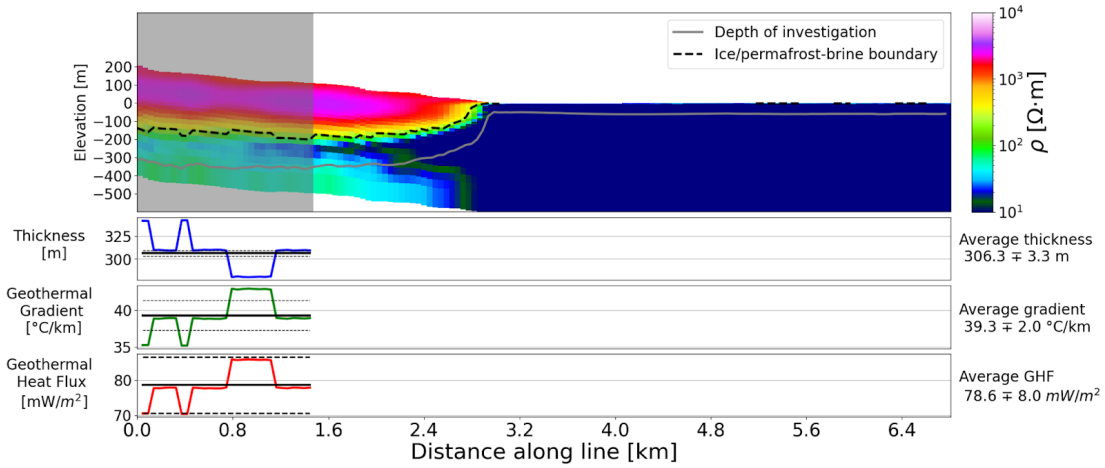

Figure C-28. Resistivity profile at Brown Peninsula 2.

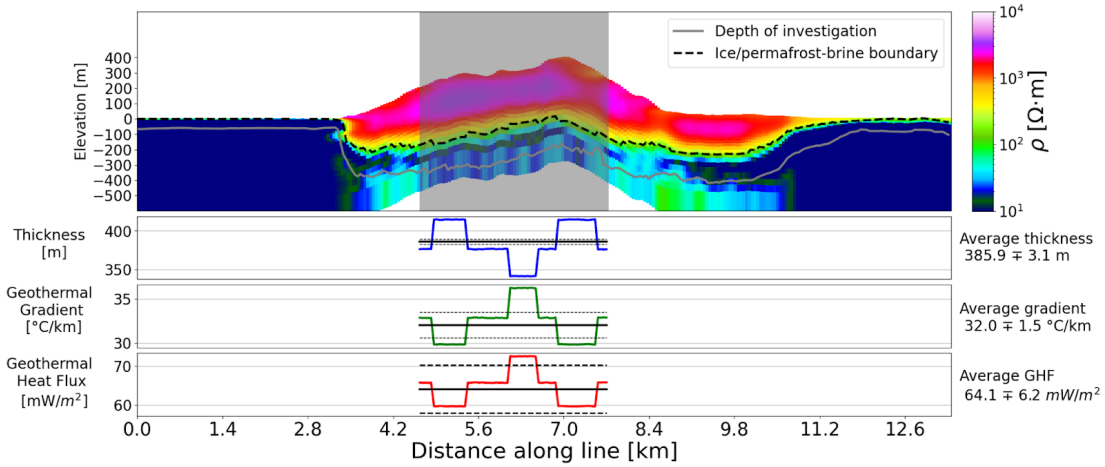

Figure C-29. Resistivity profile at Brown Peninsula 3.

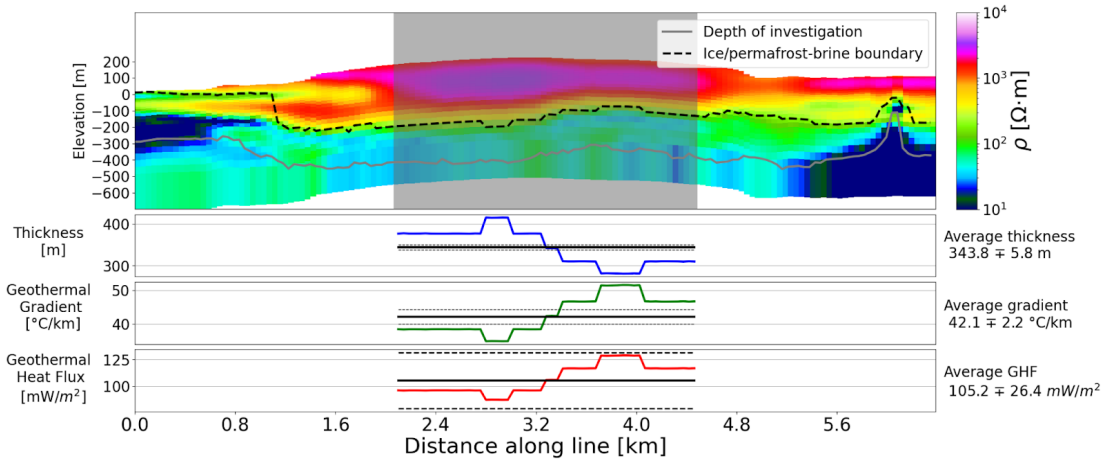

Figure C-30. Resistivity profile at Commonwealth Glacier.

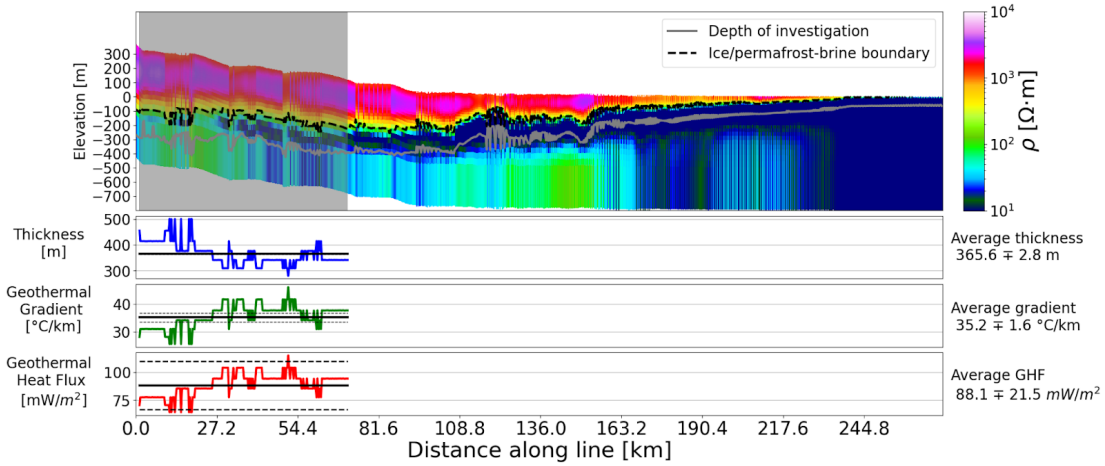

Figure C-31. Resistivity profile at Ferrar Glacier 1.

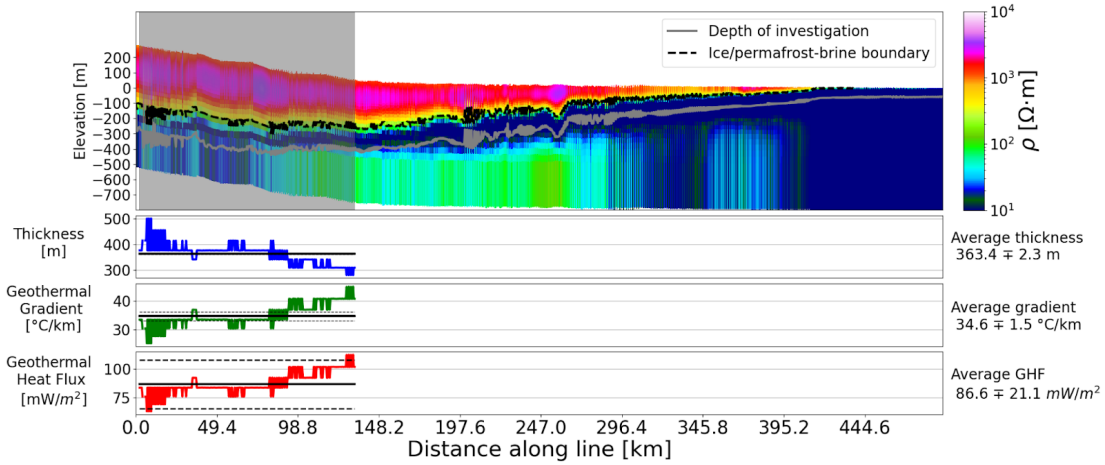

Figure C-32. Resistivity profile at Ferrar Glacier 2.

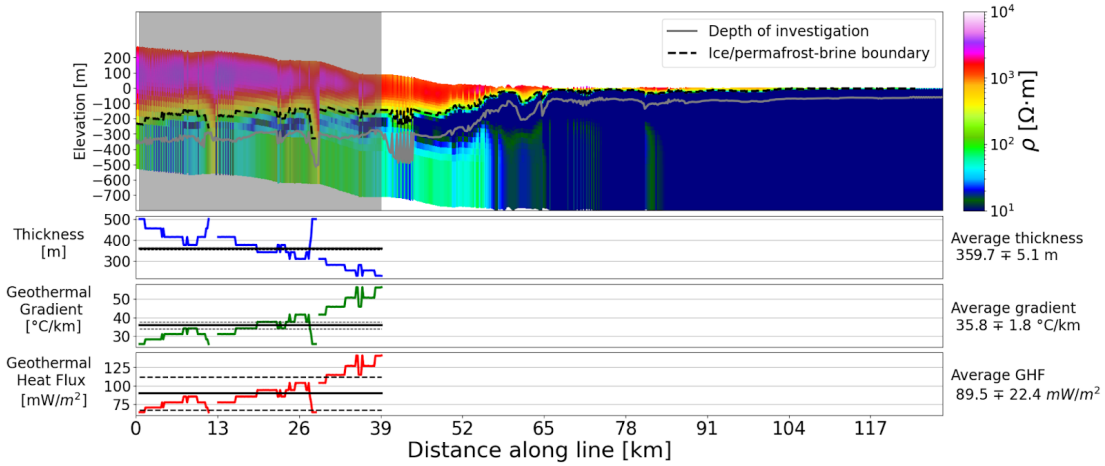

Figure C-33. Resistivity profile at Ferrar Glacier 3.

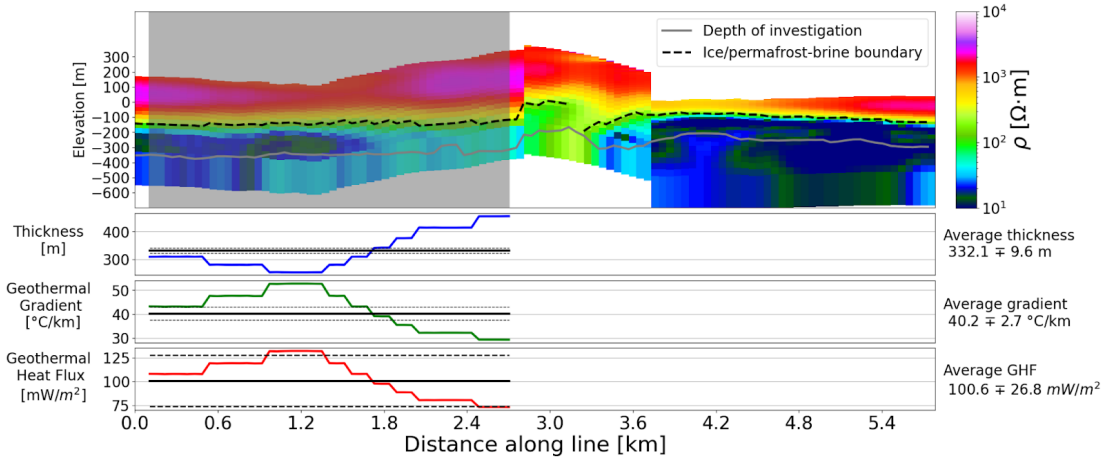

Figure C-34. Resistivity profile at Heald Island.

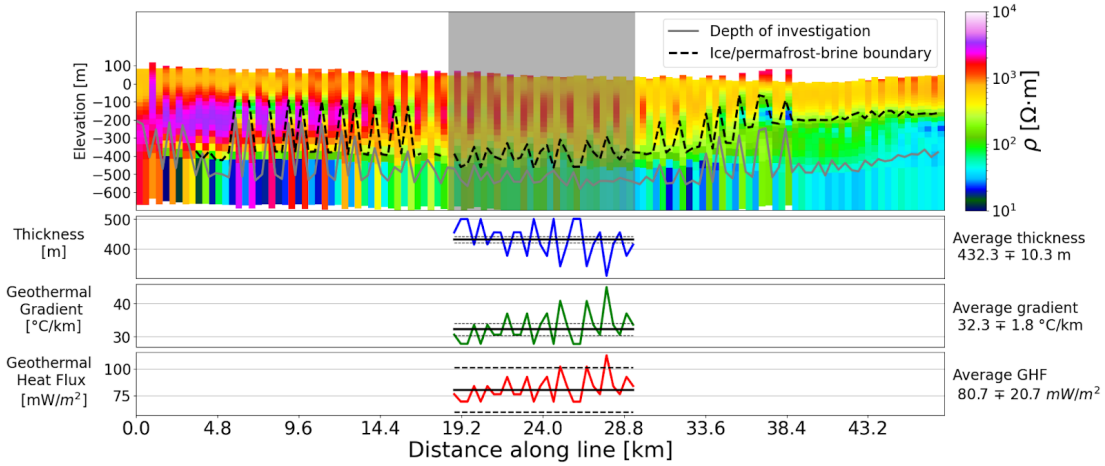

Figure C-35. Resistivity profile at Hobbs Glacier 1.

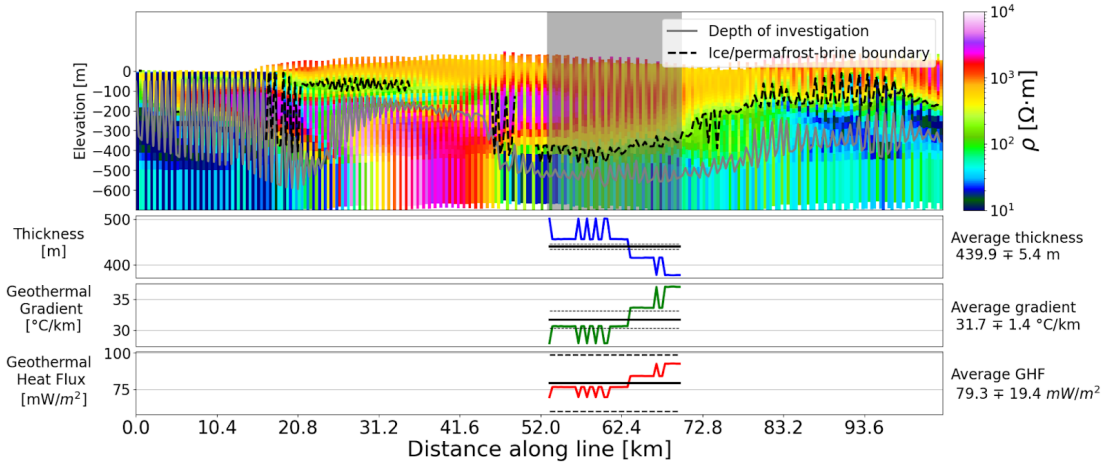

Figure C-36. Resistivity profile at Hobbs Glacier 2.

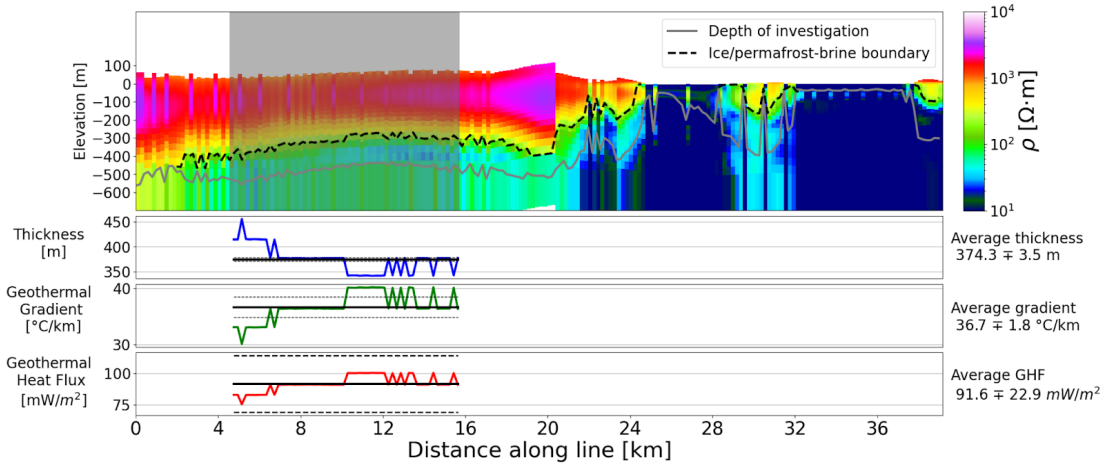

Figure C-37. Resistivity profile at Marble Point 1.

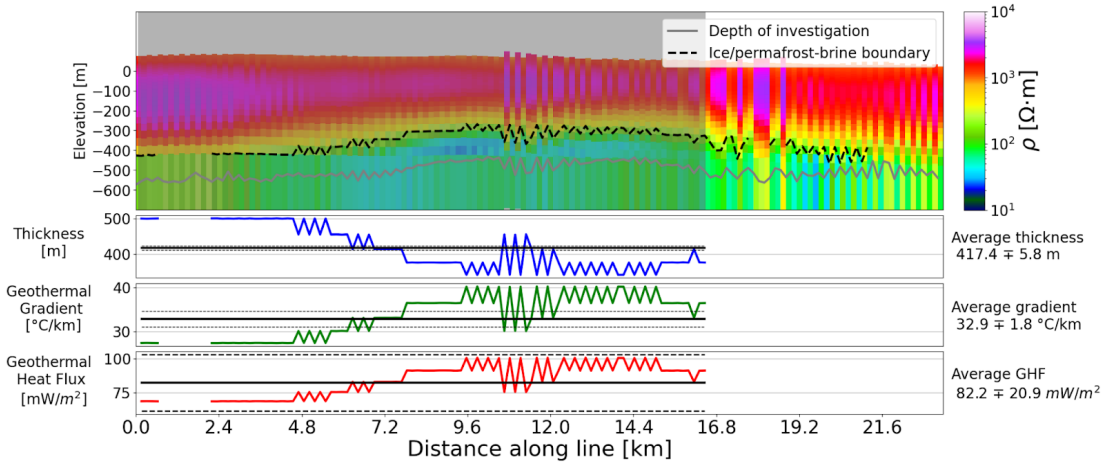

Figure C-38. Resistivity profile at Marble Point 2.

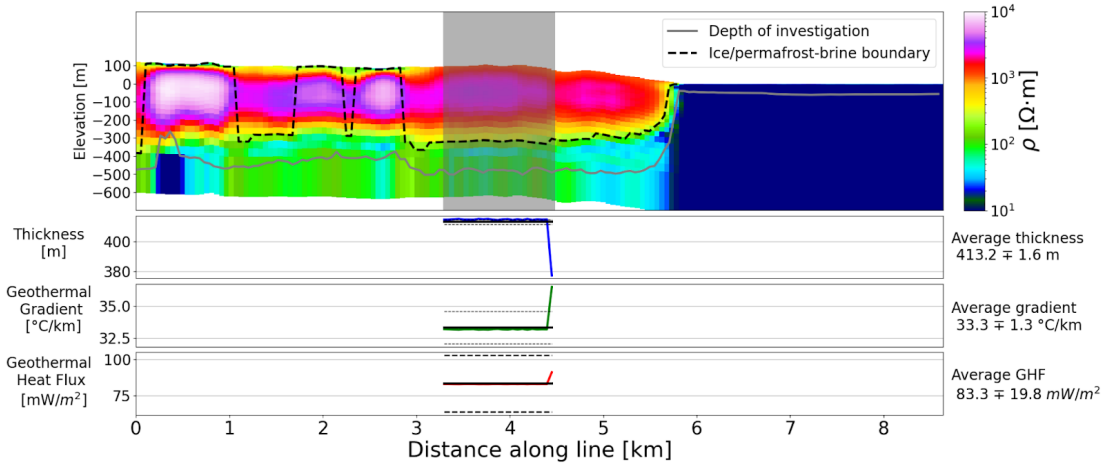

Figure C-39. Resistivity profile at Miers Glacier.

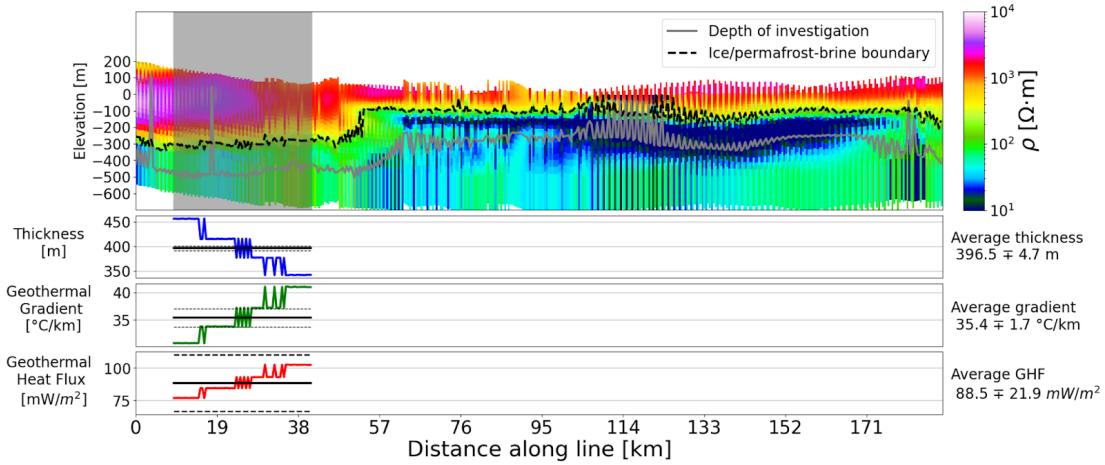

Figure C-40. Resistivity profile at Taylor Valley.

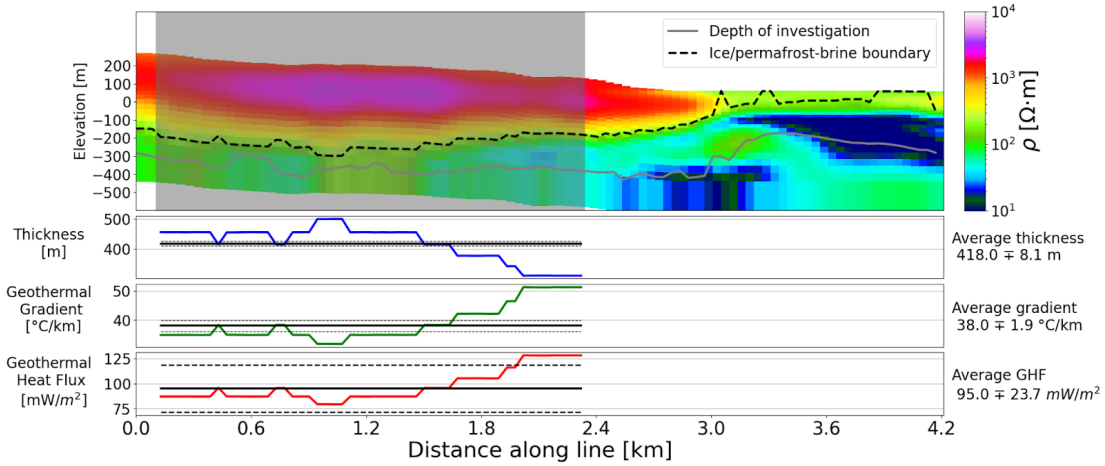

Figure C-41. Resistivity profile at Walcott Glacier.

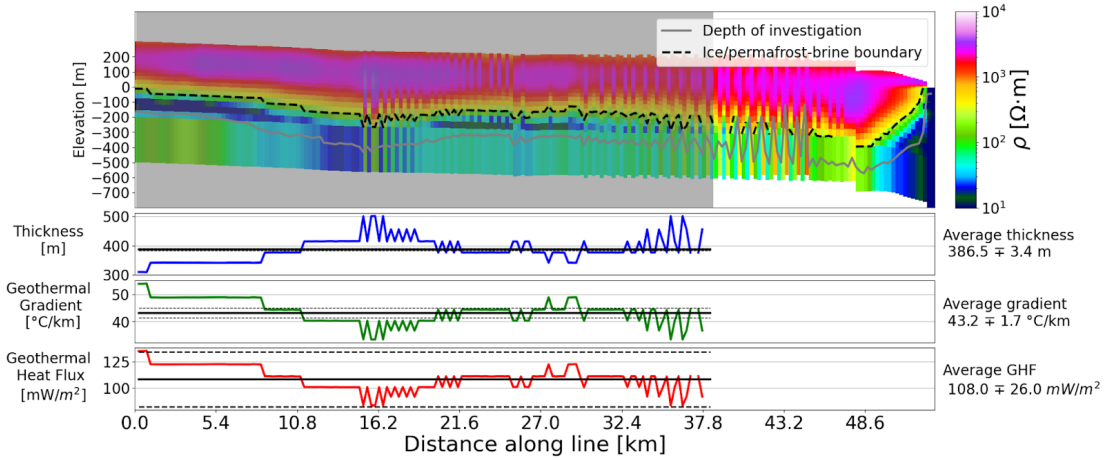

Figure C-42. Resistivity profile at Wilson Glacier 1.

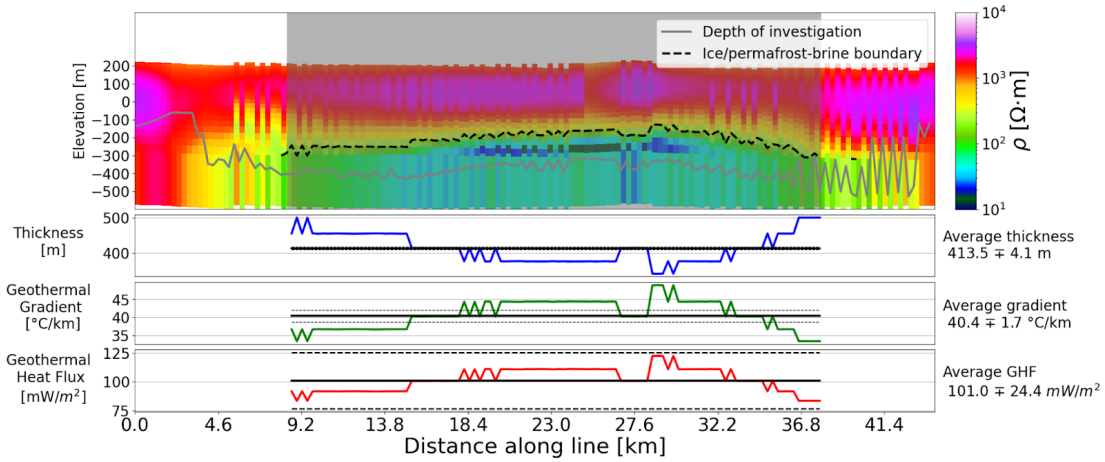

Figure C-43. Resistivity profile at Wilson Glacier 2.

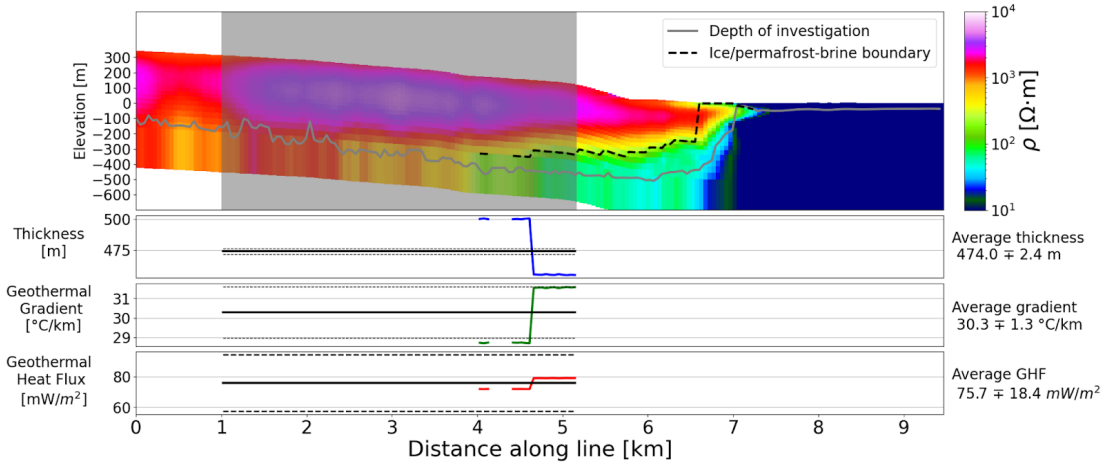

Figure C-44. Resistivity profile at Wilson Glacier 3.

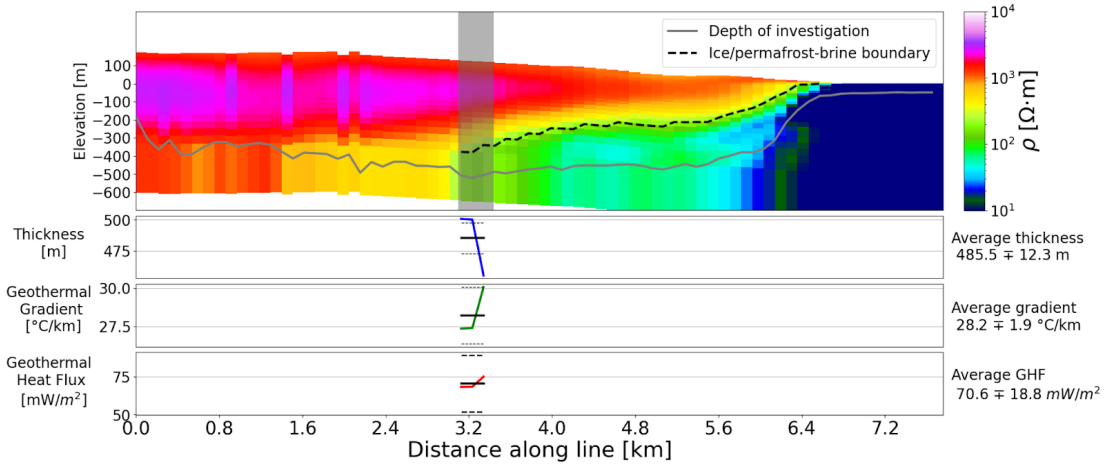

Figure C-45. Resistivity profile at Wilson Glacier 4 (short transect but representative).

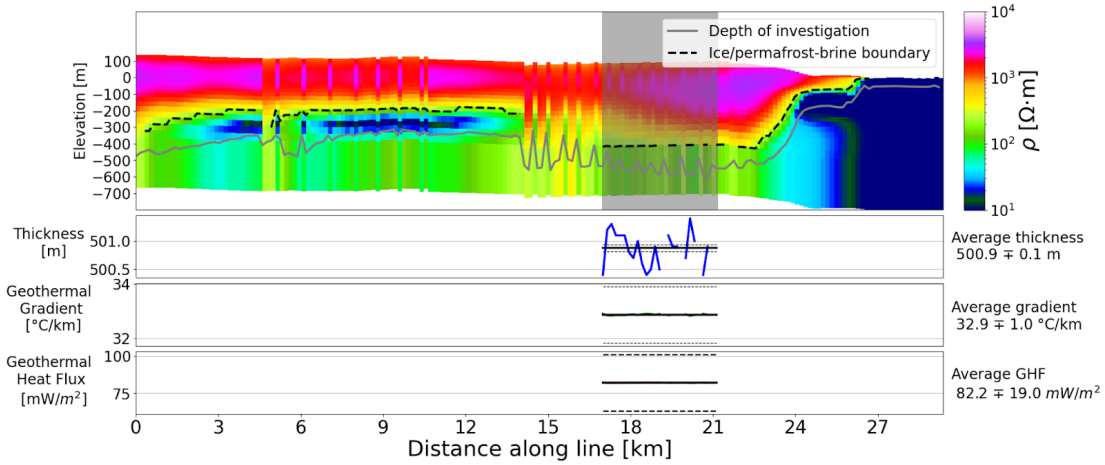

Figure C-46. Resistivity profile at Wilson Glacier 5.

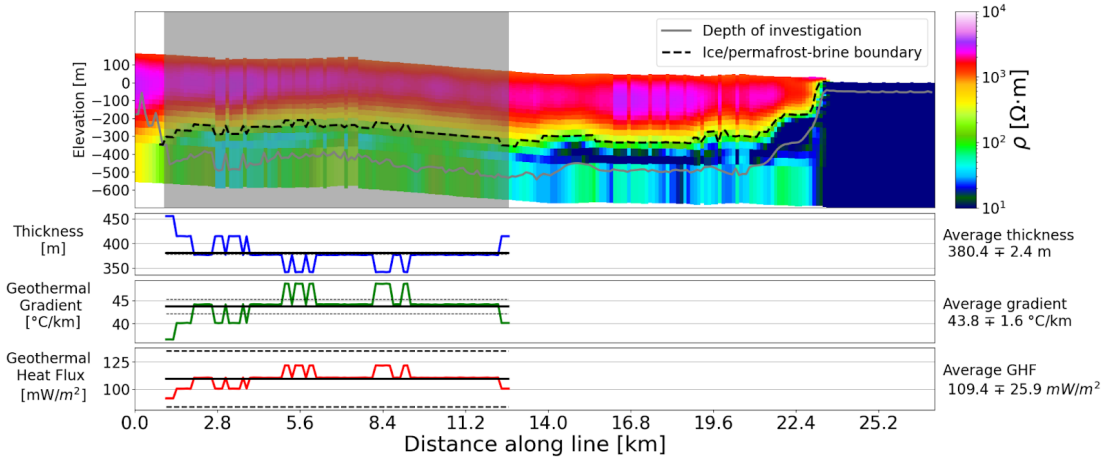

Figure C-47. Resistivity profile at Wilson Glacier 6.

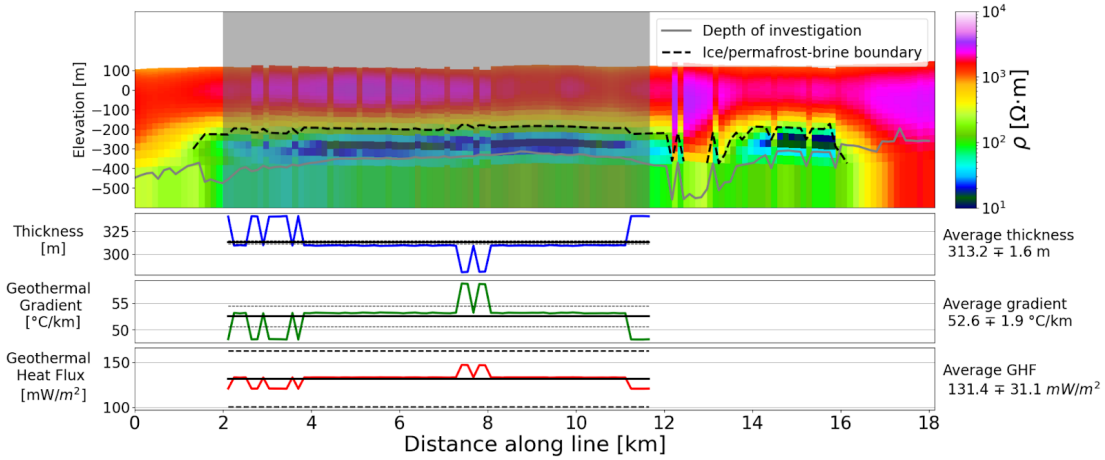

Figure C-48. Resistivity profile at Wilson Glacier 7.

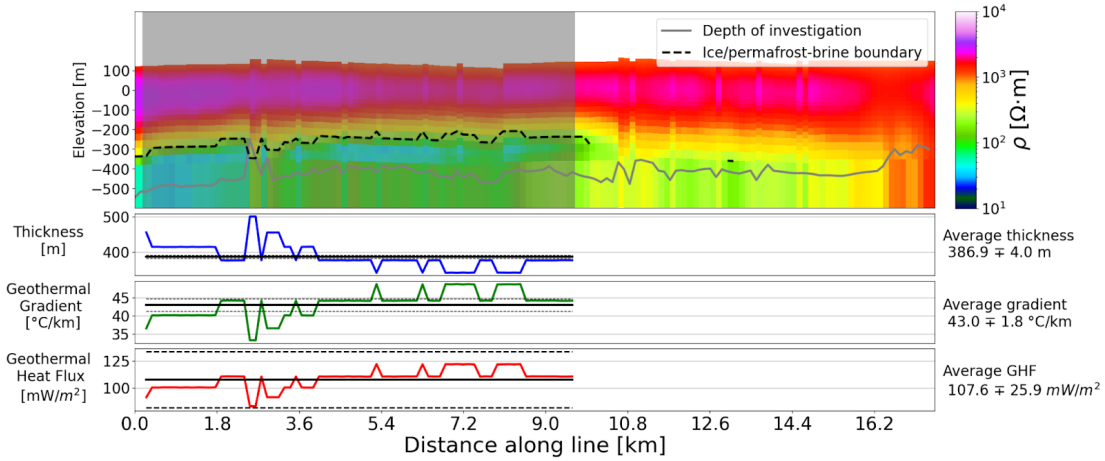

Figure C-49. Resistivity profile at Wilson Glacier 8.

Table C-2. Summary of thermal gradients and geothermal heat-flux calculated in this study and the values from other publications used here.

This study				
Latitude	***Longitude***	***Thermal gradient (°C/km)***	***GHF (mW/m²)***	***Location***
-163.7797543	-77.49087005	33.5∓ 1.9	83.7∓ 21.5	CAPE BERNACCHI
-164.4549238	-77.82949675	32.2∓ 1.5	80.4∓ 19.8	BLUE GLACIER
164.3296818	-77.8043936	30.2∓ 1.3	75.5∓ 18.4	BLUE GLACIER
-164.4069816	-77.75681679	31∓ 1.4	77.4∓ 18.9	BOWERS
-164.2921482	-77.73765425	24.6∓ 1.2	61.5∓ 15.4	BOWERS
-164.3805373	-77.70841186	21.5∓ 1.1	53.8∓ 13.5	BOWERS
164.3432863	-77.6851051	21.8∓ 1.1	54.5∓ 13.5	BOWERS
-164.3075302	-77.68266005	22.8∓ 1.2	57∓ 14.3	BOWERS
-164.2700971	-77.70153712	21.5∓ 0.9	53.8∓ 13.1	BOWERS
-164.1293767	-77.68941807	27.4∓ 1.4	68.4∓ 17.1	BOWERS
-165.7764826	-78.04194998	33.5∓ 1.9	87.5∓ 9.1	BROWN
165.2252592	-78.1112656	32.2∓ 1.5	78.6∓ 8	BROWN
-165.3257409	-78.16655482	30.2∓ 1.3	64.1∓ 6.2	BROWN
-163.3305692	-77.57599282	31∓ 1.4	105.2∓ 26.4	COMMONWEALTH
-163.2153526	-77.74238742	24.6∓ 1.2	88.1∓ 21.5	FERRAR
-163.2680308	-77.72747305	21.5∓ 1.1	86.6∓ 21.1	FERRAR

163.2262725	-77.72254075	21.8∓ 1.1	89.5∓ 22.4	FERRAR
163.8592914	-78.23608384	22.8∓ 1.2	100.6∓ 26.8	HEALD ISLAND
164.5104352	-77.89880659	21.5∓ 0.9	80.7∓ 20.7	HOBBS
164.5240624	-77.90536888	27.4∓ 1.4	79.3∓ 19.4	HOBBS
163.7538959	-77.44011018	43.8∓ 2.3	91.6∓ 22.9	MARBLE POINT
163.701719	-77.44139938	39.3∓ 2	82.2∓ 20.9	MARBLE POINT
164.1626237	-78.1150069	32∓ 1.5	83.3∓ 19.8	MIERS
163.4767162	-77.57872963	42.1∓ 2.2	88.5∓ 21.9	TAYLOR
163.4311747	-78.26061572	35.2∓ 1.6	95∓ 23.7	WALCOTT
163.1674117	-77.16889103	34.6∓ 1.5	131.4∓ 31.1	WILSON
163.0440809	-77.14440043	35.8∓ 1.8	107.6∓ 25.9	WILSON
163.439052	-77.39630174	40.2∓ 2.7	108∓ 26	WILSON
163.432771	-77.38810841	32.3∓ 1.8	101∓ 24.4	WILSON
163.4347485	-77.31658691	31.7∓ 1.4	75.7∓ 18.4	WILSON
163.4804952	-77.28439253	36.7∓ 1.8	70.6∓ 18.8	WILSON
163.2142339	-77.15926726	32.9∓ 1.8	82.2∓ 19	WILSON
163.1237556	-77.13561372	33.3∓ 1.3	109.4∓ 25.9	WILSON
167.163	-77.5285	35.4∓ 1.7	164 ∓16.4	EREBUS

Other studies				
Latitude	**Longitude**	**Thermal gradient (°C/km)**	**GHF (mW/m^2)**	**Reference**
166.68	-77.83	79.7 ∓ 18	164 ∓ 18	Risk and Hochstein (1974)
161.81	-77.38	31 ∓ 3.1	79 ∓ 7.9	Decker and Bücher (1982)
163.64	-77	28.5 ∓ 2.8	60 ∓ 6.0	Bücker et al. (2001)
164.5	-77.58	40 ∓ 4.0	80 ∓ 8.0	White (1989)
167.09	-77.89	76.7 ∓ 7.6	115 ∓ 11.5	Morin et al. (2010)
166.5	-77.58	45 ∓ 13	90 ∓ 13	Foley et al. (2020)

Appendix D – Supplemental Information for Chapter 4

Table D-1. Summary of data and results for the comparison between the 1968 earthquake recorded by the WWSSN network and the 2018 earthquake recorded in modern stations.

WWSSN station code	WWSSN station name/location	Latitude [deg]	Longitude [deg]	Modern station code	Modern station name/location	$Latitude_{MOD}$ [deg]	$Longitude_{MOD}$ [deg]	Distance between stations [km]	WWSSN magnification	Length of trace [seconds]	Cross-correlation coefficient
AAE	Addis Ababa, Ethiopia	9.03	38.77	FURI	Mount Furi, Ethiopia	8.9	38.68	17	1500	360.5	0.95
ATU	Athens, Greece	37.97	23.72	ATHU	Athens University, Greece	37.97	23.78	5	1500	586.5	0.93
COP	Copenhagen, Denmark	55.68	12.43	RGN	Ruegen, Germany	54.55	13.32	137	750	348.5	0.77
HNR	Honiara, Solomon Islands	-9.43	159.95	HNR	Honiara, Solomon Islands	-9.43	159.95	0	1500	684	0.86
KBL	Kabul, Afghanistan	34.54	69.04	KBL	Kabul, Afghanistan	34.54	69.04	0	6000	222	0.99
LPA	La Plata, Argentina	-34.91	-57.93	TRQA	Tornquist, Argentina	-38.06	-61.98	503	750	174	0.9
NUR	Nurmijarvi, Finland	60.51	24.65	MEF	Metsahovi, Finland	60.2	24.4	35	1500	220	0.97
SBA	Scott Base, Antarctica	-77.85	166.76	SBA	Scott Base, Antarctica	-77.85	166.76	0	750	442.5	0.97
SDB	Sa Da Bandeira, Angola	-14.93	13.57	TSUM	Tsumeb, Namibia	-19.2	17.58	637	1500	223	0.95
WEL	Wellington, New Zealand	-41.29	174.77	SNZO	South Karori, New Zealand	-41.31	174.7	6	750	305	0.9

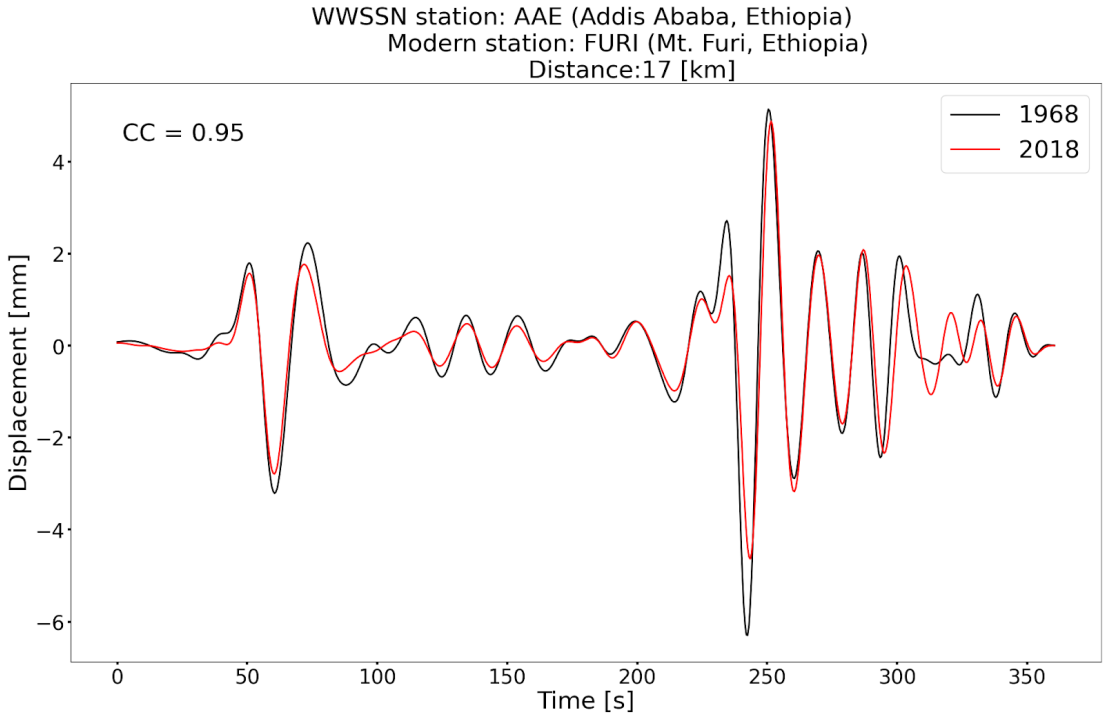

Figure D-1. 1968 earthquake recorded at the WWSSN Addis Ababa, Ethiopia station (AAE) (black) and the vertical component for the 2018 Pinotepa event (red) recorded at Mount Furi, Ethiopia (FURI), after conversion to WWSSN instrument response.

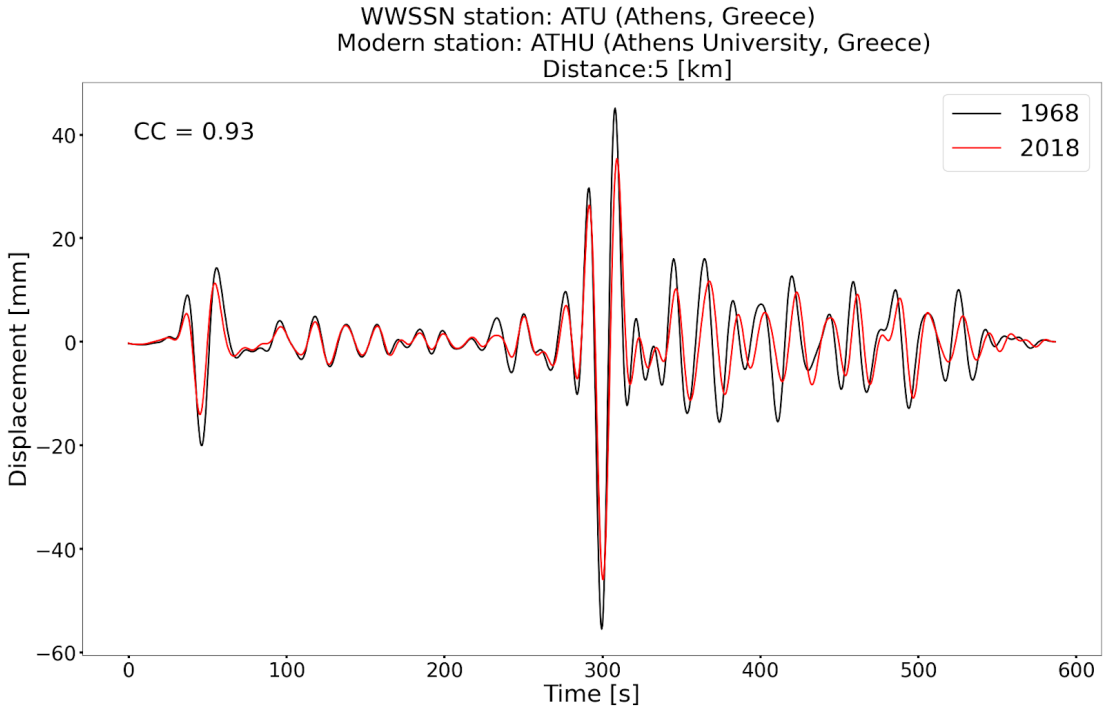

Figure D-2. 1968 earthquake recorded at the WWSSN Athens, Greece station (ATU) (black) and the vertical component for the 2018 Pinotepa event (red) recorded at Athens University, Greece (ATHU), after conversion to WWSSN instrument response.

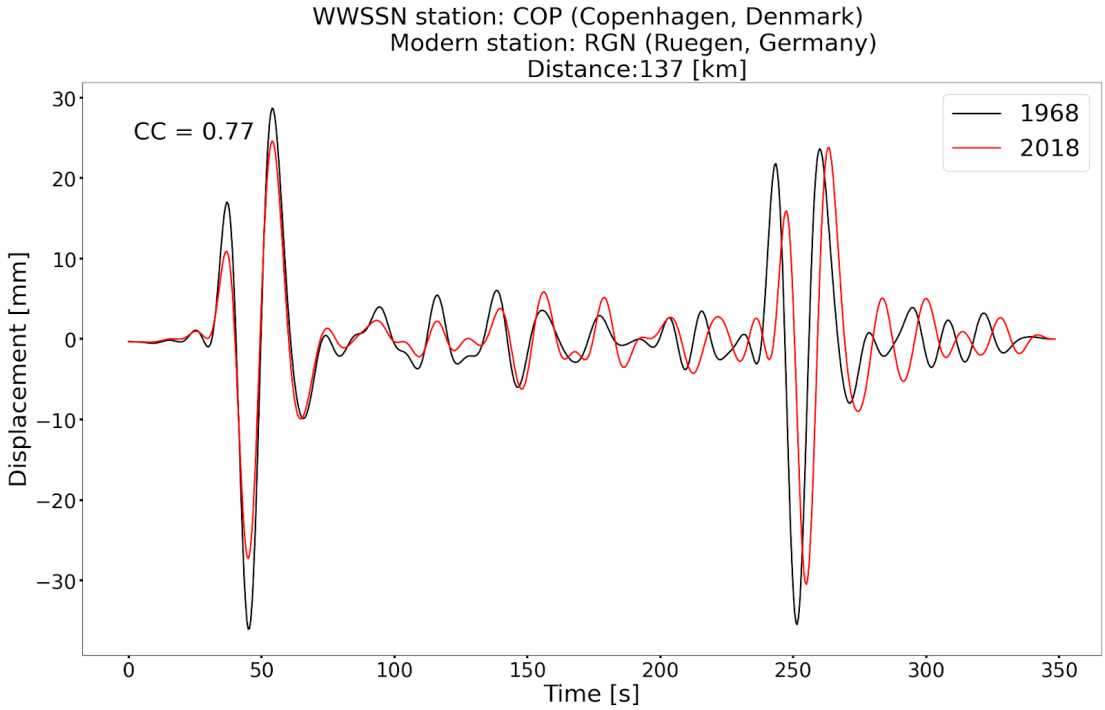

Figure D-3. 1968 earthquake recorded at the WWSSN Copenhagen, Denmark (COP) (black) and the vertical component for the 2018 Pinotepa event (red) recorded at Ruegen, Germany (RGN), after conversion to WWSSN instrument response.

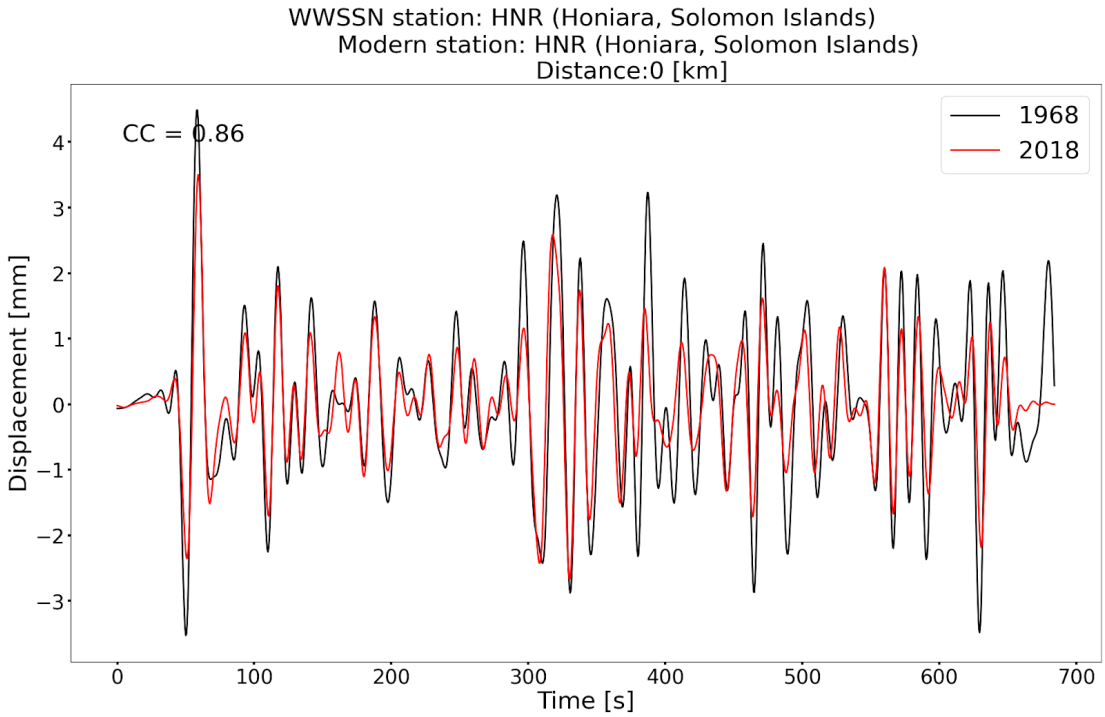

Figure D-4. 1968 earthquake recorded at the WWSSN Honiara, Solomon Islands station (HNR) (black) and the vertical component for the 2018 Pinotepa event (red) recorded at the same location, after conversion to WWSSN instrument response.

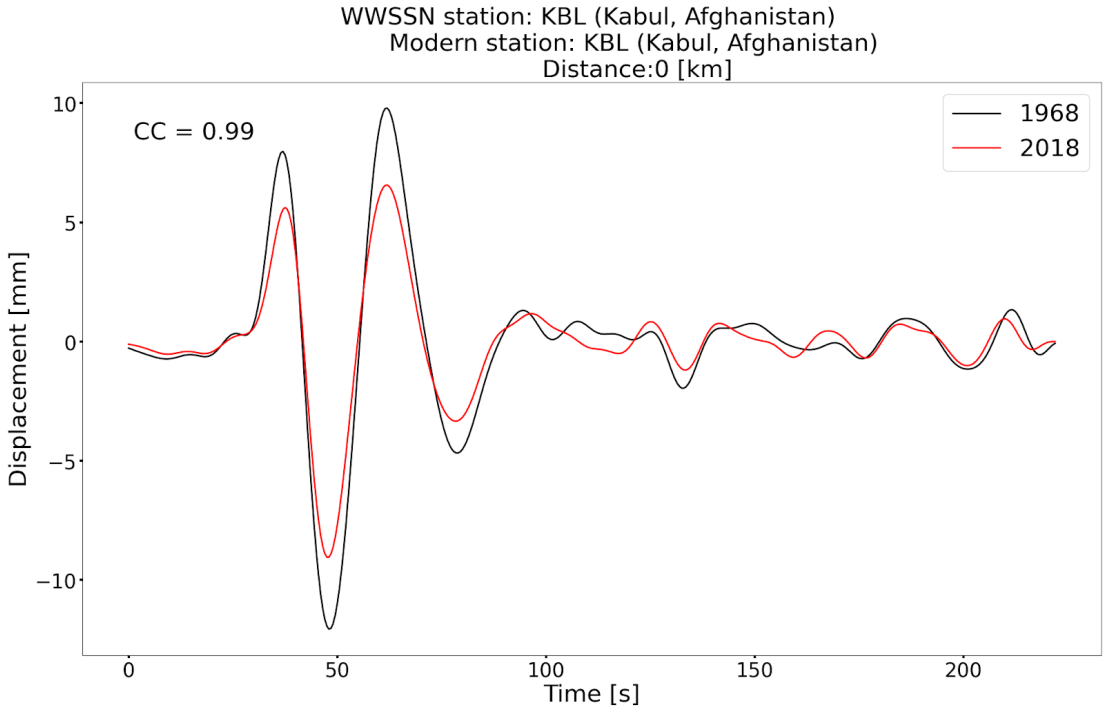

Figure D-5. 1968 earthquake recorded at the WWSSN Kabul, Afghanistan station (KBL) (black) and the vertical component for the 2018 Pinotepa event (red) recorded at the same location, after conversion to WWSSN instrument response.

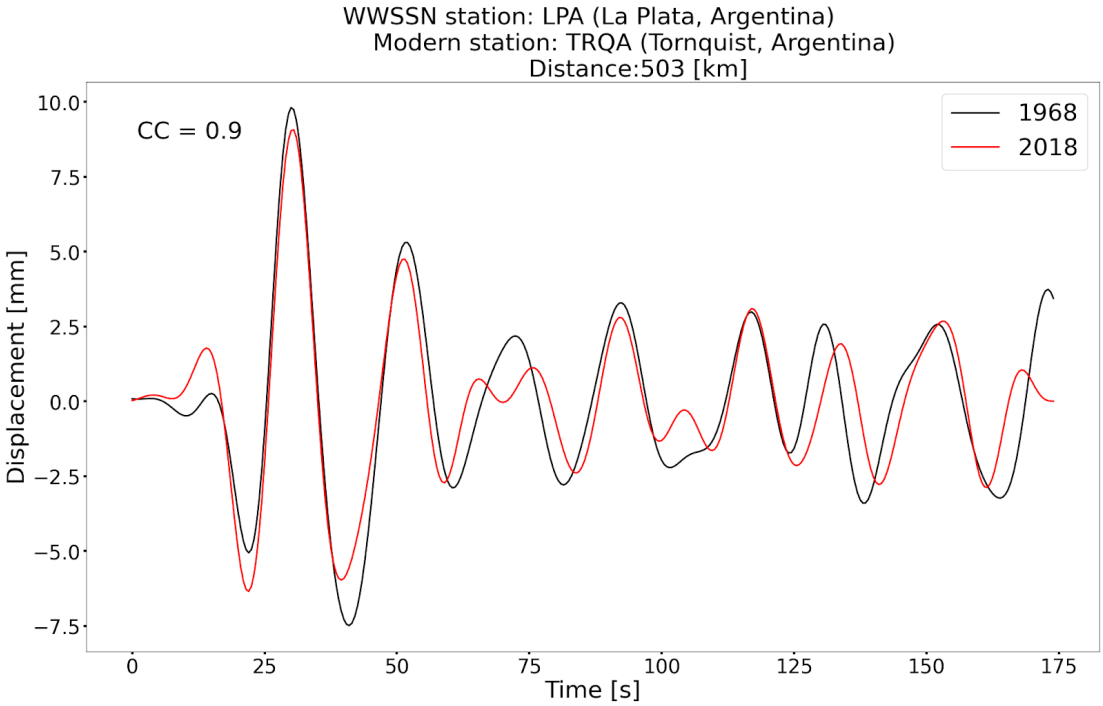

Figure D-6. 1968 earthquake recorded at the WWSSN La Plata, Argentina station (LPA) (black) and the vertical component for the 2018 Pinotepa event (red) recorded at Tornquist, Argentina (TRQA), after conversion to WWSSN instrument response.

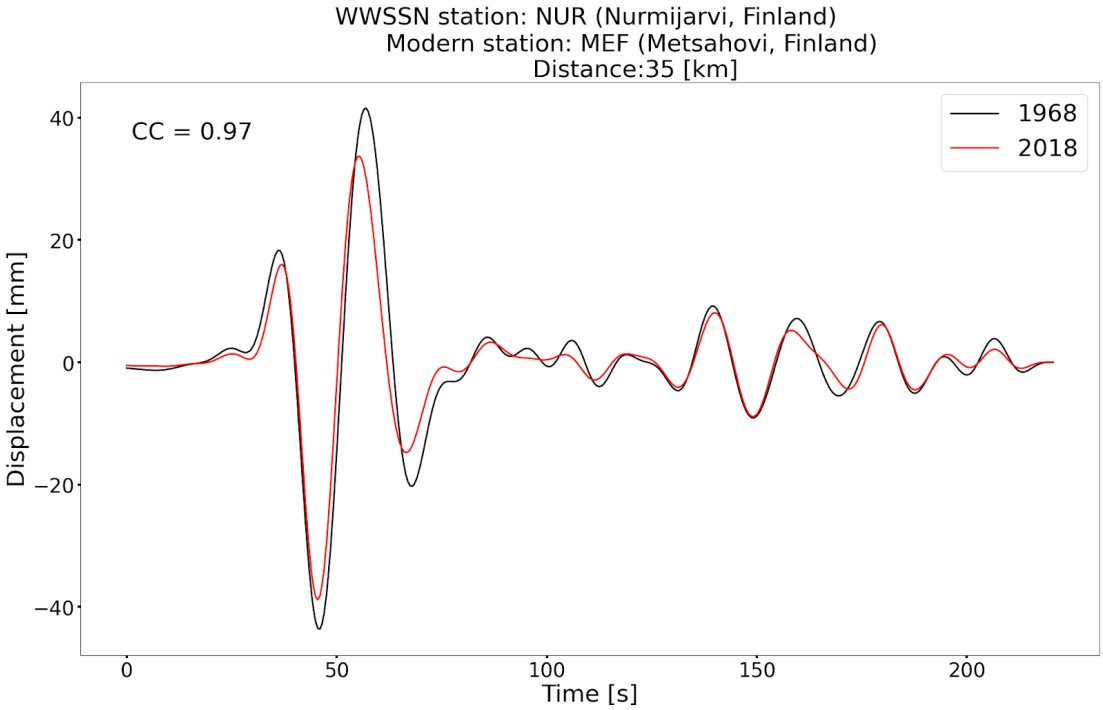

Figure D-7. 1968 earthquake recorded at the WWSSN Nurmijarvi, Finland station (NUR) (black) and the vertical component for the 2018 Pinotepa event (red) recorded at Metsahovi, Finland (MEF), after conversion to WWSSN instrument response.

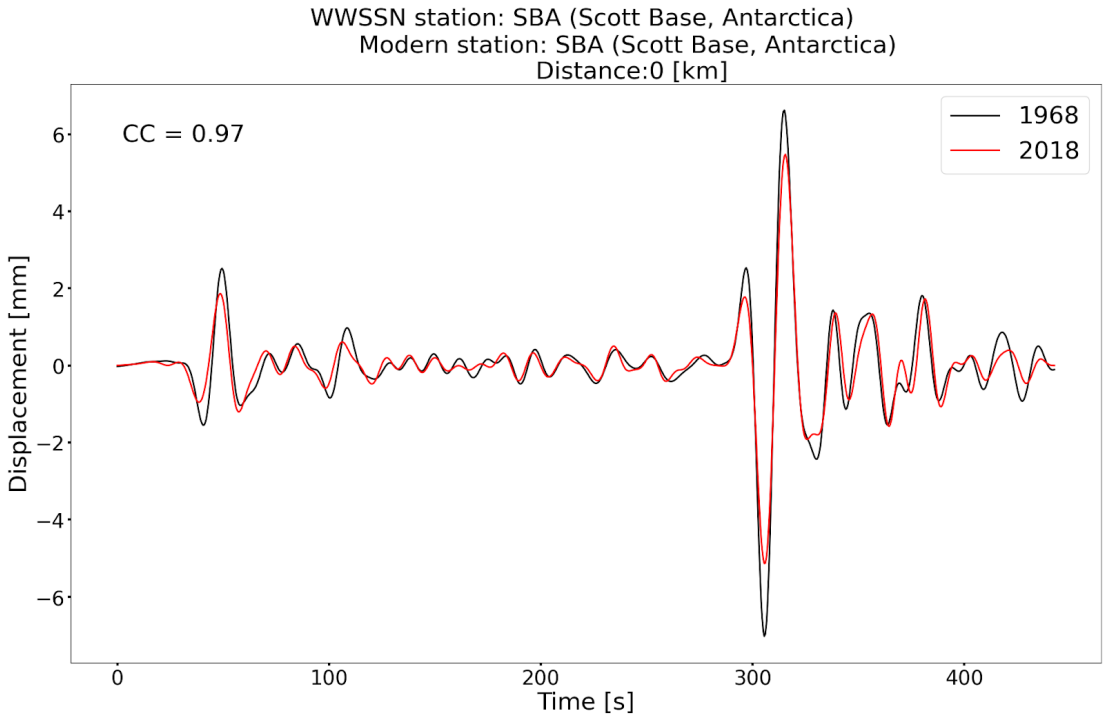

Figure D-8. 1968 earthquake recorded at the WWSSN Scott Base, Antarctica station (SBA) (black) and the vertical component for the 2018 Pinotepa event (red) recorded at the same location, after conversion to WWSSN instrument response.

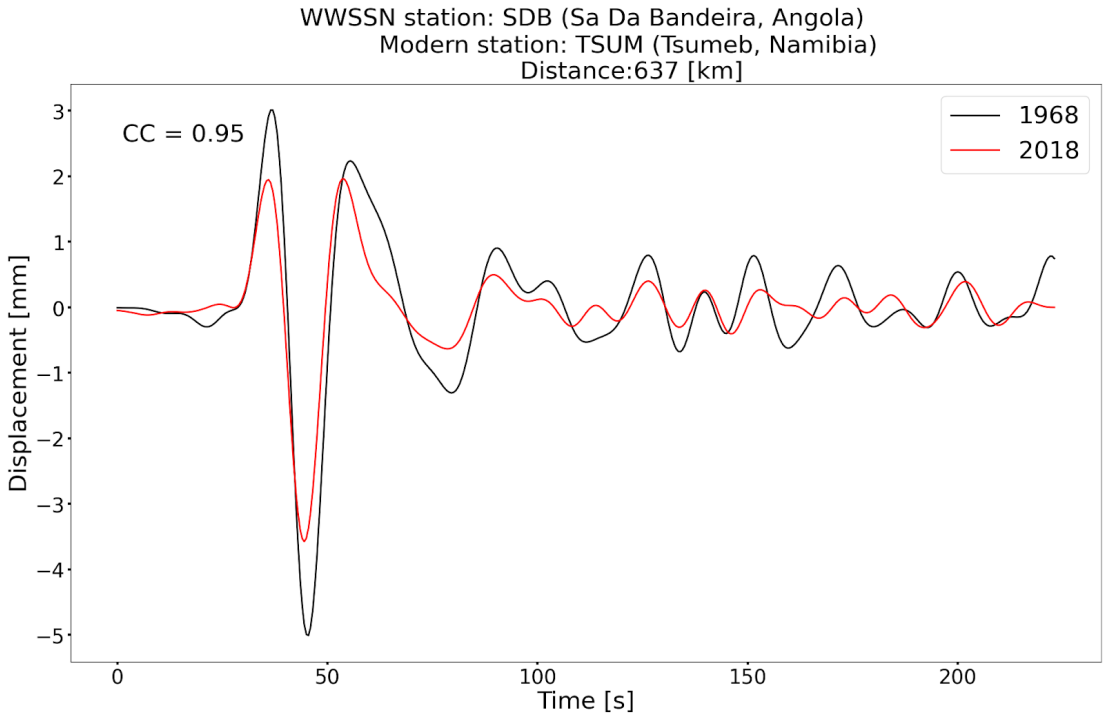

Figure D-9. 1968 earthquake recorded at the WWSSN Sa Da Banderia, Angola station (SDB) (black) and the vertical component for the 2018 Pinotepa event (red) recorded at Tsumeb, Namibia (TSUM), after conversion to WWSSN instrument response.

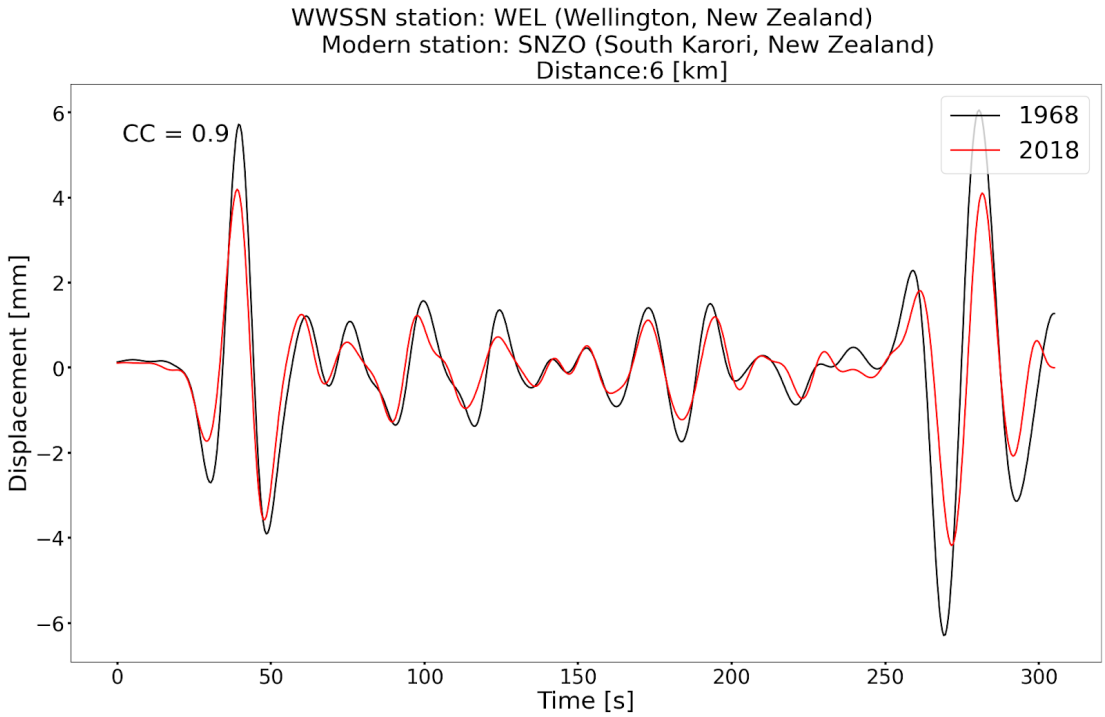

Figure D-10. 1968 earthquake recorded at the WWSSN Wellington, New Zealand (WEL) (black) and the vertical component for the 2018 Pinotepa event (red) recorded at South Karori, New Zealand (SNZO), after conversion to WWSSN instrument response.

References

Abercrombie, R. E. (1995). Earthquake source scaling relationships from− 1 to 5 ML using seismograms recorded at 2.5-km depth. Journal of Geophysical Research: Solid Earth, 100(B12), 24015-24036.

Aki, K. (1965). Maximum likelihood estimate of b in the formula log N= a-bM and its confidence limits. Bull. Earthq. Res. Inst., Tokyo Univ., 43, 237-239.

Albright, J. A., Gregg, P. M., Lu, Z., & Freymueller, J. T. (2019). Hindcasting magma reservoir stability preceding the 2008 eruption of Okmok, Alaska. Geophysical Research Letters, 46(15), 8801-8808.

Ando, M. (1975). Source mechanisms and tectonic significance of historical earthquakes along the Nankai Trough, Japan. Tectonophysics, 27(2), 119-140.

Armstrong, R. L. (1978). K-Ar dating: Late Cenozoic McMurdo volcanic group and dry valley glacial history, Victoria Land, Antarctica. New Zealand Journal of Geology and Geophysics, 21(6), 685-698.

Astiz, L., & Kanamori, H. (1984). An earthquake doublet in ometepec, guerrero, mexico. Physics of the earth and planetary interiors, 34(1-2), 24-45.

Astiz, L., Lay, T., & Kanamori, H. (1988). Large intermediate-depth earthquakes and the subduction process. Physics of the Earth and Planetary interiors, 53(1-2), 80-166.

Bean, C. J., De Barros, L., Lokmer, I., Métaxian, J. P., O'Brien, G., & Murphy, S. (2014). Long-period seismicity in the shallow volcanic edifice formed from slow-rupture earthquakes. Nature geoscience, 7(1), 71-75.

Beck, S. L., & Nishenko, S. P. (1990). Variations in the mode of great earthquake rupture along the central Peru subduction zone. Geophysical Research Letters, 17(11), 1969-1972.

Beck, S. L., & Ruff, L. J. (1984). The rupture process of the great 1979 Colombia earthquake: Evidence for the asperity model. Journal of Geophysical Research: Solid Earth, 89(B11), 9281-9291.

Beck, S. L., & Ruff, L. J. (1989). Great earthquakes and subduction along the Peru trench. Physics of the Earth and Planetary Interiors, 57(3-4), 199-224.

Begeman, C. B., Tulaczyk, S. M., & Fisher, A. T. (2017). Spatially variable geothermal heat flux in West Antarctica: evidence and implications. Geophysical Research Letters, 44(19), 9823-9832.

Benioff, H. (1955). Earthquake seismographs and associated instruments. In Advances in Geophysics (Vol. 2, pp. 219-275). Elsevier.

Benoit, J. P., & McNutt, S. R. (1996). Global volcanic earthquake swarm database 1979-1989 (pp. 96-69). US Department of the Interior, US Gological Survey.

Berg, J. H., Moscati, R. J., & Herz, D. L. (1989). A petrologic geotherm from a continental rift in Antarctica. Earth and Planetary Science Letters, 93(1), 98-108.

Bergen, K. J., & Beroza, G. C. (2019). Earthquake fingerprints: Extracting waveform features for similarity-based earthquake detection. Pure and Applied Geophysics, 176(3), 1037-1059.

Biggs, J., Lu, Z., Fournier, T., & Freymueller, J. T. (2010). Magma flux at Okmok Volcano, Alaska, from a joint inversion of continuous GPS, campaign GPS, and interferometric synthetic aperture radar. Journal of Geophysical Research: Solid Earth, 115(B12).

Bockheim, J. G., Campbell, I. B., & McLeod, M. (2007). Permafrost distribution and active-layer depths in the McMurdo Dry Valleys, Antarctica. Permafrost and periglacial processes, 18(3), 217-227.

Bormann, P., & Dewey, J. W. (2012). The new IASPEI standards for determining magnitudes from digital data and their relation to classical magnitudes. In *New Manual of Seismological Observatory Practice 2 (NMSOP-2)* (pp. 1-44). Deutsches GeoForschungsZentrum GFZ.

Bridges, D. L., & Gao, S. S. (2006). Spatial variation of seismic b-values beneath Makushin Volcano, Unalaska Island, Alaska. Earth and Planetary Science Letters, 245(1-2), 408-415.

Brodsky, E. E., and L. J. Lajoie (2013), Anthropogenic seismicity rates and operational parameters at the Salton Sea Geothermal Field, Science, 341(6), 543–546, doi:10.1126/science.1239213.

Burton-Johnson, A., Dziadek, R., & Martin, C. (2020). Geothermal heat flow in Antarctica: current and future directions. The Cryosphere, 14(11), 3843-3873.

Burton-Johnson, A., Halpin, J. A., Whittaker, J. M., Graham, F. S., & Watson, S. J. (2017). A new heat flux model for the Antarctic Peninsula incorporating spatially variable upper crustal radiogenic heat production. Geophysical Research Letters, 44(11), 5436-5446.

Buurman, H., West, M. E., & Power, J. A. (2006). Seismic precursors to volcanic explosions during the 2006 eruption of Augustine Volcano. The, 41-57.

Byers Jr, F. M., & Brannock, W. W. (1949). Volcanic activity on Umnak and Great Sitkin Islands, 1946–1948. Eos, Transactions American Geophysical Union, 30(5), 719-734.

Cattania, C., Rivalta, E., Hainzl, S., Passarelli, L., & Aoki, Y. (2017). A nonplanar slow rupture episode during the 2000 Miyakejima dike intrusion. Journal of Geophysical Research: Solid Earth, 122(3), 2054-2068.

Chael, E. P., & Stewart, G. S. (1982). Recent large earthquakes along the Middle American trench and their implications for the subduction process. Journal of Geophysical Research: Solid Earth, 87(B1), 329-338.

Chamberlain, C. J., Hopp, C. J., Boese, C. M., Warren-Smith, E., Chambers, D., Chu, S. X., ... & Townend, J. (2018). EQcorrscan: Repeating and Near-Repeating Earthquake Detection and Analysis in Python. Seismological Research Letters, 89(1), 173-181.

Chen, C., & Holland, A. A. (2016). PhasePApy: A robust pure Python package for automatic identification of seismic phases. Seismological Research Letters, 87(6), 1384-1396.

Chouet, B. A. (1996). Long-period volcano seismicity: its source and use in eruption forecasting. Nature, 380(6572), 309-316.

Chouet, B. A. (1996). Long-period volcano seismicity: its source and use in eruption forecasting. Nature, 380(6572), 309-316.

Chouet, B. A., & Matoza, R. S. (2013). A multi-decadal view of seismic methods for detecting precursors of magma movement and eruption. Journal of Volcanology and Geothermal Research, 252, 108-175.

Coats, R. R. (1950). Volcanic activity in the Aleutian Arc (pp. 35-49). US Government Printing Office.

Collier, L., and J. Neuberg. "Incorporating seismic observations into 2D conduit flow modeling." Journal of Volcanology and Geothermal Research 152, no. 3-4 (2006): 331-346.

Cooper, A. K., Davey, F. J., & Behrendt, J. C. (1987). Seismic stratigraphy and structure of the Victoria Land basin, western Ross Sea, Antarctica.

Costi, J., Arigony-Neto, J., Braun, M., Mavlyudov, B., Barrand, N. E., Da Silva, A. B., ... & Simoes, J. C. (2018). Estimating surface melt and runoff on the Antarctic Peninsula using ERA-Interim reanalysis data. Antarctic Science, 30(6), 379-393.

Cruz-Atienza, V. M., Tago, J., Villafuerte, C., Wei, M., Garza-Girón, R., Dominguez, L. A., ... & Kazachkina, E. (2021). Short-term interaction between silent and devastating earthquakes in Mexico. Nature communications, 12(1), 1-14.

Damiani, T. M., Jordan, T. A., Ferraccioli, F., Young, D. A., & Blankenship, D. D. (2014). Variable crustal thickness beneath Thwaites Glacier revealed from airborne gravimetry, possible implications for geothermal heat flux in West Antarctica. Earth and Planetary Science Letters, 407, 109-122.

Davies, J. H. (2013). Global map of solid Earth surface heat flow. Geochemistry, Geophysics, Geosystems, 14(10), 4608-4622.

Decker, E.R., and Bücker, C.J., (1982) Geothermal studies in the Ross Island-Dry Valley region: Madison, University of Wisconsin Press, p. 887–894.

Dodge, D. A., Beroza, G. C., & Ellsworth, W. L. (1996). Detailed observations of California foreshock sequences: Implications for the earthquake initiation process. Journal of Geophysical Research: Solid Earth, 101(B10), 22371-22392.

Doran, P. T., McKay, C. P., Clow, G. D., Dana, G. L., Fountain, A. G., Nylen, T., & Lyons, W. B. (2002). Valley floor climate observations from the McMurdo Dry Valleys, Antarctica, 1986–2000. Journal of Geophysical Research: Atmospheres, 107(D24), ACL-13.

Dugan, H. A., Doran, P. T., Tulaczyk, S., Mikucki, J. A., Arcone, S. A., Auken, E., ... & Virginia, R. A. (2015). Subsurface imaging reveals a confined aquifer beneath an ice-sealed Antarctic lake. Geophysical Research Letters, 42(1), 96-103.

Felzer, K. R., Becker, T. W., Abercrombie, R. E., Ekström, G., & Rice, J. R. (2002). Triggering of the 1999 Mw 7.1 Hector Mine earthquake by aftershocks of the 1992 Mw 7.3 Landers earthquake. Journal of Geophysical Research: Solid Earth, 107(B9), doi:10.1029/2001JB000911

Fielding, C. R., Henrys, S. A., & Wilson, T. J. (2006). Rift history of the western Victoria Land Basin: a new perspective based on integration of cores with seismic reflection data. In Antarctica (pp. 309-318). Springer, Berlin, Heidelberg.

Fisher, A. T., Becker, K., Narasimhan, I. T. N., Langseth, M. G., & Mottl, M. J. (1990). Passive, off-axis convection through the southern flank of the Costa Rica Rift. Journal of Geophysical Research: Solid Earth, 95(B6), 9343-9370.

Fisher, A. T., Mankoff, K. D., Tulaczyk, S. M., Tyler, S. W., & Foley, N. (2015). High geothermal heat flux measured below the West Antarctic Ice Sheet. Science advances, 1(6), e1500093.

Fitch, T. J., & Scholz, C. H. (1971). Mechanism of underthrusting in southwest Japan: A model of convergent plate interactions. Journal of Geophysical Research, 76(29), 7260-7292.

Foley, N., Tulaczyk, S., Auken, E., Grombacher, D., Mikucki, J., Foged, N., ... & Virginia, R. A. (2020). Mapping geothermal heat flux using permafrost thickness constrained by airborne electromagnetic surveys on the western coast of Ross Island, Antarctica. Exploration Geophysics, 51(1), 84-93.

Foley, N., Tulaczyk, S., Auken, E., Schamper, C., Dugan, H., Mikucki, J., ... & Doran, P. (2016). Helicopter-borne transient electromagnetics in high-latitude environments: An application in the McMurdo Dry Valleys, Antarctica. Geophysics, 81(1), WA87-WA99.

Fournier, T., Freymueller, J., & Cervelli, P. (2009). Tracking magma volume recovery at Okmok volcano using GPS and an unscented Kalman filter. Journal of Geophysical Research: Solid Earth, 114(B2).

Freymueller, J. T., & Kaufman, A. M. (2010). Changes in the magma system during the 2008 eruption of Okmok volcano, Alaska, based on GPS measurements. Journal of Geophysical Research: Solid Earth, 115(B12).

Garza-Giron, R. (2014) Spatial variation of the b value under Popocatepetl Volcano and its relation with the magma chamber. (Thesis, in Spanish) en Universidad Nacional Autónoma de México, México. Recuperado de https://repositorio.unam.mx/contenidos/428928.

Gerstenberger, M., Wiemer, S., & Giardini, D. (2001). A systematic test of the hypothesis that the b value varies with depth in California. *Geophysical Research Letters*, *28*(1), 57-60.

Geshi, N., Shimano, T., Chiba, T., & Nakada, S. (2002). Caldera collapse during the 2000 eruption of Miyakejima Volcano, Japan. Bulletin of Volcanology, 64(1), 55-68.

Goebel, T. H., & Brodsky, E. E. (2018). The spatial footprint of injection wells in a global compilation of induced earthquake sequences. Science, 361(6405), 899-904.

Grey, D. M. (2003). Post-caldera eruptions at Okmok volcano, Umnak Island, Alaska,with emphasis on recent eruptions from Cone A (Doctoral dissertation).

Grombacher, D., Auken, E., Foged, N., Bording, T., Foley, N., Doran, P.T., Mikucki, J., Dugan, H.A., Garza-Giron, R., Myers, K. and Virginia, R.A. (2021). Induced polarization effects in airborne transient electromagnetic data collected in the McMurdo Dry Valleys, Antarctica. Geophysical Journal International, 226(3), 1574-1583.

Haney, M. M. (2010). Location and mechanism of very long period tremor during the 2008 eruption of Okmok Volcano from interstation arrival times. Journal of Geophysical Research: Solid Earth, 115(B10).

Harrington, R. M., & Brodsky, E. E. (2007). Volcanic hybrid earthquakes that are brittle-failure events. Geophysical Research Letters, 34(6).

Hauck, C. (2002). Frozen ground monitoring using DC resistivity tomography. Geophysical research letters, 29(21), 12-1.

Helmstetter, A., Kagan, Y. Y., & Jackson, D. D. (2005). Importance of small earthquakes for stress transfers and earthquake triggering. Journal of Geophysical Research: Solid Earth, 110(B5) , doi:10.1029/2004JB003286.

Henrys, S. A., Wilson, T. J., Fielding, C. R., Hall, J., & Naish, T. R. (2008). Tectonic history of mid-Miocene to present southern Victoria Land Basin, inferred from seismic stratigraphy in McMurdo Sound, Antarctica.

Hersbach H, Bell B, Berrisford P, Hirahara S, Horányi A, Muñoz-Sabater J, Nicolas J, Peubey C, Radu R, Schepers D, Simmons A. The ERA5 global reanalysis. Quarterly Journal of the Royal Meteorological Society. 2020 Jul;146(730):1999-2049. https://doi.org/10.1002/qj.3803

Hersbach, H., Bell, B., Berrisford, P., Hirahara, S., Horányi, A., Muñoz-Sabater, J., & Simmons, A. (2020). The ERA5 global reanalysis. Quarterly Journal of the Royal Meteorological Society.(In print).

Hill, D., Reasenberg, P., Michael, A., Arabaz, W., Beroza, G., Brumbaugh, D., . . . Zollweg, J. (1993). Seismicity Remotely Triggered by the Magnitude 7.3 Landers, California, Earthquake. Science, 260(5114), 1617-1623.

Hjörleifsdóttir, V., Krishna Singh, S., Martínez-Peláez, L., Garza-Girón, R., Lund, B., & Ji, C. (2016, April). Observations of large earthquakes in the Mexican subduction zone over 110 years. In EGU General Assembly Conference Abstracts (pp. EPSC2016-10827).

Huang, Y., & Beroza, G. C. (2015). Temporal variation in the magnitude-frequency distribution during the Guy-Greenbrier earthquake sequence. Geophysical Research Letters, 42(16), 6639-6646.

Hutton, L. K., & Boore, D. M. (1987). The ML scale in southern California. *Bulletin of the Seismological Society of America*, *77*(6), 2074-2094.

Illsley-Kemp, F., Barker, S. J., Wilson, C. J., Chamberlain, C. J., Hreinsdóttir, S., Ellis, S., ... & Wadsworth, F. B. (2021). Volcanic unrest at Taupo¯ macr volcano in 2019: Causes, mechanisms and implications. Geochemistry, Geophysics, Geosystems, e2021GC009803.

Japan Meteorological Agency, National Catalogue of the Active Volcanoes in Japan (Fourth Edition). Retrieved from: http://www.data.jma.go.jp/svd/vois/data/tokyo/STOCK/souran_eng/menu.htm

Japan Meteorological Agency. (2016). Japan Meteorological Agency Seismological Data Format Report.

Johnson, J. H., Prejean, S., Savage, M. K., & Townend, J. (2010). Anisotropy, repeating earthquakes, and seismicity associated with the 2008 eruption of Okmok volcano, Alaska. Journal of Geophysical Research: Solid Earth, 115(B9).

Kanamori, H. (1972). Tectonic implications of the 1944 Tonankai and the 1946 Nankaido earthquakes. Physics of the earth and planetary interiors, 5, 129-139.

Kanamori, H., & Anderson, D. L. (1975). Theoretical basis of some empirical relations in seismology. Bulletin of the seismological society of America, 65(5), 1073-1095.

Kanamori, H., & Brodsky, E. E. (2004). The physics of earthquakes. Reports on Progress in Physics, 67(8), 1429.

Kanamori, H., & McNally, K. C. (1982). Variable rupture mode of the subduction zone along the Ecuador-Colombia coast. Bulletin of the Seismological Society of America, 72, 1241-1253.

Kanamori, H., Mori, J. I. M., Hauksson, E., Heaton, T. H., Hutton, L. K., & Jones, L. M. (1993). Determination of earthquake energy release and ML using TERRAscope. Bulletin of the Seismological Society of America, 83(2), 330-346.

Kato, A., & Ben-Zion, Y. (2021). The generation of large earthquakes. Nature Reviews Earth & Environment, 2(1), 26-39.

Kato, A., Fukuda, J. I., Kumazawa, T., & Nakagawa, S. (2016). Accelerated nucleation of the 2014 Iquique, Chile Mw 8.2 earthquake. Scientific reports, 6(1), 1-9.

Kato, A., Obara, K., Igarashi, T., Tsuruoka, H., Nakagawa, S., & Hirata, N. (2012). Propagation of slow slip leading up to the 2011 Mw 9.0 Tohoku-Oki earthquake. Science, 335(6069), 705-708.

Kyle, P. R. (1990). A. McMurdo volcanic group western Ross embayment. Volcanoes of the Antarctic plate and southern Oceans, 48, 18-145.

Kyle, P. R., & Cole, J. W. (1974). Structural control of volcanism in the McMurdo Volcanic Group, Antarctica. Bulletin volcanologique, 38(1), 16-25.

Kobayashi, H., Koketsu, K., Miyake, H., & Kanamori, H. (2020). Similarities and differences o the rupture processes of the 1952 and 2003 Tokach-Oki earthquakes. Journal of Geophysical Research: Solid Earth, 126, e2020JB020585.

Kong, Q., Trugman, D. T., Ross, Z. E., Bianco, M. J., Meade, B. J., & Gerstoft, P. (2019). Machine learning in seismology: Turning data into insights. Seismological Research Letters, 90(1), 3-14.

Kumazawa, T., Ogata, Y., Kimura, K., Maeda, K., & Kobayashi, A. (2016). Background rates of swarm earthquakes that are synchronized with volumetric strain changes. Earth and Planetary Science Letters, 442, 51-60, https://doi.org/10.1016/j.epsl.2016.02.049

Lachenbruch, A. H. (1957). Thermal effects of the ocean on permafrost. Geological Society of America Bulletin, 68(11), 1515-1530.

LaCoste Jr, L. J. (1934). A new type long period vertical seismograph. Physics, 5(7), 178-180.

Langer, H., Falsaperla, S., Powell, T., & Thompson, G. (2006). Automatic classification and a-posteriori analysis of seismic event identification at Soufriere Hills volcano, Montserrat. Journal of volcanology and geothermal research, 153(1-2), 1-10.

Larsen, J. F., Śliwiński, M. G., Nye, C., Cameron, C., & Schaefer, J. R. (2013). The 2008 eruption of Okmok Volcano, Alaska: Petrological and geochemical constraints on the subsurface magma plumbing system. Journal of Volcanology and Geothermal Research, 264, 85-106.

Larsen, J., Neal, C. A., Schaefer, J. R., Kaufman, M., & Lu, Z. (2015). The 2008 phreatomagmatic eruption of Okmok Volcano, Aleutian Islands, Alaska: chronology, deposits, and landform changes (No. RI 2015-2). Alaska Division of Geological & Geophysical Surveys.

Larsen,J.,Neal,C.,Webley,P.,Freymueller,J.,Haney,M.,McNutt,S.,Schneider,D.,Prejean,S.,Schaefer,J.andWessels,R.(2009).Eruption of Alaska volcano breaks historic pattern. Eos, Transactions American Geophysical Union, 90(20), 173-174.

Lay, T., & Kanamori, H. (1981). An asperity model of large earthquake sequences.

Lay, T, Kanamori, H., & Ruff, L. (1982). The asperity model and the nature of large subduction zone earthquake occurrence. Earthquake Prediction Research, 1, 3-71.

Lay, T., Kanamori, H., Ammon, C. J., Koper, K. D., Hutko, A. R., Ye, L., ... & Rushing, T. M. (2012). Depth-varying rupture properties of subduction zone megathrust faults. Journal of Geophysical Research: Solid Earth, 117(B4).

Lay, T., Kanamori, H., Ammon, C. J., Nettles, M., Ward, S. N., Aster, R. C., ... & Sipkin, S. (2005). The great Sumatra-Andaman earthquake of 26 december 2004. science, 308(5725), 1127-1133.

Lazzara, M. A., Weidner, G. A., Keller, L. M., Thom, J. E., & Cassano, J. J. (2012). Antarctic automatic weather station program: 30 years of polar observation. Bulletin of the American Meteorological Society, 93(10), 1519-1537.

Li, Y., Shan, X., Zhu, C., Qiao, X., Zhao, L., & Qu, C. (2020). Geodetic Model of the 2018 M w 7.2 Pinotepa, Mexico, Earthquake Inferred from InSAR and GPS Data. Bulletin of the Seismological Society of America, 110(3), 1115-1124.

Liu, C., Lay, T., Xiong, X., & Wen, Y. (2020). Rupture of the 2020 MW 7.8 earthquake in the Shumagin gap inferred from seismic and geodetic observations. Geophysical Research Letters, 47(22), e2020GL090806.

Lomax A, Curtis A (2001) Fast, probabilistic earthquake location in 3-D models using oct-tree importance sampling. Geophys Res Abstracts, 3:955.

Lomax, A., Zollo, A., Capuano, P., & Virieux, J. (2001). Precise, absolute earthquake location under Somma-Vesuvius volcano using a new 3D velocity model.Geophysical Journal International,146, 313–331

Lu, Z., & Dzurisin, D. (2010). Ground surface deformation patterns, magma supply, and magma storage at Okmok volcano, Alaska, from InSAR analysis: 2. Coeruptive deflation, July–August 2008. Journal of Geophysical Research: Solid Earth, 115(B5).

Lu, Z., & Dzurisin, D. (2014). InSAR imaging of Aleutian volcanoes. In InSAR Imaging of Aleutian Volcanoes (pp. 87-345). Springer Berlin Heidelberg, doi:10.1007/978-3-642-00348-6_6

Lu, Z., T. Masterlark, and D. Dzurisin (2005), Interferometric synthetic aperture study of Okmok volcano, Alaska: Magma supply dynamics and post-emplacement lava flow deformation, J. Geophys. Res., 110, B02403, doi:10.1029/2004JB003148.

Malfante, M., Dalla Mura, M., Mars, J. I., Métaxian, J. P., Macedo, O., & Inza, A. (2018). Automatic classification of volcano seismic signatures. Journal of Geophysical Research: Solid Earth, 123(12), 10-645.

Mann, D., Freymueller, J., & Lu, Z. (2002). Deformation associated with the 1997 eruption of Okmok volcano, Alaska. Journal of Geophysical Research: Solid Earth, 107(B4), ETG-7.

Masterlark, T., Haney, M., Dickinson, H., Fournier, T., & Searcy, C. (2010). Rheologic and structural controls on the deformation of Okmok volcano, Alaska: FEMs, InSAR, and ambient noise tomography. Journal of Geophysical Research: Solid Earth, 115(B2).

McCausland, W. A., Hamidah, N. N., Basuki, A., & Indrastuti, N. (2020). Local magnitude, coda magnitude, and radiated energy of volcanic tectonic earthquakes from October 2010 to December 2011 at Sinabung volcano, Indonesia. Bulletin of Volcanology, 82, 1-16.

McGinnis, L. D., Bowen, R. H., Erickson, J. M., Allred, B. J., & Kreamer, J. L. (1985). East-West Antarctic boundary in McMurdo Sound. Tectonophysics, 114(1-4), 341-356.

McNutt, S. R. (1996). Seismic monitoring and eruption forecasting of volcanoes: a review of the state-of-the-art and case histories. In Monitoring and mitigation of volcano hazards (pp. 99-146). Springer Berlin Heidelberg.

McNutt, S. R. (2005). Volcanic seismology. Annu. Rev. Earth Planet. Sci., 32, 461-491.

Melgar, D., Ruiz-Angulo, A., Garcia, E. S., Manea, M., Manea, V. C., Xu, X., ... & Ramirez-Guzmán, L. (2018). Deep embrittlement and complete rupture of the lithosphere during the M w 8.2 Tehuantepec earthquake. Nature Geoscience, 11(12), 955-960.

Mendoza, C., & Dewey, J. W. (1984). Seismicity associated with the great Colombia-Ecuador earthquakes of 1942, 1958, and 1979: Implications for barrier models of earthquake rupture. Bulletin of the seismological society of America, 74(2), 577-593.

Mendoza, C., & Martínez-López, M. R. (2021). Rupture Models of Recent Mw> 7 Thrust Earthquakes in the Guerrero–Oaxaca Region of the Mexico Subduction Zone Using Teleseismic Body Waves. Seismological Research Letters.

Menke, W. (2018). Geophysical data analysis: Discrete inverse theory. Academic press.

Miao, Q., & Langston, C. A. (2007). Empirical distance attenuation and the local-magnitude scale for the central United States. Bulletin of the Seismological Society of America, 97(6), 2137-2151.

Mignan, A. (2014). The debate on the prognostic value of earthquake foreshocks: A meta-analysis. Science Reports, 4, 4099.

Mikucki, J. A., Auken, E., Tulaczyk, S., Virginia, R. A., Schamper, C., Sørensen, K. I., ... & Foley, N. (2015). Deep groundwater and potential subsurface habitats beneath an Antarctic dry valley. Nature communications, 6(1), 1-9.

Minakami, T. (1961). Fundamental research for predicting volcanic eruptions (Part 1): earthquakes and crustal deformations originating from volcanic activities. Bull. Earthquake Res. Inst. Univ. Tokyo, 38, 497-544.

Mogi, K. (1963). Some discussions on aftershocks, foreshocks and earthquake swarms: the fracture of a semi-infinite body caused by an inner stress origin and its relation to the earthquake phenomena (third paper), Bull. Earthquake Res. Inst. Univ. Tokyo, 41,615-658.

Mousavi, S. M., Ellsworth, W. L., Zhu, W., Chuang, L. Y., & Beroza, G. C. (2020). Earthquake transformer—an attentive deep-learning model for simultaneous earthquake detection and phase picking. Nature communications, 11(1), 1-12.

Muñoz-Sabater, J., Dutra, E., Agustí-Panareda, A., Albergel, C., Arduini, G., Balsamo, G., ... & Thépaut, J. N. (2021). ERA5-Land: A state-of-the-art global reanalysis dataset for land applications. Earth System Science Data Discussions, 1-50.

Myers, K. F., Doran, P. T., Tulaczyk, S. M., Foley, N. T., Bording, T. S., Auken, E., ... & Virginia, R. A. (2020). Thermal legacy of a large paleolake in Taylor Valley, East Antarctica as evidenced by an airborne electromagnetic survey. The Cryosphere Discussions, 1-31.

Nagai, R., Kikuchi, M., & Yamanaka, Y. (2001). Comparative study on the source processes of recurrent large earthquakes in Sanriku-oki region: the 1968 Tokachi-oki earthquake and the 1994 Sanriku-oki earthquake. Zisin, 54, 267–280.

National Academies of Sciences, Engineering, and Medicine. (2017). Volcanic eruptions and their repose, unrest, precursors, and timing. National Academies Press.

Neuberg, J. W., Tuffen, H., Collier, L., Green, D., Powell, T., & Dingwell, D. (2006). The trigger mechanism of low-frequency earthquakes on Montserrat. Journal of Volcanology and Geothermal Research, 153(1-2), 37-50.

Neuberg, J., Luckett, R., Baptie, B., & Olsen, K. (2000). Models of tremor and low-frequency earthquake swarms on Montserrat. Journal of Volcanology and Geothermal Research, 101(1-2), 83-104.

Nishimura, T., Ozawa, S., Murakami, M., Sagiya, T., Tada, T., Kaidzu, M., & Ukawa, M. (2001). Crustal deformation caused by magma migration in the northern Izu Islands, Japan. Geophysical Research Letters, 28(19), 3745-3748.

Obara, K., & Kato, A. (2016). Connecting slow earthquakes to huge earthquakes. Science, 353(6296), 253-257.

Ogata, Y. (1988). Statistical models for earthquake occurrences and residual analysis for point processes. Journal of the American Statistical Association, 83(401), 9-27, doi: 10.1080/01621459.1988.10478560.

Ohlendorf, S. J., Thurber, C. H., Pesicek, J. D. & Prejean, S. G. Seismicity and seismic structure at Okmok Volcano, Alaska. Journal of Volcanology and Geothermal Research **278–279**, 103–119 (2014).

Oliver, J., and Murphy, L.M., 1971, WWNSS—Seismology's global network of observing stations. Science, v. 174, p. 254–261.

Osterkamp, T. E., & Burn, C. R. (2003). Permafrost Encyclopedia of Atmospheric Sciences 1st edn, ed JR Holton, J Pyle and JA Curry.

Page, M. T., Van Der Elst, N., Hardebeck, J., Felzer, K., & Michael, A. J. (2016). Three Ingredients for Improved Global Aftershock Forecasts: Tectonic Region, Time-Dependent Catalog Incompleteness, and Intersequence Variability. Bulletin of the Seismological Society of America.

Park, S.-C., & Mori, J. (2007). Are asperity patterns persistent? Implication from large earthquakes in Papua New Guinea. Journal of Geophysical Research, 112, B03303.

Passarelli, L., Rivalta, E., Cesca, S., & Aoki, Y. (2015). Stress changes, focal mechanisms, and earthquake scaling laws for the 2000 dike at Miyakejima (Japan). Journal of Geophysical Research: Solid Earth, 120(6), 4130-4145.

Peterson, J., & Hutt, C. R. (2014). World-wide standardized seismograph network: a data users guide (p. 82). US Department of the Interior, US Geological Survey.

Petersen, T. (2007). Swarms of repeating long-period earthquakes at Shishaldin Volcano, Alaska, 2001–2004. *Journal of Volcanology and Geothermal Research*, *166*(3-4), 177-192.

Pollard, D., DeConto, R. M., & Nyblade, A. A. (2005). Sensitivity of Cenozoic Antarctic ice sheet variations to geothermal heat flux. Global and Planetary Change, 49(1-2), 63-74.

Poupinet, G., Ellsworth, W. L., & Frechet, J. (1984). Monitoring velocity variations in the crust using earthquake doublets: An application to the Calaveras

Fault, California. Journal of Geophysical Research: Solid Earth, 89(B7), 5719-5731.

Power, J. A., Friberg, P. A., Haney, M. M., Parker, T., Stihler, S. D., & Dixon, J. P. (2019). A unified catalog of earthquake hypocenters and magnitudes at volcanoes in Alaska—1989 to 2018 (No. 2019-5037). US Geological Survey.

Power, J. A., Lahr, J. C., Page, R. A., Chouet, B. A., Stephens, C. D., Harlow, D. H., ... & Davies, J. N. (1994). Seismic evolution of the 1989–1990 eruption sequence of Redoubt Volcano, Alaska. Journal of Volcanology and Geothermal Research, 62(1-4), 69-94.

Press, F., Ewing, M., & Lehner, F. (1958). A long-period seismograph system. Eos, Transactions American Geophysical Union, 39(1), 106-108.

Quinn, J. E., Ming, D. W., Morris, R. V., Douglas, S., Kounaves, S. P., McKay, C. P., ... & Archer Jr, P. D. (2010, January). Mineralogy of Antarctica Dry Valley Soils: Implications for Pedogenic Processes on Mars. In Lunar and Planetary Science Conference.

Reasenberg, P. A., & Jones, L. M. (1989). Earthquake hazard after a mainshock in California. Science, 243(4895), 1173-1176, doi: 10.1126/science.243.4895.1173.

Richter, C. F. (1935). An instrumental earthquake magnitude scale. Bulletin of the seismological society of America, 25(1), 1-32.

Richter, C. F. (1958). Elementary Seismology. W. H. Freeman, San Francisco, 768 pp.

Roman, D. C. (2005). Numerical models of volcanotectonic earthquake triggering on non-ideally oriented faults. *Geophysical Research Letters*, *32*(2).

Roman, D. C., & Cashman, K. V. (2006). The origin of volcano-tectonic earthquake swarms. *Geology*, *34*(6), 457-460.

Ruff, L. J. (1992). Asperity distributions and large earthquake occurrence in subduction zones. Tectonophysics, 211(1-4), 61-83.

Ruiz, S., Metois, M., Fuenzalida, A., Ruiz, J., Leyton, F., Grandin, R., ... & Campos, J. (2014). Intense foreshocks and a slow slip event preceded the 2014 Iquique Mw 8.1 earthquake. Science, 345(6201), 1165-1169.

Scholz, C. H. (1968). The frequency-magnitude relation of microfracturing in rock and its relation to earthquakes. *Bulletin of the seismological society of America*, *58*(1), 399-415.

Scholz, C. H. (2015). On the stress dependence of the earthquake b value. *Geophysical Research Letters*, *42*(5), 1399-1402.

Schorlemmer, D., Wiemer, S., & Wyss, M. (2005). Variations in earthquake-size distribution across different stress regimes. Nature, 437(7058), 539, doi:10.1038/nature04094.

Schwartz, S. Y. (1999). Noncharacteristic behavior and complex recurrence of large subduction zone earthquakes. Journal of Geophysical Research, 104, 23,111-23,125.

Schwartz, S. Y., & Ruff, L. J. (1987). Asperity distribution and earthquake occurrence in the southern Kurile Islands arc. Physics of the earth and planetary interiors, 49(1-2), 54-77.

Seroussi, H., Ivins, E. R., Wiens, D. A., & Bondzio, J. (2017). Influence of a West Antarctic mantle plume on ice sheet basal conditions. Journal of Geophysical Research: Solid Earth, 122(9), 7127-7155.

Shapiro, N. M., & Ritzwoller, M. H. (2004). Inferring surface heat flux distributions guided by a global seismic model: particular application to Antarctica. Earth and Planetary Science Letters, 223(1-2), 213-224.

Shelly, D. R., Ellsworth, W. L., & Hill, D. P. (2016). Fluid-faulting evolution in high definition: Connecting fault structure and frequency-magnitude variations during the 2014 Long Valley Caldera, California, earthquake swarm. Journal of Geophysical Research: Solid Earth, 121(3), 1776-1795.

Shelly, D. R., Hill, D. P., Massin, F., Farrell, J., Smith, R. B., & Taira, T. A. (2013). A fluid-driven earthquake swarm on the margin of the Yellowstone caldera. Journal of Geophysical Research: Solid Earth, 118(9), 4872-4886.

Shelly, D. R., Taira, T. A., Prejean, S. G., Hill, D. P., & Dreger, D. S. (2015). Fluid-faulting interactions: Fracture-mesh and fault-valve behavior in the February 2014 Mammoth Mountain, California, earthquake swarm. Geophysical Research Letters, 42(14), 5803-5812.

Shi, Y., & Bolt, B. A. (1982). The standard error of the magnitude-frequency b value. Bulletin of the Seismological Society of America, 72(5), 1677-1687.

Singh, S. K., Astiz, L., & Havskov, J. (1981). Seismic gaps and recurrence periods of large earthquakes along the Mexican subduction zone: A reexamination. Bulletin of the Seismological Society of America, 71(3), 827-843.

Singh, S. K., Reinoso, E., Arroyo, D., Ordaz, M., Cruz-Atienza, V., Pérez-Campos, X., ... & Hjörleifsdóttir, V. (2018). Deadly intraslab Mexico earthquake of 19 September 2017 (M w 7.1): Ground motion and damage pattern in Mexico City. Seismological Research Letters, 89(6), 2193-2203.

Socquet, A., Valdes, J. P., Jara, J., Cotton, F., Walpersdorf, A., Cotte, N., ... & Norabuena, E. (2017). An 8 month slow slip event triggers progressive nucleation of the 2014 Chile megathrust. Geophysical Research Letters, 44(9), 4046-4053.

Sørensen, K. I., and E. Auken (2004), SkyTEM—a new high-resolution helicopter transient electromagnetic system, Explor. Geophys., 35

Sparks, R. S. J. (2003). Forecasting volcanic eruptions. Earth and Planetary Science Letters, 210(1), 1-15, https://doi.org/10.1016/S0012-821X(03)00124-9.

Suárez, G. (2021). Large earthquakes in the Tehuantepec subduction zone: evidence of a locked plate interface and large-scale deformation of the slab. Journal of Seismology, 25(2), 449-460.

Suárez, G., & Albini, P. (2009). Evidence for great tsunamigenic earthquakes (M 8.6) along the Mexican subduction zone. Bulletin of the Seismological Society of America, 99(2A), 892-896.

Suárez, G., Ruiz-Barón, D., Chico-Hernández, C., & Zúñiga, F. R. (2020). Catalog of preinstrumental earthquakes in central Mexico: epicentral and magnitude estimations based on macroseismic data. Bulletin of the Seismological Society of America, 110(6), 3021-3036.

Sykes, L. R., Kisslinger, J. B., House, L., Davies, J. N., & Jacob, K. H. (1980). Rupture zones of great earthquakes in the Alaska-Aleutian arc, 1784 to 1980. Science, 210(4476), 1343-1345.

Tajima, F. (1984). Study of the source processes of the 1965, 1968 and 1978 Oaxaca Earthquakes using short-period records. Journal of Geophysical Research: Solid Earth, 89(B3), 1867-1873.

Tetzner, D., Thomas, E., & Allen, C. (2019). A validation of ERA5 reanalysis data in the Southern Antarctic Peninsula—Ellsworth land region, and its implications for ice core studies. Geosciences, 9(7), 289.

Thatcher, W. (1989). Earthquake recurrence and risk assessment in circum-Pacific seismic gaps. Nature, 341, 432-434.

Thelen, W., West, M., & Senyukov, S. (2010). Seismic characterization of the fall 2007 eruptive sequence at Bezymianny Volcano, Russia. *Journal of Volcanology and Geothermal Research*, *194*(4), 201-213.

Thelen, W., Malone, S., & West, M. (2011). Multiplets: Their behavior and utility at dacitic and andesitic volcanic centers. *Journal of Geophysical Research: Solid Earth*, *116*(B8).

Tilmann, F., Zhang, Y., Moreno, M., Saul, J., Eckelmann, F., Palo, M., et al. (2016). The 2015 Illapel earthquake, central Chile: A type case for a characteristic earthquake? Geophysical Research Letters, 43, 574-583.

Toda, S., Stein, R. S., & Sagiya, T. (2002). Evidence from the AD 2000 Izu islands earthquake swarm that stressing rate governs seismicity. Nature, 419(6902), 58-61.

Traversa, P., & Grasso, J. R. (2009). Brittle creep damage as the seismic signature of dyke propagations within basaltic volcanoes. Bulletin of the Seismological Society of America, 99(3), 2035-2043, doi: 10.1785/0120080275.

Traversa, P., and J. R. Grasso (2010), How is Volcano Seismicity Different from Tectonic Seismicity? Bulletin of the Seismological Society of America, 100(4), 1755–1769, doi:10.1785/0120090214.

Trugman, D. T., & Shearer, P. M. (2017). GrowClust: A hierarchical clustering algorithm for relative earthquake relocation, with application to the Spanish Springs and Sheldon, Nevada, earthquake sequences. Seismological Research Letters, 88(2A), 379-391.

Uhrhammer, R. A., and Collins, E. R. (1990). Synthesis of Wood-Anderson seismograms from broadband digital records. Bull. Seism. Soc. Am., 80, 702-716.

Umakoshi, K., Takamura, N., Shinzato, N., Uchida, K., Matsuwo, N., & Shimizu, H. (2008). Seismicity associated with the 1991–1995 dome growth at Unzen

Volcano, Japan. *Journal of volcanology and geothermal research*, *175*(1-2), 91-99.

U. N. A. de México Seismology (2013). Ometepec-Pinotepa Nacional, Mexico earthquake of 20 March 2012 (MW 7.5): A Preliminary Report. Geofísica Internacional, 52(2), 173-196.

Unema, J. A., Ort, M. H., Larsen, J. F., Neal, C. A., & Schaefer, J. R. (2016). Water-magma interaction and plume processes in the 2008 Okmok eruption, Alaska. Bulletin, 128(5-6), 792-806.

Utsu, T. (1965). A method for determining the value of" b" in a formula log n= a-bm showing the magnitude-frequency relation for earthquakes. Geophys. Bull. Hokkaido Univ., 13, 99-103.

Utsu, T. (1992), Introduction to Seismicity, Surijishingaku (Mathematical Seismology) (VII), Inst. Statis. Math. 139–157 (in Japanese).

Utsu, T. (1961). A statistical study on the occurrence of aftershocks. Geophysical Magazine, 30(4).

Utsu, T. (1971). Aftershocks and earthquake statistics (2): further investigation of aftershocks and other earthquake sequences based on a new classification of earthquake sequences. Journal of the Faculty of Science, Hokkaido University. Series 7, Geophysics, 3(4), 197-266.

Vales, D., Dias, N. A., Rio, I., Matias, L., Silveira, G., Madeira, J., ... & Haberland, C. (2014). Intraplate seismicity across the Cape Verde swell: a contribution from a temporary seismic network. Tectonophysics, 636, 325-337.

Vallée, M., & Douet, V. (2016). A new database of source time functions (STFs) extracted from the SCARDEC method. Physics of the Earth and Planetary Interiors, 257, 149-157.

van der Elst, N. J. (2021). B-positive: A robust estimator of aftershock magnitude distribution in transiently incomplete catalogs. Journal of Geophysical Research: Solid Earth, 126(2),e2020JB021027.

Vidale, J. E., K. L. Boyle, and P. M. Shearer (2006), Crustal earthquake bursts in California and Japan: Their patterns and relation to volcanoes, Geophys. Res. Lett., 33, L20313, doi:10.1029/2006GL027723.

Villafuerte, C., Cruz-Atienza, V., Tago, J., Solano, D., Garza-Girón, R., Franco, S., ... & Kostoglodov, V. (2021). Slow slip events and megathrust coupling

changes reveal the earthquake potential before the 2020 Mw 7.4 Huatulco, Mexico, event. Earth Space Sci. Open Archive, 56(10.1002).

Waldhauser, F., & Ellsworth, W. L. (2000). A double-difference earthquake location algorithm: Method and application to the northern Hayward fault, California. Bulletin of the Seismological Society of America, 90(6), 1353-1368.

Waldhauser, F., & Schaff, D. P. (2008). Large-scale relocation of two decades of Northern California seismicity using cross-correlation and double-difference methods. Journal of Geophysical Research: Solid Earth, 113(B8).

Warren, N. W., & Latham, G. V. (1970). An experimental study of thermally induced microfracturing and its relation to volcanic seismicity. Journal of Geophysical Research, 75(23), 4455-4464.

Wech, A., Tepp, G., Lyons, J., & Haney, M. (2018). Using earthquakes, T waves, and infrasound to investigate the eruption of Bogoslof volcano, Alaska. Geophysical Research Letters, 45(14), 6918-6925.

Wessel, P., Luis, J. F., Uieda, L., Scharroo, R., Wobbe, F., Smith, W. H. F., & Tian, D. (2019). The generic mapping tools version 6. *Geochemistry, Geophysics, Geosystems*, *20*(11), 5556-5564.

Wetzler, N., Brodsky, E. E., & Lay, T. (2016). Regional and stress drop effects on aftershock productivity of large megathrust earthquakes. Geophysical Research Letters, 43(23).

White, R., & McCausland, W. (2016). Volcano-tectonic earthquakes: A new tool for estimating intrusive volumes and forecasting eruptions. Journal of Volcanology and Geothermal Research, 309, 139-155, doi: 10.1016/j.jvolgeores.2015.10.020.

Wiemer, S., & McNutt, S. R. (1997). Variations in the frequency-magnitude distribution with depth in two volcanic areas: Mount St. Helens, Washington, and Mt. Spurr, Alaska. Geophysical Research Letters, 24(2), 189–192, http://doi.org/10.1029/96gl03779

Wiemer, S., & Wyss, M. (2000). Minimum magnitude of completeness in earthquake catalogs: Examples from Alaska, the western United States, and Japan. Bulletin of the Seismological Society of America, 90(4), 859-869.

Wiemer, S., & Wyss, M. (2002). Mapping spatial variability of the frequency-magnitude distribution of earthquakes. Advances in Geophysics, 45, 259-V.

Wilch, T. I., Denton, G. H., Lux, D. R., & McIntosh, W. C. (1993). Limited Pliocene glacier extent and surface uplift in middle Taylor Valley, Antarctica. Geografiska Annaler: Series A, Physical Geography, 75(4), 331-351.

Wyss, M., Klein, F., Nagamine, K., & Wiemer, S. (2001). Anomalously high b-values in the South Flank of Kilauea volcano, Hawaii: evidence for the distribution of magma below Kilauea's East rift zone. *Journal of Volcanology and Geothermal Research*, *106*(1-2), 23-37.

Yamanaka, Y., & Shimazaki, K. (1990). Scaling relationship between the number of aftershocks and the size of the main shock. Journal of Physics of the Earth, 38(4), 305-324.

Yang, W., & Ben-Zion, Y. (2009). Observational analysis of correlations between aftershock productivities and regional conditions in the context of a damage rheology model. Geophysical Journal International, 177(2), 481-490.

Ye, L., Kanamori, H., & Lay, T. (2018). Global variations of large megathrust earthquake rupture characteristics. Science advances, 4(3), eaao4915.

Ye, L., Kanamori, H., Avouac, J. P., Li, L., Cheung, K. F., & Lay, T. (2016). The 16 April 2016, M_w 7.8 (MS 7.5) Ecuador earthquake: A quasi-repeat of the 1942 MS 7.5 earthquake and partial re-rupture of the 1906 MS 8.6 Colombia–Ecuador earthquake. Earth and Planetary Science Letters, 454, 248-258.

Ye, L., Lay, T., Bai, Y., Cheung, K. F., & Kanamori, H. (2017). The 2017 M_w 8.2 Chiapas, Mexico, earthquake: Energetic slab detachment. Geophysical Research Letters, 44, 11824-11832.

Ye, L., Lay, T., Kanamori, H., Yamazaki, Y., & Cheung, K. F. (2021). The 22 July 2020 MW 7.8 Shumagin seismic gap earthquake: Partial rupture of a weakly coupled megathrust. Earth and Planetary Science Letters, 562, 116879.

Yoon, C. E., O'Reilly, O., Bergen, K. J., & Beroza, G. C. (2015). Earthquake detection through computationally efficient similarity search. Science advances, 1(11), e1501057.

Zobin, V. M. (2012). Introduction to volcanic seismology (Vol. 6). Elsevier.